NOVEL VENTURI TECHNOLOGY FOR THE PURPOSE OF GAS-LIQUID MASS TRANSFER

A Thesis submitted to Cardiff University for the Degree of

Doctorate of Philosophy

By

Paul Ryan

Division of Mechanical Engineering,

School of Engineering,

Cardiff University,

Wales, U.K.

June 2013

DECLARATION

This work has not been submitted in substance for any other degree or award at this or any other university or place of learning, nor is being submitted concurrently in candidature for any degree or other award.

Signed ..... Date .....

STATEMENT 1

This thesis is being submitted in partial fulfilment of the requirements for the degree of Doctorate of Philosophy.

Signed ..... Date .....

STATEMENT 2

This thesis is my own independent work/investigation, except where otherwise stated. Other sources are acknowledged by explicit references. The views expressed are my own.

Signed ..... Date .....

STATEMENT 3

I hereby give consent for my thesis, if accepted, to be available for photocopying and for inter-library loans **after expiry of a bar on access previously approved by the Academic Standards and Quality Committee.**

Signed ..... Date .....

ABSTRACT

The introduction of a gas into a liquid occurs in many chemical and biological engineering processes which require a chemical or biological reaction to occur. In the case of aeration, air is introduced into water. The aim of this thesis is to investigate the use of a novel venturi technology, termed the insert that can alleviate the problems of existing technologies such as, restricted depth of use, mechanical wear and failure due to the moving parts and problems with clogging and fouling, whilst providing high aeration efficiency.

The inserts tested comprise of a central hub surrounded by a number of aerofoil shaped vanes, which have air orifices located on their surfaces. The vanes create a number of discrete channels, which separate the flow and each channel is representative of a venturi. Three inserts and a regular venturi were tested. The inserts had different angles of attack and a blockage ratio of either 1.5 or 4. Three orientations of the air orifices with respect to the vanes were considered. All inserts were compared to a regular venturi of blockage ratio 1.5, which was made to British Standard 5167-4:2003.

Two flow regimes were identified. The first is when a bubbly flow exists throughout the entire length of the downcomer. The second is when a large ventilated cavity forms at the point of air injection, which is typical at low water and higher air flow rates and was more prominent with the lower blockage ratio inserts. The ventilated cavity was seen to have a negative effect in terms of bubble size, specific power and mass transfer performance. The results show that the bubble size produced depends on the air and water flow rates, the flow regime and the insert design. The average bubble size at fixed flow rates is essentially the same (differences within ± 10 %), when a ventilated cavity is present. However, when a full bubbly flow is present throughout the downcomer there were smaller average bubble sizes. Also inducing a swirl in combination with a high blockage ratio resulted in coring of the air at the higher flow rates. Reducing the air to water velocity slip ratio at the throat, by increasing the blockage ratio and the amount of air orifices, reduces the length of a ventilated cavity.

This study also examines the hydrodynamic and mass transfer characteristics of the inserts. The inserts were tested in a laboratory scale experimental setup within a 100 mm ID pipe, where they were located above the liquid surface. The results show that increasing the blockage ratio of the insert promoted a smaller mean bubble size, resulting in an increased mass transfer rate. However, the increased blockage ratio results in significantly higher specific power consumption. The effect of insert design on the volumetric mass transfer coefficient was measured using a dynamic method outlined in the ASCE standard ASCE/EWRI 2-06. The results confirmed that a reduced bubble size had a superior performance. The mass transfer coefficient is observed to be up to 50 % larger with a higher blockage ratio at higher flow rates.

Computational fluid dynamic simulations are validated against the laboratory scale experimentation to

determine the average bubble size, specific power consumption and the mass transfer coefficient, which were found to be within 6, 15 and 25 % of the laboratory scale values respectively. In addition to with these validated models, geometric scaling was investigated for the one of the inserts, where it was geometrically scaled from 100 mm to 190 mm ID. It was found that the geometrically scaled insert had an increased Sauter mean bubble size of 18.6 %, an increased pressure loss of 14.5 % and increased specific power consumption of 18.5 %.

Along with the laboratory scale experimental work, hydrodynamic and mass transfer testing was conducted on high strength wastewater and clean water with an insert geometrically scaled up to 150 and 190 mm respectively. A number of key parameters were seen to affect the system performance, including the physical properties of the water, such as dissolved solids, the upstream geometry and mixture outlet.

In conclusion it was found that the inserts in this experimental work have an improved aeration performance in comparison to the regular venturi, at the lower air and water flow rates. However, above these lower flow rates, the regular venturi has the best aeration performance. Areas for improvement have however been identified for the inserts, such as decreasing the air to water velocity slip ratio at the throat, where the performance of the redesigned insert can successfully be investigated using CFD simulations.

ACKNOWLEDGEMENTS

I would like to express my appreciation to my research supervisors Dr Daphne O'Doherty, Professor Tim O'Doherty, Dr Devin Sapsford for their valuable guidance and encouragement. I believe I have been really lucky to have been given the opportunity to work under their supervision.

The experiments reported here in this thesis would not have been possible without the help of the technicians of the Mechanical Engineering Discipline, Mr Stephen Mead, Mr K.S Lyall and Mr Malcolm Seaborne. Also I would like to thank Mr Daniel Pugh for his valuable advice concerning the high-speed photography experiments. I am also very grateful to Mr Martyn Griffiths for his advice on safety issue associated with this research.

Finally, I would like to thank HydroVenturi Ltd for their support in the early stages of this study, in particular Dr Mike Faram and Mr David Roberts, who both provided valuable technical support and guidance.

P. Ryan

Cardiff

June 2013

CONTENTS

LIST OF FIGURES

LIST OF TABLES

NOMENCLATURE

Symbol	Description	Units
a	Interfacial area for mass transfer	$\frac{m^2}{m^3}$
$a(V,V')$	Aggregation rate	$\frac{1}{s}$
A	Area	m^2
A_δ	Falling film area	m^2
b	Jet to column area ratio	$[-]$
c	Concentration	mg/l
c_∞^*	Equilibrium saturation concentration	mg/l
$C_1\ to\ C_7$	Empirical constants	$[-]$
C_D	Coefficient of drag	$[-]$
C_f	Coefficient of friction	$[-]$
d	Diameter	m
d_1	Major axis bubble diameter	m
d_2	Minor axis bubble diameter	m
d_b	Average bubble diameter	m
d_m	Mixture diameter in plunging liquid jet	m
d_v	Volume average bubble diameter	m
D	Diffusivity	$\frac{m^2}{s}$
e	System efficiency (Delivered power over wire power)	$[-]$
e'_{mass}	Average energy dissipation per unit mass	$\frac{1}{m^2 s^3}$
e'_{vol}	Average energy dissipation per unit volume	$\frac{kg}{ms^3}$
E	Specific power	$\frac{W}{m^3}$
E_{Fr}	Friedel dimensionless factor	$[-]$
$E\ddot{o}$	Eötvös number $\left(\frac{\Delta P g L^2}{\sigma}\right)$	$[-]$
f	Friction factor	$[-]$
F_{Fr}	Friedel dimensionless factor	$[-]$
F_i	External body force	N
F_{ji}	Virtual mass force	N
$\vec{F}_{lift,i}$	Lift force	N
Fr	Froude number $\left(\frac{u^2}{dg}\right)$	$[-]$

Symbol	Description	Units
Fr_H	Friedel dimensionless factor	$[-]$
g	Gravity (- 9.81)	$\frac{m^2}{s}$
$g(V)$	Breakage rate	$\frac{1}{s}$
G_x	Axial flux of axial momentum	$\frac{kg.m^2}{s^2}$
G_θ	Axial flux of tangential momentum	$\frac{kg.m^3}{s^2}$
h	Frequency of collision in population balance model	$\frac{1}{s}$
h_f	Head loss due to friction	m
h_i	Specific enthalpy	$\frac{J}{kg}$
h_{ji}	Interphase enthalpy	W
h_L	Head loss	m
H	Henry constant	$[-]$
H_{Fr}	Friedel dimensionless factor	$[-]$
I	Unit tensor	$[-]$
j	Superficial velocity	$\frac{m}{s}$
j_{GL}	Drift flux	$\frac{m^3}{m^2 s}$
J	Mass flux	$\frac{kg}{m^2 s}$
k	Mass transfer coefficient	$\frac{m}{s}$
k	Turbulent kinetic energy, when related to turbulence in computational fluid dynamics	$\frac{m^2}{s^2}$
k_L	Liquid film mass transfer coefficient	$\frac{m}{s}$
$k_L a$	Overall oxygen mass transfer coefficient	$\frac{1}{s}$
K	Proportionality constant $\frac{U_{z(max)}}{U_{film}}$	$[-]$
l	Characteristic mixing length	m
L	Length	m
L_B	Bubbly flow length	m
L_C	Ventilated cavity length	m
L_W	Length of recirculation beneath a ventilated cavity	m
$\dot{m}$	Mass flow rate	$\frac{kg}{s}$

Symbol	Description	Units
$\dot{m}_{ji}$	Mass transfer from phase j to phase i	$\frac{kg}{s}$
M	Mass	kg
n	Chemical amount	$moles$
N_b	Number of bubbles sampled	$[-]$
N_p	Pressure number $\left(\frac{\rho A^2 \Delta P}{\dot{m}^2}\right)$	$[-]$
N_μ	Viscosity number $\left(\frac{\mu}{\rho\left(gd^3\right)^{0.5}}\right)$	$[-]$
$pg(V')$	Number of fragments from bubble breakage	$\frac{1}{s}$
P	Pressure	Pa
q_i	Heat flux	$\frac{W}{m^2}$
Q	Volumetric flow rate	$\frac{m^3}{s}$
Q_{ji}	Flow rate of enthalpy between phase j to phase i	W
r	radius	m
r_s	Surface renewal rate	$\frac{m^2}{s}$
R	Ideal gas constant (8.314)	$\frac{J}{K.mol}$
Re	Reynolds number $\left(\frac{\rho u d}{\mu}\right)$	$[-]$
R_0	Endogenous respiration of bacteria	$\frac{mgDO}{L.hr}$
R_v	Blockage ratio	$[-]$
S	Slip velocity ratio	$[-]$
Sc	Schmidt number $\left(\frac{\mu}{\rho D}\right)$	$[-]$
S_n	Swirl number	$[-]$
Sh	Sherwood number $\left(\frac{jd}{D\Delta c}\right)$	$[-]$
t	Time	s
T	Temperature	$°C$
U	Velocity	$\frac{m}{s}$
ΔU^2	Square of the velocity difference across the bubble	$\frac{m}{s}$
u^*	Friction velocity	$\frac{m}{s}$
U_s	Shock propagation velocity	$\frac{m}{s}$
$U_{z(maz)}$	Maximum axial velocity inside the vortex beneath a ventilated cavity	$\frac{m}{s}$

Symbol	Description	Units
V	Volume	$\frac{m^3}{s}$
W	Hydraulic power	W
We	Weber number $\left(\frac{\rho u^2 d}{\sigma}\right)$	$[-]$
x	Vapour quality	$[-]$
$\vec{x}$	External set of co-ordinates in population balance model	$[-]$
y	Distance	m
y^+	Non-dimensional wall distance for a wall-bounded flow $\left(\frac{u^* y}{\nu}\right)$	
z	Height	m
	Greek letters	
α	Alpha factor, ratio of $k_L a$ in wastewater to tap water	$[-]$
α_i	Volume fraction of phase i in FLUENT	$[-]$
β	Beta factor, ratio of C_s in wastewater to tap water	$[-]$
β	Distribution of daughter bubbles in population balance model	$[-]$
γ	Relative humidity	$\%$
Γ_a	Vorticity	$\frac{1}{s}$
δ	Film thickness	m
ε	Surface roughness	m
ε_G	Gas void fraction	$[-]$
ϵ	Energy dissipation	$\frac{W}{kg}$
η	Kolmogorov micro-scale	$[-]$
θ	Angle	$^\circ$
θ	Temperature correction factor for $k_L a$	$[-]$
λ	Bulk viscosity	$\frac{kg}{ms}$
λ	Efficiency of collisions in population balance model	$[-]$
Λ	Pressure loss coefficient	$[-]$
Λ_e	Pressure loss coefficient for a sudden expansion	$[-]$
μ	Dynamic viscosity	$\frac{kg}{ms}$
ν	Kinematic viscosity	$\frac{m^2}{s}$
ρ	Density	$\frac{kg}{m^3}$
σ	Surface tension	$\frac{N}{m}$

Symbol	Description	Units
τ	Shear stress	Pa
τ	Temperature correction factor for C_s	$[-]$
τ_w	Wall shear stress	Pa
φ	Flow variable in FLUENT	$[-]$
Φ	Internal set of co-ordinates in population balance model	$[-]$
Φ_{Fr}	Friedel two-phase multiplier	$[-]$
ω	Specific dissipation rate	$\frac{1}{s}$
Ω	Saturation pressure correction factor	$[-]$

Subscripts

1	Upstream
2	Downstream
20	At standard conditions a temperature of 20˚C and a pressure of 101.325 kPa
$2ph$	Two-phase
32	Sauter mean
a	Air
A	Acceleration
$ATMOS$	Atmospheric conditions
b	Bubble
$crit$	Critical
f	Friction
f	In-process conditions when related to mass transfer
g	Gravity
G	Gas
i	Dispersed or secondary phase
j	Continuous or primary phase
J	Jet
L_1	Active bulk liquid for mass transfer
L	Liquid
max	Maximum
N	Nozzle
O_2	Oxygen
s	Saturation
t	Throat
TH	Throat
$TOTAL$	Total

Symbol	Description	Units
w	Water	
	Abbreviations	
$A1$	Non-zero angle of attack insert, vane pitch of 4.5˚, air orifices located on both sides of the vanes, blockage ratio of 4.	
$A2$	Zero angle of attack insert, air orifices located on both sides of the vanes, blockage ratio of 4.	
$A2b$	A2 insert with air orifices located on just the lower side of the vanes	
AE	Aeration efficiency	$\frac{kgO_2}{kWh}$
$ASCE$	American Society of Civil Engineers	
ASP	Activated sludge plants	
BOD	Biological oxygen demand	$\frac{mg}{L}$
BS	British Standards	
CFD	Computational fluid dynamics	
COD	Chemical oxygen demand	$\frac{mg}{L}$
CS	Central sparger	
DO	Dissolved oxygen	$\frac{mg}{L}$
DNS	Direct numerical simulation	
DP	Deliver power	W
DS	Downstream	
$E-E$	Eulerian-Eulerian	
EPA	Environmental Protection Agency	
EWT	Enhanced wall treatment	
FDM	Finite difference method	
FEM	Finite element method	
FVM	Finite volume method	
HS	Horizontal sparger	
HV	Non-zero angle of attack insert, vane pitch of 4.5˚, blockage ratio of 1.5.	
$HV1$	HV insert with air orifices located on both sides of the vanes	
$HV1_a$	Air inlet on the lower side of the vanes on HV1 insert	
$HV1_b$	Air inlet on the upper side of the vanes on HV1 insert	
$HV1_{190}$	HV1 insert geometrically scaled up to 190 mm ID	
$HV2$	HV insert with air orifices located on just the lower side of the vanes	
$HV3$	HV insert with air orifices located on just the upper side of the vanes	
ID	Internal diameters	

Symbol	Description	Units
LES	Large eddy simulation	
MS	Microsoft	
$NLRA$	Non-linear regression analysis	
OTE	Oxygen transfer efficiency	$\%$
OTR	Oxygen transfer rate	$\frac{kgO_2}{hr}$
$QMOM$	Quadrature method of moments	
PBE	Population balance equation	
PBM	Population balance model	
PDE	Partial differential equation	
PJS	Plunging jet sparger	
PS	Peripheral sparger	
$RANS$	Reynolds average Navier-Stokes	
RSM	Reynolds stress model	
SAE	Standard aeration efficiency	$\frac{kgO_2}{kWh}$
$SOTE$	Standard oxygen transfer efficiency	$\%$
$SOTR$	Standard oxygen transfer rate	$\frac{kgO_2}{hr}$
SMM	Standard method of moments	
SST	Shear stress transport	
TI	Turbulence intensity	$\%$
TDS	Total dissolved solids	$\frac{mg}{L}$
TKE	Turbulent kinetic energy	$\frac{m^2}{s^2}$
US	Upstream	
$V1$	Venturi made to British standards (BS EN ISO 5167-4:2003), convergent and divergent angles of 21˚ and 7˚ respectively, blockage ratio of 1.5.	
VOF	Volume of fluid	
WP	Wire power	W
$WWTP$	Wastewater treatment plant	

CHAPTER 1

INTRODUCTION

1.1. Motivation for the thesis

In the water sector, aeration process optimisation has become particularly topical, with over 55% of the energy consumed in wastewater treatment being estimated as stemming from aeration delivery, with the aeration market itself being predicted to be worth €4.56 billion worldwide (Helmut Kaiser Consultancy, 2006). Process optimisation can be achieved through the use of better condition monitoring and control systems, while another option has been to implement more energy efficient aeration technology. Within the wastewater sector there is a plethora of technologies designed for introducing a gas into a liquid, which in the case of aeration air is introduced into water, wastewater or any other liquid for the purpose of transferring oxygen. Many of these technologies have a number of operational problems, such as clogging and fouling, maintenance and installation, or operational instabilities due to phase separation. In practice, there appears to be little consensus on what is the optimum option. There appears to be no single system that presents the ideal combination of cost effectiveness, low maintenance, consistent performance, high delivery capacity, low energy, long life and technical performance. Therefore, there is the potential for a new and novel technology to make a significant impact in the aeration market, with the market itself presenting a great deal of financial opportunities.

1.2. Overview of gas to liquid mass transfer

Throughout chemical and biological engineering, many processes require a chemical or biological reaction to occur between a gas and some form of soluble or insoluble material which is often present in a liquid. The gas presented to the liquid may come in the form of a pure gas or as a mixture. The gas is dissolved within the liquid phase so that the required chemical reaction can take place. There are many names given for a device where a gas is introduced into a liquid, such as gas-liquid reactors, gas-liquid contactors and aerators. Aerators are the commonly used expression for when the gas phase, air or pure oxygen is introduced to a liquid phase typically water or wastewater for the process of oxygenation.

Naturally occurring gas-liquid reactions take place, for instance, aeration takes place in streams, rivers and lakes. Within water, the natural soluble constituents are removed by any micro-organisms that are found in the water (Boyle, et al., 2002). The micro-organisms require oxygen to survive and to oxidise the constituents, for example, carbon into carbon dioxide. In natural waters the source of the oxygen is the ambient air, the diffusion of air into the water is as a result of the concentration difference between the two phases at the interface, which is the liquid surface. The process is carried out in nature without any additional mechanical energy because of this, the overall transfer of the oxygen to the water is very slow and the amount of biochemical reactions is also low (Boyle, et al., 2002). In many situations artificial

aeration and agitation is required to achieve a suitable level of mass transfer.

In the treatment of water, a certain concentration of dissolved oxygen, DO, is necessary in any body of water to ensure the occurrence of the self purification processes. If the oxygen requirement cannot be supplied naturally, then the purification processes cease and the water turns septic. Engineering techniques exist to avoid this extreme condition occurring. Assisted aeration maintains DO levels and accelerates the purification processes. An added advantage of assisted aeration may be the removal of volatile organic compounds, which are ultimately responsible for the tastes and odours.

1.3. Use of aerators in industry

In the treatment of industrial or municipal wastewater, higher mass transfer rates are required due to the higher levels of soluble and insoluble constituents found in the liquid phase, the wastewater. Mass transfer rates are enhanced through increasing the interfacial contact surface area between the two phases, as well as increasing the intensity of the mass transfer fluxes through increasing the turbulence in the process. This can be achieved with additional mechanical energy. Therefore, high performance aerators with high mass transfer rates usually require a high consumption of mechanical energy (Gaddis, 1999). Within industrial and municipal wastewater treatment the oxygen concentration in water is a prime indicator of the water quality for human use, as well as for aquatic flora and fauna. The aim of artificial aeration, like naturally occurring aeration, is to replenish the used oxygen in the liquid.

Aerators are found in vertical pipe flows and occur in many industrial situations. According to Boyle (2002), they are found typically in industrial and water purification processes such as,

a) Aeration and DO transfer for industrial and municipal wastewater treatment.
b) Preventing the deterioration and improving the water quality in storage reservoirs, through oxygenation.
c) Maintaining an adequate supply of oxygen for DO transfer in industrial fermentation.

Aerators in the form of venturi type devices are designed to mix the air and the relevant liquid together prior to injection into the bulk liquid. A typical venturi can be used to entrain air at its point of maximum constriction. This is where the flowing liquid is accelerated to a higher velocity stream, resulting in a decrease in static pressure, in accordance with Bernoulli's theorem. At this constriction point air can be entrained into the liquid flow as a result of the reduction in static pressure. This entrainment of air can be done either from the atmosphere or through imposed means, such as a compressor. In the resultant two-phase flow, mass transfer can occur. Mass transfer can occur from the air into the liquid or vice-versa, through the processes of absorption or gas stripping. Due to the turbulent nature of the flow, mixing occurs which can remove the requirement for mechanical agitation or mixing in the bulk liquid.

According to Bagatur (2005) aerators that use a venturi device can be used to solve a number of problems

including the following: -

a) Excessive biological and chemical oxygen demand, BOD and COD, in wastewater treatment
b) Increasing the level of DO for drinking water and in aquariums and fish farms.
c) Oxidisation of compounds dissolved or suspended in water.
d) Disinfection in drinking water treatment.
e) Dispelling other dissolved gases such as carbon dioxide, sulphur and methane.
f) Reduction in odour in wastewater treatment plants

1.4. The wastewater treatment market and aeration

Aeration and aeration systems in the industrial and municipal wastewater treatment market were predicted to be worth €4.56 billion worldwide by 2010 (Helmut Kaiser Consultancy, 2006). For manufacturers of aeration products this segment of the aeration market presents a great deal of financial opportunities. Other less profitable sectors include fisheries and river quality maintenance (Helmut Kaiser Consultancy, 2006).

There are a number of end user groups that require wastewater treatment. One of these is municipal wastewater treatment, which concerns the treatment of domestic waste from populated areas. This water treatment is generally funded by government or by national water companies. Pharmaceutical and chemical industries also produce various wastes or materials that can potentially contaminate water supplies. Other industries include petrochemical, textiles, paper and pulp, as well as food and food processing industries (Helmut Kaiser Consultancy, 2006).

Performance, pricing and energy usage are the deciding factors for any equipment installation. Durability is also a major factor in industrial processes as it can affect how well a plant can function. For an aerator it should not be easily clogged and the system needs to be able to withstand aggressive wastewater and industrial waste.

1.5. Wastewater treatment process

Aeration or more specifically, oxygenation plays an important role in many water and wastewater treatment processes. In these processes, aeration provides oxygen which is then dissolved in the water to establish an aerobic environment to support the microbial degradation of organic matter. Further to supplying oxygen, aeration also provides mixing to enhance the level of interaction between microorganisms and the organic matter, whether dissolved or suspended. A number of methods for artificially enhancing oxygen transfer rates beyond what can be achieved naturally are available, (Tchobanoglous, et al., 2002) and will be discussed later in this chapter.

Artificially aerated treatment processes, such as activated sludge treatment, were developed from initial

research work carried out in the early 1900's presenting opportunities beyond those offered by conventional fixed-film processes, of which the trickling filter is an example (Alleman, 1996). Between the end of the Second World War and the present day, activated sludge plants, ASPs, became a dominant feature in most secondary wastewater treatment process designs. In the operation of such plants, air is introduced to secondary wastewater to provide DO, resulting in the formation of biological flocs and so reducing the organic content of the sewage. Biologically activated sludge is recycled from the tail end of the process to the head in order to re-seed the wastewater.

Both industrial and municipal wastewater contains many impurities. Although the type and sequence of wastewater treatment may vary from one treatment plant to another. The process shown in Figure 1.1, for the Regional Municipality of Ottawa-Carleton's, Canada wastewater treatment plant is fairly typical. The impurities are treated in wastewater treatment and purification plants using a variety of methods, these methods are split into three main categories including mechanical, biological and chemical-physical techniques.

A Wastewater Treatment Plant, WWTP, can be divided in 4 stages. The first stage in the wastewater treatment process is the mechanical process where the aim is to remove solid waste from the sewage. This prevents damage to pumps and the clogging of pipes. The raw sewage passes through a number of decreasingly sized screens to remove larger debris. Lighter organic solids will still remain suspended in the water which flows into large tanks, called primary clarifiers. In the primary clarifiers the heavier organic solids settle by gravity. The settled solids are called primary sludge. This is removed along with any floating matter.

The primary effluent is then transferred to the biological or secondary stage. Here, the wastewater is mixed with a controlled population of bacteria and a supply of oxygen. The microorganisms are used to eliminate colloids, which is a substance microscopically dispersed evenly throughout the sewage, dirt and other impurities through aerobic and anaerobic digestion (Indicators and Assessment Office of Environment Canada, 2001). There are two aspects of aeration. The first is that aeration supplies the required oxygen to the metabolising microorganisms and the second is that it provides mixing. The mixing enables the micro-organisms to come into contact with the dissolved and suspended organic matter. The effluent is then transferred to secondary clarifiers, which serve the same role as the primary clarifier. The clear secondary effluent may flow directly to the receiving environment or to a disinfection facility prior to release.

Before the final effluent is released into the receiving waters, it may be disinfected to reduce the disease-causing microorganisms that remain in it. Chemicals are added to remove phosphorous and nitrogen from the clean water. Chlorine gas or a chlorine-based disinfectant such as sodium hypochlorite is used to remove any remaining bacteria (Indicators and Assessment Office of Environment Canada, 2001). To avoid excess chlorine escaping to the environment, the effluent may be de-chlorinated prior to discharge. Before

the clean water is finally released into a river system, aeration may be required to bring the DO level of the clean water up to the same level as the river water.

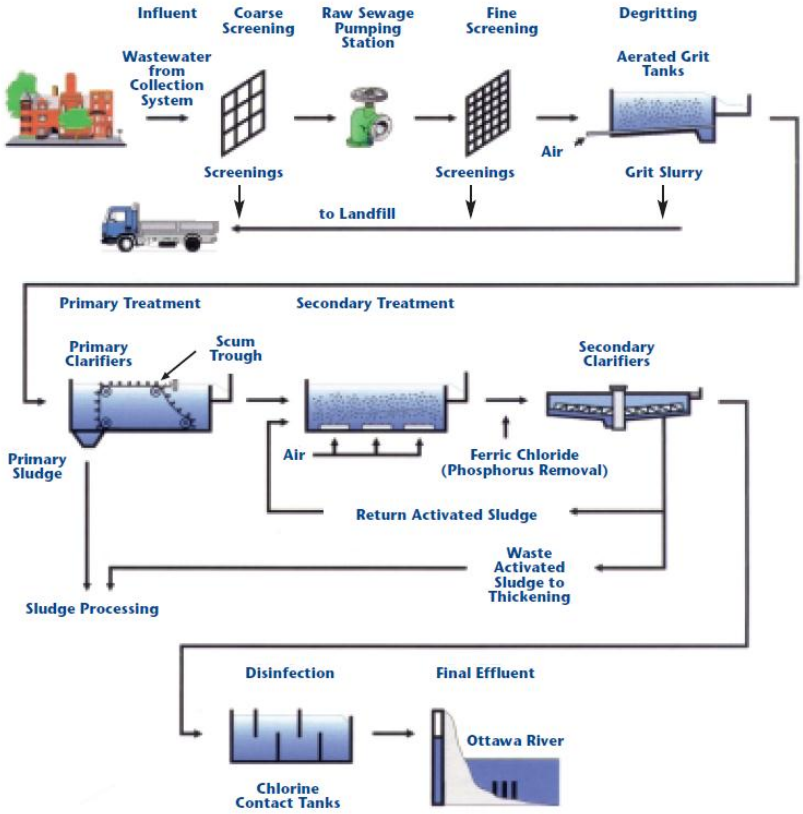

Figure 1.1: - Illustration of a typical wastewater treatment plant. (Indicators and Assessment Office of Environment Canada, 2001).

1.6. Aerators currently used

There are several different designs of aerators. They are classified into two broad types, surface aerators and dispersed air systems. Surface aerators, which are mainly used in biological wastewater treatment processes operate at the liquid surface and entrain air by violent agitation of the liquid surface. As would be expected these types of devices generally are only used on basins with a relatively shallow depth. The dispersed air systems introduce the air usually at the base of the aeration tank in the form of small bubbles, as a result increasing the interfacial area for mass transfer within the bulk liquid.

Comparisons between the various types of aerators and their relative advantages are reported in a standardised form, for example the standard oxygen transfer efficiency, SOTE, which is the fraction of oxygen brought in contact with the water that actually dissolve into it, at a standardised temperature and pressure conditions of 20˚C and 101.325 kPa, as set out by the British standard, BS EN 12255-15:2003 and the ASCE standard, ASCE/EWRI-2-06. The standard oxygen transfer rate, SOTR, is the rate of oxygen transfer observed at standard conditions, when the concentration of DO in the water is initially zero. The standard aeration efficiency, SAE, is the energy consumed in dissolving a specific amount of oxygen. These are most commonly used methods for comparison between aeration technologies (ASCE, 2007). The ASCE standard

EWRI-2-06 will be referred to in this study because it is the standard used by consultants Wastewater Management, whom are used in this study for the large scale experimental mass transfer testing, outlined in Chapter 9. The ASCE standard also comments on spatial variation testing when only one DO probe is used, when conducting mass transfer testing in clean water, shown in Appendix B. Although, the outlined procedures for determining mass transfer are identical between the British standard, BS EN 12255-15:2003 and the ASCE standard, ASCE/EWRI-2-06. A further parameter termed the alpha factor, α, presents the ratio of oxygen transfer in wastewater compared to clean water. This factor can vary depending on effluent characteristics. An alpha factor of 1 suggests a performance that is unaffected by the presence of wastewater components. For some high agitation aeration systems, alpha factors of 1 have occasionally been reported (Fabiyi, 2008).

1.7. Surface aerators

Surface aerators can be divided into two further sub-divisions, impellor or liquid jet aerators. The first group is defined by an impeller or rotor, which is submerged in the bulk liquid. The impeller or rotor is used to create the interfacial area for mass transfer. Examples of these types of aerators are low speed or radial aerators, high speed or motor speed aerators, and horizontal rotors. Low speed aerators use an impellor that is positioned at the water surface. The impellor pulls liquid vertically up from directly below it, which is accelerated by the vanes of the impeller and then the water is ejected horizontally at the impeller rim. A hydraulic jump occurs as the high speed liquid plume ejected from the impeller meets the slow or none moving bulk liquid. High speed or motor speed aerators vary from low speed or radial aerators because there is no gear reducer and therefore the impellor rotates on a vertical axis at the same speed as the motor. In a high speed or motor speed aerator the flow may be ejected horizontally, upward or downward away from the unit. Horizontal rotor aerators use a horizontal cylinder where curvilinear blades or plastic bars are attached. Oxygen is transferred in a similar fashion to high speed aerators where an air-water interface is created from the water droplets which are ejected from the rotating surfaces.

The second type of surface aerators creates the required interfacial area by means of liquid jets impinging on the liquid surface, for example submerged turbine or aspirating aerators. A submerged turbine aerator comprises of an open bladed turbine which is mounted on a shaft driven by a gear motor assembly. An air sparger is located under the turbine. Designs to improve oxygen transfer include using a draft tube to encase the downward pumping impellor, along with a sparger ring. Aspirating aerators differ from most aerator systems that inject air into the wastewater because it draws atmospheric air into a mixing chamber, rather than using compressed air. The air is then mixed with the wastewater and then ejected back into the aerator basin. The mechanism through which an aspirator draws air into the wastewater is by accelerating the wastewater through a channel, which creates an area of low pressure that entrains the air. There are two main types of aspirating aerators currently used in aeration, one of which falls into the category of a surface aerator and the second is a dispersed air system, which will be discussed later in this chapter. The first uses a tube mounted at an angle and connected to an air intake and motor above the water. The motor

is connected to a propeller that is located below the water surface. Liquid is drawn through the tube by the propeller creating the area of low pressure that draws air into the tube. The turbulence created in the tube from the flow breaks up the air into small bubbles. This mixture then discharges into the aerator basin. More details information about surface aerators can be found in Boyle et al (2002).

Table 1.1 lists the typical performance characteristics for surface aerators and shows that the maximum achievable SAE with surface aerators is 2.4 kgO_2/kWh. Dispersed air systems however, typically have a higher SAE, as will be outlined later in this chapter. Despite this surface aerators do have a number of operational benefits over dispersed air systems, these include ease of access in terms of both maintenance and installation, which is in comparison to dispersed air systems, which are located and mounted beneath the water surface. Surface aerators can also serve a dual purpose. Aside from the primary function of oxygenating water, surface aerators can add aesthetic appeal as they are available with different spray patterns.

Table 1.1: - Surface aerator efficiency and uses, information taken from (Boyle, et al., 2002).

Aerator	SAE (kgO_2/kWh)	Application
Low speed/ Radial Flow aerator	1.9 - 2.2	Low depth Oxidation ditches or highly mixed aeration tanks.
High speed/ Motor Speed aerator	1.1 - 1.4	Lagoon applications, where low mixing is required.
Horizontal rotors	1.5 - 2.1	Oxidation ditches up to a depth of around 4m.
Submerged turbine aerators – open turbine	1.0 - 1.6	Aerobic digesters where independent mixing and aeration processes are desired.
Submerged turbine aerators – draft tube turbine	1.6 - 2.4	Deep tank applications
Aspirating Aerators	0.4 - 0.9	Lagoon systems to supplement mixing or direct sludge.

1.8. Dispersed aerators

The air within dispersed aerators may be distributed via several methods and may be introduced to the bulk liquid in varying bubble sizes. The most common methods are through spargers, liquid jets through two-mixture nozzles or by hollow rotating mixers. Within the wastewater applications spargers are known as diffusers and are split into the categories of fine and coarse-bubble diffusers. They are available in an array of porous and non-porous configurations and materials, more details about the materials are available within Boyle et al (2002). Fine-bubble diffusers typically generate bubbles of between 2 and 5 mm in diameter, whereas coarse-bubble diffusers generate larger bubbles in the region of 6 to 10 mm in diameter (Shammas, 2007).

The main design issues associated with fine and coarse bubble diffusers are that they have to generate relatively small bubbles to ensure a large interfacial area for mass transfer. At the same time there are practical problems, such as clogging and installation. Clogging in fine and coarse bubble diffusers can occur during periods of low or intermittent use. This is when the dissolved solids in the wastewater could settle as a result of quiescent conditions and backflow into the diffusers can occur, resulting in issues with clogging. Fine-bubble diffusers are more prone to clogging due to their smaller diameter orifices (Environmental Dynamics Inc, 2013). A further disadvantage of base mounted dispersed air systems and therefore fine and

coarse bubble diffusers are that the aeration basin must incorporate a means to be easily dewatered for cleaning, maintenance and the installation of the system. In small systems where no redundancy of aeration tanks exist, an in situ, non-process interruptive method of cleaning has to be utilised (Shammas, 2007).

The fine-bubble diffusers, which belong to the family of dispersed air systems are the most commonly used aerators (West, 2009). Fine air bubbles are injected at the bottom of an aeration tank, typically via a series of porous ceramic plates or perforated membranes. These diffusers rely on an energy intensive process because of the compression of the air. However, they provide a high performance in oxygen transfer with SAE values typically quoted up to 4.65 kgO_2/kWh (Rosso, et al., 2008). Whereas coarse-bubble diffusers have a lower performance, with SAE values in the region of 1.22 to 2.13 kgO_2/kWh (Environmental dynamics Inc, 2003).

Another type of dispersed air system is a venturi based device, which are the second form of aspirating aerators. They combine a submersible pump located near to the base of the aerator basin with a horizontal tube, which the liquid is pumped through. This tube houses a venturi. The operating theory of a venturi aerator is based on the Bernoulli's principle. Within a venturi aerator the liquid flows through a converging section before being accelerated in the constriction, termed the throat. Thus creating a reduced pressure that causes the entrainment of a continuous air stream into the water, through orifices within the throat. The air and liquid mixture penetrates the diverging section and the oxygen transfer from the air to the liquid begins. The kinetic energy of an air and liquid jet entering the bulk liquid from the device produces intense turbulence and mixing. As a result of this intense turbulence and mixing, a dispersion of the air is formed. The advantages of venturi aerators are that they can be relatively inexpensive, small and can easily be retrofitted to an existing aeration basin. For example, a venturi can be connected directly to a submersible pump. However, due to the high velocities that are required to give a sufficient negative static pressure at the throat to entrain air to the bottom of the aeration basin, can result in low efficiencies. However, these devices are less expensive in terms of energy consumption than diffusers but they suffer an inferior performance in terms of SOTE (Taricska, et al., 2008). They typically have SAE values of between 0.5 and 3.0 kgO_2/kWh (Gourich, et al., 2007; West, 2009)

1.9. Dispersed aerator aeration basin structures

Within the category of dispersed air systems there are many structures and configurations currently in use for promoting mass transfer between air and a bulk liquid. For example, bubble columns, stirred vessels, jet loop reactors and impinging-stream reactors.

Bubble columns typically consist of a vessel where a diffuser or series of diffusers are located at its base. The diffuser may take the form of a disc, dome, plate or tube on which, a series of perforations, orifices or slits are located. There is a vast array of diffuser designs available to suit the individual characteristics of a system. Typical SAE values of 0.5 to 2.5 kgO_2/kWh have been found for a central diffuser located within an

aeration basin (Gourich, et al., 2007). Values in the region of 4.65 kgO_2/kWh have been found for fine-bubble diffusers when they cover the entire base of an aeration basin (Rosso, et al., 2008).

A bubble column may be combined with a draft tube to encourage recirculation and mixing. Recirculation occurs when the denser non-aerated liquid at the outer vessel wall recirculates at the bottom of the draft tube into the less dense and lower pressure aerated liquid within the draft tube. Typical values for these types of bubble columns with a central diffuser are between 2.0 and 3.0 kgO_2/kWh (Gourich, et al., 2007).

A stirred vessel is an adaptation of a bubble column, where an impeller is located above a central diffuser. The vessel in this instance is typically cylindrical, the inclusion of the impellor helps to increase the dissipation of energy inside the vessel, as a result reducing the produced bubble size. Therefore increasing the surface area of air per unit volume and as a result improving the mass transfer characteristics. The impellor also increases the turbulent mixing within the liquid. Typical values for these types of bubble columns are between 1.0 and 2.5 kgO_2/kWh (Gourich, et al., 2007).

A jet loop reactor consists of a two-phase mixture nozzle located at either the top or the bottom of the vessel. The shear field produced at the nozzle outlet causes air dispersion and generates bubbles of very small size, whilst the liquid momentum from the nozzle leads to circulation of the two-phase mixture. An advantage of locating the nozzle at the top of the vessel enables air to be entrained from the surroundings, removing the requirement for a compressor. However the jet velocity may have to be high to achieve full penetration into the bulk liquid, which can lead to higher power requirements. ValorSabio Engineering Innovation (2013) quotes their jet loop reactors as being able to achieve SAE values of 4.6 kgO_2/kWh.

Impinging stream reactors consist of a number of two-mixture nozzles located at the base of a vessel. These nozzles are configured in such a way that as the two-phase mixture is emitted up symmetrically arranged guide tubes. The streams impinge upon each other at the top of the vessel in an impinging-zone, creating an area of high turbulence and mass transfer between the phases. Typical SAE's of between 1.4 and 3.3 kgO_2/kWh are quoted (Saien & Moradi, 2012).

A summary of the different types of aerators and aeration basin structures are presented in Table 1.2.

Table 1.2: - A summary of aerator types and structure and their respective aeration efficiency.

Aerator or structure	SAE (kgO_2/kWh)	Authors
Surface aerators	0.4 – 2.4	Boyle et al (2002)
Fine-bubble diffusers	≤ 4.65	Rosso et al (2008)
Coarse-bubble diffusers	1.2 – 2.1	Environmental Dynamics Inc (2003)
Venturi aerators	0.5 – 3.0	Gourich et al (2007) and West (2009)
Bubble columns with central diffuser	0.5 – 2.5	Gourich et al (2007)
Bubble columns with central diffuser and draft tube	2.0 – 3.0	Gourich et al (2007)
Stirred vessel	1.0 – 2.5	Gourich et al (2007)
Jet loop reactor	≤ 4.60	ValorSabio Engineering Innovation (2013)
Impinging stream reactors	1.4 – 3.3	Saien and Moradi (2012)

1.10. In-process performance considerations

A number of alternative approaches to aeration are used or have been proposed, with the recent drive towards increased efficiency, there has been much interest in novel approaches in recent years (West & Faram, 2010). Typically, these claim to offer enhanced energy efficiency, for example improved SAE. Despite the technical claims however, it has become recognised that there is no single preferred solution that meets all requirements. In-process performance for many systems can fall significantly below the performance measured in clean water. For certain systems, performance levels can deteriorate over time due to fouling and clogging. Maintenance or replacement cycle requirements vary, as do installation requirements and associated costs. Aeration system selection is therefore a process that needs to take into account a wide range of considerations, including both technical issues and cost factors.

Energy consumption issues in wastewater aeration have generally been tackled from two angles. One approach is to implement a lower-energy aeration technology. Another is to optimise processes using control systems to closer match oxygen supply with process demand, rather than possibly exceeding it. In either case, the course of action will typically be dictated by discharge content issues, investment payback considerations and operational demands.

In-process performance needs to be considered when comparing aeration systems. In fact, many technologies with a high SAE, such as fine-bubble diffusers, can have a low alpha factor, while others with a low SAE, for example, conventional jet aeration systems can have a high alpha factor. Rosso et al (2008) presented an analysis of clean water and in-process data for several of these types of system. It was shown in Rosso et al (2008) that fine-bubble diffuser systems produce an average SAE of 4.65 kgO_2/kWh. However the in-process performance, SAE_f, of these aerators is reduced to an average value of 1.38 kgO_2/kWh Rosso et al (2008). This is because they have a relatively low alpha factor. Coarse-bubble diffuser systems were found to produce in Rosso et al (2008) to have an average SAE of 1.61 kgO_2/kWh, which was significantly lower than fine-bubble diffusers. However, coarse-bubble diffusers provided a SAE_f of 1.0 kgO_2/kWh, therefore a much higher alpha factor. It was therefore found that despite the fine-bubble systems being overall more energy efficient, a moderate in-process differential between them and coarse-bubble diffusers was demonstrated, compared to a significant differential when assessed on clean water. A further observation by Rosso et al (2008) was that coarse-bubble systems generally had capacity to deliver higher overall air flow rates, sometimes making them the only option where space was a constraint. Therefore serious consideration is required towards in-process performance when choosing an aeration system.

1.11. Theoretical performance considerations

Venturi type devices are regularly used as flow measuring devices due to the minimal losses that are present across the device. Bernoulli's Principle states that as the flow travels through the throat of the venturi, the flow velocity increases through the reduced flow area, which results in a reduction in static pressure. Careful design of the system can ensure that the resultant static pressure in the throat is below

atmospheric and therefore, if orifices are located there, the air from the atmosphere or any other gas can be entrained into the flow. Entraining a gas at nearly atmospheric pressure can lower energy requirements, by minimising compression work and pressure losses.

Jackson and Collins (1964) discussed the location of mass transfer downstream of the point of injection. They believed that very little to none of the mass transfer occurred at the point of injection and for the initial two-thirds of the divergent section. It was considered that the bulk of the transfer occurred in the remaining third of the divergent section and in the first few pipe diameters downstream. The experimental work in Jackson and Collins (1964) was conducted using a regular venturi in the horizontal orientation, where after a few pipe diameters downstream of the venturi the flow began to separate, with the air occupying the upper section of the downstream pipe. Therefore reducing the interfacial area available for mass transfer. By having a venturi device in a vertical downward flow, the potential for the flow separation of the phases due to buoyancy will be negated. This in turn will enhance mass transfer.

The transfer of oxygen from air to a liquid is important in many applications, including wastewater treatment and industrial processing. Unfortunately, the solubility of oxygen into water is very low, approximately 7 to 10 p.p.m. at atmospheric pressure and temperatures (Jackson & Collins, 1964). It is for this reason that very little oxygen is transferred by a single pass through an aerator (Jackson & Collins, 1964). Therefore, recirculation systems and loop reactors are beneficial for mass transfer.

A significant problem with introducing a gas into a liquid within a pipe flow is that the flow regime often resembles a slug flow regime. This is because a large ventilated cavity can form at the point of gas injection (Sotiriadis, 2005). Further information about flow regimes is found in Chapter 2. Around the formed ventilated gas cavity the liquid flows in a high velocity thin falling film, which can lead to problems with the mechanical integrity of the pipe work within the system (Hill & Wood, 1994). At the base of the ventilated cavity where the liquid film plunges into the bulk liquid flow, small bubbles of the gas are entrained. The work by Sotiriadis (2005) studied mass transfer using various sparger designs in a vertical downward flow and showed that the presence of a large ventilated cavity reduces the mass transfer coefficient of the sparger. This is due to the reduced interfacial area for mass transfer, which is in comparison to a homogenous bubbly flow. However, the sparger designs which resulted in a shorter length of ventilated cavity or no ventilated cavity required a greater amount of mechanical power input. Therefore, the overall aeration efficiency across the sparger designs was approximately equal. From this is can be identified that careful consideration is needed with the aim of preventing the formation of a ventilated cavity.

Kulkarni and Shah (1984) studied the performance of a down-flow bubble column where the gas and liquid flowed concurrently downwards. It was concluded that a two-phase vertical down-flow system has a number of advantages over a vertically upward flowing system. These included the generated bubbles being smaller and more uniform in size, bubble coalescence was also considered as being negligible, and the

flow structure was identified as being more homogeneous. In addition to this the gas-liquid contact time was greater in a down-flow orientation.

The aeration performance of a given device depends not only on how the oxygen is supplied, but also on the distribution of the air within the diffusion region. There are clear advantages to the use of a cylindrical geometry, as with venturi based aerators, in terms of reducing energy losses. However, this argument becomes less clear when large volumes of air are introduced along the tube wall. In this case, a major difficulty with such devices is the tendency of the air bubbles to accumulate in the boundary layer at the walls of the pipe. The phenomenon may be responsible for creating instabilities in the diverging section of a venturi, resulting in separation, stall and high energy losses.

It may be advantageous to use the flow of gas not only to provide a gas-liquid mixture but also to drive a fluid drivable engine, such as a turbine. This is when a sufficient amount of gas is able to be drawn into the liquid flow within venturi based aerator. If for example this device was located somewhere remotely, this turbine could then be used to power control systems, which might be needed for this device. French and Widden (2010) conducted research into the exploitation of low-head hydropower using the air stream being entrained through a turbine. They found that the system offered a significant prospect for economically harnessing power.

It can therefore be considered that the use of a venturi aerator can have a significant number of benefits when located in a vertically downward flow, such as negating the effects of buoyancy in terms of flow separation. However, careful consideration and a significant understanding of two-phase flow regimes are required to prevent the formation of a ventilated cavity.

1.12. Design considerations

There are many technical issues that surround the development of new technologies for promoting gas-liquid mass transfer in two-phase flow. The main process parameters relate to the performance efficiency of the aerator. For example, a device for mass transfer must be able to provide the required amount of species for transfer and must be able to do this efficiently by having a suitable SOTE, which can be done by through increasing the interfacial area for mass transfer. In conjunction to this, the performance efficiency of any newly designed and marketed technology should be able to meet any functional requirements. For example, the aerator must achieve the required oxygen transfer but must also do this efficiently, such that the power consumption required is suitably low, therefore achieving a high SAE.

Due to the wide variety of industries requiring gas-liquid mass transfer. Fouling may be an issue and therefore the technology must be designed for purpose. Fouling can be split into two main categories, one of which is dependent upon the entrained air flow, where particles within the air flow may block any passageways or cause corrosion. The second kind is as a result of the liquid flow, where organic matter

could build up on surfaces of a device and at the air inlets causing back pressure problems and inefficiencies. Therefore, an adequate design must be durable and potentially require minimal maintenance and/or be easily accessible. Therefore, locating an aerator above the water surface will present a number of operational benefits including, ease of access for maintenance and it will also be resistant to fouling from the liquid side, as a result of intermittent use because the technology would not being submerged in the bulk liquid during these periods of low or intermittent use.

Further to main process parameters, other factors that should be considered in aeration system selection include, that for certain technology types SOTE can degrade over time (Rosso & Stenstrom, 2005). This is often accompanied with increased back-pressures due to blockages and hence increased energy consumption. Base mounted fine-bubble diffuser systems are particularly known to suffer from biological and mineral precipitate fouling, which if not suitably addressed, can result in significant performance reductions. Therefore, performance consistency over time needs to be considered.

Generally, aeration technologies are either base mounted or mounted from above. Base mounted systems such as fine-bubble diffusers are often popular due to high claimed levels of efficiency. Their installation however requires sump access, which in the retrofit context requires draining and/or the diversion of the bulk liquid. The option of locating the aerator above the water level presents convenience benefits, with regards to both installation and accessibility for maintenance.

With relevance to the prior two points, many aerators need to be regularly maintained to provide consistent performance. Some need to be entirely replaced or some components, after a moderate period of time, if effective and continuous operation is to be expected. Therefore, the maintenance requirements and replacement period needs to be built into the lifetime cost assessment.

Previous work to this project, has taken into consideration some of the outlined theoretical, design and practical considerations outlined in this section. This work resulted in two initial designs for a novel venturi based technology, which have been designed for promoting gas-liquid mass transfer within a conduit. The work was previously conducted by HydroVenturi Ltd. This work is outlined in the following section.

1.13. Background to the project and previous work

HydroVenturi Ltd was established as a spin-out company from Imperial College, London in 2001, where a novel approach to low-head hydropower generation had been conceived. The system involved the utilisation of the venturi effect to draw air into a head-driven water flow. The air was being drawn through a turbine, located in the airflow pipe work, to generate electricity. This was proposed as a low capital cost means of extracting useful energy from water in which no moving parts are in direct contact with it.

A process schematic and demonstration project photo for the Derwent demonstration tests between 2006

and 2007 are shown in Figure 1.2. The experimental set up included multiple venturi tubes which were connected to a single air manifold. The turbine was located on dry land, remote from the harsh environment of the watercourse.

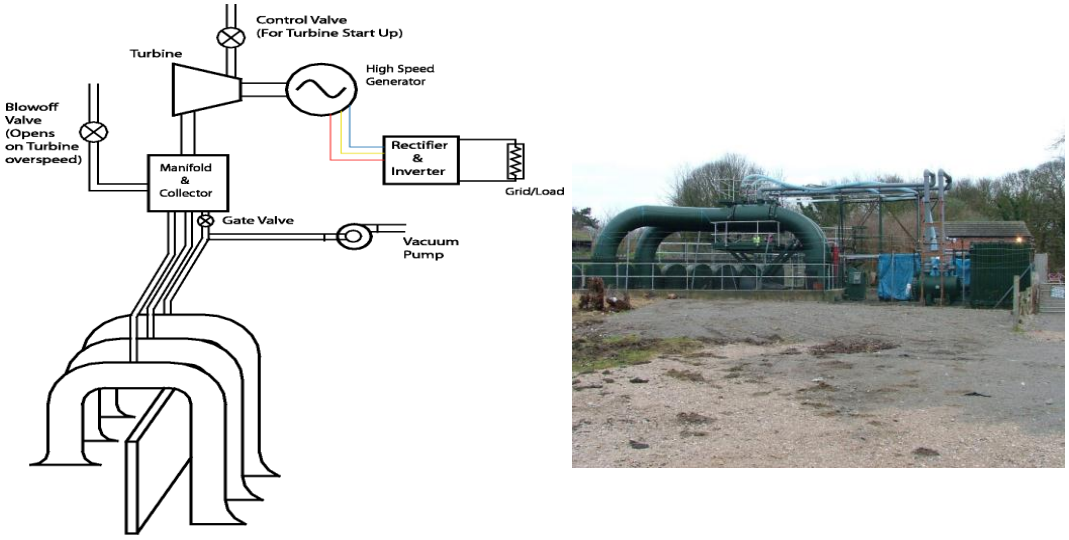

Figure 1.2: - HydroVenturi Ltd technology as applied to low-head hydropower generation in a Derwent test site, taken from West and Faram (2010).

A core component of the HydroVenturi hydropower technology is the ejector insert, which facilitates the entrainment and dispersion of air. In the practical demonstration project at the Derwent test site, which used 1 m ID pipe work, the insert was installed in a siphon arrangement to supplement the air entrainment. A schematic representation of one of the designs of injector insert used is shown in Figure 1.3.

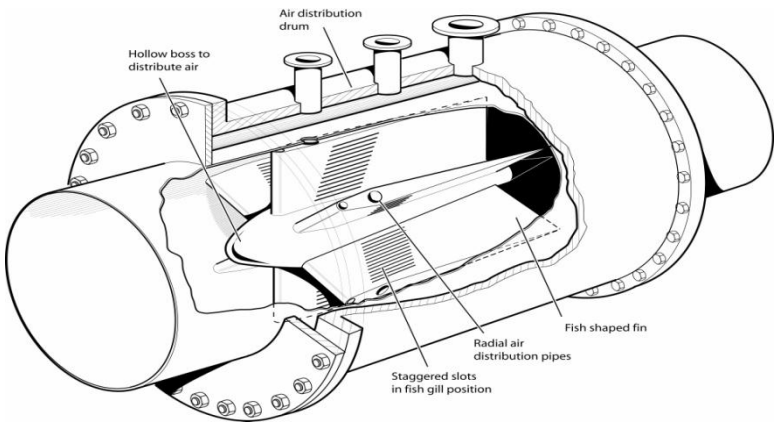

Figure 1.3: - The large scale injector insert as applied in low-head hydropower demonstration project in Derwent, taken from West and Faram (2010).

Following the demonstration of the technology for power generation in 2006 and 2007, a programme of work was commenced to explore application opportunities in the field of gas exchange.

Through a development programme, using a combination of Computational Fluid Dynamics, CFD, analysis, laboratory testing and site trials, the adaptation of the HydroVenturi technology for gas exchange applications culminated in the refinement of the core injector insert, as shown in Figure 1.4 and described in Chapter 4.

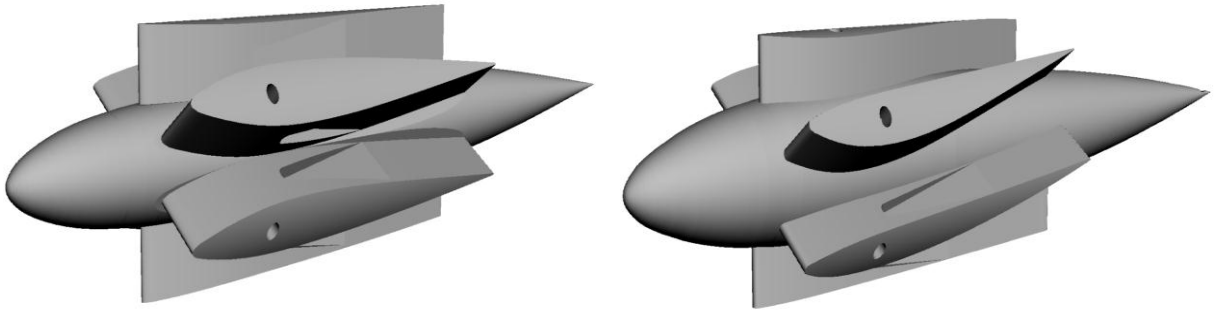

(a) (b)

Figure 1.4: - Initial designs developed from the low-head hydropower inserts for use in the field of gas exchange, (a) zero angle of attack insert, (b) non-zero angle of attack insert, taken from West and Faram (2010).

In the early stages of the design and development, HydroVenturi Ltd used an independent consultancy to provide a feasibility study. From the findings in the study a prototype development programme was commissioned, with the intention of manufacturing and testing a small number of designs for a water aeration device.

The principal objective of the design process was to generate defensible intellectual property and to maximise the value of any intellectual property generated. A range of factors was chosen that would ultimately contribute to the value of any given design. These were, operational flexibility and manufacturing cost, but it was a high SAE that was the dominant objective.

In addition to optimising the SAE, some thought was given to the implication of design choices on manufacturing costs, operational reliability and maintenance costs. However, many of these parameters would be heavily influenced by a combination of the final form of the design and the chosen field of application. Therefore, it was considered by the independent consultancy and HydroVenturi Ltd that the greatest emphasis should be placed on achieving a high standardised test performance before a full consideration of all other commercial factors. The principal initial constraint applied was that any design would be based on the technological principle of the venturi pump. For example, the water would be accelerated through a constriction, creating sub-atmospheric pressures and thus allowing the air to be entrained from the atmosphere, another constraint adopted was the avoidance of moving parts.

A wide range of constriction geometries were considered with the base case for comparison being a conventional straight pipe within a convergent and divergent section, resembling a regular venturi. There are clear advantages to using a simple cylindrical geometry in terms of energy loss. However, the argument becomes less clear when introducing large volumes of air along the tube wall, resembling a peripheral sparger, since the air will tend to accumulate in the boundary layer. This accumulation would need to be handled within the divergent section after the constriction. If not there would be a high risk of flow separation.

Assuming that any air introduced via the walls of the constriction will remain near the boundary layer suggests that an advantage could be gained by increasing the surface area to volume ratio within the constriction. The chief disadvantage of this approach is that the risk of blocking on the liquid side is invariably increased. However, increased head loss and flow separation are also important factors.

A low head loss concept would not suffer from the problems of a decreasing the level of vacuum generated in the constriction, as a result of the lack of pressure recovery and head loss. It would require a simple and streamlined insert geometry, which would minimise turbulence and separation. Initial work identified that this concept presented a good source of intellectual property and some basic CFD analysis on single phase flows highlighted that the operational performance would be at least as efficient as a conventional straight tube Venturi. The necessary simplicity of a low head loss insert design may also help to suppress manufacturing costs and the insert would facilitate retrofitting to existing processes.

Two alternative approaches were also considered that incorporated relatively simple open tube geometries but would use conditions within the flow to draw air away from the walls. These approaches were also seen to be a promising source of intellectual property. Two mechanisms were considered to aid in drawing the air away from the walls. The first was high turbulence intensity and the second looked at secondary flow currents, particularly swirling flows. High turbulence was shown by the independent consultancy to increase the rate of spread for air emanating from a single orifice, while swirling flows create centripetal forces which would tend to draw the low density air towards the centre of the flow.

A number of concepts were considered but only two underwent significant numerical analysis. The first was a series of conical frustums and the second was a straight tube with a helical lip. In both cases the head loss was increased. The results suggested that the oxygen transfer rate in both cases would need to be roughly an order of magnitude higher than the comparable straight tube geometry, such that some advantage in terms of SOTE would be gained.

It was deemed by the independent consultancy that the conical frustum design would have potential. However, they considered that it would most likely work best as a single element rather than several in series. In this sense, the concept begins to resemble a nozzle that injects a low pressure, high velocity jet of water into a region of air, resulting in jet break up and phase entrainment at the interface. A device employing a similar system has been patented by other manufacturers. Therefore, the concept was dropped due to it being unable to generate defensible intellectual property.

The helical lip was intended to produce something resembling a classical helical flow pattern. However, preliminary numerical simulations revealed that the flow pattern was more complex. There was an outer helical component with a linear core punching through the centre. The interaction of these two components of the flow generated a high level of turbulence alongside the intended swirling current. To

avoid these problems it was considered that the constriction would need to be divided into a greater number of streams to exploit this mechanism fully, increasing any risk of blocking on the liquid side as well as material and manufacturing costs.

From the subsequent trials and numerical simulations that followed, the two inserts, shown in Figure 1.4, were established as a starting point for future work and a suitable insert for use within the field of gas-liquid mass exchange would be based on the predetermined criteria of SAE.

1.14. In-process application

It is considered by HydroVenturi Ltd that the injector insert would be installed in a vertical or horizontal pipe in an in-process condition. The insert would be preceded with a pump, or built into a weir wall, or a siphon passing over a weir wall, or alternatively on a flow inlet or discharge outlet. As the water flow passes through the insert, the high water velocity through the venturi section and over the six lateral vanes, seen in Figure 1.4, results in a reduction in static pressure. These wings represent individual venturi channels, where the reduction in static pressure causes air to be drawn in through carefully designed injection slots on the wing surfaces. Downstream of the insert, effective mixing takes place, creating a dispersion of very fine bubbles.

The HydroVenturi Ltd technology has significant and diverse potential for adoption in the water, wastewater and industrial process industries, based on a number of key areas, such as,

a) It was previously suggested by West and Faram (2010) that the technology has the potential to deliver competitive process parameter outputs, such as SAE and SOTE that are higher than would typically be expected for other systems in this class, such as standard venturi aerators.
b) Venturi-style aeration systems are typified as having high alpha factors, often approaching 1 (West & Faram, 2010). Based on this, the technology presents opportunity to deliver efficient overall operation and has the potential to exceed the performance in high suspended solids environments, in comparison to other types of aerators. For example, dispersed air systems such as fine and coarse bubble diffusers, where the alpha factors can be low.
c) Due to its simplicity, the system would not be prone to physical degradation over time and would also tolerate intermittent use. However, due to the individual venturi channels represented by the individual vanes, there is a potential for blockage on the liquid side if the insert were to be used on unfiltered wastewater.
d) As the system uses fluid momentum to project bubbles to the sump of a tank, it can be installed from above, providing convenience for installation and maintenance access as well as intermittent visual inspection.
e) A characteristic of the system is that it can support turbulent mixing processes, due to the high velocity bubbly discharge produced, where mixing is an important parameter in any aeration system.

f) In certain circumstances, the system can be used to extract energy from a head of water, either with power generation as the main objective, or to deliver combined aeration and energy recovery. As was shown in the large scale low-head hydropower work conducted in Derwent in (2006) and (2007).

Pressure on the water and process industries in recent years has fuelled a major interest in-process optimisation, with a focus on achieving higher levels of process performance with lower energy input.

In the water sector, aeration process optimisation has become particularly topical, with over 55% of the energy consumed in wastewater treatment being estimated as stemming from aeration delivery (Helmut Kaiser Consultancy, 2006). Process optimisation through the use of better monitoring and control systems has presented one route to improvement, while another option is to implement more energy efficient aeration technology.

A plethora of different aeration technologies have been used historically and many more have emerged in recent years in response to the market demand for improved efficiency systems. In practice, there appears to be little consensus on what is the optimum option. There appears to be no single system that presents the ideal combination of cost effectiveness, low maintenance, consistent performance, high delivery capacity, low energy, long life and technical performance.

The venturi system presented in this work, adapted from a novel low-head hydropower system, presents new opportunities. The work carried out to date suggests an ability to deliver high levels of efficiency with the added benefit that performance will not deteriorate over time. This has implications to both maintenance requirements, which will be minimal, and product lifetimes, which will be extensive.

1.15. Project aims and objectives

The aim of this project is to analyse and develop the HydroVenturi technology, in order to improve performance and investigate process parameters, with comparisons to be made with similar technologies. This will be done through the following objectives,

a) Initially a hydrodynamic understanding of the system is to be developed through obtaining pressure losses, entrainment rates, air bubble sizes and monitoring of any flow regimes. The effects of the various designs and geometric changes are to be monitored, with correlations to be established between produced bubble sizes and void fraction, flow rates and energy consumption.
b) Volumetric mass transfer coefficients and aeration efficiencies for the various designs are to be established and comparisons made, along with expressions established, where the mass transfer will be conducted in accordance with ASCE standard, ASCE/ EWRI 2-06.
c) Computational fluid dynamics, CFD, simulations are to be used to develop simulations for the existing inserts, which can be validated based on results in sections a) and b). From this

improvements to the inserts can be made based on the correlations, as well as observations from the experimental work and theoretical research.

d) Geometric scaling will also be investigated using Computational Fluid Dynamics, CFD, simulations and considerations will also be made towards in-process operation.

e) Throughout all of this work, comparisons will be made with a regular venturi with a similar blockage ratio and designed to British Standards (BS EN ISO 5167-4:2003).

CHAPTER 2

LITERATURE REVIEW

2.1. Introduction

The correct functioning of an aerator depends on the existence of a two-phase flow and the interfacial interactions between the air bubbles and the liquid. Therefore, the analysis and understanding of this two-phase flow is of paramount importance, especially if the physical and chemical processes involved are to be optimally and safely, designed and controlled.

This chapter presents the knowledge and ideas that have been established, including their strengths and weaknesses, with the aim being to establish what is known about the subject, so that knowledge of past research can be built upon. Within the literature there is some research into the use of venturi aerators, although, there is not a significant amount due to commercial sensitivity. However, some research has been conducted at Firat University, Turkey and Casablanca University, Morocco, into the use of venturi aerators located above the water level within a downcomer for the purpose of gas-liquid mass transfer and in particular aeration. A downcomer is the term used for the downward leg of a test section. The following sections discuss their findings and other similar areas of research and potential issues that could be expected within this programme of work.

Also the study of bubbly flows is complex with an increased number of fluid properties and a variety of flow patterns and regimes. In addition, the physical and chemical processes such as turbulent effects and oxygen transfer are not well understood and often rely on empirical observations. An overview of the relevant literature is discussed in this chapter, where the published work into bubble formation in gas and liquid systems with submerged injectors, the influence of physicochemical properties of the two-phase flow, the injector configuration and the operating conditions being of particular interest. With the overall aim being to develop a review into the injection and entrainment of air bubbles through a venturi type device and the impact on the transfer of oxygen from the entrained air into the flowing liquid.

2.2. Venturi aeration

Researchers in the Department of Civil Engineering, Firat University, Turkey conducted research that looked into the bubble formation, where venturi style geometries were used to entrain air within a concurrent water flow. The research included using a venturi in a plunging jet system for the purpose of aeration, where the water jet entered a pool at rest. Initially the study compared a venturi to a nozzle, the geometries of which are shown in Figure 2.1, where both devices were placed in a plunging jet set up, shown in Figure 2.1 (a). During the initial work by Baylar and Emiroglu (2003), it was shown that including the venturi improved the aeration efficiency of the system, in comparison to just a nozzle. In addition to this having air

inlets within the throat of the venturi also aided in improving the aeration efficiency. Reducing the water velocity was found to increase the aeration efficiency. However, these higher efficiencies were at lower water flow rates, which corresponded to a reduced air entrainment. Therefore, these conditions would potentially have a limited use.

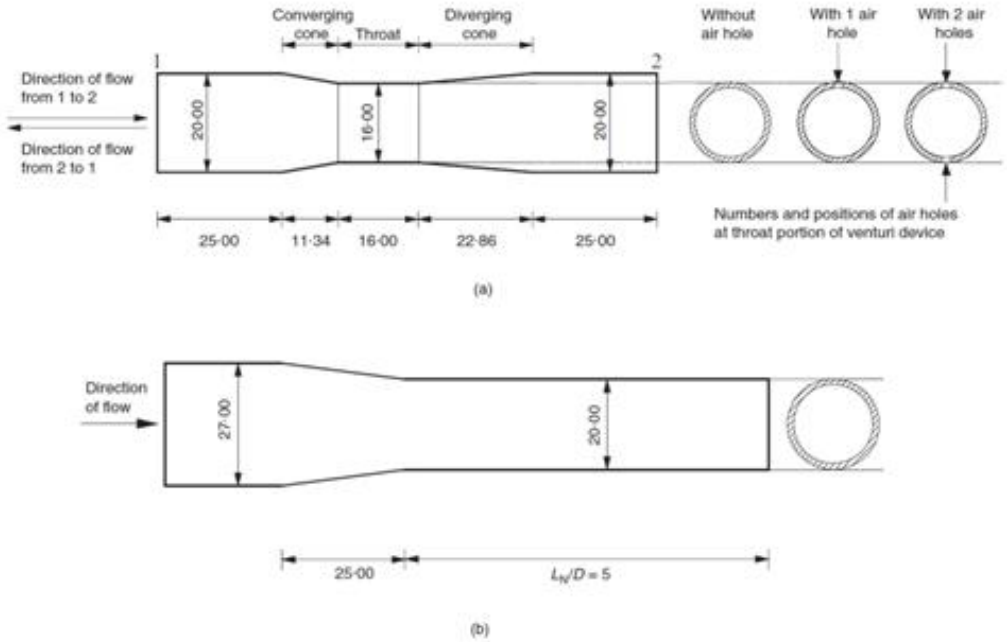

Figure 2.1: - Dimensions of (a) Venturi and (b) Nozzle used in Baylar and Emiroglu (2003).

In 2005, Baylar et al, conducted research in to the convergent and divergent angles of the venturi, whilst still conducting research using the plunging jet set up. It was discovered that adjusting the convergent and divergent angles of the venturi had a significant impact on its performance. Angles of 5, 10 and 20˚ were tested for both the convergent and divergent sections. The optimum angle arrangement was found to be 20˚ convergent and 10˚ divergent, above a divergent angle of 10˚ the entrained air began to decrease. The study also showed that increasing the water flow rate increased the air entrainment at the throat. Within this study air was entrained into the flow through the venturi via two orifices at the throat. Experiments were also conducted to investigate the effect of the orifice diameter. Two diameters were tested, 5 and 10 mm, and it was found that the increasing the orifice diameter increased the air entrainment.

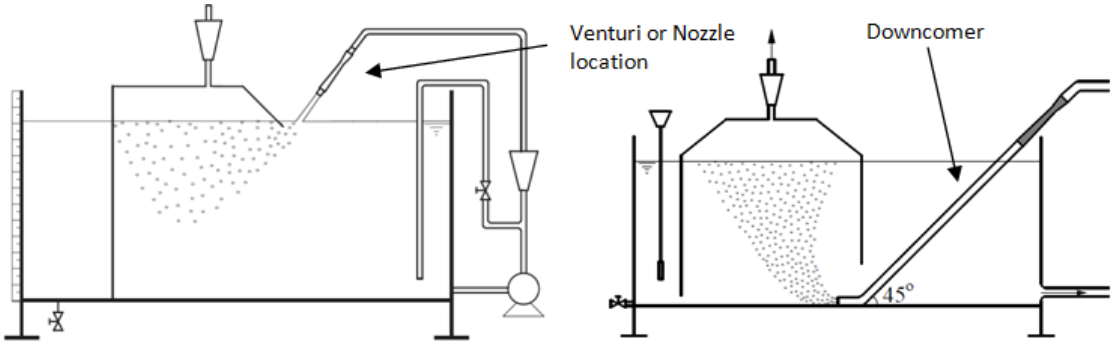

(a) (b)

Figure 2.2: - Experimental set up for (a) when a venturi and nozzle were tested in a plunging jet set up from the work by Baylar and Emiroglu (2003) and Baylar et al (2005) and (b) the experimental set up for when a downcomer was in situ, in the work Baylar et al (2006) and (2007).

Baylar and Emiroglu (2003) and Baylar et al (2005) showed the potential for the using a venturi in aeration. Despite their experimental work using a plunging jet set up, rather than having a pipe extending into the bulk liquid. There were clear signs that the divergent angle of an insert and the open area for air entrainment could have a significant impact on the performance of a venturi. From this initial investigation by Baylar and Emiroglu (2003) and Baylar et al (2005), Baylar et al (2006) and (2007) conducted a series of experiments to look at the potential for mass transfer whilst using a venturi connected to a downcomer, which stretched to the base of the tank, a schematic of the experimental set up is shown in Figure 2.2 (b).

In Baylar et al (2006) and (2007), the experimental work was conducted on different sized venturi tubes with inlet pipe diameters of 36, 42 and 54 mm, with either a throat diameter to pipe diameter ratio of 0.5 or 0.75, within this work experiments were also conducted on two depths of water, 0.5 and 1 m. For all venturi tubes a convergence angle of 21˚ was used with a divergent angle of 7˚. Unfortunately there is no mention in this experimental work for the reasoning of these angles. However, it can be assumed that these angles were chosen based in the previous work by Baylar et al (2005). This in conjunction with British Standards 5164-4 (2003), which recommends the angles of 21˚ convergent and 7˚ divergent for using a venturi to measure fluid flow. These angles would potentially provide the most efficient venturi aerator, in terms of pressure loss. Alongside this work, experiments were undertaken to determine the optimum location for the orifices within the venturi, the locations of which are shown in Figure 2.3.

Measurements taken included the volume of entrained air and SOTR. The study showed that for a throat to venturi diameter ratio, d_{th}/d of 0.5 the volume of air entrained increased up to a velocity of 3.0 ms^{-1}, where the range in the experiments were 1.5 to 4.5 ms^{-1}. However above this, the volume of entrained air decreased. For the d_{th}/d ratio of 0.75 all water velocities produced a decreasing air entrainment, where the range tested in the experimental work was 2.5 to 7.5 ms^{-1}. For all d_{th}/d ratios air entrainment and SOTR increased with pipe diameter and water velocity, despite the reduction in entrained air with increased water velocity in some cases. SOTR was also found to increase with water depth.

In the experimental work by Baylar et al (2006) there was no mention of the cause of the reduced volume of air entrainment, despite an increased water velocity. Within the paper there was also no mention of the flow regime in the downcomer, this was also the case for the work conducted by Baylar et al (2007). As can be seen in Figure 2.2 (b) there was a pipe bend at the base of the downcomer. This bend can have a significant effect on the flow and distribution of the air in the downcomer. This will be discussed in further detail in Chapter 9. When a two-phase flow travels around a pipe bend, flow separation can occur due to the increased momentum of the heavier phase, which moves towards the outer wall of the pipe bend. In this case, this would cause the water to move towards the outer pipe wall causing the air to accumulate at the top of the bend. This accumulation of air provides a blockage to the flow, which causes a significant back pressure. As a result reducing the negative pressure within the throat, which in turn would decrease the level of air entrained.

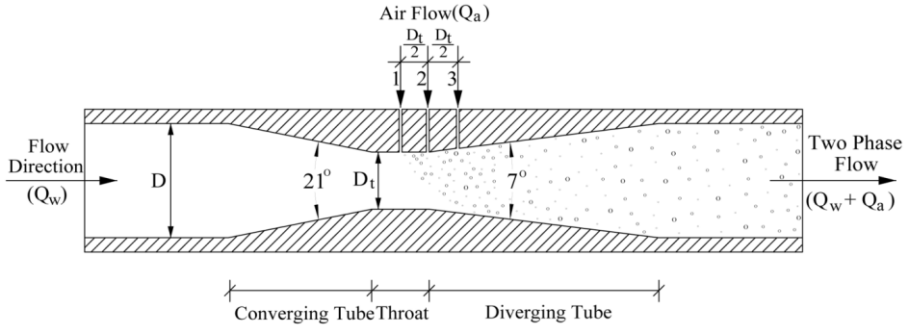

Figure 2.3: - Venturi aerator used in Baylar et al (2006) and (2007), and the location of the air orifices, taken from Baylar et al (2007).

Baylar et al (2007) showed that the location of the air orifices within the venturi had a significant impact on the amount of air entrained into the flow. Consistently in their work, the air orifice in position 1, which was located in the middle of the throat, shown in Figure 2.3, entrained more air than any of the other positions. Therefore, locating the orifices for air injection at the point of maximum constriction can provide the greatest amount of entrained air. However, during this work there was no mention of how the location of the air inlets affected the mass transfer and like Baylar et al (2006) there was no mention of pressure losses through the venturi or in the downcomer, or the resulting flow regime.

Baylar and Emiroglu (2003) and Baylar et al (2005) to (2007) provide an indication with regards to the design of an insert and how it can affect the overall performance, with divergent angle, air inlet location and open area, as well as the d_{th}/d ratio all having an impact on air entrainment. Other characteristics that could affect the performance of a venturi type aerator include, the depth of the receiving tank, the water flow rate and the internal pipe diameter, ID. However, this was an incomplete series of research work, as there is little observation conducted into the flow regime and bubble size.

Gourich et al, (2005) and (2007) at Casablanca University, Morocco, studied the mass transfer characteristics of venturi used within a loop reactor set up. The type of venturi used was a conventional venturi design with holes around the throat for air to either be imposed or induced into the flow. The d_{th}/d ratio of the venturi was not stated in the papers but convergent and divergent angles of 20˚ and 7˚ were reported. Four air inlets were located around the throat and their combined surface areas varied from 2 to 4.5 cm^2, which corresponds to an orifice of radius, 4 and 6 mm respectively.

The liquid flow rates used in Gourich et al (2005) and (2006) were between 4.0 x 10^{-4} and 8.0 x 10^{-3} m^3/s in a 50 mm ID pipe which corresponds to 0.2 and 4.1 ms^{-1}, with air flow rates between 10^{-4} and 2.5x10^{-3} m^3/s, corresponding to 6 to 150 L/min. For the comparison of reactor performance, hydrodynamic and mass transfer parameters were expressed as a function of specific power input, E, this was calculated using Equation 2.1. For Equation 2.1, the air supply pressure, P_A, was required and active volume for mass transfer, V_{L1}, which included the volume of the divergent section of the venturi, the downcomer and the recirculation tank, which the two-phase mixture exited into.

$$E = \frac{Q_W}{V_{L1}}\left[(P_{TH} - P_{ATMOS}) + \frac{1}{2}\rho_w U_{TH}^2 + \rho_w g \Delta z\right] + \frac{Q_A}{V_{L1}}[P_A - P_{ATMOS}] \quad [2.1]$$

Unlike the work by Baylar and Emiroglu (2003) and Baylar et al (2005) to (2007) the work by Gourich et al (2005) and (2007) referred to and commented on the flow regime within the downcomer. Two primary flow regimes were identified. The first was when an annular water film flowed around a central air core along the pipe wall. The central air core resembled a ventilated air cavity. This central core formed from the air inlets and remained until just below the venturi. The second flow regime was when the air core was broke down and dispersed as small bubbles, which flowed down the pipe with the water in a homogeneous bubbly flow.

Whilst the experiments were run with a constant volumetric air flow rate the bubbly flow regime occurred at the higher water flow rates for both an induced and imposed air supply. As the water flow rate increased the size of the air core decreased. The results showed that the volume of air entrained increased steeply as a function of Q_W^2 , when the flow was in an annular flow regime. However, the entrained air flow rate only increased as a function of $Q_W^{0.5}$, during the bubbly flow regime.

It was deduced that power input was mainly governed by the geometrical dimensions of the venturi and the water flow rates, while the air flow rate and tank dimensions, such as water level only played a secondary role. Air induced and air imposed experiments provided similar overall oxygen mass transfer coefficients, $k_L a$. Therefore, air induced operations would be more beneficial from an economic point of view. The total surface area of the air inlets at the throat was seen not to act significantly on the venturi performance when the total area was above 2 cm^2. The liquid level in the tank however, effected the performance of the venturi, as the level was increased while the maximum air induced flow rate decreased. This is in contrast to the mass transfer performance which improved with increasing water depth.

The work by Baylar and Emiroglu (2003) and Baylar et al (2005) to (2007) and Gourich et al (2005) and (2006) showed that a significant number of factors can affect the air entrainment rate, pressure loss and oxygen transfer of a venturi aerator. These included the geometric characteristics of the venturi, such as convergent and divergent angles, internal pipe diameter and throat to venturi diameter ratio. In addition to these characteristics air orifice location and dimensions, along with the receiving water depth, all can have a significant impact on the performance of an aerator. Within Gourich et al (2005) and (2007), there were two types of flow regimes identified. Unfortunately, there was no mention of how they affected the performance of the aerator. It would be expected that the presence of a large ventilated air cavity would lower the performance, due to a reduced interfacial area for mass transfer, when compared to a bubbly flow. The ventilated air cavity would also be expected to increase pressure losses due to the increase in water velocity around the core, which would therefore increase frictional losses. Within the work of Baylar et al (2006) and (2007) the performance of different sized venturi aerator were studied, however there was no consideration to geometric scaling and how it affected performance.

2.3. Geometric scaling of venturi aerators

It was shown by Baylar et al (2006) that the inlet and outlet diameter of the venturi had an impact on the air entrainment and SOTR of the venturi. However, there was no mention of how increasing the diameter of the venturi affected the aeration efficiency of it. Jackson and Collins (1964) conducted experiments on the geometric scale up of a venturi aerator. The experimental set up involved two venturi designs geometrically scaled down from a 4 inch to a ¾ inch device, therefore a geometric scaling factor of 5. Both devices were tested with water and air flowing concurrently in the horizontal direction. Samples of DO were taken immediately downstream of the venturi and at the end of the outlet pipe, which extended 4.2 m, approximately 42 ID at the 4 inch scale, from the end of the venturi.

During the experimental work it was noted that in the larger venturi, less than 2 % of the oxygen transfer occurred in the downstream section of the outlet pipe. This was as a result of the horizontal orientation of the set up. It was observed that rapid separation of the air from the water occurred downstream of the venturi, due to buoyancy effects. Operating a venturi aerator in a vertical orientation would prevent the separation of the air and water and therefore there would be an increase oxygen transfer through prolonging the interfacial contact.

Geometric similarity in scaling is when two objects are comparable in every respect apart from size, such that the one object can be obtained from the other by uniformly enlarging or shrinking. Measures of similarity include geometric, kinematic, dynamic, thermal and chemical. Geometric similarity occurs when all ratios of dimensions are equal at equivalent points in a system. Kinematic similarity is when the fluid flow associated with both objects undergoes similar time rate changes of motions, for example fluid streamlines are similar. Dynamic similarity requires that relative deformations be geometrically similar, moving points follow geometrically similar paths and corresponding forces have equal ratios. Thermal and chemical similarities require that temperature and concentration differences are equal, (Jackson & Collins, 1964).

To ensure similarity dimensionless groups, for example Reynolds, Froude, Weber, Schmidt, Pressure and Sherwood Number can be used. Maintaining constant values between these dimensionless groups for the small and large scale objects ensures similarity between them.

$$Reynolds\ Number - Re = \frac{\rho u d}{\mu} \quad [2.2]$$

$$Froude\ Number - Fr = \frac{u^2}{dg} \quad [2.3]$$

$$Weber\ Number - We = \frac{\rho u^2 d}{\sigma} \quad [2.4]$$

$$Schmidt\ Number - Sc = \frac{\mu}{\rho D} \quad [2.5]$$

$$Pressure\ Number - \ N_P = \frac{\Delta P}{\rho u^2} = \frac{\rho A^2 \Delta P}{\dot{m}^2} \quad [2.6]$$

$$Sherwood\ Number - Sh = \frac{jd}{D\Delta c} \quad [2.7]$$

From Equations 2.2 and 2.7 it can be seen that similarity between more than one dimensionless number is sometimes impossible, especially when looking at velocity and diameter terms. For instance, when looking at Reynolds number. This is because as the diameter increases the velocity would have to be decreased proportionally. However, for Froude number the velocity would have to be increased proportionally to the power of one half of the diameter increase and for Weber number the velocity would have to be decreased proportionally to the one half power of the diameter increase. Therefore, maintaining a constant for all three numbers would be improbable. If two of the groups have little effect on the scale the other may be controlling. However, if two or more of the groups are controlling, then the system cannot be scaled up similarly, if this is the case then the regime is said to be 'mixed', (Jackson & Collins, 1964).

The dimensionless groups which control a system can be determined using dimensional analysis. In terms of mass transfer, dimensional analysis enables the relationships between average transfer rates and the applied forces, which are used to drive the transport to be established. This is done through the use of dimensionless groups and the correlations between them. A deeper understanding is obtained by interpreting the dimensionless groups as the ratio of fluxes and driving forces, or as the ratio of two driving forces. The magnitude of dimensionless groups makes it possible to differentiate between the dominant and the negligible forces in the transport process.

When considering oxygen transfer, the average mass flux depends on the bulk concentration of the water and the diffusion coefficient of oxygen into water, as well as the bubble diameter of the air. However, the fluid density, viscosity and the bubble velocity relative to the water need to be considered. This is because the bubble moves relative to the water and the flow pattern of the water alters the distribution of the air in it, which thereby modifies the diffusion flux at the particle surface.

Table 2.1: - Relevant quantities and their dimensions for aeration.

Quantity	Symbol	Dimension
Mass transfer coefficient	k	$\frac{L}{t}$
Diffusion coefficient	D	$\frac{L^2}{t}$
Bubble diameter	d	L
Bubble velocity	U_b	$\frac{L}{t}$
Water density	ρ	$\frac{M}{L^3}$
Water Viscosity	μ	$\frac{M}{Lt}$

In Table 2.1, it is shown that there are six dimensional quantities and three dimensions, which are mass, M, length, L, and time, t, that are associated with mass transfer. Using Buckingham Pi Theorem, it is expected there would be three independent dimensionless groups.

Using the Buckingham method of grouping variables, Appendix A shows that the three dimensionless groups for mass transfer are Sherwood Number, Reynolds Number and Schmidt Number where, (Welty, et al., 2000)

$$Sh = f(Re, Sc) \quad [2.8]$$

The overall aeration efficiency of a system depends on the power, where power consumption is a function of pressure loss. Table 2.2 shows the seven dimensional quantities associated with pressure loss.

Table 2.2: - Relevant quantities and their dimensions for pressure loss.

Quantity	Symbol	Dimension
Pressure Loss	ΔP	$\frac{M}{Lt^2}$
Velocity	U	$\frac{L}{t}$
Density	ρ	$\frac{M}{L^3}$
Viscosity	μ	$\frac{M}{Lt}$
Diameter	d	L
Length	L	L
Surface roughness	ε	L

In Table 2.2 there are seven dimensional quantities and three dimensions, mass, M, length, L, and time, t. Using Buckingham Pi Theorem it is expected there would be 4 independent dimensionless groups. Using the Buckingham method of grouping variables, Appendix A shows that the four dimensionless groups for pressure loss are Pressure Number, Reynolds Number, entrance length and relative roughness where,

$$N_P = f(Re, \frac{L}{d}, \frac{\varepsilon}{d}) \quad [2.9]$$

As will be shown in Chapter 3, pressure drop is a function of friction factor, where friction factor is a function of entrance length, $\frac{L}{d}$, the relative roughness in the pipe, $\frac{\varepsilon}{d}$ and Re.

As shown in Equations 2.8 and 2.9, the primary dimensionless numbers for overall aeration efficiency are Sherwood and Pressure Number. Therefore when geometrically scaling, if the fluid properties such as diffusivity and density are maintained, as well as flow characteristics such as mass flux and therefore velocity, similarity can be achieved between geometrically scaled aerators.

Jackson and Collins (1964) decided that scaling by Reynolds or Weber number were not practical as their geometric scaling was to the factor of 5, which would mean that if scaled by Reynolds or Weber Number the liquid velocity in the large venturi would be in an impractical operating range for their experimental set. The operating range of the 4 inch venturi was between 2 and 4.6 ms^{-1}, if scaled by Reynolds Number then the velocities through the ¾ inch venturi would be between 10 and 23 ms^{-1}. These high velocities would result in significantly higher pressure loss, as shown by the Pressure number, where pressure loss is a function of velocity squared. Therefore, Jackson and Collins (1964) considered it more practical to compare the devices based on upstream and throat water velocities, with considerations being made towards the fact that the

Reynolds number in the larger venturi would be 5 times that of the smaller unit. However, the Pressure numbers tended to be similar. This was shown in the measured pressure drops for water flow only across the devices. When air was entrained pressure losses were consistently around 1.4 times greater in the larger venturi than the smaller device. Air entrainment increased 27 times for the larger venturi compared to the smaller one, which was comparable to the 25 times increase in capacity factor of the liquid flow. Despite this, the transfer factors for the larger venturi were only 9 times that of the small device. As a result the 4 inch venturi was only 25% as efficient as the smaller venturi, under the same flow conditions. Within the work by Jackson and Collins (1964), it was highlighted that higher aeration efficiencies occurred at the lower liquid flow rates, similar to that found in Baylar and Emiroglu (2003).

The work by Jackson and Collins (1964) has shown than careful consideration is required when geometrically scaling venturi aerators and that operating in a horizontal orientation can significantly hamper the performance of an aerator due to flow separation.

2.4. Overview of downward two-phase flow patterns

As was shown in Gourich et al (2005) and (2007) there were two distinct flow regimes present in the downcomer of the system, a bubbly flow pattern and an annular liquid falling film around a central air core. To be able to maximise the interfacial area for mass transfer an understanding to two-phase flow regimes is required. There has been considerable research in the literature looking at the formation of the flow regimes in vertically downward two-phase flow, an outline of which will be discussed in this section.

Gas, liquid and solid are states of matter and a phase is simply one of these states, therefore two-phase flow is the simultaneous flow of two states, in the case of aeration, the gas and liquid phases correspond to air and water. Two-phase flows obey the basic laws of fluid dynamics and there are many characteristics that can affect the structure of the flow, such as (Wallis, 1969),

a) The inertia of the gas on the liquid,
b) The viscosity of the gas and the liquid,
c) The density difference and buoyancy,
d) The surface tension and surface contamination,
e) Heat and mass transfer may also affect the dynamics of a gas bubble,
f) The surface roughness of the pipe wall.

When considering two-phase vertical flow patterns in pipes, it can be seen in Figure 2.4 that they are symmetrical about the central pipe axis. The flow pattern or regime is governed by the interactions between the liquid inertia, buoyancy, gravity and surface tension. Bhagwat and Ghajar (2012) studied the similarities and differences in the flow patterns of vertical upward and downward air-water two-phase flow on 12.7 mm ID pipe. The major flow patterns observed in vertical two-phase flow include bubbly, slug, froth, falling film and annular flow, as shown in Figure 2.4.

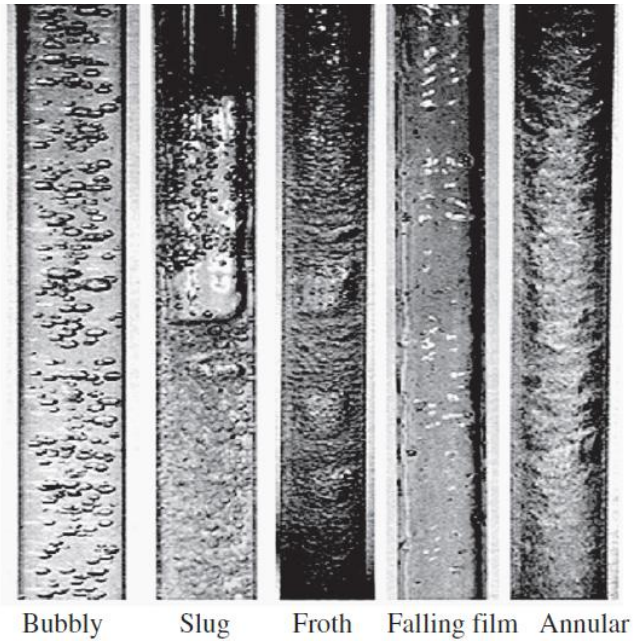

Figure 2.4: - Flow patterns in vertical downward two-phase flow taken from Bhagwat and Ghajar (2012)

2.5. Bubbly flow regime

A bubbly flow pattern consists of very small bubbles dispersed uniformly in the liquid phase, which are distributed throughout the pipe cross section. It was reported by Oshinowo and Charles (1974) that the bubbles speed and size increased as liquid and gas flow rates increased respectively. During vertically downward flow the inertia forces of the liquid and the buoyancy force of the gas act in opposite directions, therefore the flow of the gas and liquid oppose each other.

In Kashinsky and Randin (1999) and Bhagwat and Ghajar (2012) the bubbles observed in downward vertical two-phase flow concentrated near the central axis of the pipe, leaving the flow near the pipe walls single phase. It was suggested by Zun (1980) that the main reason for the bubble centring in downward flow was due to lateral force acting on the bubble in the flow with the velocity gradient and pressure profile. The study concluded that for a constant gas flow rate with increasing liquid flow rate, the bubbles reduced in size and were more evenly distributed across the diameter of the pipe, as a result of the dominant liquid inertia forces, as shown in Figure 2.5. However, if the liquid flow remained constant but the gas flow rate was increased, the bubbles elongated in the lateral direction and the flow regime tended to transition towards the slug flow regime, as shown in Figure 2.6.

During the experimental work by Kashinsky and Randin (1999) on 42.3 mm ID pipe, it was concluded that bubble size had a strong effect on the flow parameters and that the momentum exchange between the two phases was dependent upon the bubble diameter and its relative velocity. With the relative velocity of the bubble increasing with the increase in bubble size, therefore momentum exchange increases with increasing bubble diameter.

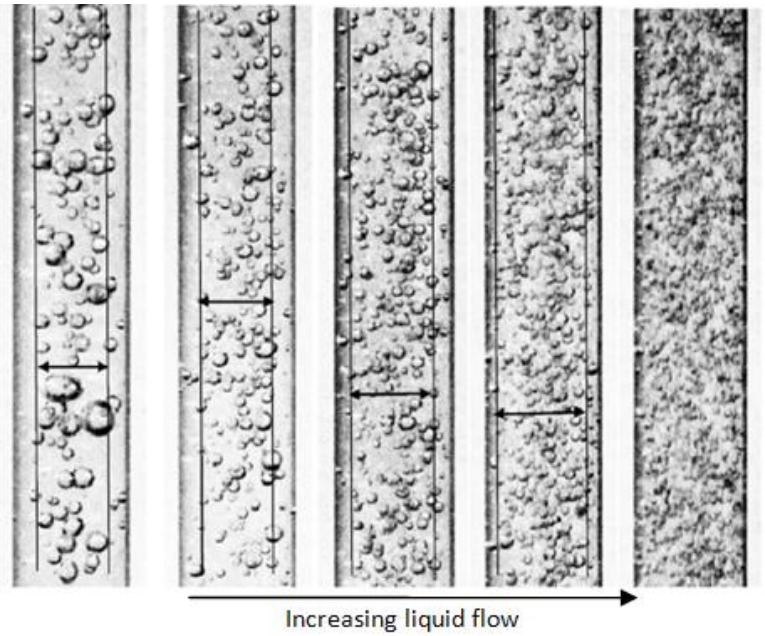

Figure 2.5: - Effect of increasing liquid superficial velocity on bubble shape and size and distribution for vertical downward bubbly flow adapted from Bhagwat and Ghajar (2012)

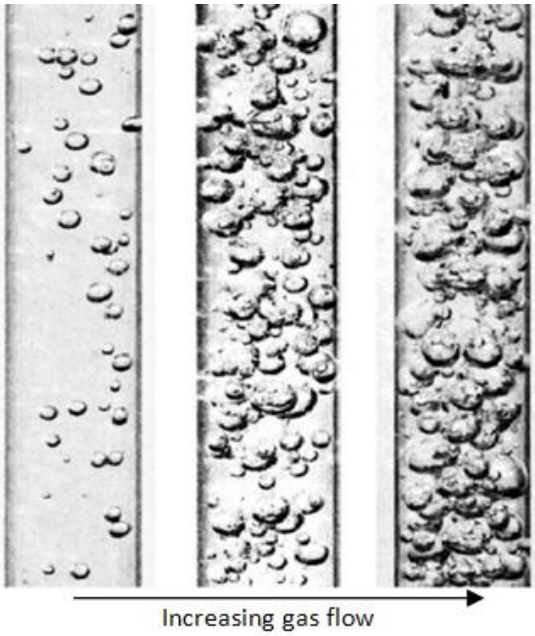

Figure 2.6: - Effect of increasing gas superficial velocity on bubble size and distribution for vertical downward flow taken from Bhagwat and Ghajar (2012)

2.6. Slug flow regime

The slug flow regime is characterised by an intermittent flow of long elongated gas slugs, whose diameter is comparable to the pipe diameter, as shown in Figure 2.4. In vertical downward flow these elongated slugs or large bubbles have a comparatively blunt nose for low gas and liquid flows. These bubbles are known as Taylor bubbles (Sotiriadis, 2005).

In many two-phase downward flow experiments such as, Gourich et al (2005) and (2007), Lee at al (1997)

and (2000), and Sotiriadis (2005) a ventilated cavity is seen to form beneath the point of air injection into a vertically downward water flow. Sotiriadis (2005) described this ventilated cavity as representative of a Taylor bubble in a slug flow regime. A slug flow regime exists over a range of gas and liquid flow rates and the pattern in each case is characterised by a sequence of large coherent bubbles, which are longer than they are wide, where the width almost spans the entirety of the pipe diameter. In between these large bubbles, slugs of aerated liquid exist. At the base of these large bubbles a liquid film at the wall of a pipe plunges into the liquid beneath and entrains a certain amount of gas in the form of small bubbles. These bubbles then flow with the bulk of the liquid flow. However, a fraction of these entrained bubbles coalesce back into the large bubble.

It is considered to be a fully developed slug flow, when the Taylor bubbles and the liquid slugs descend steadily and follow each other at a constant distance, where the flow can be considered as a train consisting of so called slug-cells, a slug cell is illustrated in Figure 2.7.

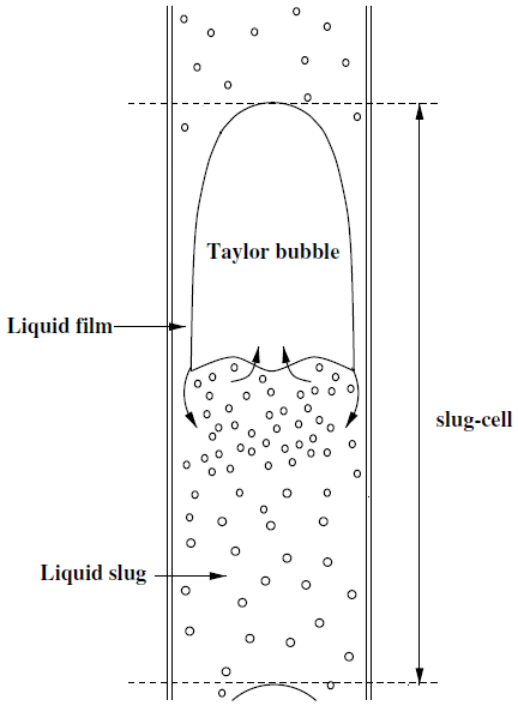

Figure 2.7: - Schematic picture of a slug cell in a vertical slug flow adapted from Sotiriadis (2005).

There are two main differences between the Taylor bubbles and a ventilated cavity formed beneath a point of gas injection. The first is that a ventilated cavity is static and remains attached to the point of air injection or another object that exists in the flow. This is in contrast to a Taylor bubble, which flows with the liquid flow. The second difference is that the liquid film falling around a ventilated cavity plunges concurrently into a down flowing liquid. This is in comparison to the liquid falling around a slug bubble which can fall counter currently into slugs of up flowing aerated liquid, depending on the overall direction of flow, for example vertically upwards or downwards. Therefore, there may be some hydrodynamic differences in the behaviour in the wake of the two types of flows.

2.7. Other two-phase flow regimes

Froth flow occurs when the gas flow rate is further increased from a slug flow regime, such that the Taylor bubbles disintegrate and merge with the liquid, forming a turbulent mixture, similar to that in a bubbly flow. Froth flows are difficult to distinguish due to their turbulent nature (Bhagwat & Ghajar, 2012)

The falling film or annular flow regimes occur during two-phase flow under the conditions of low liquid and high gas flow rates. The falling film flow regime is depicted by a wavy liquid film falling down the pipe wall with a central gas core, where the falling liquid phase travels at a higher velocity than the gas core due to gravitational forces and high inertia. As the gas flow rate is increased, bubbles are entrained into the liquid film, which has been observed to cause dry spots along the pipe wall (Bhagwat & Ghajar, 2012). The main difference between the falling film and annular flow regimes is that the annular film is more chaotic and turbulent than the falling film. However, there is no quantitative distinction between them (Bhagwat & Ghajar, 2012).

2.8. Void fraction and slip velocity

In a two-phase vertical downward flow the buoyancy forces of the gas act in the opposite direction to the inertia forces of the liquid, as a result the gas phase moves slower than the liquid. Therefore, a negative slip velocity is seen, where slip velocity is given by Equation 2.10. However, it was observed in the study by Bhagwat and Ghajar (2012) that this holds true for gas void fractions between 0 and 0.4, above this inertia overcomes the buoyancy of the gas phase and the gas velocity becomes greater than the actual liquid velocity, resulting in a velocity slip ratio greater than unity.

$$U_s = U_G - U_L \qquad [2.10]$$

Therefore, In a vertically downward orientation up to a gas void fraction of 0.4 the velocity slip ratio would be less than unity, where velocity slip ratio is given by,

$$S = \frac{U_G}{U_L} \qquad [2.11]$$

2.9. Interfacial structures differences in downwards two-phase flow

Ishii et al, (2004) tried to quantify the presence of the various flow regimes in a vertically downward two-phase flow and develop flow regime maps, such that it would be possible to determine which flow regime would be present for a set of flow conditions. The work focused on an adiabatic, air-water, concurrent vertically downward two-phase flow. In the work two pipes of 25.4 and 50.8 mm ID were used. Flow regime maps, as shown in Figure 2.8, were developed and several observations noted.

There were significant changes in the flow regime maps between the 25.4 and 50.8 mm ID pipe, showing that the flow regime was affected by the test section geometry. Throughout the experimentation, centre peaked void distributions were noticed during the bubbly flow regime and the centre peaking was more pronounced at higher superficial liquid flow rates. It was also noted that during bubbly flow, the bubbles

moved slower than the liquid flow rate, which is attributed to the directions of buoyancy and drag forces acting on the bubbles. The maximum gas void fractions tested were 0.23 and 0.062 in the 25.4 and 50.8 mm ID test sections respectively, which are less than 0.4, the value quoted by Bhagwat and Ghajar (2012) where the gas velocity becomes faster than the liquid velocity.

The study showed that an increase in the superficial liquid velocity increased turbulence and therefore increased the level of bubble breakage caused by the impact of turbulent eddies, resulting in smaller gas bubbles, as was also shown in Bhagwat and Ghajar (2012). However, coalescence was dominant at lower superficial liquid velocities, therefore resulting in larger gas bubbles. This again was shown in Bhagwat and Ghajar (2012), as is highlighted in Figure 2.5.

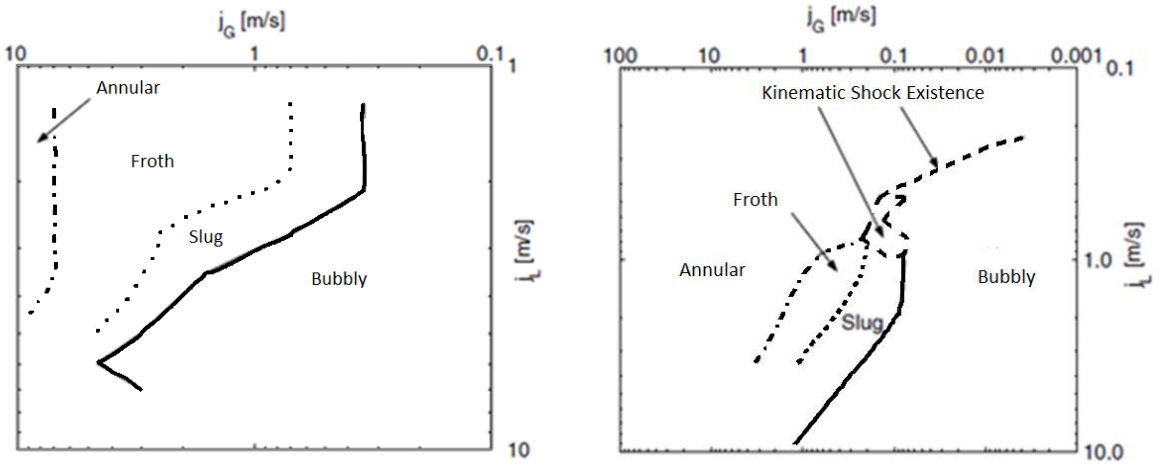

(a) (b)

Figure 2.8: - Flow regime maps for (a) 25.4mm and (b) 50.8mm pipe ID in an air and water concurrent vertically downwards two-phase flow as proposed by Ishii et al (2004).

It was noted that in the 50.8 mm ID test section a kinematic shock was observed. This kinematic shock represented the abrupt transition from the bubbly to annular flow regime within the test section. Under this condition, annular flow appeared on the upstream side of the kinematic shock and bubbly flow on the downstream region. This kinematic shock was not observed in the span of flow conditions tested for the 25.4 mm ID test section.

A kinematic shock is when there is a significant gradient or discontinuity in the air volume fraction. In this instance, there is a central air core on the upstream side, so therefore a high air volume fraction compared to the bubbly flow downstream of the kinematic shock, corresponding to a significantly lower air volume fraction.

To speed of shock or shock propagation velocity, u_s, is the condition where a kinematic shock will occur and it is said by Brennan (2005) to conform to Equation 2.12.

$$u_s = j + \frac{j_{GL_{us}} - j_{GL_{ds}}}{\varepsilon_{us} - \varepsilon_{ds}} \qquad [2.12]$$

where j is the total volumetric flux and j_{GL} is the drift flux between the gas and liquid phase.

Figure 2.9 shows a graphical schematic of the drift flux against gas volume fraction for a vertically downward gas-liquid two-phase flow. It is seen that the maximum drift flux occurs at approximately a volume fraction of 0.4.

In Equation 2.12, the differences, if any in the component densities across the shock are considered negligible. Due to the low pressures experienced in this experimental work and therefore minimal density variation of the air, the assumption of constant density can be considered valid. In Equation 2.12, it can be seen that for a constant water flow rate, as the air flow rate is increased so will u_s. This is because the total volumetric flux will increase and so will the air volume fraction downstream of the venturi.

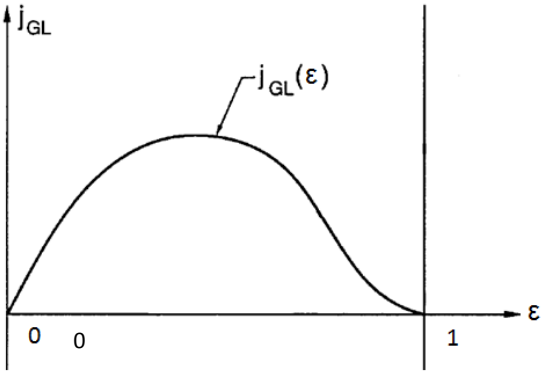

Figure 2.9: - Drift flux chart for a vertically downward gas-liquid two phase flow adapted from Brennan (2005).

2.10. Spargers in vertically downward two-phase flow.

The research of Bacon et al (1995) and Lee et al (1997) focussed on the formation and characteristics of a ventilated cavity, which formed beneath a sparger in a down flowing liquid. It has been documented in many experiments including Riiser et al (1992), Fabre and Line (1992) and Gourich et al (2005) and (2007) that a ventilated cavity can form at the base of the sparger and remains despite fast flowing liquid around it, which would otherwise cause a free bubble to travel down and out of the pipe with the flowing liquid. The presence of this large bubble in a bubble column is considered to be undesirable because it reduces the potential interfacial area for mass transfer, in comparison to a bubbly flow. This reduced potential for mass transfer may lead to anoxia in many biochemical reactions. The presence of a large bubble also reduces the density of the driving force in a loop reactor for example, and therefore the possibility of stall and flow reversal is likely.

Riiser et al, (1992) studied the mechanism for air entrainment, having measured the entrainment rate from the base and along the length of a Taylor bubble using high speed photography. A Taylor bubble is one that occurs in multiphase flows, where large bubbles of the lighter phase form by the coalescence of the smaller bubbles under certain flow conditions, similar to a ventilated cavity forming beneath a point of air injection. The waves moving down the thin liquid film, that surrounds the ventilated cavity, shear at the gas-liquid interface to entrain a thin film of gas down from the periphery of the ventilated cavity. This thin film then breaks up into a number of small bubbles, as a result of eddies that exist below the ventilated cavity. Some

of the small bubbles rejoin the larger bubble and the rest are drawn down with the flowing liquid, a schematic of which is shown in Figure 2.10.

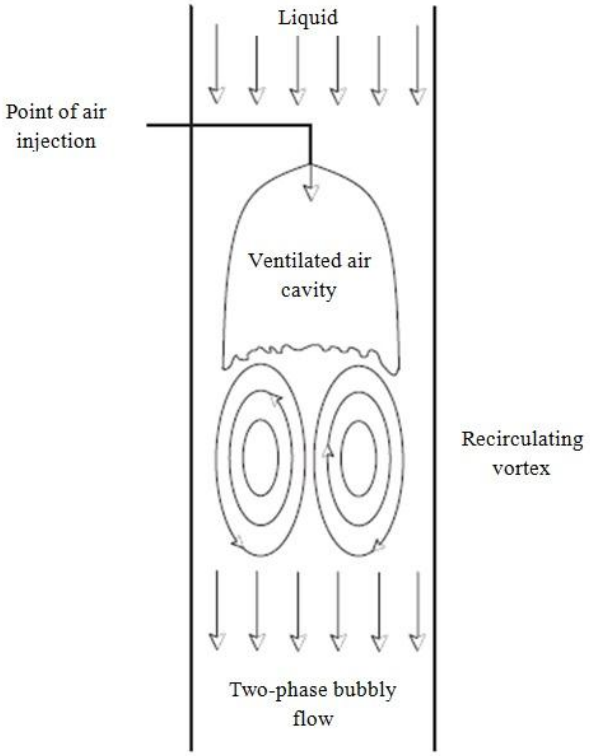

Figure 2.10: - Flow geometry for ventilated cavity and recirculation region, adapted from Sotiriadis and Thorpe (2005).

Bacon et al, (1995) showed that for each constant liquid flow rate a stable ventilated cavity length was achieved. This stable ventilated cavity length represented a point at which the liquid is able to entrain air at the same rate that it is supplied by the sparger. Then any step increase in the supplied air flow rate would cause the ventilated cavity to increase in length downwards until stability was reached again, at this point the new entrainment rate matches the supply rate. When the ventilated cavity grows sufficiently the annulus of flowing liquid around it achieves a characteristic film thickness with waves of a characteristic height (Aragaki, et al., 1987; Karapantsios, et al., 1989). Any increase in the air supply above this will cause the ventilated cavity to grow unbounded. The value for which this occurs is called the maximum entrainment rate and at this point an infinite ventilated cavity exists causing a bubble column within a loop reactor to stall (Bacon, et al., 1994).

During the experimentation of Bacon et al (1995), maximum entrainment rates were established from liquid flow rates between 1.4 and 3.4 L/s, which correspond to $U_w \approx 0.5$ and 1.3 ms^{-1} respectively, with air flow rates of between 1.5 to 20 L/min. The experiments were conducted on 57 mm ID pipe using peripheral, PS, central, CS and horizontal, HS, spargers. It was shown that the PS exhibits ventilated cavity lengths that are consistently shorter that those of the other spargers, schematics of the HS, CS and PS are shown in Figure 2.11.

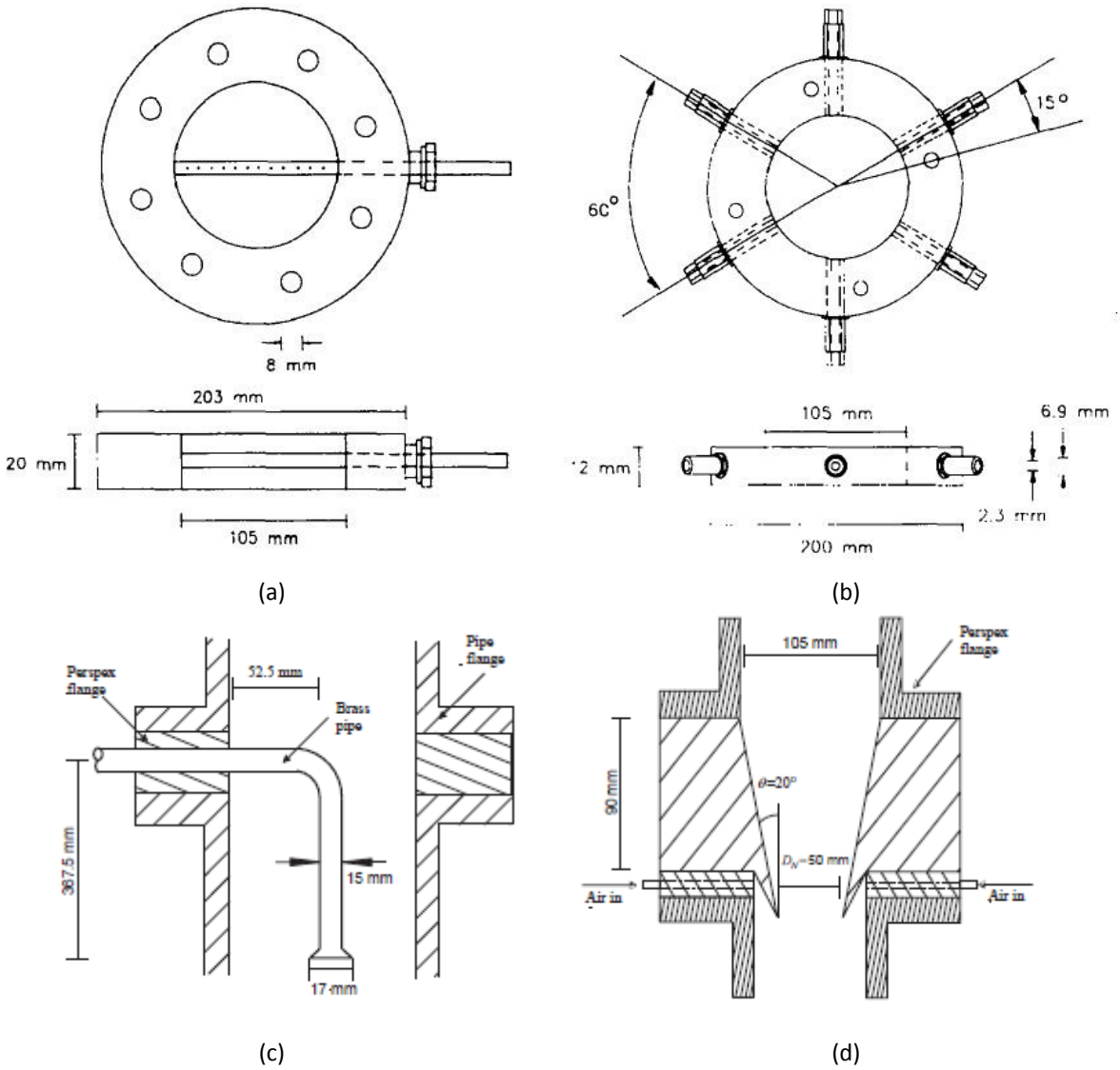

Figure 2.11: - (a) horizontal sparger and (b) peripheral sparger from 0.105 m ID pipe from Lee et al (1997), (c) a central and (d) plunging jet sparger used in the experimental work by Sotiriadis et al (2005).

In 1997, Lee et al conducted research based on the spargers used in Bacon et al (1995) where they were geometrically scaled up to be used within a 105 mm ID pipe. The original PS and HS were used in the experiments as well as their geometrically scaled up equivalents. Observations in the experiment included jumps in the ventilated cavity length as the air was steadily increased. This only happened with the PS and at the lower water flow rates, below $U_w \approx 1$ ms^{-1}. This phenomenon did not happen as the air was being reduced. The jumps in the ventilated cavity length were believed to have been caused by the individual air streams merging randomly to form a larger ventilated cavity. Once coalescence occurred in the flow, the reverse process to separate the streams was a more gradual process, thus showing hysteresis effect with the PS (Lee, et al., 1997).

Dimensional analysis was undertaken and it was determined that the maximum air entrainment rate was a function of the liquid Froude number, Fr_L, Eötvös, Eö, and Viscosity, N_μ, numbers. Using this it was possible

to establish correlations and compare the maximum entrainment rates of the HS and PS, with results falling within ± 15 and ± 20 % for the HS and PS respectively. The Eö may be regarded as being proportional to the buoyancy force divided by the surface tension force and N_μ is given by Equation 2.13. Therefore, it is possible to compare directly the air entrainment between two geometrically scaled systems. However, there was no consideration in this work to mass transfer or pressure losses.

$$N_\mu = \frac{\mu}{\rho(gd^3)^{0.5}} \qquad [2.13]$$

Lee et al (2000) further developed the work from 1997 by measuring the pressure losses along the length of the ventilated cavity beneath the sparger. The energy loss was determined from pressure profiles which were measured along the ventilated cavity. It was shown that a percentage of the hydrostatic potential energy associated with the ventilated cavity length is lost, typically 70% (Lee, et al., 2000). The pressure profile from the point of air injection to a bubbly flow was documented as having, a constant pressure along the entire length of the ventilated cavity, which is because the density of the air in the bubble is small. However, the differential pressure measurements at the bubble base had a high degree of scatter. This was attributed to the bubble length fluctuations that were occurring (Lee, et al., 2000). Pressure recovery was identified in the wake of the bubble, where the flow was converted from a small annulus to a bubbly flow which filled the entire pipe. This momentum transfer resulted in a pressure increase. Below this wake region the hydrostatic pressure increase was less than that above the point of air injection for the same distance. This was due to the presence of bubbles in the flow lowering the flow density (Lee, et al., 2000).

Lee et al, (1998) showed that the longer the ventilated cavity the further downstream it was before pressure recovery occurred. It was shown in Lee et al (2000) that approximately 70% of the hydrostatic head associated with the bubble length was lost, whilst the rest was recovered in the wake of the bubble. The fraction of hydrostatic head lost, appeared to be independent of bubble length and water flow rate. For the longer ventilated cavities there is a significant frictional energy loss at the walls of the pipe, where the falling film velocity is much greater than the upstream velocity. This loss was seen to be as a first approximation to be proportional to bubble length (Lee, et al., 2000). Within the work by Lee et al (2000) there was no mention to the cause of the ventilated cavity and under what conditions it formed, there was also a limited range of water flow rates tested in the experiments, U_W = 0.8 and 1.7 ms^{-1}.

Sotiriadis et al (2005) continued the work of Bacon et al (1995), Lee at al (1997) and (2000) by investigating the bubble size and mass transfer characteristics of the HS, PS and CS's as well as a plunging jet sparger, PJS, which is shown in Figure 2.11 (d). A plunging jet sparger deliberately channels the liquid to the centre of the pipe and air is injected perpendicularly to the liquid flow through the pipe wall, the air is then deflected downwards by the lip of the sparger. Offering some similarities to the convergent and throat section of a venturi aerator.

Water flow rates measured were between 8.2 and 15.5 L/s, corresponding to U_w = 0.95 and 1.57 ms^{-1}

respectively, and air flow rates of between 2.2 and 52.8 L/min, corresponding to void fractions of between 0.4 and 8.1 %. The bubbles of the experiments were measured using high speed photography at a point 18 ID below the sparger inlets, it was also just below this point where a DO probe was located in the side of the pipe, with minimal physical intrusion into the liquid flow. The results from the experimental work showed the PJS did not allow the formation of a ventilated cavity and also produced a higher specific interfacial area for mass transfer, when compared to the other three spargers. The PS, CS and HS essentially produced the same overall mass transfer coefficient and bubble size within 10 % of each other and the PJS had an increase of 19 % in terms oxygen transfer over the HS (Sotiriadis, et al., 2005).

It was shown however that when power consumption was taken into account the PJS and HS had similar aeration efficiencies. However, the PJS has operational advantages of producing shorter ventilated cavity lengths and therefore, having a greater resistance to stall at low liquid flow rates (Sotiriadis, et al., 2005).

Therefore, the results of the work by Sotiriadis et al (2005) showed that using a PJS and therefore introducing the air closer to the pipe wall than the existing liquid flow can cause the reduction or complete removal of the ventilated cavity. Section 2.5 showed that during a two-phase vertically downward bubbly flow regime, the dispersed phase, in this case the air, centres within the pipe due to the lateral force acting on the bubbles caused by the velocity gradient. Through introducing the air at the pipe wall causes the air and the water to interact, due to the movement of the air from the pipe wall to the centre of the pipe, thus causing bubble breakage.

The work by Sotiriadis et al (2005) provides an insight into the flow regimes, mass transfer and power consumption as a result of the flow regime. However, there was a limited range of water and air flow rates tested, as well as consideration as to why the ventilated cavity formed.

2.11. Plunging liquid jet reactor

It was previously thought in Bacon et al (1995) and Lee at al (2000) that the mechanisms involved with in air entrainment in plunging jet systems could be comparable to a ventilated cavity attached to a point of air injection. A liquid film surrounding a Taylor bubble or by analogy a ventilated cavity beneath an air injection source, forms an annular plunging jet, which produces a ring like surface depression at the rear part of the ventilated cavity. This is in a similar fashion to a typical plunging liquid jet (Sotiriadis, 2005). Therefore this section reviews and also emphasises any similarities that might exist between plunging jets and a ventilated cavity, which is present in a down flowing liquid. There is a wealth of information in the literature regarding plunging liquid jets and confined jet systems.

Evans et al (1992) studied the bubble size generated beneath a plunging jet in an air and water system, a schematic of a plunging jet is shown in Figure 2.12. It can be seen to be representative of a ventilated cavity, where a high speed liquid jet or liquid film, passes through a head space or around a ventilated cavity, and

plunges into the bulk liquid below, where a region of high recirculation and energy dissipation, known as the mixing zone is generated. In the mixing zone the entrained air is broken down into fine bubbles before being transported downward by the liquid flow.

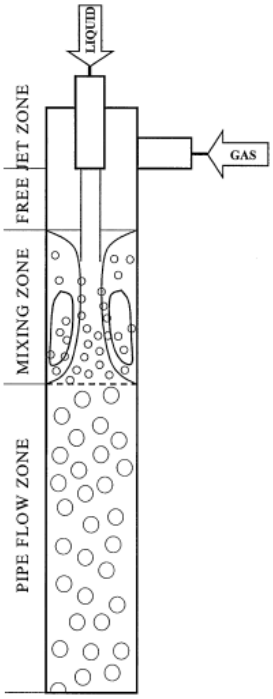

Figure 2.12: - Schematic of a plunging liquid jet adapted from Evans et al (1996).

Within the work by Evans et al (1992) experiments were conducted on various bubble column diameters of 44 to 95 mm ID, with a jet velocity of 11.5 ms^{-1}. In the work by Evans et al (1992) it was shown that theory suggested through combining the Kolmogoroff energy distribution law, Equation 2.14, with Weber number, an expression for the maximum stable bubble diameter can be formed, as shown in Equation 2.15.

$$\overline{u^2} = C_1 \left(\frac{\epsilon d}{\rho}\right)^{\frac{2}{3}} \quad [2.14]$$

According to Batchelor (1951), C_1 approximated to 2.0.

$$d_{max} = \left(\frac{We_{crit}\sigma}{2}\right)^{0.6} \rho^{-0.2}\epsilon^{-0.4} \quad [2.15]$$

The energy dissipation rate that determines the maximum bubble size in the mixing zone can be found by considering what happens to the entrained air. Initially, all of the entrained air enters the mixing zone at the plunge point of the liquid jet. Similar to when a falling liquid film around a ventilated cavity enters the liquid beneath. The high energy dissipation in this region results in the generation of a number of very fine bubbles that are carried downward by the bulk water and leaves the mixing zone (Evans, et al., 1992). Along with the fine bubbles a number of larger bubbles are also generated which re-circulate within the mixing zone, where they are eventually broken down into finer bubbles, which are then carried downward by the liquid flow. Evans et al (1992) stated that the residence time of the larger bubbles inside the mixing zone was in the order of 1 s and they believed that this amount of time was plenty to allow a sufficient number of breakages to occur, so that an equilibrium maximum stable bubble diameter is reached. Within the

experimental work by Evans et al (1992) it was found that a critical Weber number of 1.2 gave good agreement with the experimental results of the maximum stable bubble diameter. This was in good agreement to the value of 1.18 found by Hinze (1955), which was based on the breakup of a droplet or bubble in a viscous shear flow. It was also found that the ratio of Sauter mean bubble diameter to the maximum bubble was equal to 0.61.

When considering a plunging jet or liquid falling film, it is important to consider the mechanisms for air entrainment. In Evans et al (1992), it was discovered that a bi-modal bubble size distribution existed. This could be caused by the different sizes of bubbles generated in the region close to the point of impact of the plunging liquid jet. The smaller bubbles spend only a short time in the mixing zone before being carried downward by the liquid flow, whereas the larger bubbles are re-circulated for a much longer period of time before being broken down. The secondary breakup of the larger bubbles could possibly result in a second distribution, which is different to the initial distribution of finer bubbles.

During the experimental work by Evans et al (1992) a very limited range of jet velocities were tested with the vast majority of the experiments conducted at a jet velocity of 11.5 ms^{-1}. A stable liquid falling film velocity of 11.5 ms^{-1} would correspond to an upstream water velocity of 5.6 ms^{-1}, in this experimental work according to Aragaki et al (1987), the method for this calculation is discussed in Chapter 6. An upstream water velocity of 5.6 ms^{-1} is higher than the velocities considered within this experimental work.

Evans et al (1996) noticed that increasing the air flow rate in a plunging jet system affected the level of the receiving water below the liquid jet. It was shown that with lower air flow rates the level of the air-water mixture was sustained just below the nozzle. However, as the air flow rate was increased, a point was reached where the jet could no longer entrain all of the air being introduced into the headspace, as a result the air-water mixture level in the column started to drop, until a new equilibrium height was reached. In a sense, the jet is self regulating, such that the length of the jet will increase to accommodate the increase in the amount of air being entrained into the column. Figure 2.13 illustrates this phenomenon. This is representative of the results found in Bacon et al (1995), where the length of ventilated cavity increased with increasing air entrainment.

Ohkawa et al (1987) made the assumption of a plug flow within the pipe flow zone beneath the mixing zone, which is shown in Figure 2.12. Mao et al (1993) justified this assumption and also considered the mixing zone as being perfectly mixed. These assumptions were also validated by Evans et al (1996).

Evans et al (1996) considered that mass transfer in the mixing zone was over an order of magnitude greater than that in the pipe flow zone. Therefore, the turbulent mixing in the mixing zone has a significant impact on the performance of the plunging liquid jet reactor. Therefore, it can be assumed that if a ventilated cavity is present, the resulting mixing zone beneath it can have an important affect on the performance of a

venturi type aerator.

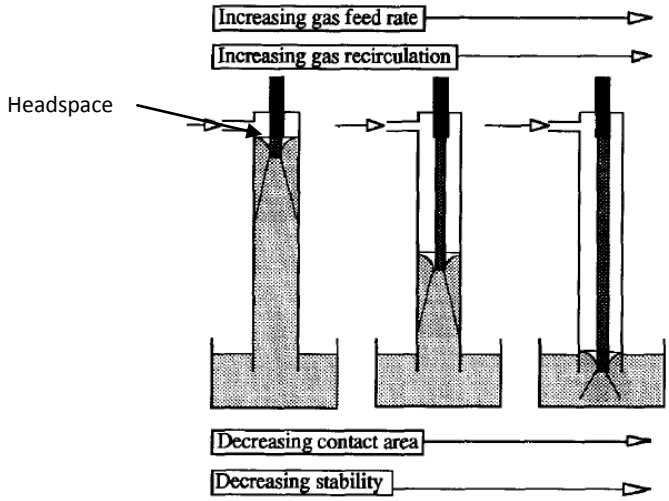

Figure 2.13: - Plunging liquid jet length and the affect of increased air flow rate, taken from Evans et al (1996)

Evans et al (2001) confirmed that the turbulence level in the pipe flow zone is significantly lower than that in the mixing zone. It was also shown in Evans et al (2001) that the coalescence of the bubble is not hindered in the pipe flow zone. However, the coalescence and breakage rates were in equilibrium, such that a constant mean bubble size existed down the length of the pipe flow zone. Within Evans at al (2001) a mean bubble diameter of between 3 and 4 mm was observed.

Cramers and Beenackers (2001) conducted experimental research on how the geometrical design parameters of a plunging liquid jet reactor within an open pool affected its performance. The various parameters tested included inducing a swirl upstream of the nozzle through the use of a spinner. The mixing tube length and the nozzle to mixing tube diameter ratio were also adjusted. All of these parameters were shown to influence the mass transfer characteristics of the system.

The key finding in the experimental work by Cramers and Beenackers (2001) was the affect of inducing swirl upstream of the nozzle and how it affected the flow regime and mass transfer coefficient of the system. The experiments showed two distinct flow regimes in an air-water ejector, where the flow regime depended upon the air-water flow ratio. At low ratios the mixing zone formed close to the nozzle of the ejector, but as the air flow rate is increased the mixing zone moves further towards the ejector outlet. The mixing zone is the location where the liquid jet discharges into a bubbly mixture. The bubbly mixture was present with both swirl and no swirl being present. However, when the swirl was present and the air flow rate was increased an annular flow regime was identified. This is where a thin water film was present at the walls of the ejector and surrounded a central air core, representative of a ventilated cavity. This annular flow eventually formed into a bubbly flow, as can be seen in Figure 2.14. The presence of a swirl in the upstream flow was also shown to reduce the overall oxygen transfer coefficient, when compared to having no swirl

induced under the same flow conditions. Inducing a swirl was also shown to increase the pressure loss across the ejector and reduce the SOTE.

It was also found that increasing the length of the mixing tube in the plunging liquid jet reactor increased the mass transfer coefficient. The mixing tube is the straight section beneath the nozzle prior to the divergent section of the system, as shown in Figure 2.14. The mixing tube is representative as the point of maximum constriction or the throat in a venturi type aerator. With the plunging jet system it was found that the mass transfer coefficient reduced with an increase in the nozzle to mixing tube diameter ratio, therefore representative of a lower blockage ratio. However there was no relation between how the mixing tube length and nozzle to mixing tube diameter affected the pressure loss in the system.

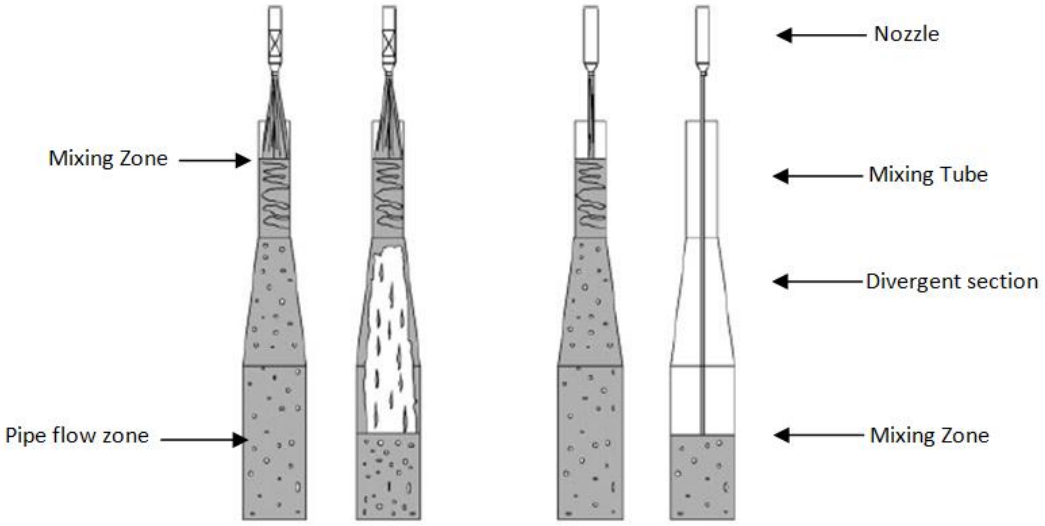

Figure 2.14: - Flow regimes in a gas liquid ejector, (a) with and (b) without swirl and low and high gas-liquid flow ratios adapted from Cramers and Beenackers (2001).

A number of alternate gases were also tested in Cramers and Beenackers (2001), including helium, nitrogen and argon. It was shown that as the density of the gas increases so does the mass transfer coefficient. The results were explained using Levich's theory which states that as the gas density increases, smaller bubbles are dispersed resulting in an increase in interfacial area, therefore improving mass transfer rates (Cramers & Beenackers, 2001). Cramers et al, (1993) demonstrated the bubble diameter of a gas was proportional to $\left(\rho_G\right)^{-0.2}$, therefore its interfacial area should also be proportional to $\left(\rho_G\right)^{-0.2}$. Cramers and Beenackers (2001) plotted the mass transfer coefficients for the various gases against void fraction multiplied by $\left(\rho_G\right)^{-0.2}$. The results are shown in Figure 2.15 and they show a clear and conforming relationship.

It was concluded that to maintain the mass transfer coefficient for the correct geometric scale up of an ejector. The power input per unit volume of the ejector and the relative dimensions of the ejector need to be scaled appropriately. Also, when swirl is present within a device, the swirl number is required to be constant when geometrically scaling, otherwise the flow transition point between the regimes would be

affected by geometric scale (Cramers & Beenackers, 2001).

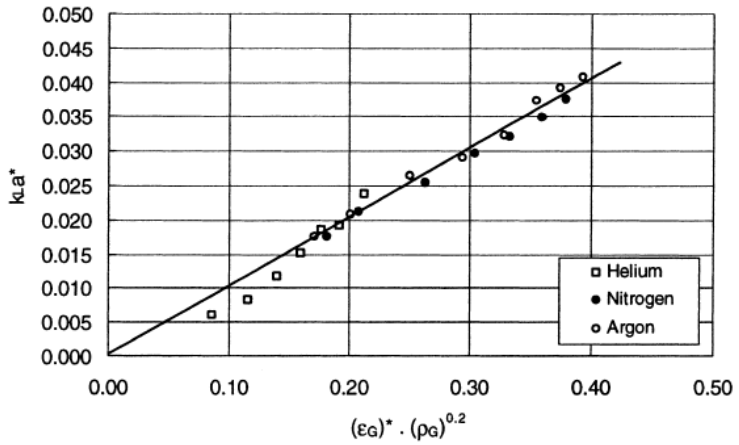

Figure 2.15: - Plot of volumetric mass transfer coefficient for a swirling gas-liquid ejector at Q_w = 0.5 L/s with a nozzle diameter of 4.7 mm, taken from Cramers and Beenackers (2001).

2.12. Mechanisms for air entrainment

Through introducing a air into a vertically downward water flow, it has been shown by Lee et al (1997), Lee (1998), Gourich et al (2005) and (2007), and Sotiriadis (2005) that a ventilated cavity is likely to form. Therefore, knowledge of the entrainment mechanism beneath this ventilated cavity is important. Bacon et al (1995), Lee et al (1997) and (2000) investigated the gas entrainment beneath ventilated cavities. They considered that the mechanisms for air entrainment beneath a ventilated cavity were similar to that of a plunging liquid jet.

With plunging liquid jets there are two distinct regions of air entrainment. The first of which is when the liquid jet nozzle was far enough away for the water surface and at a low velocity where the jet began to break up into small droplets prior to the liquid surface (Lara, 1979). The second is when the jet flows at a higher velocity and remained coherent from the nozzle to the surface. If the coherent jet length is equal to that of the distance between the nozzle and liquid surface then the entrained air stopped. The velocity at which this occurs is referred to as the inception velocity (Sotiriadis, 2005). Mckeogh and Ervine (1981) and Sene (1988) studied the effect of turbulence intensity on the inception velocity, finding that as turbulence intensity increased the inception velocity decreased.

Sene (1988) studied the entrainment rates of jets and offered the following explanations. It was concluded that for jets below 4 ms^{-1} the surface disturbances of the jet are the primary mechanism for air entrainment and for jets above 4 ms^{-1}, a thin layer of air existed at the surface of the jet which was set in motion by shear forces. Mckeogh and Ervine (1981) observed that for a circular turbulent jet, the air entrainment rate was equivalent to the area enclosed between the crests of the disturbances that were present in the surface of the falling liquid.

Riiser et al, (1992), Su (1995) Lee (1998), Delfos et al (2001), and Sotiriadis and Thorpe (2005) all

investigated air entrainment from the base of a ventilated cavity. They found that the air entrainment increases with the ventilated cavity length, air and liquid flow rates. Riiser et al (1992) viewed their experiments using high speed photography and identified that waves developed at the air and water interface of the falling liquid film, similar to that found in a plunging liquid jet and that these waves are responsible for the entrainment of the air at the base of the ventilated cavity.

Kockx et al (2005) suggested that the air entrainment was a result of the perturbations on the falling film at the base of a ventilated cavity. This statement is similar to what is observed in Sene (1988) with a rough turbulent plunging jet, where the Re in the falling film is greater than 2000. It was observed by Kockx et al (2005) that as surface roughness increases so does the air entrainment. They concluded that the air entrainment was a result of the free pool surface not being able to cope with the transverse oscillations of the incoming falling water film. As an incoming wave on the falling water film approached the free liquid surface a gravity wave resulted which propagated on the pools surface. When the two waves intersected a portion of air would be encased and therefore entrained into the flow, a schematic representation is shown in Figure 2.16.

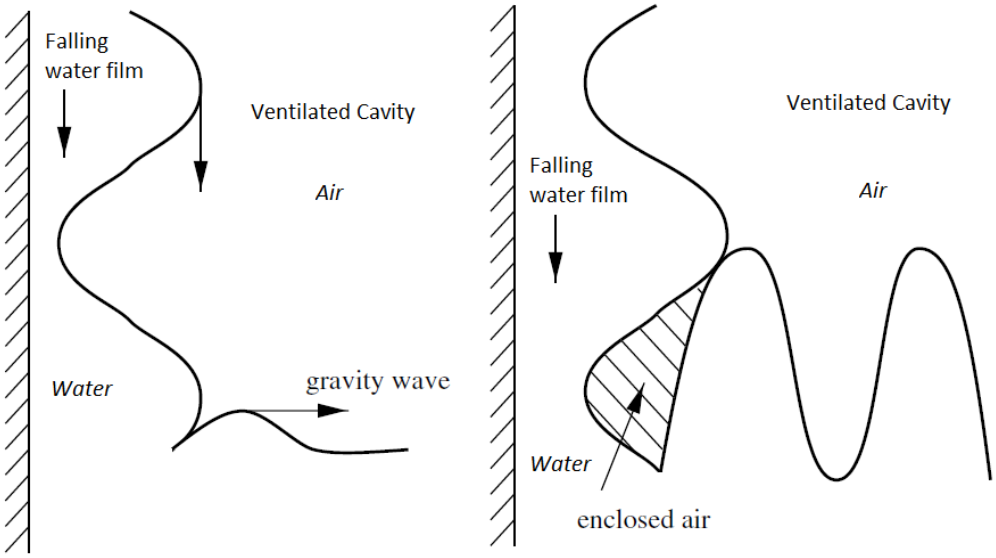

Figure 2.16: - An illustrated representation of the air entrainment mechanism at the bottom of a ventilated cavity, in a downward vertical air and water two-phase flow as proposed by and adapted from Kockx et al (2005).

Delfos et al (1993) analysed video motion pictures taken at the flow field below a ventilated cavity, from this they suggested that a toroidal vortex was formed as the liquid film plunged at the base of the ventilated cavity. The vortex was seen to influence the dispersion of the entrained bubbles. It was concluded that the vortex was axisymmetric for low air entrainment rates. However, at higher air entrainment rates the vortex became unstable and oscillated across the diameter of the pipe. Unfortunately, no quantitative results were presented to support these observations. Su (1995) also observed that a toroidal vortex formed in the wake field of a ventilated cavity, which was attached to a CS. He considered that the air was entrained because the vortex became asymmetric and enclosed a small amount of air from the base of the ventilated cavity. Su

(1995) commented that at higher ventilated cavity lengths the vortex became highly turbulent and was continuously entraining air bubbles along the entire perimeter of the ventilated cavity base.

Therefore, from research it can be seen that the mechanisms for air entrainment from a ventilated cavity can be summarised into three categories as described by Sotiriadis (2005), such that,

a) The air entrainment occurs due to the waves at the air and water interface along the surface of the film around the ventilated cavity. This type of mechanism occurs for turbulent falling films, where waves of significant amplitude are present on the surface of the film. These waves have peak heights greater than the mean film thickness, δ, and carry the majority of the liquid (Sotiriadis, 2005). When these waves reach the oscillating bottom of the ventilated cavity, they come into contact with the receiving flow, the recirculating vortex. The interaction with the waves and the vortex results in air entrainment. It can be considered that the surface roughness of the film increases with increasing Re, therefore the air entrainment will also increase with increasing Re. The mechanism is essentially the same as proposed by Kockx et al (2005), where air entrainment occurred due to the interaction of a travelling wave and a gravity wave of a turbulent plunging jet.
b) Air entrainment due to shear in laminar falling films, where no waves are present on the falling film surface. The air is entrained because of the velocity difference between the fast falling film and the slow receiving flow. This velocity difference creates a shear layer between the two adjacent liquid surfaces that is responsible for the fragmentation of the ventilated cavity at the plunge point and subsequent entrainment of the air. The amount of air entrained with this mechanism is much less than compared to waves present in a turbulent film (Sotiriadis, 2005).
c) Intermittent entrainment, where the falling film is in transition between laminar and turbulent flow. Under these conditions the film is mainly smooth along its length with some large isolated waves. The entrainment of the air is a combination of the two other mechanisms. More air is entrained when a large wave comes into contact with the receiving flow, than as a result of entrainment due to shear. This type of mechanism has been observed in Bacon (1995) and Lee (1998) for ventilated cavities attached to HS and CS's at low water and air flow rates.

2.13. Effects of liquid physical properties on air entrainment and ventilated cavity lengths

Bacon (1995), Su (1995) and Lee (1998) all monitored the effects of liquid surface tension on air entrainment rates, it was noted that decreasing the surface tension by using various aqueous solutions in the liquid, increased the air entrainment. It is believed that reducing the surface tension allows larger waves to be developed in the falling liquid film. Therefore, producing a greater volume of air between the wave peaks that can be encased and entrained, due to the interaction between these waves on the falling film surface and the receiving flow.

The effect of viscosity is currently unclear, with much contradiction between studies. Bacon (1995) concluded that increasing the liquid viscosity slowed down the flow and therefore decreased air

entrainment. This is in contrast Su (1995) and Lee (1998) who concluded that increasing the viscosity increased gas entrainment. They believed that the higher viscosity liquid produced a thicker falling film thickness, which allowed the development of greater amplitude disturbances and as a result entrained a greater level of air.

2.14. Bubble formation in flowing liquids

Bubble formation at an orifice contained in a tank filled by a liquid is a very complex phenomenon (Clift, et al., 1978). It is considered as a multistage process, a static or quasi static operation follow by a dynamic process (Kulkarni & Joshi, 2005). The later involves the coalescence of the bubbles, dispersion or break up which in turn is governed by local turbulence. Interactions also occur between the liquid and gaseous phase, such as interfacial transport process.

Ideally, an aeration device should be designed based on the knowledge of the suitable hydrodynamic parameters to achieve the desired performance. This involves the accurate prediction of the volume of the discrete phase, its residence time and contribution to mixing. As well as an understanding of the influence of the physicochemical properties of the liquid on the bubble formation and its behaviour.

Most research in the area of bubble formation at submerged orifices is experimental. Published studies focus on the formation and rise of bubbles ejected from a single orifice submerged in a tank filled with a stagnant Newtonian fluid. However, there is limited research on the mechanisms of bubble formation in flowing liquids with a single submerged orifice.

The mechanism of bubble formation when the liquid is also in motion is different and more complex than in stagnant water. The motion of the liquid phase has an important effect on the bubble growth, detachment and trajectory. In conjunction with this the parameters of the liquid velocity and its direction of flow with respect to the gas flow is of importance. There are three types of situations, concurrent flow, cross-flow in a tank type system and cross-flow over a blade section.

In concurrent flow, the resultant force due to the liquid flow and buoyancy is the dominant factor affecting bubble formation. This results in early detachment of the bubbles and hence a smaller produced bubble size. As an effect, these smaller bubble sizes are greater in number. Resulting in dispersion with a narrow bubble size distribution and high void fraction.

Figure 2.17 shows the formation of a bubble within a cross flowing liquid. When a growing bubble is exposed to liquid cross-flow, several mechanisms take place (Marshall, et al., 1993; Tan, et al., 2000; Kulkarni & Joshi, 2005),

a) The primary growth or expansion of the bubble, where the centre of the bubble moves in the direction of the flow by expansion. This mechanism is controlled by the liquid inertia forces and the

dynamics of the gas flow from the supply chamber to the bubble.

b) Horizontal translation, where the bubble centre moves parallel to the liquid flow due to the drag force. This results in necking and the bubble moves downstream and is flattened in shape by the motion of the liquid.

c) The drag force exerted by the liquid flow causes the severance of the neck and is responsible for early detachment. It was shown by Maier (1927) that the shear experienced by a growing bubble in a flowing liquid is at a maximum when the liquid flows at right angles to the nozzle axis.

d) The liquid flow prevents coalescence, such that the detached bubbles are swept away from the orifice.

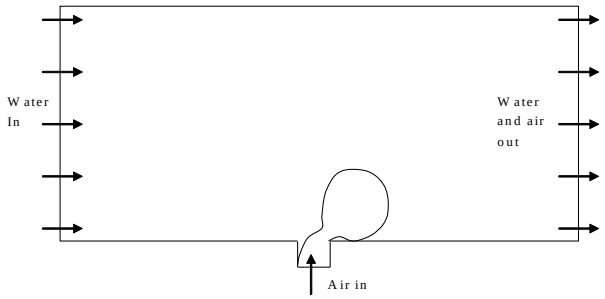

Figure 2.17: - Bubble growth in a liquid cross-flow from a bottom submerged orifice.

It was found that for air flow rates, the frequency of bubble production is not affect by the liquid cross flow (Suvillan, et al., 1964). However, at higher air flow rates, the frequency decreases as the velocity of liquid increases.

Marshall et al (1993) conducted an experimental study in which an orifice was positioned on the horizontal base of a two-dimensional, 2D, water tunnel. The submerged air was then exposed to a 2D fully turbulent flow. Three principal regimes of gas emission were identified.

a) Single bubbling

b) Pulse bubbling

c) Jetting

It was also found in Marshall et al (1993) that for a given gas and liquid system, the principal variables for determining the bubble formation regime were,

a) The liquid cross flow velocity,

b) The gas velocity through the orifice,

c) The orifice diameter.

2.15. Bubble formation in a liquid cross-flow over a blade section

Forrester and Rielly (1998) designed and built a rig to study the formation of bubbles from an orifice mounted on a blade section, which was then exposed to a strong liquid cross flow. The flow over the blade had a 2D turbulent profile. Three designs of blade were considered, a cylindrical, a flat and a concave

section. With two blade angles of 0 and 90˚. High speed photography showed the existence of four regimes of bubble formation.

a) Single bubbling occurs at very low gas flow rates. This regime is characterised by the regular production of almost spherical bubbles, of approximately uniform size and detaching close to the orifice. The bubbles follow the blade profile into the wake region. Then they join the bulk liquid flow over the blade.
b) Pulse bubbling occurs when the gas flow rate increases, while the liquid velocity remains constant. The growing bubbles lose their spherical shape. The detachment occurs further away from the orifice, due to the presence of an elongated neck joining the bubble to the orifice. The regime consists of two or three pulses resulting from successive bubbles running into each other to produce agglomerated doublet or triplet. The bubbles continue to form individually at the orifice and detachment occurs by rupture of the neck. At higher gas flow rates, the number of pulses increases. It results in an irregular and chaotic detachment rate.
c) Jetting mode appears as the gas flow rate becomes bigger and a jet of the gas is formed. The emerging gas stream takes on the appearance of a continuous jet. It breaks up under capillary actions at a small distance downstream from the orifice. The bubble formation process is now completely chaotic, where lumps of gas are torn off the end of an undulating jet of gas, which is permanently attached to the orifice. Bubble size, shape and frequency are irregular.
d) Cavitating mode occurs at very high gas flow rate. The jet emerging from the orifice follows the blade profile into the wake region and feeds a large clinging gas ventilated cavity behind the blade. This ventilated cavity spans the full-width of the water tunnel. Bubbles break off from the end of this ventilated cavity in a chaotic manner similar to that observed within the jetting regime.

The experimental work by Forrester and Rielly (1998) showed that, the bubbling regime for given gas and liquid velocities is independent of both the angle of attack and the blade design. Also the pulse bubbling regime is predominant when the angle of attack is 0° and the orifice is positioned either at 0 or 60°. When the angle of attack is 90°, the regime switches to the jetting mode. As well as for a fixed gas velocity, increasing the liquid velocity up to a certain threshold results in a significant decrease in bubble size. Above the threshold, the effect is much smaller and the bubble size at detachment varies with both gas and liquid velocities.

2.16. Factors governing bubble formation

The influence of the liquid properties, on the bubble regime, formation and size is summarised in this section. With a view of designing an aeration device for use within the water industry, there will be little scope to change the liquid and gas properties to improve the aeration efficiency. However, these effects should be noted with the potential of adapting the design to work in other industrial applications.

According to Kulkarni and Joshi (2005), the reported observations from experimental studies are

contradicting, where some authors claim that the bubble sizes increase with viscosity, for example Quigley et al (1955), and Khurana and Kumar (1969). On the other hand other authors believed that the sizes of the bubbles are independent of the liquid viscosity, such as Benzing and Mayers (1955), Hughes et al (1955), and Kumar and Kuloor (1970).

Viscosity does affect the bubble size and shape although its evidence diminishes for large diameters and higher gas velocities. Research indicates that at low liquid viscosities there is little influence of viscosity on bubble size, whereas at higher viscosity, an increase in viscosity leads to an increase in bubbles size. At higher liquid viscosities Thoroddsen et al (1997) found that the bubbles are more spherical in shape. There is less oscillation in the shape, as the excess surface energy is dissipated by the viscous stresses within the liquid. The length of the air neck connecting the bubble to the orifice was found to increase with increasing liquid viscosity. Very small satellite bubbles can be formed as the neck pinches off and the bubble breaks away.

Detachment happens when the internal forces acting on the bubble surface, for example the surface tension forces, are overcome by the liquid static head, which is dependent on the liquid density. According to Kulkarni and Joshi (2005) the bubble volume decreases when the liquid density increases. This is the case when the flow rate and the viscosity are small. However, the liquid density does not have any effect on the growth of a bubble. This is the case for very shallow liquid heads with large flow rate and both small viscosity and orifice diameter.

Surface tension forces are the result of intermolecular interactions inside the bubble with different forces of attraction coming from the other medium, for example the liquid. According to Kulkarni and Joshi (2005), surface tension forces involved in the bubble formation process can be categorised into two types:

a) Dynamic forces which occur during the initial part of the growth phase when the contact angle with the orifice changes continuously, retarding the stretching of the bubble.
b) Static forces which occur during the later part of the growth when the contact angle reaches a constant value.

The effects of surface tension forces have been found to increase with the diameter of the orifice and the flow rate (Maier, 1927; Kulkarni & Joshi, 2005). As a result, the detachment process is delayed, thus affecting the bubble size.

The strength of the intermolecular forces depends on the chemical structure of the bubble. The effect of surface tension forces on clean and contaminated bubbles, for example absorbed contaminants are totally different. Current research work is undergoing in order to understand the effect of surfactants on the bubble surface causing surface tension to vary across the interface (Kulkarni & Joshi, 2005).

The effects of gas density have been researched by Kulkarni and Joshi (2005) and it has been found that, for small orifice diameters, gas density has a negligible influence on detachment. However, for large orifice diameters, the formation of the bubble is faster when the gas density is high and delayed for low gas density and low gas flow rate.

2.17. Summary

In summary, the work by Baylar and Emiroglu (2003) and Baylar et al (2005) to (2007) and Gourich et al (2005) and (2007) into the use of a venturi for the purpose of aeration, showed that a significant number of factors, such as venturi and air orifice geometry can affect the air entrainment rate, pressure loss and oxygen transfer of a venturi device. This was also the case with the work carried out by Evans at al (1992) to (2001) and Cramers and Beenackers (2001), when researching into the performance characteristics of plunging liquid jet, where diameter ratios and constriction lengths as well as swirl was seen to influence the mass transfer performance of the plunging liquid jet.

Within Gourich et al (2005) and (2007), there were two types of flow regimes identified, a bubbly and annular flow regime. Lee at al (1997) and (2000), Lee (1998) and Sotiriadis and Thorpe (2005) observed a ventilated cavity attached to the base of the point of air injection. It was observed that the presence of a ventilated cavity lowered the performance due to a reduced interfacial area for mass transfer when compared to a bubbly flow. It was also observed that there were significantly higher pressure losses, due to the increased water velocity around the ventilated cavity causing increased frictional losses.

When a ventilated cavity is formed, it has been identified by Riiser et al, (1992), Delfos et al (2001), Lee (1998), Su (1995) and Sotiriadis (2005) that the air entrainment mechanism depends on the Reynolds number of the falling film. Air entrainment is caused by either the disturbances of the liquid film surface interacting with the receiving pool, or as a result of a shear layer at the film surface, or a combination of the two mechanisms.

The generation of air bubbles and the transfer of oxygen from the bubble to the surrounding liquid is a highly complex problem. The aeration device needs to be designed based on the knowledge of the hydrodynamics parameters which are suitable for the desired performance. The mechanism of bubble formation is a sequential process of expansion, elongation, detachment and ascendance, which decides the primitive bubble size in the system, where smaller bubbles have a higher surface area and therefore provide better oxygen transfer. Depending on the configuration of the air orifice, the liquid flow and the air velocity through the orifice, three different regimes of bubble formation have been observed,

a) Single bubbling, where discrete, almost identical and spherical bubbles are regularly formed,
b) Pulse bubbling, where two or three pulses occur, during which successive bubbles collide and produce an agglomerated doublet or triplet,

c) Jetting, where the production of bubbles results from the break-up of the jet of air due to capillary instabilities.

In order to control these factors, consideration is required towards, the direction and magnitude of the liquid flow where increasing the liquid velocity results in larger air entrainment rates. However, the oxygen transfer efficiency is reduced because the bubbles coalesce and become bigger. The trajectories of the bubbles are strongly dominated by the liquid flow and the turbulence generated.

CHAPTER 3

THEORY

3.1. Introduction

To be able to develop the inserts to be used for aeration and assess their potential design improvements, comparable measures of performance between varying designs need to be made. There are a number of characteristic values that are used to compare the performance of various types of aerators. These are Standard Oxygen Transfer Efficiency, SOTE, which represents the fraction of oxygen brought in contact with the water that actually dissolved in it, at standard temperature and pressure conditions, which are outline in Table 3.1. The Standard Oxygen Transfer Rate, SOTR, which represents the rate of oxygen transfer observed when the DO concentration in the water is initially zero, also quoted at standard conditions, and the Standard Aeration Efficiency, SAE, which represents the energy consumed in dissolving a specific amount of oxygen and again is quoted at standard conditions. These comparative values are most commonly determined using the ASCE standard, EWRI 2-06 (ASCE, 2007), the details of which are discussed later in this chapter.

To calculate SAE, the energy losses associated with the presence of the inserts need to be established. The specific power, E, can be used as a comparison between the inserts and for determining SAE, the calculation of which is outlined in Section 3.2.

3.2. Specific power calculation

For comparison between the insert designs, not only are mass transfer performance coefficients required but also the specific power consumption. Specific power consumption, E, for bubble columns, airlift reactors and aerated stirred vessels have been described in a number of literature sources, including Bouaifi et al (2001). In Bouaifi et al (2001) power consumption was considered for a bubble column reactor. The specific power consumption was calculated by considering the total gas pressure drop using,

$$\left(\frac{P_G}{V_L}\right)_{Total} = \frac{Q_G(\rho_L g z + \Delta P_G)}{V_{L1}} \quad [3.1]$$

For a venturi system where the liquid is a driving fluid, the pressure drop of the fluid needs to be included for the pressure calculation. Therefore, the equation for specific power from Gourich et al (2007) can be used as a bases for the calculation,

$$E = \frac{Q_L}{V_{L1}}\left[(P_{TH} - P_{ATMOS}) + \frac{1}{2}\rho_L U_{TH}^2 + \rho_L g \Delta z\right] + \frac{Q_G}{V_{L1}}(P_G - P_{ATMOS}) \quad [3.2]$$

Due to the expected varied pressure profile within the throat of the inserts, caused by the aerofoil profiles of the vanes. It can be expected that there will be significant variations in the pressure measurements across a small distance within the throat. This in conjunction with the requirement to include the pressure loss of the convergent section of the inserts, Equation 3.2 was modified for this experimental work to

include the convergent section of the insert, as shown in Equation 3.3.

$$E = \frac{Q_L}{V_{L1}}\left[(P_{US} - P_{ATMOS}) + \frac{1}{2}\rho_L U_{US}^2 + \rho_L g \Delta z\right] + \frac{Q_G}{V_{L1}}(P_G - P_{ATMOS}) \quad [3.3]$$

In Equation 3.3, Δz is the height difference between the upstream pressure measurement and the water surface.

In order to fully understand the hydrodynamic efficiencies of the inserts, so that it is possible to develop them for improved performance. An understanding of the flow though the inserts and the overall system is required. To measure the power consumed across the insert, the pressure drop across it needs to be determined. As a result of the nature of the system, one and two-phase pressure drop theory needs to be incorporated to allow for the decrease in density, as a result of the air entrainment into the fluid flow. The power loss across the inserts can be separated into two sections, a one-phase flow prior to the air injection and a two-phase flow after the point of air entrainment. In general, hydraulic power can be calculated using the following equation, (Douglas, et al., 2005).

$$W = (\rho . g . h_L) . Q = \Delta P . \frac{\dot{m}}{\rho} \quad [3.4]$$

3.3. One-phase pipe flow

Energy input to a gas or liquid flow in pipes is needed to overcome energy losses which are caused by the friction between the fluid and the pipe wall, as well as internal friction within the fluid. This is in addition to losses that are a result of changes in direction of flow, obstructions in the flow path, sudden or gradual expansions and contractions, and changes in the shape of the flow path. The smoother the pipe walls the lower the pressure drop due to friction. For example, pipes made from glass, copper, brass and polyethylene will cause lower frictional pressure drops compared to materials, such as concrete, steel and cast iron. One of the most common problems in fluid mechanics is the estimation of pressure loss in pipe flows. Determining pressure losses is essential so that pumps can be sized for specific applications. The magnitude of the frictional losses is important because it determines the power requirements of the pump, which forces the fluid through the pipe network.

The fluid properties themselves can have a significant impact on the pressure loss. Fluids with a high viscosity will flow slower than those with a low viscosity. High viscosity fluids will generally not support eddy currents, which form as a result of the internal roughness of the pipe wall. These eddies result in an increased resistance to the flow. Therefore, the internal roughness of the pipe will have no effect on the frictional resistance in high viscosity fluids. This condition is known as laminar flow, (Douglas, et al., 2005).

In general there are three types of flow profiles, laminar, transitional and turbulent. The non-dimensional Reynolds number, Re, is used to determine which flow regime is present and is calculated by Equation 3.5 (Douglas, et al., 2005).

$$Re = \frac{\rho . \bar{u} . d}{\mu} \qquad [3.5]$$

The laminar flow regime for a pipe has a Reynolds number of less than 2000, transitional flow occurs between 2000 and 4000 and turbulent flow has Reynolds numbers greater than 4000, (Douglas, et al., 2005). It is important to determine the flow type because the flow type governs how much energy will be lost due to friction.

In laminar flow regimes, viscous forces are dominant compared to inertial forces, therefore the pressure drop per unit length is proportional to the velocity, (Massey, 2006), as shown in Figure 3.1. In turbulent flow the fluid moves erratically as a result of cross currents and eddies. Turbulent flows are generally present in larger pipes of high flow rates, (Massey, 2006). Under turbulent flow the pressure drop becomes proportional to the velocity raised to the power of 1.7 to 2, as shown in Figure 3.1. Transient flow is a mixture of laminar and turbulent flow, with laminar flow at the pipe wall and turbulent flow in the centre of the pipe.

During this experimental work it is expected that due to the density and viscosity of water that, this work will be conducted in the turbulent flow regime.

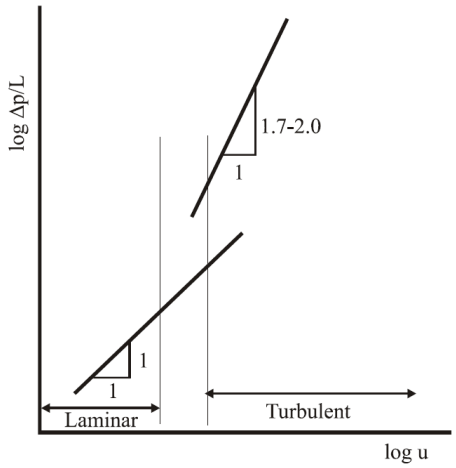

Figure 3.1: - Relationship between velocity and pressure drop per unit length in pipes, adapted from (Massey, 2006).

3.4. Pressure loss in a pipe due to turbulent flow.

In most engineering applications, flow through closed systems, for example pipes and ducts, as well as open systems, including rivers and channels will be turbulent. Analytical expressions for head loss in flows are not available. Therefore empirical relationships derived from experiments measurements are used. The Darcy-Weisbach equation is used for head loss calculations for both laminar and turbulent flows in circular pipes, (Douglas, et al., 2005).

$$h_f = \frac{4 . f . L . u^2}{2 . g . d} \qquad [3.6]$$

An assessment of the physics governing the value of friction in a fluid has led to the following relationships,

(Douglas, et al., 2005).

a) $h_f \propto L$

b) $h_f \propto u^2$

c) $h_f \propto {}^1/_d$

d) h_f depends on surface roughness of pipes.

e) h_f depends on the fluid properties including viscosity and density.

For laminar flows an equation for determining the friction factor, f, has been established by equating the Hagen-Poiseuille and the Darcy-Weisbach equations.

$$\frac{32.\mu.L.u}{\rho.g.d^2} = \frac{4.f.L.u^2}{2.g.d} \quad [3.7]$$

Therefore f equates to, (Massey, 2006): -

$$f = \frac{16}{Re} \quad [3.8]$$

Blasius in 1913, was the first to give an accurate empirical expression for friction factor for turbulent flow in smooth pipes, which is shown in Equation 3.9 (Massey, 2006). This equation is fairly accurate, giving head losses ± 5 % of actual value of Re up to 100,000.

$$f = \frac{0.079}{Re^{0.25}} \quad [3.9]$$

Equation 3.9 is used for determining the fiction factor in the procedure outlined for calculating the two-phase flow multipliers, which are used to determine the pressure loss in two-phase flow. The procedure is outlined later in this chapter.

3.5. Pressure losses due to fittings in the pipe work

Other energy losses in pipes include bends, junctions, valves and expansions and contractions. In reality within pipelines of long lengths the effect of these pipe fitting losses are likely to be negligible compared to the frictional losses. However in short pipelines the losses may be greater than that of friction. The energy loss due to the turbulent flow through a fitting is calculated using a simple head loss formula, Equation 3.10 (Massey, 2006): -

$$h_L = \Lambda.\frac{u^2}{2.g} \quad [3.10]$$

A pressure loss factor associated with a fitting, Λ, can be derived for sudden enlargements and contractions. However, for bends and valves the loss factor must be derived experimentally. It can be shown for a sudden expansion using the Bernoulli principle that the loss coefficient for an expansion can be calculated using, (Douglas, et al., 2005),

$$\Lambda_e = \left(1 - \frac{A_1}{A_2}\right)^2 \quad [3.11]$$

3.6. Further causes of pressure losses

As fluid flows over a stationary surface, the fluid in contact with the surface is brought to rest as a result of

the friction at the surface, or wall of a pipe. The velocity of the flow increases from the wall to a maximum, as can be seen in Figure 3.2, which shows the velocity profile. The boundary layer is a region of flow where the velocity profile exists due to shear stress at the wall. The boundary layer thickness is the point at which the velocity of the boundary layer is 99% of the mainstream velocity, for example the middle of a pipeline or river, (Massey, 2006).

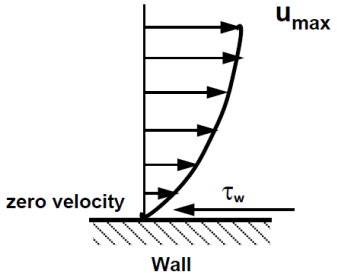

Figure 3.2: - Velocity profile across a flat surface, adapted from (Massey, 2006).

Typically large losses of energy in fluid flows occur during expansions. The cause of these losses is due to the velocity decrease in the flow as a result of the expansion. The decreasing velocity of the flow leads to a pressure increase, in accordance with Bernoulli's theorem. As the pressure increases in the direction of the fluid outside the boundary layer, the flow slows through the expansion. If the flow has enough momentum, if will overcome the pressure that is trying to force it backwards. However, if the fluid at the boundary layer has too little momentum, then the pressure can bring the flow to rest and in some cases reverse the flow direction. If reversal occurs, the boundary layer is lifted from the wall of the pipe. This phenomenon is known as boundary layer separation and is shown schematically in Figure 3.3.

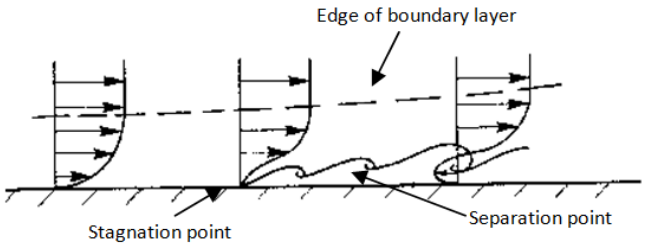

Figure 3.3: - Boundary layer separation, adapted from Douglas et al (2005).

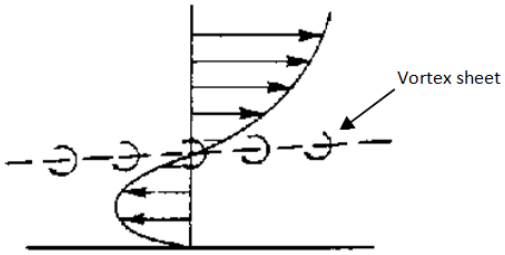

Figure 3.4: - Vortex sheet, as a result of boundary layer separation, (Massey, 2006).

At the edge of a separated boundary layer, where the flow streams are in opposite directions a line of vortices occur, called a vortex sheet, as shown in Figure 3.4 (Massey, 2006). The boundary layer separation and resultant increase in turbulence, as a result of the vortices cause large energy losses. Separating and

divergent flows are very unstable and have a significant risk of flow separation and therefore cause greater losses than parallel or convergent flows, (Massey, 2006). Increasing the angle of a divergent section increases the risk of boundary layer separation. British Standard 5167:4 (2003) recommends that a divergent angle of between 5 and 7˚ for a venturi meter. This range provides the optimum balance between the risks of boundary layer separation and a suitable length of venturi meter.

3.7. Fluid flow over aerofoils

To fully utilise the benefit of aerofoils as streamline bodies in the design of the insert, thus minimising pressure losses and maximising the potential for air entrainment, a theoretical understanding of aerofoils and there design is required.

An aerofoil is defined as a streamlined body that is designed to produce lift whilst in a fluid stream, which flows across their surface. The Kutta-Joukowsky law, derived for a cylinder, states that lift exists only if there is circulation around the section, (Douglas, et al., 2005).

As shown in Section 3.6, vortices are formed due to boundary layer separation. It has been shown that if two parallel streams of different velocity meet, the discontinuity of their velocities at their interface produces a vortex, (Douglas, et al., 2005). This is in similar manner to what happens over an aerofoil. When an inclined aerofoil is placed in a fluid stream, the leading edge causes the flow to split into two streams, one over the upper surface and the other under the lower surface. The velocities of the two streams are unequal due to the inclination of the aerofoil and therefore a vortex is created at the trailing edge due to the two streams meeting. This vortex is cast off soon after the beginning of the motion. The vortex does however give rise to circulation around the aerofoil in the opposite direction to the circulation of the starting vortex, Γa, as is shown in Figure 3.5 (Douglas, et al., 2005).

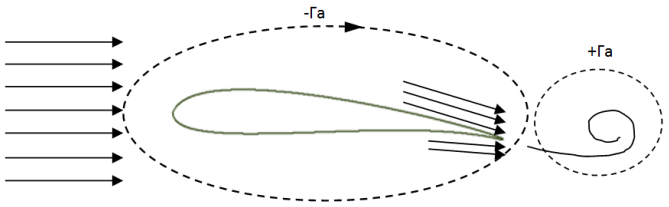

Figure 3.5: - Flow Across Aerofoil, adapted from Douglas et al (2005).

Within the boundary layer of the aerofoil, vorticity exists as a result of the velocity gradient. The value of the vorticity depends on the velocity gradient itself (Douglas, et al., 2005). It can be shown that due to the circulation the velocity gradients at the top and bottom surfaces of the aerofoil are in opposite directions. The vorticity in the upper boundary layer is in the clockwise direction and anticlockwise in the lower boundary layer, (Douglas, et al., 2005). If the magnitudes of the vortices are of equal strength, for example if the aerofoil is of symmetrical geometry, then zero lift is generated. If however a positive camber exists, then the overall circulation around the aerofoil will be in the clockwise direction, as shown in Figure 3.6.

Therefore, the velocity over the upper surface will be greater than that over the lower surface, (Douglas, et al., 2005). Due to Bernoulli's equation, the higher velocity on the upper surface must be accompanied by a lower pressure and the reverse on the lower side. The resultant force is known as lift.

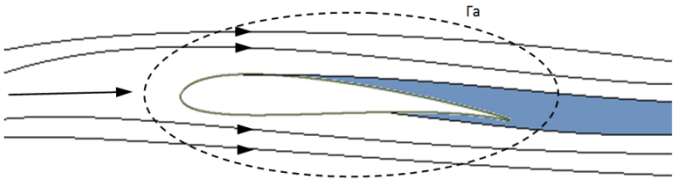

Figure 3.6: - Clockwise circulation around an aerofoil, adapted from Douglas, et al (2005).

The angle of attack for an aerofoil is measured from the position for which the aerofoil will produce zero lift. At small angles of attack there is no separation of the boundary layer. However, as the angle of incidence increases, separation occurs at the trailing edge on the upper surface. As the angle of incidence is increased the separation point moves further forward on the upper surface (Douglas, et al., 2005). Therefore careful consideration of the angle of attack of the vanes within the insert needs to be taken, in order to maximise the suction pressure but maintaining a low level of flow separation, and therefore minimising pressure losses.

3.8. Two-phase flow theory

When considering the two-phase flow in the divergent section of the insert and in the downcomer. Two-phase flow theory needs to be evaluated in order to determine and minimise the pressure losses, to improve performance.

The basic equations for steady state one and two-phase flows are continuity, momentum and energy. It is often possible to use energy and momentum when considering changes between points. The momentum equation is often written as an explicit equation for the pressure gradient, (Wallis, 1969).

$$\frac{dp}{dz} = \left(\frac{-P}{A}.\tau_w\right) - \left(\frac{\dot{m}}{A}.\frac{du}{dz}\right) - \rho_{2ph}.g.\cos\theta \qquad [3.12]$$

The three terms on the right hand side of the equation are regarded as frictional, acceleration and gravitational components of the pressure gradient. Therefore the total pressure gradient or pressure drop can be written as, (Wallis, 1969).

$$\frac{dp}{dz} = \left(\frac{dp}{dz}\right)_f + \left(\frac{dp}{dz}\right)_A + \left(\frac{dp}{dz}\right)_g \qquad [3.13]$$

Wallis (1969) has shown that the frictional pressure drop can be expressed as a function of a two-phase friction factor and for a steady flow with a constant cross sectional area, in terms of mass flow rate is,

$$\left(\frac{dp}{dz}\right)_f = 4.f_{2ph}.\frac{L}{d}.\frac{\dot{m}_{total}^2}{2.\rho_{2ph}.A^2} \qquad [3.14]$$

Wallis (1969) also showed that the two-phase friction factor can be expressed using the Blasius (1913) equation for flow through a smooth pipe as,

$$f_{2ph} = \frac{0.079}{Re^{0.25}} \qquad [3.15]$$

where the Re can be expressed in terms of mass flow rate, as shown in Equation 3.16 (Thorne, 2006). Calculating the Re using a mass flow rate can help where the mixture velocity could be unknown.

$$Re = \frac{\dot{m}_{total}.d}{\mu_{2ph}.A} \quad [3.16]$$

The two-phase average viscosity is calculated using,

$$\mu_{2ph} = x.\mu_G + (1-x)\mu_L \quad [3.17]$$

and vapour quality is calculated by,

$$x = \frac{\dot{m}_G}{\dot{m}_G + \dot{m}_L} \quad [3.18]$$

The acceleration pressure drop, expressed in Equation 3.13 reflects the change in the kinetic energy of the flow and it can be calculated using, (Wallis, 1969; Thorne, 2006)

$$\left(\frac{dp}{dz}\right)_A = \frac{\dot{m}_{total}^2}{A^2}\left\{\left[\frac{(1-x)^2}{\rho_L(1-\varepsilon_G)} + \frac{x^2}{\rho_G.\varepsilon_G}\right]_2 - \left[\frac{(1-x)^2}{\rho_L(1-\varepsilon_G)} + \frac{x^2}{\rho_G.\varepsilon_G}\right]_1\right\} \quad [3.19]$$

where the vapour quality and volumetric fraction are calculated using Equations 3.18 and 3.22 respectively.

The gravitational pressure drop in Equation 3.13 is calculated from,

$$\left(\frac{dp}{dz}\right)_g = \rho_{2ph}.g.\cos\theta \quad [3.20]$$

where the two-phase density is expressed by,

$$\rho_{2ph} = \varepsilon_G.\rho_G + (1-\varepsilon_G)\rho_L \quad [3.21]$$

and the volumetric fraction is given by Equation 3.22.

$$\varepsilon_G = \frac{Q_G}{Q_G + Q_L} \quad [3.22]$$

In calculating pressure drops in one-phase flows through fittings, including bends, expansions and contractions a suitable equivalent length of pipe is used to represent the equivalent frictional losses caused by the fittings. The same procedure is applied for two-phase flows. However, these lengths tend to be longer than in one-phase flows. As in one-phase flows a friction factor can be substituted with a pressure loss factor, Λ, which can either be calculated empirically or supplied by the manufacturer of a fitting. The frictional pressure drop equation can be adapted so that,

$$\left(\frac{dp}{dz}\right)_f = 4.f_{2ph}.\frac{L}{d}.\frac{\dot{m}_{total}^2}{2.\rho_{2ph}.A^2} = \Lambda.\frac{\dot{m}_{total}^2}{2.\rho_{2ph}.A^2} \quad [3.23]$$

Therefore for the same flow conditions, Λ can be used to compare the performance of various inserts.

3.9. Frictional two-phase multipliers

To allow for the additional frictional losses caused by a second fluid phase, two-phase multipliers are used. Wallis (1969) and Thorne (2006) outlined the calculations for three multipliers which are Lockhart and Martinelli, Friedel and Chisholm. These multipliers are applied to a calculated frictional pressure drop to give a more accurate theoretical value, where the different multipliers are applied for different scenarios depending on, for example various mass flow rates, pipe diameters and viscosity ratios, (Wallis, 1969)

(Thorne, 2006).

The two-phase flow frictional pressure drop is usually calculated using separated flow models. Lockhart and Martinelli (1949), was the first analyses that predicted the two-phase frictional pressure drop based on a two-phase multiplier for the liquid or the gas phase, (Shannak, 2008). The method has widely been used in industry, especially for low gas and liquid flow rates. In 1968, Baroczy captured the mass flux effect of the fluid property by fitting a large set of data taken for different flow rates with different fluids. However, the graphical form represented did not allow for easy application, (Thorne, 2006). Chisholm (1973) combined the results of Lockhart and Martinelli (1949) with Baroczy (1968) and with further analysis obtained an analytical expression for pressure drop, which was more convenient to use, (Chisholm, 1973).

The Chisholm (1973) method is applicable for a wide range of operating conditions and is given as a function of mass flow rate, vapour quality and friction pressure gradient for both liquid and vapour phases. In this method, turbulent flow is considered to be a Reynolds number greater than 2,000 and the correlation is applicable for all vapour qualities (Shannak, 2008).

The correlation outlined by Friedel (1979) utilises a two-phase liquid multiplier considering the liquid phase flowing alone in a channel with the total mass flow rate. The Friedel multiplier is a function of vapour quality, as well as viscosity and density ratios, and non-dimensional numbers including Reynolds, Weber and Froude. The method is believed to be applicable on viscosity ratios of less than 1,000 on both horizontal and vertical flows, (Friedel, 1979; Shannak, 2008).

Whalley (1980) made extensive comparisons between the various published correlations. The recommendations he made were: -

- For $\mu_L/\mu_G < 1000$ and mass flux less than 2000 kg/m^{2}s, the Friedel (1979) correlation should be used.
- For $\mu_L/\mu_G > 1000$ and mass flux greater than 100 kg/m^{2}s, the Chisholm (1973) correlation should be used.
- For $\mu_L/\mu_G > 1000$ and mass flux less than 100 kg/m^{2}s, the Lockhart and Martinelli (1949) correlation should be used.

The dynamic viscosity ratio for water to air, the fluid and gas used in this experimental work, is approximately 52. Therefore the Friedel (1979) two-phase multiplier is the most suitable, as recommended by Whalley (1980). Therefore, the calculation for the Friedel two-phase multiplier is outlined in the following section. Information about the other multipliers are outlined in Wallis (1969) and Thorne (2006)

3.10. Friedel correlation

The correlation method of Friedel (1979) utilises a two-phase multiplier, where the frictional pressure drop

is calculated using,

$$\left(\frac{dp}{dz}\right)_f = \Delta P_L . \Phi_{fr}^2 \quad [3.24]$$

where ΔP_L is calculated for the liquid phase flow using,

$$\Delta P_L = 4 f_L \frac{L}{d} \frac{\dot{m}_{total}^2}{2 . \rho_{2ph} . A^2} \quad [3.25]$$

The liquid friction factor, f_L, and liquid Re are obtained from Equations 3.15 and 3.16 respectively.

The two-phase multiplier is calculated by,

$$\Phi_{fr}^2 = E_{fr} + \frac{3.24 . F_{fr} . H_{fr}}{Fr_H^{0.045} . We_L^{0.035}} \quad [3.26]$$

and the dimensionless factors, Fr_H, F_{fr}, E_{fr} and H_{fr} are calculated as follows,

$$E_{fr} = (1 - x)^2 + x^2 . \frac{\rho_L . f_G}{\rho_G . f_L} \quad [3.27]$$

$$Fr_H = \frac{\dot{m}_{total}^2}{g . d_i . \rho_H^2} \quad [3.28]$$

$$F_{fr} = x^{0.78} . (1 - x)^{0.224} \quad [3.29]$$

$$H_{fr} = \left(\frac{\rho_L}{\rho_G}\right)^{0.91} . \left(\frac{\mu_G}{\mu_L}\right)^{0.19} . \left(1 - \frac{\mu_G}{\mu_L}\right)^{0.7} \quad [3.30]$$

The Liquid Weber number, We_L is defined as,

$$We_L = \frac{\dot{m}_{total}^2 . d}{\sigma . \rho_{2ph} . A^2} \quad [3.31]$$

In the Friedel correlation the two-phase density is calculated using Equation 3.21.

3.11. Principles of mass transfer

The term mass transfer refers to the movement of mass or molecules from one location to another as a result of a driving force. Convection and diffusion are the main mechanisms through which mass transfer occurs. Convection is the transport of species by currents in the fluid field, while diffusion is a molecular process driven by concentration gradients. This movement can occur between one of a number of fluid phases. Interphase mass transfer refers to the movement of mass across the interface between two phases. In terms of aeration, mass transfer is the transfer of oxygen from the air into water. The knowledge of the rate of oxygen transfer is important to be able to specify and utilise an aerator in the appropriate process and use it efficiently.

Oxygen transfer from a gaseous to an aqueous phase occurs in the three steps. The first is the saturation of the liquid surface between the two phases. This rate of transfer is very fast as it is assumed in this instance that the gas film resistance is negligible, especially in low solubility compounds such as nitrogen and oxygen, as a result this step is not the controlling one in aeration (Boyle, et al., 2002). The second step, is the diffusion of oxygen molecules through the liquid interface, which when low mixing levels are present, the rate of transfer is controlled by this step. However, when high turbulence in the mixture occurs, the

interface film is broken up and the rate of renewal of the film controls the rate of transfer of oxygen to the bulk liquid (Boyle, et al., 2002). The surface renewal rate is the rate at which the liquid with a concentration of oxygen equal to that in the bulk air is replaced at the interface with liquid with an oxygen concentration equal to that of the bulk liquid. The final step is the transfer of oxygen to the bulk of the liquid through diffusion and convection (Rorrer, et al., 2000).

Fick's first law (1855) is used to define diffusion for dormant conditions, the principles defining the movement of oxygen molecules are similar to that defined by Newton's and Fourier's law. Newton's Law governs the transfer of momentum in fluid flow and Fourier's law is used to define the transfer of heat when temperature gradients exist. When a concentration gradient exists, Fick's first law (1855), Equation 3.32, is used to define mass transfer.

$$J = -D.{}^{dC}/_{dy} \qquad [3.32]$$

The diffusion coefficient, D is used to define the linear dependency of the molar flux due to molecular diffusion and the concentration gradient of the species. For oxygen into water, diffusivity is around 2.1 x10^{-9} m^2/s at a temperature of 25˚C, (Cussler, 1997).

Boyle et al (2002) proposed an equation for determining the diffusivity of oxygen into water,

$$D = \frac{6.85 \times 10^{-12}.T}{\mu} \qquad [3.33]$$

As can be seen in Equation 3.33, as the temperature increases the diffusivity will also increase. However, as the temperature of the water increases, the saturation concentration decreases (Rorrer, et al., 2000).

In a static system, for example a tank of de-aerated water that is open to the atmosphere, there will initially be high rates of mass transfer occurring at the surface. This is because the saturated air is in contact with the unsaturated water. Therefore during the first few seconds of exposure the oxygen flux is high. However, as the oxygen builds up in the layers of water adjacent to the air, which is the water free surface, the transfer rate reduces. As a result this creates a requirement for the removal of the upper saturated layers of liquid, which can be achieved through mixing the saturated liquid into the bulk solution, through convective transport.

It has been shown by Boyle et al (2002) that molecular diffusion only occurs in the upper layers of the water, generally less than a few centimetres, whereas convective transport occurs over the entire bulk of the liquid.

The mass transfer in a system can be determined by considering the concentration difference and using an experimentally achieved mass transfer coefficient, k, Such that the mass flux can be calculated using, Equation 3.34.

$$J = k.(C_s - C) \qquad [3.34]$$

Unfortunately, it is not always possible to experimentally determine the mass transfer coefficient, for reasons such as cost and time. Therefore, there have been a number of theories proposed for predicting the mass transfer in a system. Some of these include the two film theory, the penetration theory and the film-penetration theory and are outlined in the following sections.

3.12. Two film theory

Lewis and Whitman (1924) derived an equation for the two film theory which was first proposed by Nernst and Lehfeldt (1904). The basis of the two film theory is the assumption that the areas that provide resistance to mass transfer can be replaced hypothetically by two layers called films, which exist either side of the gas-liquid interface. In these layers mass transfer is entirely by diffusion and in the films the concentration gradient is linear and then is zero outside of them, this is depicted in Figure 3.7. The dashed red lines represent the linear concentration gradient within the films and then zero outside. The discontinuity between the concentrations is governed by the thermodynamic equilibrium relationship. For gasses of high solubility on the liquid phase, the major resistance to mass transfer is that offered by the gas film. With gases of low solubility in the liquid phase, for example the absorption of oxygen by aqueous liquor, the controlling resistance exists in the liquid film (Rorrer, et al., 2000). Therefore, in an aeration system the rate of oxygen transfer into the water is determined by the liquid film coefficient, k_L.

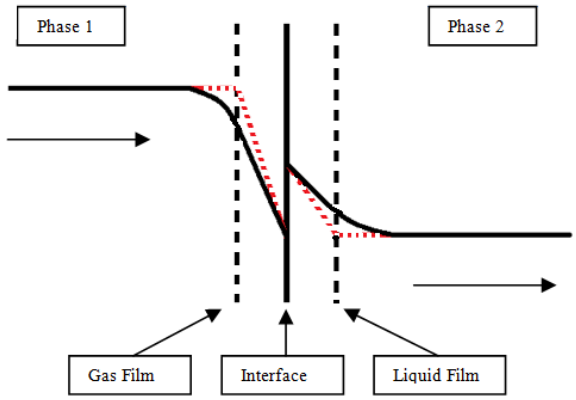

Figure 3.7: - Two film theory Diffusion Gradients, adapted from Rorrer et al (2000).

The liquid film coefficient for mass transfer is given as a function of diffusivity and liquid film thickness. Typical liquid films over which a concentration gradient occurs vary from 10 to 200 µm thick and depend upon the level of turbulence (Binder & Hanratty, 1991), k_L is calculated by,

$$k_L = \frac{D}{\delta_L} \qquad [3.35]$$

The two film theory considers that turbulence dies out at the interface and as a result of this a laminar layer exists in each of the two films. Outside this laminar layer the turbulent eddies enhance the Brownian motion of the molecules and the resistance to transfer reduces. Brownian motion is the random drifting of particles suspended in a liquid. For equimolecular counter-diffusion the concentration gradient is linear close to the interface and reduces as the distance increases from the interface. This is represented by solid the black lines in Figure 3.7. Equimolecular counter-diffusion is when the mass transfer between two

components is equal and opposite.

In two film theory, mass transfer is considered to be a steady state process. It is unlikely that an aeration system for wastewater would be steady state unless significant condition monitoring was in place, with the aim of maintaining a constant DO level. The two film theory can only be applied if the time taken for the concentration gradient to form is noticeably less than the time of transfer. The disadvantage of this theory is the unknown of the film thickness and the ability to determine it in many situations.

3.13. Penetration theory

Higbie (1935) described the mass transfer process as a transient occurrence, which is the most likely occurrence in an aeration system, where a small fluid element of initial concentration is brought by eddies to the interface for a short time, t. Diffusion takes place into the element, where the rate of diffusion decreases with time and then the element is replaced at the interface by another element, as a result of turbulence after t. The liquid film coefficient is then defined by,

$$k_L = 2\sqrt{\frac{D}{\pi t}} \qquad [3.36]$$

During bubble aeration the time of contact is defined as the time for a single bubble to travel through the liquid at a distance equal to its diameter, using the bubble velocity (Calderbank, 1958), such that in this case t can be calculated by Equation 3.37.

$$t = \frac{d_b}{u_b} \qquad [3.37]$$

Higbie (1935) investigated whether or not a resistance existed at the interface when pure gas was absorbed into a liquid. The experiment conducted was to allow a slug like bubble of carbon dioxide to rise through a vertical column of water within a 3 mm ID glass tube. Therefore as the bubble rose through the liquid, the liquid was displaced as a thin film between the bubble and the tube. The assumption was that each element of water was exposed to the gas for the time taken for the gas to pass it. Higbie (1935) supposed that during the short time that it took for the bubble to pass an element of water, approximately between 0.01 and 0.1 seconds, unsteady state diffusion and absorption occurred from carbon dioxide into the water. Due to the short period of exposure time he regarded the depth of the liquid to be infinite.

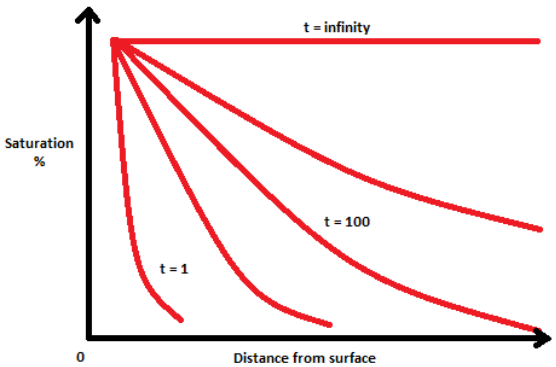

Figure 3.8: - Percentage saturation against distance from surface for various exposure times, which are in arbitrary units.

Figure 3.8 shows various profiles based on Higbie's calculations such that at any time the effective depth of liquid, which contains a noticeable concentration can be specified. Provided the depth of penetration is less than the total depth of the liquid, no significant error is introduced by assuming the total depth to be infinite.

This work carried out by Higbie (1935) provided the basis for the penetration theory, where it is assumed that eddies in the fluid bring an element of fluid to the interface. The element is exposed to the gas for a definite period of time where unsteady state molecular diffusion takes place. After the fixed period of time the element is remixed back into the bulk liquid. In penetration theory it is also assumed that the fluid at all depths is moving at the same speed as the interface. The main disadvantage with the Penetration theory is that it does not take into consideration the velocity distribution at the interface. However, it is considered by Boyle et al (2002) that the square root dependence of diffusivity gives greater accuracy then compared to the linear dependence in the two film theory.

The penetration theory was later expanded by Danckwerts in 1951, where a greater interest was taken at the processes occurring near the interface. Instead of using a single contact time he replaced this with a spectrum of times for which an element was exposed to saturation concentration at the interface, such that, (Rorrer, et al., 2000)

$$k_L = \sqrt{D r_s} \qquad [3.38]$$

where r_s is the surface renewal rate.

Danckwerts (1951) suggested that each element of surface renewal would not be exposed to the soluble gas at the interface for the same time and that a random distribution of times would exist. The assumption is that the probability of any element at the surface becomes mixed with the bulk of the fluid was independent of how long the element was at the interface. However, the contact time t, cannot be predicted and significant experimental work would be needed. Calculating k_L using surface renewal is most accurate when the surface renewal rates are high (Boyle, et al., 2002).

3.14. Film-Penetration Theory

Toor and Marchello (1958) expanded upon the two film theory and the penetration theory. The theory is based on the thinking that all of the resistance to transfer is located within a thin laminar film at the interface, like the two film theory. However, the transfer is regarded as being an unsteady state process. Therefore the film-penetration theory provides the potential for accurate prediction of the mass transfer. The theory assumes that, like the penetration theory, the surface at the interface is regularly renewed as a result of eddy currents, which is likely to be the case in a highly turbulent process. The theory also makes the assumption that the resistance to mass transfer is confined to a finite film, which is able to provide a simplistic picture of a complicated process. For short exposure times none of the diffusing material reaches

the far side of the film, like penetration theory. However for longer exposure time a concentration gradient will develop across the film, similar to the method described for two film theory.

Using Fick's' second law, which predicts how diffusion causes the concentration change with time (Boyle, et al., 2002), with the boundary conditions that at time is zero, the gas concentration in the liquid is equal and uniform and also that at time greater than zero the concentration of the gas at the interface is constant and the concentration of the gas at the gas film is equal to that of the gas bulk solution. These conditions are likely in a suitably mixed system and where there is a continuous supply of the gas phase to the interface.

According to Boyle et al (2002) using Laplace transforms, two equations are developed for the mass transfer rate at any time, using film-penetration theory such that,

$$FOR \quad \pi \leq \frac{\delta_L^2}{Dt} < \infty \qquad (J)_t = (C_{Li} - C_L)\sqrt{\frac{D}{\pi t}}\left(1 + 2e^{\frac{-\delta_L^2}{Dt}}\right) \qquad [3.40]$$

$$AND\ FOR \quad 0 \leq \frac{\delta_L^2}{Dt} < \pi \qquad (J)_t = (C_{Li} - C_L)\frac{D}{\delta_L}\left(1 + 2e^{\frac{-(\pi^2 Dt)}{\delta_L^2}}\right) \qquad [3.41]$$

Equation 3.40 is commonly used for a dispersed second phase, where it may be in the form of droplets or a bubbly flow regime and Equation 3.41 is used for wetted wall column, typically slug and annular flow regimes. Equation 3.40 generally conforms to the penetration theory, as the exposure time is very small whereas Equation 3.41 coincides with the two film theory as the exposure time is slightly longer and therefore the concentration gradient through the film has developed.

In general liquid film mass transfer coefficients are not known and have to be determined empirically, except for bubble aeration using the penetration model, where suitably defined equations and coefficients exist (Boyle, et al., 2002). In 1958, O'Connor and Dobbin expanded upon Danckwerts theory for surface renewal rate by expressing it as a function of the fluid turbulence parameters, characteristic mixing length and vertical velocity fluctuation,

$$r_s = \frac{\bar{u}}{l} \qquad [3.42]$$

However, throughout all of the theory for the predictions of a liquid mass transfer coefficient the determination of governing parameters such as eddy size distribution, film thickness and surface renewal rate make it extremely difficult to accurately predict mass transfer in complex aeration systems. As a result there is no simple theoretical expression for the liquid film mass transfer coefficient that would satisfy for all aeration systems. Any expression would need to be a function of energy input, interfacial area, hydrodynamics and velocity profile at the interface. Generally the interfacial area per unit volume for mass transfer, defined by a, is combined with the liquid film mass transfer coefficient to give an overall oxygen transfer coefficient, termed as $k_L a$.

3.15. Theoretical application to aeration

Equation 3.34 can be used as the basis for all aeration systems for determining the mass transfer rate, such that the oxygen flux can be defined by,

$$J = k_L(C_\infty^* - C_L) \quad [3.43]$$

where the oxygen saturation concentration, C_∞^* is defined as the equilibrium value in the bulk liquid at time is infinity.

Multiplying the oxygen flux by the interfacial area per unit volume, Equation 3.43 becomes,

$$\frac{dC_L}{dt} = k_L a(C_\infty^* - C_L) \quad [3.44]$$

This is the basic equation for all aeration systems, the maximum transfer rate is when the liquid concentration rate is zero and the slowest rate of transfer is when the liquid concentration is approaching the saturation concentration.

In all but the simplest aeration systems $k_L$and a are impossible to measure. There are many factors in an aeration system that will affect the saturation concentration, as well the overall oxygen transfer coefficient, $k_L a$. For example, the liquid temperature, the amount of dissolved solids in the liquid, the composition of the wastewater as well as barometric pressure. Correction factors are typically used when the sample system varies from standard conditions, these correction factors are outlined below. The correction factors enable comparisons to be made between different aeration systems and technologies when they may have been tested under different conditions.

For any given aeration system all the parameters are given at standard conditions. Standard conditions for the ASCE standard EWRI 2-06 is shown in Table 3.1.

Table 3.1: - Standard conditions values for ASCE/EWRI 2-06 (ASCE, 2007).

Paramater	U.S Practice
Water	Tap
Water Temp	20˚C
C_L	0 mg/L
Barometric Pressure	1 atm
Air Flow	20˚C 36% Relative Humidity γ = 0.075 lb air/ft^3

3.16. Factors that affect oxygen transfer in aeration systems

Using the ideal gas law, the bulk gas concentration can be shown to be a function of oxygen partial pressure, molecular weight and temperature,

$$C_G = \frac{nM}{V} = \frac{pM}{RT} \quad [3.45]$$

For dry air, oxygen is 20.95 % by volume. Therefore the oxygen partial pressure is related to the total pressure, by Equation 3.46.

$$p = 0.2095(p_{total} - p_v) \quad [3.46]$$

For open systems such as surface and diffused aerators, it is shown that the vapour pressure is saturated at the liquid temperature, with the temperature of the gas having no affect on the vapour temperature or C_G (Cussler, 1997).

The temperature as well as the amount of dissolved solids in the water affects the Henrys law constant, which in turn affects the saturation concentration, shown by Equation 3.47 (Cussler, 1997). As temperature and dissolved solids increase so does H, which results in a decrease in the oxygen concentration. Saturation H is defined as a function of temperature, where Equations 3.45, 3.46 and 3.47 are combined to give equation 3.48 for oxygen.

$$C_G = HC_\infty^* \quad [3.47]$$

$$(*)H = \frac{0.2095(p_{TOTAL} - p_v)}{259.8.\, C_s^* T} \quad [3.48]$$

The observed oxygen saturation values in water are tabulated in Table 3.2, from Benson and Krause (1984) using standard conditions of one atmospheric total pressure and tap water with no dissolved solids.

Table 3.2: - Oxygen and Henrys Constant Saturation Values (Benson & Krause, 1984)

Temperature ˚C	C_s^* mg/L	(*)H $\frac{(mg/L)air}{(mg/L)water}$
0	14.62	20.3
10	11.29	25.1
20	9.09	29.8
30	7.56	34.0
40	6.41	37.6

A temperature correction factor, τ exists for when the temperature of the liquid varies from the standard temperature and is given by Equation 3.49.

$$\tau = \frac{C_s^*}{C_{s20}^*} \quad [3.49]$$

In wastewater, various components of its composition, such as inorganic dissolved solids can have a major effect on the oxygen saturation of the liquid. A β factor is used to give a ratio of the wastewater to tap water saturation.

$$\beta = \frac{C_{s\,wastewater}^*}{C_s^*} \quad [3.50]$$

However, in active aeration systems it is sometimes impossible to conduct aeration testing on tap water within the system. The American Public Health Association in (1995) conducted experimental work to derive an analytical expression for determining the β factor for when the amount of total dissolved solids, TDS of the wastewater were known. The TDS range was between 0 to 20000 mg/L, this work was also later validated by the American Society of Civil Engineers in 2001. The expression for determining β is shown in Equation 3.51.

$$\beta = 1 - (5.7 \times 10^{-6} \times TDS) \quad [3.51]$$

Typical values of TDS from municipal and industrial wastewater are less that 1,500 mg/L and 10,000 mg/L

respectively (Boyle, et al., 2002).

Barometric pressure also has an effect on the oxygen saturation, such that if the experimental pressure is greater than that of standard conditions then an increased saturation concentration would be experienced. The pressure correction factor is given by Ω and is calculating using, (Boyle, et al., 2002)

$$\Omega \approx \frac{p_{ATMOS}}{p_s} \quad [3.52]$$

Equation 3.52 is an acceptable approximation for tanks of less than 6 m in depth, where the actual barometric pressure was within 5 % of standard conditions (ASCE, 2007).

Using all the above correction factors for temperature, TDS and pressure, Equations 3.49, 3.50 and 3.52 respectively, gives an expression for relating the in-process oxygen saturation concentration with the saturation concentration at standard conditions, which is given by Equation 3.53.

$$C^*_{\infty f} = \tau.\beta.\Omega.C^*_{\infty 20} \quad [3.53]$$

3.17. Overall oxygen transfer coefficient, $k_L a$

The $k_L a$ is affected like the oxygen saturation by a number of factors, including temperature and the constituency of the liquid, as well as the type of aerator equipment and the level of turbulence within the system. The majority of manufacturers of aeration equipment quote their equipments performance for tap water at standard conditions, usually as a function of gas flow rate or power input.

Temperature affects the $k_L a$ in accordance with Equation 3.54, where a temperature correction factor, θ is given as equal to 1.024 (Jensen & Hvitved-Jacobsen, 1991; ASCE, 2007). However, Jensen and Hvitved-Jacobsen (1991) also showed that θ can vary from 1.006 for high turbulence systems to 1.047 for low turbulence levels.

$$k_L a_{20} = k_L a \theta^{T-20} \quad [3.54]$$

Dissolved organics in the wastewater can have the most significant effect on the $k_L a$ compared to the other factors combined. The correction factor for dissolved organics is termed the alpha factor, α and is given by,

$$\alpha = \frac{k_L a_{wastewater}}{k_L a_{tap\ water}} = \frac{k_L a_f}{k_L a} \quad [3.55]$$

Asher and Pankow (1991) showed, using surface fluorescence fluctuations, that there was a significant difference between surface renewal rates of tap water with and without surfactants. There was a higher rate of surface renewal for clean water. The additional resistance to transfer due to organics is a result of the surfactants damping the turbulent motion, due to increased shear stress at the interface.

In many cases after aeration systems have been installed for a period of time, a deterioration factor is calculated by comparing current performance with the performance initially after installation. The effect of the deterioration of performance is particularly noticeable in fine bubble diffusers, where fouling and clogging on the liquid side of the diffusers occurs. This is typically caused by periods of low air input flow

rates or intermittent use. Therefore, some diffusers may be switched off and thus the settling matter within the wastewater can block the diffusers.

Transfer coefficients are usually derived using unsteady state experiments using tap water and then adapted for wastewater (ASCE, 2007). Unsteady state testing is when the DO levels increase with time, in contrast to steady state testing, where the DO concentration is kept constant with time. The procedure for determining $k_L a$ using the unsteady state method can be split into 4 steps.

The first step is to deoxygenate the water to almost a zero concentration of DO. This is done through introducing deoxygenating chemicals to the water or through nitrogen sparging. Common chemicals used include sodium sulphite or cobalt chloride (ASCE, 2007). After this is completed the second step is to begin aerating the water, through this stage measurements are taken of DO at regular intervals. Measurements are taken primarily at a point just above the maximum depth of water and also just below the surface, other measurements if possible, are also being taken in between these depths. After the data has been collected a plot of oxygen deficit against time is generated. Oxygen deficit, $(C_\infty^* - C_L)$, is the difference between the saturation concentration of oxygen in the water the current DO concentration in the water. The gradient of this graph corresponds to the $k_L a$. The $k_L a$ is then converted to standard conditions using Equation 3.54, therefore $k_L a_{20}$. Throughout this study the overall oxygen transfer coefficient will be quoted at standard conditions, $k_L a_{20}$.

3.18. Design equations for aeration systems

The three main sets of parameters for determining the performance of an aeration system, are the mass of oxygen transferred per unit time into a given volume of liquid, oxygen transfer rate, OTE, the rate of transfer per unit power, aeration efficiency, AE and the ratio of oxygen supplied to oxygen transferred, oxygen transfer efficiency, OTE. These parameters are then converted to standard conditions through the relevant conversion factors outlined previously, such that OTR, AE and OTE become SOTR, SAE and SOTE respectively and are given by the Equations 3.56, 3.57 or 3.58 and 3.60 respectively.

SOTR is given by,

$$SOTR = V\left(\frac{dC_L}{dt}\right) = k_L a_{20} C_{\infty 20}^* V \quad [3.56]$$

SAE is a measure of SOTR per unit power. The power used can vary from manufacture to manufacture, when SAE's are quoted they are mainly based on either delivered, DP, or wire power, WP.

$$SAE = \frac{SOTR}{DP} \; or \; SAE = \frac{SOTR}{WP} \quad [3.57] \; [3.58]$$

The relationship between DP and WP is given by the overall efficiency of the aeration equipment, e.

$$WP = \frac{DP}{e} \quad [3.59]$$

Typical efficiencies for blowers used in diffuser systems are between 50 and 80% and for motors, coupling and a gearbox are around 95% each giving a total efficiency of approximately 85%, for turbine and venturi aerators (EPA, 1983).

SOTE is given by Equation 3.60.

$$SOTE = \frac{SOTR}{\dot{m}_{o2}} \quad [3.60]$$

where $\dot{m}_{o2}$ represents the mass flow rate of oxygen.

In any aeration system under in-process conditions, the oxygen transfer rate must meet the demand of the biomass in the aeration tank. The DO level in the tank will always move towards a level where the oxygen transfer rate balances with the demand. In steady state conditions these two values will be equal and therefore can be used for the basis of an overall design equation. The oxygen transfer rate for in-process conditions is given as,

$$OTR_f = V\left(\frac{dC_L}{dt}\right)_f = k_L a_f . C^*_{\infty f} . V \quad [3.61]$$

where subscript *f* represents in-process conditions.

Therefore, combining Equations 3.53, 3.54 and 3.55 with Equation 3.61 gives an overall design equation of,

$$OTR_f = \alpha . k_L a_{20} \theta^{t-20} . \tau . \beta . \Omega . C^*_{\infty 20} . V \quad [3.62]$$

CHAPTER 4

EXPERIMENTAL SET UP AND PROCEDURES

4.1. Introduction

This chapter contains the description of the experimental apparatus and the methods used in this study. An experimental investigation was undertaken to determine the optimum variables for the design of the insert. The aim was also to develop a number of coefficients, such as SAE, as well as relationships that would comprise of the primary parameters for determining the performance of the insert, such as E, $k_L a_{20}$ and bubble size. From these derived relationships and performance coefficients, it is possible to validate CFD models, so that the insert can be developed for improved performance, based on the laboratory scale experimental findings.

An optimum design would be an insert that would minimise energy consumption whilst maximising oxygen transfer to a level that would meet any in-process requirements. Therefore achieving a high SAE, in conjunction with a high SOTR. Factors that could influence the performance of an insert include the blockage ratio, R_v, which is calculated using,

$$R_V = \frac{Pipe\ Area}{Open\ Area} \quad [4.1]$$

The open area of a pipe is calculated at the point of maximum restriction of the insert. Other factors that could affect an inserts performance could include the number and location of the air orifices, such to alter the entry velocity of the injected air, the number of vanes and their associated pitch angle, to affect the pressure distribution within the throat. These factors could all play a vital role in determining hydrodynamics, as well as mass transfer efficiencies of a designed insert.

4.2. Experimental apparatus

The experiments in this work were performed using the recirculation system shown in Figures 4.1 and schematically in Figure 4.2. The test facility consisted of two 0.92 m^3 tanks. The liquid was drawn from the secondary, in-active tank of liquid volume 0.74 m^3 by a three-phase submersible pump into a vertical pipe of 100 mm ID, termed the riser. The flow was controlled using butterfly valves and a bi-pass line, which returned excessive flow back into the in-active tank. The test circuit finished with a pipe of the same ID coming vertically downward, termed the downcomer, into the primary, active tank, also of liquid volume of 0.74 m^3. The active tank was connected to the in-active tank by a series of return lines.

Having two tanks allowed for clear distinction of the active volume of liquid and also to prevent bubbles being drawn into the pump potentially causing cavitations to occur. The inserts were located in the downcomer. A constant liquid level was maintained at 0.55 m, with the downcomer pipe discharging into the active tank at a depth of 0.28 m below the free surface. The temperature of the water within the system

was kept between 18 and 24 ˚C. When the temperature of the water rose above 24 ˚C, the tanks were drained and the water was replaced. 18 ˚C was the typical temperature of the water at room temperature within the lab, during the course of the experimental work. Any water system, with the right environmental conditions, could be a source for legionella bacteria growth. There is a reasonably foreseeable legionella risk if the water system has a water temperature between 20 – 45 °C and the system creates and/or spreads breathable droplets (Health and Safety Executive, 2000). Therefore, a temperature of 24 ˚C was deemed as acceptable because of the low risk of the presence of liquid spray from the system. Also this temperature provided a suitable level of testing between changing the water in the system.

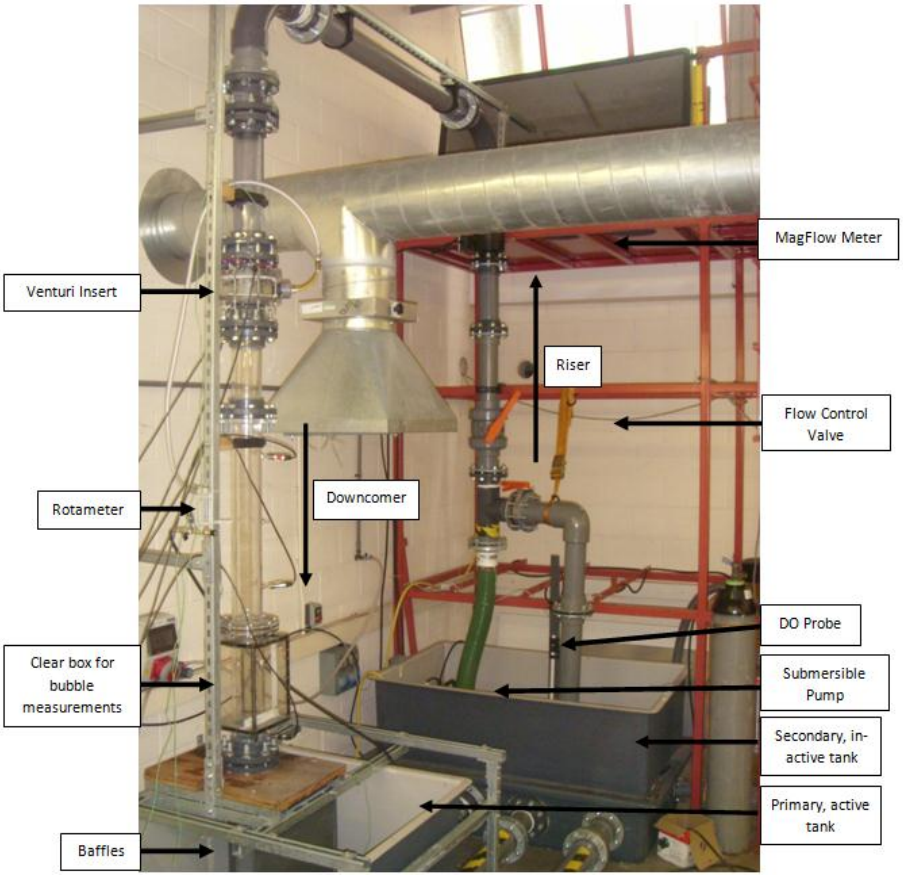

Figure 4.1: - Laboratory scale experimental set up.

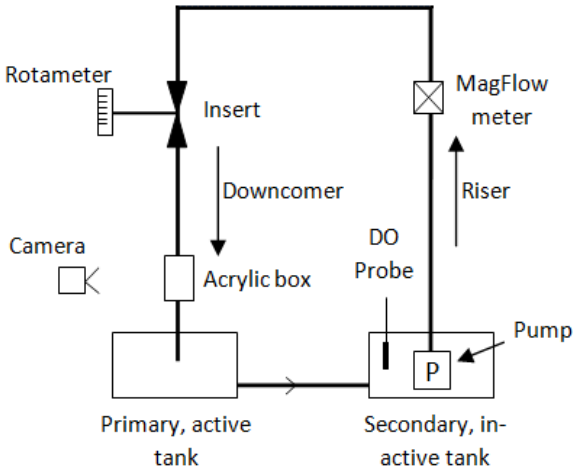

Figure 4.2: - A schematic of laboratory scale experimental set up.

At the point of disengagement inside the tank, two baffles were installed that ran the depth of the tank. The baffles were used to control the disengagement of the bubbles and prevent them from being entrained into the pump and therefore the riser. The presence of the baffles was to essentially achieve a well mixed behaviour inside the tank for the mass transfer experiments. This was confirmed by a mixing study, the results of which are shown in Appendix B.

Due to the restricted height of the Laboratory a length of 1 m, 10 ID was only achievable between the upstream pipe bend exit of the downcomer and the throat of the insert. Figure 4.3 shows a comparison between the upstream pressure loss coefficients of the HV1 insert, where the insert was located 10 ID and 22 ID, termed HV1L, below the pipe bend in the downcomer. 22ID was the lowest that the insert could be located from the upstream pipe bend due to the support structure of the system.

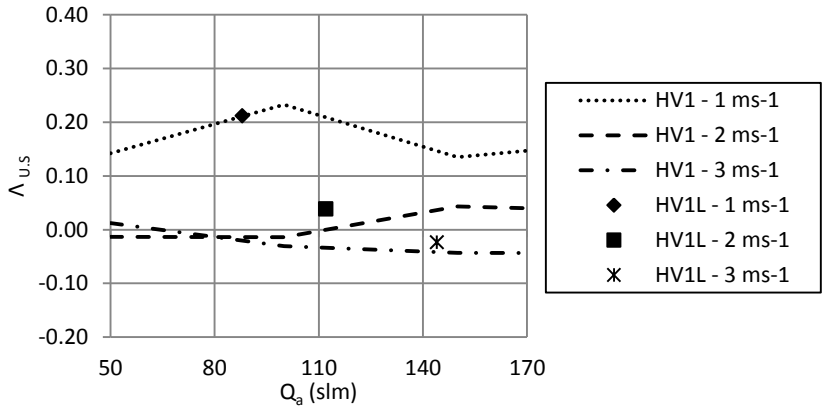

Figure 4.3: - Pressure loss coefficient of $\Lambda_{u.s}$ for when Insert was located 10 and 22 ID below the pipe bend.

The differences in the upstream pressure loss coefficient between the HV1 insert being located closer to the upstream bend and at the bottom of the downcomer are negligible, where the HV1L is within ± 10 % of the average value for the all air flow rates for the HV1 insert. Therefore, having the insert located closer to the pipe bend should not have had an impact of the pressure loss across the insert. The reason for locating the inserts at 10 ID from the pipe bend was to be able to analyse the flow regime, both through visual methods and by measuring the ventilated cavity and bubbly flow length, where applicable. Also having the insert located 10 ID below the pipe enabled a greater range of operating conditions where the generated bubble size could be measured. This is because having the insert lower to the water surface restricted the amount of measurements possible because the ventilated cavity stretched the entire visible section of the downcomer.

Beneath the aerator was a clear acrylic pipe, through which bubble size and ventilated cavity lengths were measured and observed. The bubbles were accurately photographed using high speed photography. The camera was focused at the base of the downcomer pipe, where a clear acrylic box filled with water was located around this section of pipe. This was to prevent the images being distorted during photography because of the curvature of the pipe. This method for negating the effects of the curvature of a pipe has

successfully been used in measuring velocity profiles using LDA in a number of studies including, Therning and Rasmuson (2005) and Kulkarni et al (2001). The acrylic box can be seen in Figure 4.1. The ventilated cavity was measured from the point of air injection to its base. The length of the turbulent zone was also measured and this went from the base of the ventilated cavity to the end of the turbulent mixing region, which was defined as the point in which a bubbly flow was distinguishable. During the experiments the length of the ventilated cavity fluctuated by approximately ± 0.05 m and therefore it was measured 5 times during the hydrodynamic testing to gain an average.

4.3. Liquid flow rates

A non-intrusive, fast response magnetic flow meter (ABB Kent-Taylor Ltd) supplied by Cardiff University was used to measure and record the liquid flow rate. It was recommended that a distance of 10 ID was present before and 2 ID after the magnetic flow meter for accurate readings. These recommendations were adhered to in the experimental set up.

To establish a suitable range of water and air flow rates to be used in the experimental work, typical ranges within existing technologies and previous research were analysed. An outline of existing similar technologies within the wastewater market is presented in Appendix C.

Due to the low net positive suction head in the tanks a submersible pump has to be utilised and the maximum achievable value for U_w was dependent upon the insert used and its associated pressure loss. The maximum U_w that was achievable across all the inserts was 3 ms^{-1}. Therefore the range of water velocities for the experimental was between 1 and 3 ms^{-1}. This range falls nicely with the available venturi aerators from ABS and Mazzei, outlined in Appendix C, as well as the research conducted by Jackson and Collins (1964), Gourich et al (2005) and (2007), Sotiriadis (2005) and Baylar et at (2005), whose ranges were between 2.3 and 4.6 ms^{-1}, 0.1 and 1 ms^{-1}, 1 and 1.8 ms^{-1} and 1.5 to 7.5 ms^{-1}, respectively.

4.4. Air and nitrogen flow rates

Air was supplied to the system from the high-pressure mains at a gauge pressure of 14 bar. A pressure regulator was used to reduce and maintain the air at a supply pressure of 1 bar, atmospheric pressure. A pre-calibrated rotameter (Omega Engineering FL-2064) was used to measure the flow rate of air with an accuracy of ± 3 % full scale, where the range of the rotameter was 30 to 300 L/min at standard conditions. The rotameter was calibrated for air at a temperature of 20˚C and a gauge pressure of 1 bar. The temperature and pressure of the supplied air was monitored and recorded. The pressures throughout this experimental work were measured using Druck XT1500, 0 to 1.5 bar, pressure transducers with an accuracy of ± 1 % full scale. The temperatures of the air and the water were measured using Omega pipe plug type J thermocouples with an accuracy of ± 2.2 %. A correction factor was used to take into account of any variation from standard conditions for the air flow, using the ideal gas law, as shown in Equation 4.2.

$$Q_{G,2} = Q_{G,1}\frac{P_1 T_2}{T_1 P_2} \quad [4.2]$$

If subscripts 1 and 2 represent the calibrated and experimental flow conditions respectively, then Equation 4.2 can be used to determine the actual air flow rate through the rotameter and can be taken further to determine the air flow rate within the pipe flow system, if the pressure at that point is known.

All air flow rates quoted in this experimental work will be for standard conditions, at 20˚C and 1 bar atmospheric pressure, in standard litres per minute, slm, unless otherwise stated.

The compressed nitrogen used during the DO experimentation was supplied from a pressurised cylinder at a pressure of 1 bar by means of a pressure regulator and was also controlled using a rotameter.

Experiments were conducted with the air both being induced and imposed. For the induced experiments a plenum was located around the pipe work containing the insert and the air was entrained through a 55 mm ID tube of length 935 mm, 17 ID. An air anemometer (Kimo VT 100) with temperature and pressure correction was used to measure the velocity of the entrained air though the pipe. The anemometer was located 10 ID downstream of the inlet and 7 ID upstream of the outlet of the pipe, as recommended by the manufacturers and had an accuracy of ± 3 %. The anemometer was calibrated for the pipe using a pre-calibrated mass flow meter (Omega FMA-1844), where air was imposed through the pipe using the compressed air mains. The mass flow meter had an error of ± 1.5 % at full scale with a range of 0 to 500 slm. The mass flow meter was not used during the imposed air experiments because it did not have a flow control valve, whereas the rotameter did.

It is considered by French and Widden (2001) and Wallis (1969) that in vertical pipe flows, where the air void fraction exceeded 30 %, significant coalescence of the bubbles within the two-phase flow would occur, leading to stall conditions. It was decided that appropriate air flow rates within this experimental work would not exceed a void fraction in the region of 30 %. Due to the low head nature of the experimental set up and the specified pump, the maximum upstream water velocity achievable within the experimental work was approximately 3 ms^{-1}. Table 4.1 shows the range of water and air flow rates studied in this experimental work.

Table 4.1: - Water and air flow rates used within this experimental work.

U_w (ms^{-1})	Q_a (slm)		ε_G	
1	50	300	9.59 %	38.90 %
2	50	300	5.04 %	24.15 %
3	50	300	3.42 %	17.51 %

4.5. Insert designs

The inserts provide an apparatus for introducing air or any other gas into a liquid flow. The insert consists of a number of discrete channels, as shown in Figure 4.4. These discrete channels are isolated from each other in a direction perpendicular to a direction of fluid flow through them. Each of the channels provides an

accelerating constriction to the fluid flow such that the fluid flow is caused to accelerate by the constriction. Wherein the channels comprise of orifices in which the air is entrained through, by virtue of the reduced pressure in the channels caused by the accelerating fluid flow.

The inserts are designed to alleviate the problems associated with introducing air into a liquid flow, such as coalescence of the bubbles resulting in increased resistance to the flow and the possible stalling of the device. This problem can be particularly acute where a large volume of air is introduced. The inserts addresses the problem by segmenting the flow such that a plurality of discrete channels is provided, that are isolated from one another in a direction perpendicular to the overall direction of the fluid flow through the conduit. The air is introduced into the liquid in these discrete channels, which is a simple yet effective way of helping to avoid coalescence because portions of the flow are physically isolated from each other. When the portions of the flow later join, the bubbles are potentially distributed across the flow which reduces the risk of them coalescing.

Increasing the blockage ratio of an insert and therefore increasing the flow acceleration and achieving a greater reduction in pressure, can initially be seen to be a positive attribute. However there would be an increase in the air entrainment, which would cause the flow to be more constricted and as such, there is a greater likelihood of bubbles coalescing. Although the number of channels could alleviate the problem by introducing the entrained air into different parts of the flow.

In some of the inserts, the orifices comprise of shielding elements which are arranged at an upstream side of the orifices at an angle of less than 45˚ with respect to the direction of the fluid flow, as shown in Figure 4.5. The use of shielding elements arranged at an angle helps divert the flow away from the orifice and allows the air stream to emerge with greater momentum and align itself to the flow direction. It potentially enables smaller bubbles to be generated (West, 2009). These effects reduce energy losses and thereby increase the amount of air that can be entrained into the flow (West, 2009).

All the inserts comprise of a central structure supporting a plurality of vanes, whereby the vanes define the channels. Such a shape can be aerodynamic and thus, produce little resistance to the flow increasing the inserts overall efficiency. The orifices on the vanes are arranged such that they are located at the region of reduced pressure. Therefore encouraging the maximum amount of air that can be introduced into the fluid flow, as per the recommendation by Baylar et al (2007). The length of the vanes and the central structure affect the flow and bubble coalescence. A long structure separates the flow for a longer time and decreases turbulence. It also increases the extent of the flow experiencing strong strain, which is beneficial to bubble break up (West, 2009). However, there is an increased resistance to flow in the constricted region, leading to a greater pressure loss. An advantageous length for the central structure and blades is one that provides a good balance of these effects.

There were three main inserts used in the physical testing, two of which were previously developed through a design and development programme by HydroVenturi Ltd and the independent consultancy. The third insert was designed based on the results obtained from the two previous inserts and other theoretical findings.

4.6. Preliminary designed inserts

The two preliminary designs inserts both have a blockage ratio of 4 and have 6 vanes located around a central hub. The first design is the non-zero angle of attack, A1, insert where the blades had a 4.5 degree pitch to the flow and have the air orifices located on both sides of the vanes. The second insert is the zero angle of attack, A2, insert with slots again located on both sides of the vanes.

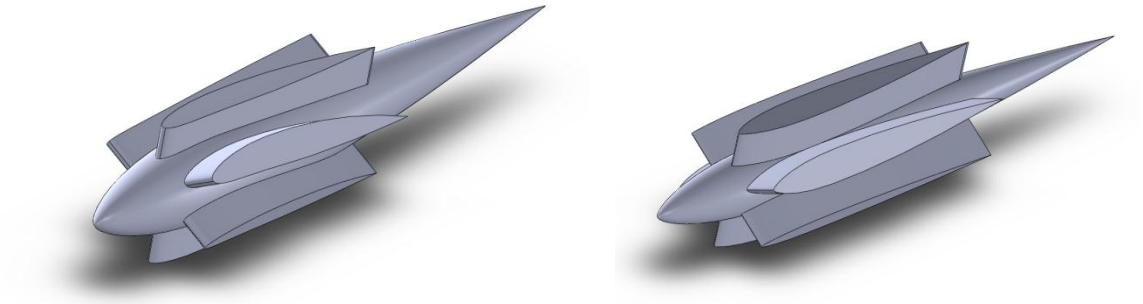

(a) (b)

Figure 4.4: - A representative 3D illustration of the (a) A1 and (b) A2 inserts.

The orifices on the vanes are located within a region on an apex of a wedge shaped depression, as shown in Figure 4.5 (a). The concept of the wedge shaped depression is that it allows the air to spread out into a broad sheet, which is swept along the face of the vane. Therefore giving a large surface area from which bubbles can be generated.

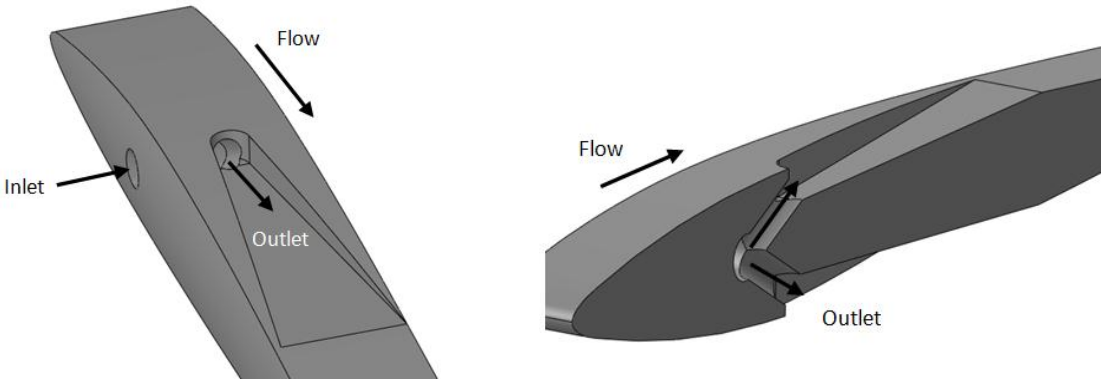

(a) (b)

Figure 4.5: - A schematic of the (a) wedge shaped depression of the A1 and A2 inserts on the vane surfaces and (b) a slice through of the vanes of the A1 and A2 inserts.

The A1 and the developed third insert, HV, both generated a swirl within the flow due to the pitching of the vanes. The swirl helps with the mixing of the air and liquid and also tends the air towards the centre of the flow stopping it adhering to the pipe wall and therefore restricting the flow. If the flow is orientated

horizontally, the rotational acceleration also acts to counteract the effects of gravity by suppressing the bubble rise due to buoyancy. This can enhance mass transfer due to the prolonged existence of a bubbly flow. Turbulence in the region downstream of the device may also be reduced leading to a reduced energy demands.

4.7. HV inserts

The third insert tested, HV, shown in Figure 4.6, had a blockage ratio of 1.5 and had 5 vanes around the central hub. The vane number was reduced to 5, due to the chosen blockage ratio. If the vane number remained at 6 then the maximum thickness of the blade would have been too small for a reasonable sized channel to exist within it for the air to travel through. Therefore, the vane count was reduced to 5 in order to have thicker vanes. Air slots were located on both sides of the vanes. The blocakge ratio of 1.5 was chosen based on the experimental pressure loss findings of the A1 and A2 inserts, discussed in Chapter 6. In conjunction with Equation 3.11, which is used for predicting the loss in expansions. A blockage ratio of 1.5 would correspond to a pressure loss coefficient based on the throat to pipe area that is 20 % of what was predicited with the blockage ratio of 4 inserts. As a result of the third insert having a lower blockage ratio than the A1 and A2 inserts, the resulting length of the HV insert was approximately 20 % of that of the A1 and A2 inserts. This is a result of the hub and vanes having similar NACA profiles.

The HV insert was tested with air inlets on both of the sides of the vanes, HV1, just the lower side, HV2, and just the upper side of the vane, HV3. The air inlet on the bottom and top side of the vanes were of the same area. Therefore, the HV2 and HV3 inserts have the same air injection surface area and the HV1 insert has twice the open area for air injection, when compared to the HV2 and HV3 inserts.

For the basis of this experimental work all comparisons in performance will be made towards the HV1 insert. This is because it was expected that this insert would provide the highest overall performance.

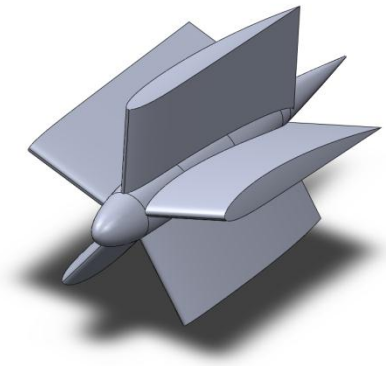

Figure 4.6: - A representative 3D illustration of the HV insert.

4.8. Regular venturi

Comparisons between all the inserts and a regular venturi, V1 were made. This was to provide a comparative measure of performance between the novel venturi inserts and existing aeration technology. The regular venturi was made to British standards (BS EN ISO 5167-4:2003) for the measurement of flows

using venturi tubes. Therefore convergent and divergent angles of 21˚ and 7˚ respectively were used. The V1 insert had a blockage ratio of 1.5, the same as the HV insert. Within the throat, 6 orifices were machined that provided the passage way for the air to be entrained. The venturi was located and fitted using these holes which were machined to fit ¼" BSP fittings.

The angle of the divergent section is important to prevent flow separation, as discussed in Chapter 3. The angle of 7˚ was used because within the throat of the venturi, where several continuous air streams are entrained via the orifices around the wall. The flow will take the form of several mixed streams stemming from the orifices. In the diverging section the diameter increases up to a fixed value, where it matches the diameter of the conduit. In this section, the flow regime becomes more complex and the behaviour of the mixture is likely to be strongly influenced by the air and water distribution as it enters the mixing zone. Energy losses are dominated by the generation of turbulence and flow separation. The risk of the formation of air pockets is high, with the detrimental consequences such as, reduced performance and stalling. Therefore, careful consideration of this section is important in preventing flow separation, hence the divergent angle of 7˚ was chosen in accordance with BS EN OSI 5167-4 (2003).

For the technology investigated in this research to be viable commercially, the inserts would have to have an increased SAE and SOTR when compared to a regular venturi, with other operational conditions being taken into consideration, such as the potential for the formation of a ventilated cavity.

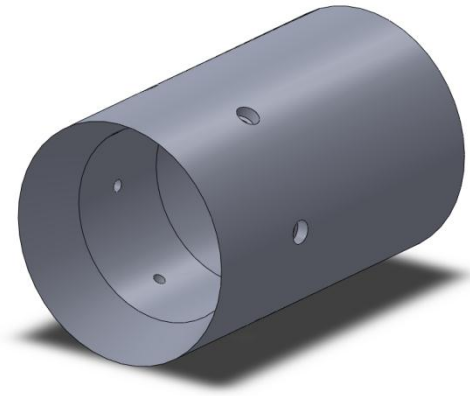

Figure 4.7: - A representative 3D illustration of the V1 insert.

4.9. Dissolved oxygen probes

The DO transfer rate in the aerated volume, which includes the divergent section of the insert, the two-phase section of the downcomer and the active tank, was determined for tap water and air. The overall oxygen mass transfer coefficient, $k_L a$ was determined using the well known dynamic method, by using unsteady state absorption (Chisti, 1989), in accordance with the ASCE (2007) standard for measurement of oxygen transfer in clean water, ASCE-EWRI 2-06.

To get the dynamic value of the $k_L a$, the first step was to switch the air being entrained from air to nitrogen, termed the down step. Once the DO in the system reached a stable value of below 2 mg/L, the nitrogen was

turned off and air was entrained again and therefore the DO level in the system began to rise, termed the up step. A polarographic (Clark cell), temperature compensated oxygen electrode from Data Harvest Ltd, model 3131 was used to monitor the variation of the DO concentration in the system, with respect to time. Details about the measurements and principles of the electrode can be found in Appendix B. The electrode was placed in the in-active tank, where there was no two-phase flow, further details on this can also be found in Appendix B. The measured DO profiles were recorded and stored for future analysis in a computer via a data logger, where the $k_L a_{20}$ and other aeration performances characteristics were determined.

4.10. Bubble size measurements

Along with $k_L a$, the bubble size and distribution needed to be established. This would provide an indication of interfacial area for mass transfer. A wide number of techniques have been developed to measure bubble sizes in two-phase flows. Schurgerl (1991) summarised these techniques into three main categories,

a) Optical techniques such as photography, where the sensor does not contact the bubble phase, which is a non-intrusive method.
b) Measurement of bubble penetration length in the direction in which most movement takes place. In this method the sensors contacts the bubble phase, therefore this is an intrusive method.
c) Measurement of bubble volume through the use of either isokinetic sampling probes or ultrasound. Isokinetic probes involve sucking a small portion of dispersion from the vessel into a capillary where the bubbles form elongated slugs. Ultrasound methods are inverse methods, relying on the fact that bubbles have a strong effect on the propagation of acoustic waves.

Photography was used in this work to characterise the resulting bubble size as a function of the operating conditions using the inserts described in Sections 4.5, 4.6 and 4.7. Photography was chosen as it is non-intrusive and it is extensively used in the literature, regarding bubble size measurements, for example Sotiriadis (2005). The photographs were taken at a position of 15 ID below the location of the insert. This location was chosen as being able to provide the greatest amount of measureable photographs, where a fully developed bubbly flow was present, as well as it only being functionally viable with the nature of the experimental set up, in terms of providing a secure platform for the high speed camera. The procedure for taking the photographs of the bubbles involved setting the water and air flow rates then allowing a short amount of time, approximately 5 minutes, for a stable ventilated cavity length to be established, if one was present. Each time the water or air flow rates were adjusted the ventilated cavity length was again allowed to stabilise. The photographs were taken with a Photon Ultima Fastcam APX-RS that was provided by the department. The camera was placed at 1 m, 10 ID from the downcomer which was the closest it could be, because of the tank and the dimensions of the tri-pod provided. The technical specifications of the camera are summarised in a Table 4.2.

There are some limitations for the use of photography to measure bubble sizes inside pipes. The cylindrical surface of the pipe distorts the view of the bubbles. To overcome the distortion due to the curvature of the

pipe a rectangular box was used to surround the pipe with a flat bottom and series of collars to fit on to the Perspex pipe. The dimensions of the box were 400 x 300 x 300 mm. The box was filled with water and scales were placed along its length and width at the pipe wall to provide a measure of the bubbles. This method for negating the effects for the curvature of a pipe has successfully been used in measurement of gas and liquid velocities in a number of studies including, Kulkarni et al (2001), and Therning and Rasmuson (2005).

The fast shutter speed used in the measurements combined with high levels of lighting focused on a small area allowed for the capturing of high quality images. Lighting was provided by two Helder 1250 W tungsten halogen photographic lamps. Each light source was mounted on a telescopic stand to allow better direction of the lighting at the measurement location. Care was undertaken to ensure that no shadows were produced by the lighting and to avoid specular reflections off the lens.

The images acquired by the camera were processed manually using a ruler, unfortunately due to the dispersions of the bubbles and highly compact nature especially at the higher void fractions it was not possible to digitally analyse the images.

Table 4.2: - Technical specifications of Photon Ultima Fastcam APX-RS.

Feature	Camera specifications
Image Pixels	1024 x 1024 max, down to 128 x 16
Frames per second	60 to 250,000
Shutter speed	16.7 ms to 2 µs
File format	AVI, BMP, JPEG, PNG

The image was digitised in a computer and the printed images were divided into 4 equal sections across the width of the pipe, so that an even number of bubbles were measured in each section. The aim of this was to give a better indication of the distribution of the bubbles sizes across the entire span of the pipe. Therefore no bias would occur towards the bubbles at the edges of the images, which were generally clearer. A rule was used to measure the minor and major axis for each bubble. All overlapping bubbles were eliminated consistently from the measurements, to avoid interpretation as one big bubble and only well focused bubbles were measured.

4.11. Experimental conditions summary

Table 4.3 summaries the inserts used and operating conditions for this experimental work.

Table 4.3: - Inserts and operating conditions used in this experimental work.

Insert	Description	Orifice location	R_v	U_w (ms^{-1})	Q_a (slm)
A1	6 vanes of 4.5˚ pitch,	Both sides	4	1 - 3	50 - 300
A2	6 vanes of 0˚ pitch,	Both sides	4	1 - 3	50 - 300
HV1	5 vanes of 4.5˚ pitch,	Both sides	1.5	1 - 3	50 - 300
HV2	5 vanes of 4.5˚ pitch,	Lower side only	1.5	1 - 3	50 - 300
HV3	5 vanes of 4.5˚ pitch,	Upper side only	1.5	1 - 3	50 - 300
V1	Regular venturi to BS EN OSI 5167-4 (2003)	6 holes around circumference of throat	1.5	1 - 3	50 - 300

CHAPTER 5

FLOW REGIME, BUBBLE SIZE AND DISTRIBUTION

5.1. Introduction

Within this experimental work, the two-phase flow regime in the downcomer was identified and the generated bubble size was determined. An understanding of these characteristics of the flow will give an indication of the interfacial area available for mass transfer and therefore the potential mass transfer performance of the inserts.

The interfacial area for mass transfer is the available area per unit volume for mass transfer and is an essential parameter when considering the operational efficiencies of any aerator. The established interfacial area determines the productivity of aerator and can often be the limiting factor in performance. Bubbly flows within a gas-liquid system are the usual form of flow that achieves a high interfacial area for mass transfer. However, in a confined system the level of bubble dispersion can be hampered by the presence of a ventilated cavity attached to the air inlets of the aerator. The presence of a ventilated cavity can reduce the interfacial area per unit volume for mass transfer, which can result in a reduced performance of the system.

Within the experiment work outlined here, two types of flow regimes were present. The first is a bubbly flow regime where the entire downcomer was bubbly. This flow regime was generally present in the higher water flow rates experimented with lower air void fractions. The second flow regime was when a ventilated cavity was typically present in the downcomer with the lower water flow rate experiments and higher air void fractions. In the majority of cases the flow in the downcomer was a combination of the two flow regimes, where beneath the ventilated cavity a kinematic shock was observed and beneath this, a bubbly flow was present. However, in some instances the ventilated cavity was seen to stretch the entire length of the visible section of the downcomer. The visible section was from the throat of the insert to 8 ID above the water free surface. Below this point it was impossible to see the flow regime. This is because of the experimental set up, where the support structure for the downcomer, the tank and the water level obscured the view of the downcomer. In this chapter the flow regimes within the experimental work will be discussed along with ventilated cavity length, L_c, the bubble dispersion and the bubble size.

5.2. Flow regime and ventilated cavity length

Within the data from the experimental work, which is presented in this section, there were clear relationships between L_c and the upstream water velocity, as well as air flow rate. The length of the ventilated cavity increased with the increasing air flow rates for a constant water velocity and decreased with an increasing water velocity for a constant air flow rate. These findings are in agreement with the

literature, for example Evans et al (2004) and Sotiriadis (2005). Across the various inserts there were significant changes in the L_c under the same operating conditions. Figure 5.1 shows the bubbly flow lengths at $U_w \approx 1$, 2 and 3 ms^{-1}, where the bubbly flow length is the total length of the two-phase section of the downcomer, 25 ID, minus L_c.

Due to the experimental set up it was impossible to measure the ventilated cavity length for lengths greater than 17 ID. This is because of the pipe work submerging below the water free surface and the downcomer being obscured by the support framework. Consequently, ventilated cavity lengths greater than 17 ID were not measured and therefore their respective bubbly flow lengths are not plotted in Figure 5.1.

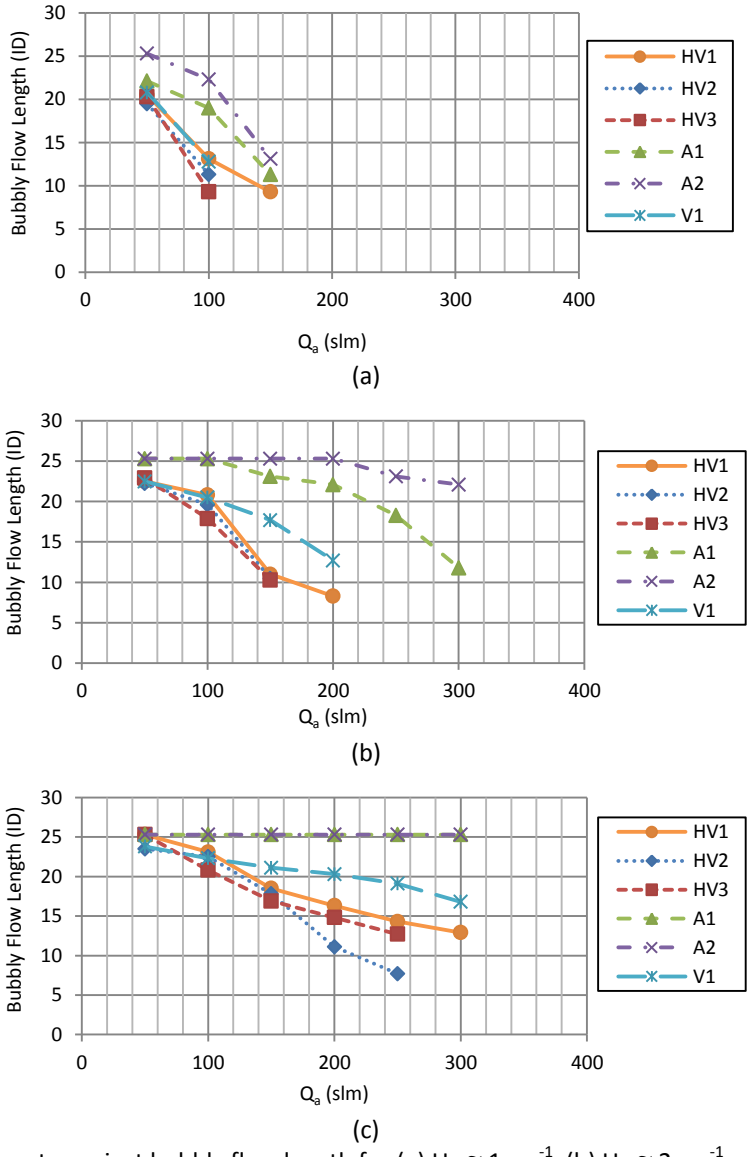

Figure 5.1 – Air flow rate against bubbly flow length for (a) $U_w \approx 1$ ms^{-1}, (b) $U_w \approx 2$ ms^{-1} and (c) $U_w \approx 3$ ms^{-1}.

Ventilated cavity length measurements were taken from the point of air injection. The ventilated cavity was determined to have ended at the point where the turbulent flow transition became present at the base of the ventilated cavity. The turbulent transition region was taken to be a part of the bubbly flow length. It is

considered, and has been shown in the literature (for example Sotiriadis (2005)) that increasing the length of the bubbly flow within a system would increase the mass transfer, through increasing the interfacial area. As well as improving efficiencies, through lowering power consumption. Therefore, the operating conditions when a bubbly flow regime is present in the downcomer are of great interest.

It is shown in Figure 5.1 that the A2 insert consistently had the greatest bubbly flow length, through all the flow settings. At $U_w \approx 3$ ms^{-1}, Figure 5.1 (c), the A1 and A2 inserts both had a fully developed bubbly flow regime in the entire downcomer for all air flow rates. Throughout the flow rates tested the HV3 insert generally had the shortest bubbly flow length, except air flow rates above $Q_a = 150$ slm at $U_w \approx 3$ ms^{-1} at this point the HV2 insert had the shortest bubbly flow length. When comparing the V1 and HV1 inserts, the HV1 insert has a greater bubbly flow length at $U_w \approx 1$ ms^{-1}. However, at $U_w \approx 2$ and 3 ms^{-1} which is shown in Figures 5.1 (b) and (c) respectively, there are transition points between $Q_a \approx 100$ and 150 slm, where the V1 insert has the greatest bubbly flow length, when compared to the HV1. There are a number of reasons for why this may have occurred, such as the velocity slip ratio between the air and water and the merging of the individual air streams, more details of these will be discussed later in the Chapter.

With the A2 insert having the shortest ventilated cavity lengths and therefore the greatest bubbly flow lengths, it can be assumed that this would result in a higher interfacial area for mass transfer. It is therefore expected that the A2 insert would have the highest $k_L a_{20}$ of all the inserts. At the lower flow rates, it would be expected that based on the above criteria the HV1 insert would have the highest $k_L a_{20}$ of the $R_v = 1.5$ inserts, which would then be superseded by the V1 insert at the higher volumetric flow rates.

5.3. Causes of a ventilated cavity

Ishii et al (2004) proposed a flow regime map for a two-phase, air and water downward flow for two distinct downcomers of 25.4 and 50.8 mm ID, which predicts the flow regime based on the superficial velocities of the individual phases. The superficial velocity of each phase is calculated by assuming that each phase is the only one flowing at that point in the downcomer. Therefore it is a ratio of the phase volumetric flow rate over the open area. Figures 5.2 (a) and (b) are the proposed flow regime maps by Ishii et al (2004) for 25.4 and 50.8 mm ID respectively. The superficial air and water velocities at the throat of the inserts from this experimental work have been plotted on to Figures 5.2 (a) and (b), where the data points are distinguished between when a full bubbly flow regime and when a ventilated cavity was present in the downcomer.

Figure 5.2 (a) predicts that there would be a bubbly flow for all operating conditions tested in this experimental work, which was not the case. However, when analysing Figure 5.2 (b), it can be seen that the data from this experimental work closely conforms to the predictions of the flow regime map proposed by Ishii et al (2004), where a Taylor bubble within a slug flow is representative of a ventilated cavity. This highlights the importance of the velocities of the respective phases and also the ID of the downcomer, when predicting the onset of a ventilated cavity. It is shown that as the downcomer ID is increased the chance of

achieving a ventilated cavity in the downcomer is also increased. Therefore, there may be operational benefits with operating using smaller ID downcomer. The annular, froth and slug flow regimes are discussed in Chapter 2.

The air to water velocity slip ratio, S, which is calculated using Equation 2.11, between the two phases within the throat of the inserts can have a significant impact on the formation of the ventilated cavity. It can be seen in Figure 5.1, that the shortest bubbly flow lengths and hence the greatest ventilated cavity lengths occurred at the higher air flow rates and the lower water flow rates, which correspond to the highest air volumetric void fractions. Under these conditions it would be expected that S would be the highest, because for the same air flow rate, the velocity slip ratio in the throat will be higher at the lower water flow rates. The velocity slip ratio will be higher through the throat of the R_v = 1.5 inserts than the A1 and A2 inserts because the water is not accelerated to the same velocity. This is highlighted with the A1 and A2 inserts consistently having the shortest ventilated cavity lengths under the same operating conditions. Therefore, it can be seen that the length of ventilated cavity depends on the velocity slip ratio of the two phases.

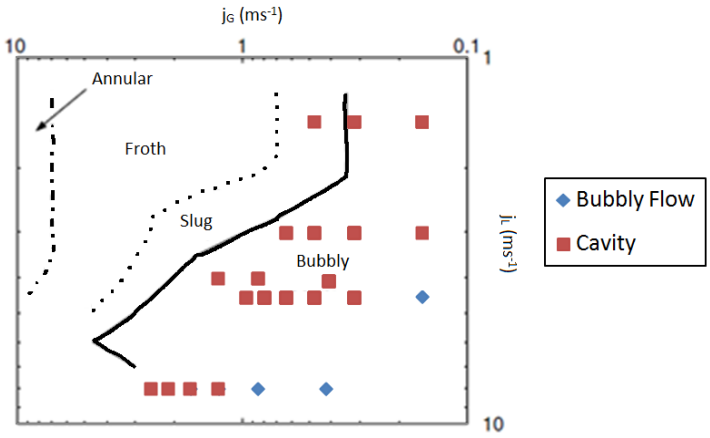

(a)

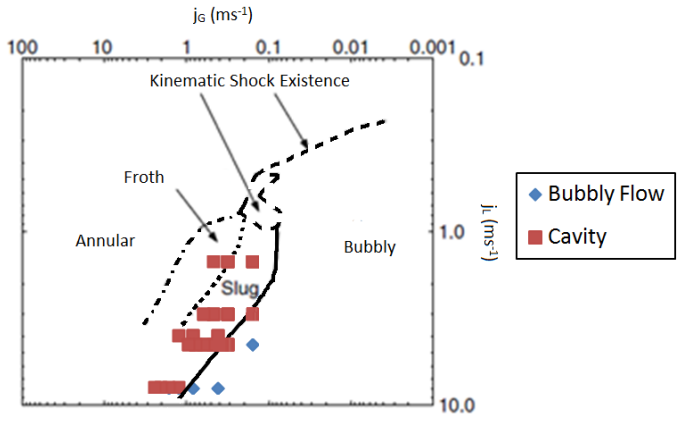

(b)

Figure 5.2: - The superficial water and air velocities at the throat from this experimental work, overlaid on to the proposed Ishii et al (2004) flow regime map for an (a) ID of 25.4 mm and (b) 50.8 mm.

Further investigation was undertaken to determine the effect of the velocity slip ratio by conducting ventilated cavity length measurements, when the A2 insert had half of its air inlet holes closed, termed as

A2b. Figure 5.3 shows that reducing the air inlet area and therefore increasing the air inlet velocity at the point of injection for the same total flow rate, reduced the bubbly flow length, corresponding to an increased L_c.

The results for when $U_w \approx 2$ ms^{-1} are shown in Figure 5.3. It can be seen that with all the air holes open a ventilated cavity began to form at approximately twice the air flow rate, when comparing it to when half the air inlets were closed. It can be seen in Figure 5.3, that a ventilated cavity formed after $Q_a = 200$ slm with the A2 insert, whereas for the A2b configuration a ventilated cavity began to form after $Q_a = 100$ slm. This relationship was not distinguishable at $U_w \approx 1$ ms^{-1} because a ventilated cavity was present for all the air flow rates. At $U_w \approx 3$ ms^{-1} for the A2 insert there was no ventilated cavity present for any of the air flow rates, however for the A2b set up, a ventilated cavity formed after $Q_a = 200$ slm. It is for these reasons that the data for $U_w \approx 1$ and 3 ms^{-1} have not been plotted. Therefore, it can be assumed that the velocity slip ratio between the air and water at the point of air injection is an important factor when designing an insert to prevent the formation of a ventilated cavity.

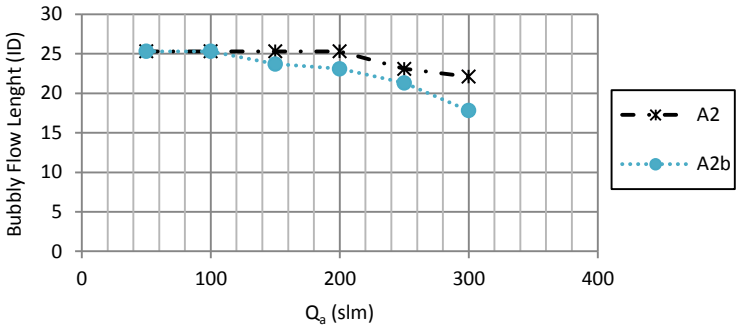

Figure 5.3: - The bubbly flow length for the A2 insert at $U_w \approx 2$ ms^{-1} for when all the air inlets were open and when half were closed (A2b)

Using CFD the air and water velocities were determined for the A2 insert. It can be approximated that the velocity of the air at the throat at the point of injection was 1.31 ms^{-1} per 50 slm or air entrained and the water velocity in the throat at the point of injection is approximated to 3.65 ms^{-1} per ms^{-1} of water in the upstream pipe. The A2 insert was chosen due to the symmetry of the wings, therefore it was expected that the air distribution from the top and the bottom of the vanes would be equal. Table 5.1 shows the predicted velocity slip ratio for the results of the A2 and A2b inserts.

For the A2 insert it can be seen in Table 5.1 that the value of the velocity slip ratio, S, for when a bubbly flow was present in the entire downcomer varied depending upon the upstream water velocity. As the upstream water velocity was increased, the velocity slip ratio that corresponded to a ventilated cavity forming also increased. This is shown in Table 5.1 for the A2b where at $U_w \approx 3$ ms^{-1}, $Q_a = 200$ slm and S = 0.96 there was no ventilated cavity present in the downcomer. However, at $U_w \approx 1$ ms^{-1}, $Q_a = 50$ slm, a velocity slip ratio of 0.72 corresponded to a ventilated cavity being formed in the downcomer, for the A2b insert. Therefore it can be seen that the onset of a ventilated cavity is a function of S as well as the water velocity.

Table 5. 1: - The predicted slip velocity ratio for the A2 and A2b inserts for $U_w \approx 1$, 2 and 3ms^{-1}.

Q_a (slm)	U_a (ms^{-1})	$U_w \approx 1$ ms^{-1} S	$U_w \approx 1$ ms^{-1} Flow Regime	$U_w \approx 2$ ms^{-1} S	$U_w \approx 2$ ms^{-1} Flow Regime	$U_w \approx 3$ ms^{-1} S	$U_w \approx 3$ ms^{-1} Flow Regime
Predicted A2 velocity slip ratio							
50	1.31	0.36	Bubbly Flow	0.18	Bubbly Flow	0.12	Bubbly Flow
100	2.62	0.72	Ventilated Cavity Present	0.36		0.24	
150	3.93	1.08		0.54		0.36	
200	5.24	1.44		0.72		0.48	
250	6.55	1.79		0.90	Ventilated Cavity Present	0.60	
300	7.86	2.15		1.08		0.72	
Predicted A2b velocity slip ratio							
50	2.62	0.72	Ventilated Cavity Present	0.36	Bubbly Flow	0.24	Bubbly Flow
100	5.24	1.44		0.72		0.48	
150	7.86	2.15		1.08	Ventilated Cavity Present	0.72	
200	10.48	2.87		1.44		0.96	
250	13.10	3.59		1.79		1.20	Ventilated Cavity Present
300	15.72	4.31		2.15		1.44	

When comparing the HV1 and V1 inserts at $U_w \approx 3$ ms^{-1} and $Q_A = 50$ slm, the V1 insert had a ventilated cavity of approximately 1.5 ID and the HV1 insert was entirely bubbly. The velocity slip ratios of the HV1 and V1 insert, as predicted by CFD are shown in Figure 5.4. The air-water velocity slip ratio of the HV1 insert on both the upper, HV1a, and lower, HV1b, vane surfaces were approximately 0.94 and 0.8 respectively. Whereas the V1 insert had a velocity slip ratio of approximately 1.2. Therefore, taking this into consideration and also the data presented in Table 5.1, as a first approximation when designing any future inserts. The velocity slip ratio at the throat should be less than 1 to ensure a bubbly flow at $U_w \approx 3$ ms^{-1}.

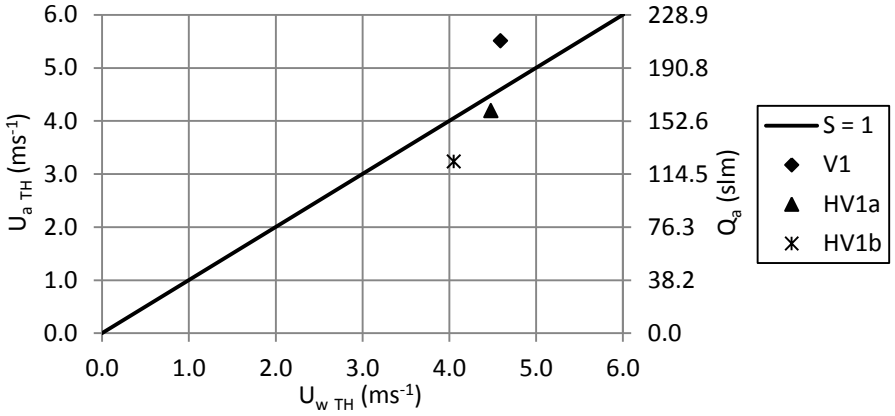

Figure 5.4: - The velocities of the air and water at the point of air injection obtained from CFD for V1 and HV1 insert at $U_w \approx 3$ ms^{-1} and $Q_a = 50$ slm.

It is not a surprise that the upstream water velocity has a significant effect on the onset of a ventilated cavity. It was shown by Riiser et al (1992), Su (1995), Lee (1998), Delfos et al (2001) and Sotiriadis (2005), that there were two main mechanisms for air entrainment around a ventilated cavity or from a plunging liquid jet. The first was as a result of the turbulence of the falling film, where the more turbulent the film, the greater the amplitude of the surface waves and therefore the greater the entrained air. This is representative of the water flowing past the air injection, where at higher velocities the flow through the throat will be more turbulent. Therefore, the water flow will be more likely to breakdown the stream of air being ejected from the orifices in the throat. The second mechanism of entrainment is as a result of shear,

where the air is entrained because of the velocity difference between the fast liquid falling film and the slow moving receiving flow, or in the case of this experimental work the fast moving water in the throat and the slower moving air flow. Shear stress as shown in Equation 5.1 is a function of velocity difference, therefore the greater the velocity difference, the greater the shear and as a result the greater the air entrainment and breakup of the air stream at its inlet.

$$\tau = \mu . \frac{du}{dy} \qquad [5.1]$$

In conjunction to this, it was shown by Bhagwat and Ghajar (2012) that an increase in the superficial liquid velocity increased the turbulence and therefore increased the level of bubble breakage caused by the impact of turbulent eddies, resulting in smaller air bubbles, where bubble breakage is a result of the kinetic energy which is transferred to the bubble surface being greater than the surface tension. In contrast, bubble coalescence was dominant at lower superficial liquid velocities, therefore resulting in larger air bubbles and the potential formation of a ventilated cavity.

5.4. Bubble dispersion

Within the experimental work there was generally a good distribution of bubbles through the cross section of the downcomer, based on visual inspection. Table 5.5 shows the distribution for the A1, A2 and HV1 inserts at $U_w \approx 3$ ms^{-1} and $Q_a = 50$ slm and the A1 insert at $U_w \approx 3$ ms^{-1} and $Q_a = 100$ slm.

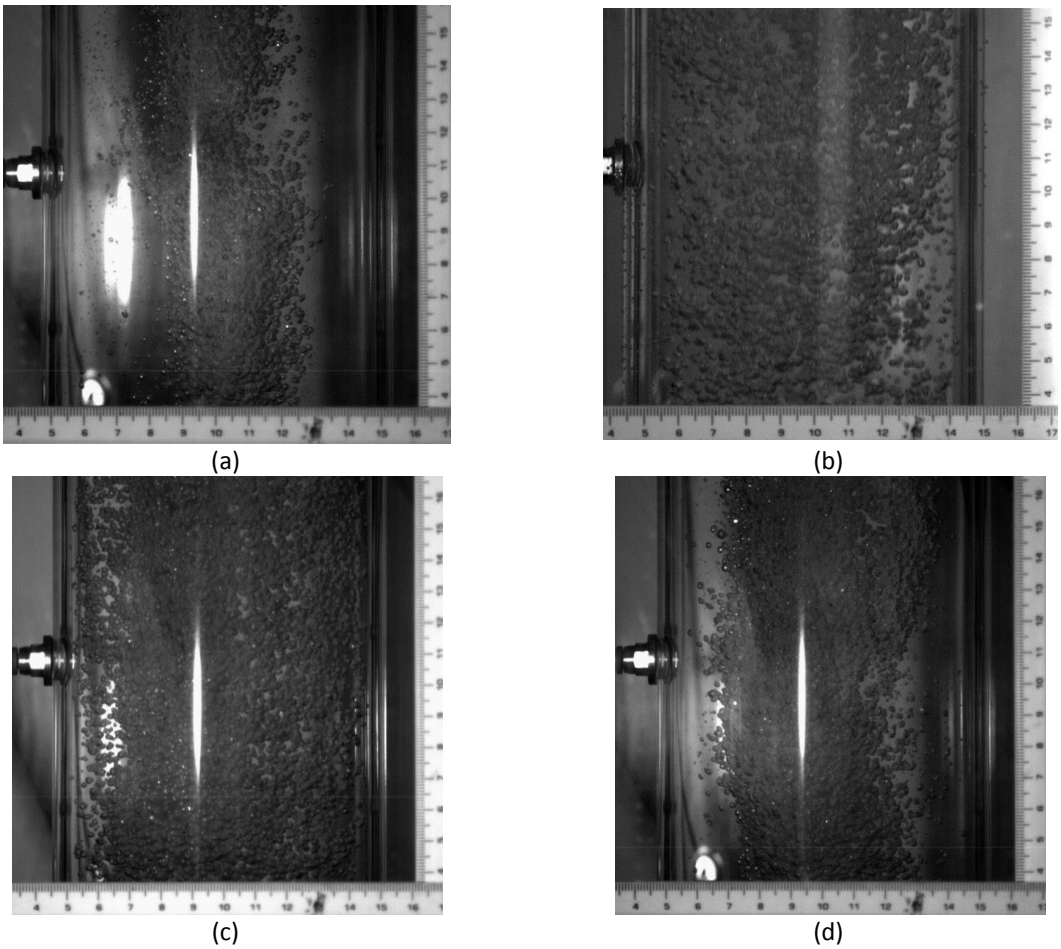

(a) (b) (c) (d)

Figure 5.5: – Bubble distribution across a number of inserts and flow rate settings, (a) A1, (b) HV1 and (c) A2 inserts at $U_w \approx 3$ ms^{-1} and $Q_a = 50$ slm, and (d) the A1 insert at $U_w \approx 3$ ms^{-1} and $Q_a = 100$ slm.

For the A1 insert at air flow rates of below 150 slm for $U_w \approx 2$ and 3 ms^{-1} coring of the air occurred, which is shown in Figures 5.5 (a) and (d). This was not noticeable with the HV inserts, or the A2 insert, examples are shown in Figures 5.5 (b) and (c). The absence of air coring in the HV1 insert could be as a result of a lower swirl number in the flow or because of a ventilated cavity being was present through all of the operating conditions, except for $U_w \approx 3$ ms^{-1}, $Q_a = 50$ slm. However, for this operating condition there was no noticeable coring in the downcomer, shown in Figure 5.5 (b).

The swirl numbers for the HV1 and A1 insert at $U_w \approx 3$ ms^{-1}, $Q_a = 50$ slm from 1 ID downstream of the insert are shown in Figure 5.6, as predicted using CFD. It can be seen in Figure 5.6 that the swirl number, S_n downstream of the inserts is considerably higher in the A1 insert than the HV1. Although all swirl numbers indicate a very weak swirl, as defined by Gupta et al (1984). A weak swirl is defined as having a swirl number of below 0.3, whereas a strong swirl has a swirl number greater than 1 (Gupta, et al., 1984). The photographs were taken 15 ID below the point of air injection and S_n is calculated by, (Gupta, et al., 1984)

$$S_n = \frac{G_\theta}{G_x}.\frac{1}{r} = \frac{\frac{2}{3}\pi.\rho_w.r^3.u_{axial}.u_{tangential}}{\pi.\rho_w.r^2.{u_{axial}}^2.r}.\frac{1}{r} \qquad [5.2]$$

Figures 5.5 (a) and (d) show that as the air flow rate increased for the A1 insert the air became more dispersed through the pipe, as the central core is seen to spread out across the diameter of the pipe. This air coring was not noticeable in the A1 insert for all the air flow rates at $U_w \approx 1$ ms^{-1} or for when $Q_a \geq 150$ and 200 slm at $U_w \approx 2$ and 3 ms^{-1} respectively.

With air coring it could be expected that this would reduce the mass transfer within the system because the water within the core may become saturated whilst there is still oxygen available within the air for transfer. Whereas, in the outer sections of the downcomer there may be little to no mass transfer occurring. A possible benefit of the air coring is that in a horizontal set up this coring may prevent the separation of the phases due to the buoyancy force. In this instance the HV1 insert may not be suitable for horizontal flows because the angular momentum of the water may not be able to overcome the buoyancy force of the air.

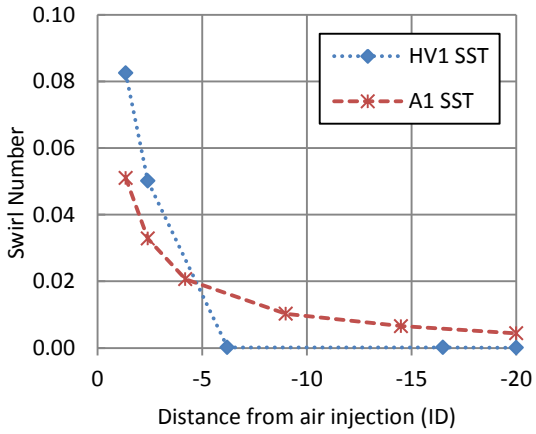

Figure 5.6: - The swirl number of the HV1 and A1 inserts down the length of the downcomer using the E-E SST PBM CFD simulation for $U_w \approx 3$ ms^{-1}, $Q_a = 50$ slm.

5.5. Bubble sizes

The bubble sizes within the downcomer were determined by non-invasive image processing, as described in Chapter 4. The captured images provided a two-dimensional representation of the bubbles in the column and the outline of the bubbles needed to be interpreted accurately, to reflect the volume of the bubble in three dimensions. There are two different approaches for measuring the bubble size based on a two dimensional image, the first assumes nearly spherical bubbles and leads to the area average bubble diameter and is defined by Equation 5.3 (Camarasa, et al., 1999).

$$d_{area} = \sqrt{\frac{4A_b}{\pi}} \qquad [5.3]$$

However, the bubbles in this experimental work were not always spherical, as can be seen in Figure 5.7. For ellipsoidal bubbles, the minor and major axis are measured and the bubble is assumed to be symmetric about its minor axis. The bubble diameter is calculated by assuming a sphere of volume equal to the volume of the ellipsoidal bubble (Couvert, et al., 1999; Wongsuchoto, et al., 2003). The vast majority of the bubbles in this work were ellipsoidal with their minor axis parallel to the liquid flow. Figure 5.8 shows the orientation of the bubble in relation to the liquid flow within the pipe. The volume equivalent bubble diameter was therefore calculated using, (Sotiriadis, 2005).

$$d_v = \sqrt[3]{d_1^2 \times d_2} \qquad [5.4]$$

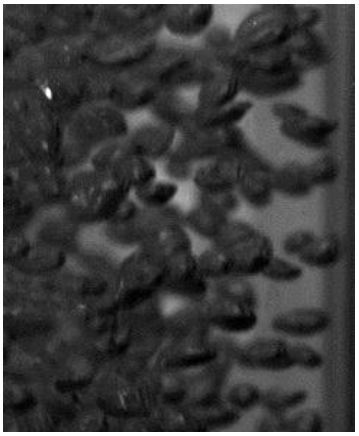

Figure 5.7: - Sample bubble image from experimental work, depicting non-spherical bubbles, HV1 $U_w \approx 1$ ms^{-1}, Q_a = 100 slm.

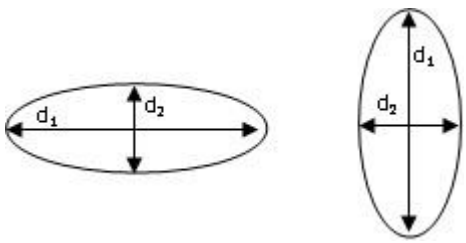

Figure 5.8: – Major, d_1, and minor, d_2, axis lengths of an ellipsoidal bubble in relation to liquid pipe flow.

Using Equation 5.4 the number average bubble diameter, d_b and the Sauter mean bubble diameter, d_{32} were subsequently calculated from the sample of, $N_{b,}$ bubbles for each experiment by Equation 5.5 and 5.6 respectively, where a sample of 100 bubbles were measured.

$$d_b = \sum_{i=1}^{N_b} \frac{d_{vi}}{N_b} \quad [5.5]$$

$$d_{32} = \frac{\sum_{i=1}^{N_b} {d_{vi}}^3}{\sum_{i=1}^{N_b} {d_{vi}}^2} \quad [5.6]$$

The Sauter mean bubble diameter is a useful comparison measure for analysing the experimental results for different bubble size distributions and is regularly used in the Literature for example, Calderbank (1958), Varley (1995) and Sotiriadis (2005). The range of the bubble sizes can be indicated by the standard deviation and the number average bubble diameter. For unimodal distributions the standard deviation and mean value are clearly defined. However, for bimodal distributions the interpretation of the number average bubble diameter and standard deviation are not clear. In this instance the ratio of Sauter mean diameter to maximum bubble diameter is used to indicate the spread of distribution. Therefore, to achieve an indication of the overall spread of the bubble sizes, the d_b will be quoted with an uncertainty based on a 95 % confidence level and the d_{32} will be quoted with the ratio of d_{32}/d_{max}.

For each set of measurements the maximum bubble diameter was determined by observing the maximum diameter across five separate images. The average value of the five images was taken to be the maximum bubble diameter. Most of literature quotes the 99.9th percentile rather than d_{max}. However, due to the number of samples taken in this experimental work, the maximum bubble diameter will be used for determining the distribution of bubble sizes. This was not seen to be a problem because the upper and lower boundary limits for a 95 % confidence level fell within 7.5 % of the number average bubble diameter for all measurements, as shown in Table 5.2.

Table 5.2: - Summary of bubble size and cavity length results for Cases 1, 2 and 3.

Insert	N_b	L_c (mm)	d_b[a] (mm)	d_{32} (mm)	d_{max} (mm)	d_{32}/d_{max}	Difference[b] (%)
Case 1: - $U_w \approx 1$ ms^{-1}, Q_a = 50 slm							
HV1	100	330	3.223 ± 0.18	3.762	5.824	0.65	-
HV2	100	580	3.365 ± 0.14	3.658	5.408	0.68	- 2.8
HV3	100	500	3.162 ± 0.19	3.708	5.802	0.64	- 1.4
A1	100	320	3.178 ± 0.15	3.543	5.173	0.68	- 5.8
A2	100	150	3.340 ± 0.18	3.800	5.802	0.66	1.0
V1	100	400	3.114 ± 0.17	3.604	6.166	0.58	- 4.3
Case 2: - $U_w \approx 2$ ms^{-1}, Q_a = 50 slm							
HV1	100	280	2.369 ± 0.14	2.806	4.807	0.58	-
HV2	100	305	2.550 ± 0.15	2.953	4.543	0.65	5.2
HV3	100	240	2.552 ± 0.15	3.025	4.782	0.63	7.8
A1	100	0	2.291 ± 0.11	2.583	4.543	0.57	- 7.9
A2	100	0	2.090 ± 0.10	2.327	3.276	0.71	- 17.1
V1	100	230	2.593 ± 0.11	2.845	5.223	0.55	1.4
Case 3: - $U_w \approx 3$ ms^{-1}, Q_a = 50 slm							
HV1	100	0	2.089 ± 0.14	2.525	3.799	0.66	-
HV2	100	180	2.180 ± 0.13	2.581	3.947	0.65	2.2
HV3	100	0	1.912 ± 0.16	2.557	4.037	0.63	1.3
A1	100	0	1.454 ± 0.10	1.805	2.900	0.62	- 28.5
A2	100	0	1.250 ± 0.09	1.567	2.900	0.54	- 37.9
V1	100	150	2.107 ± 0.13	2.534	4.501	0.56	0.4

[a] The uncertainty is based on a 95 % confidence level

[b] difference is defined by $\frac{d_{32} - d_{32\,HV1}}{d_{32\,HV1}} \times 100\%$

The bubble size was determined from images for the operating conditions of U_w = 1 to 3 ms^{-1} and Q_a = 50 to 300 slm for all inserts. The results are presented for 3 cases in Table 5.2, Case 1: - $U_w \approx 1$ ms^{-1} and Q_a = 50 slm, Case 2: - $U_w \approx 2$ ms^{-1} and Q_a = 50 slm, and Case 3: - $U_w \approx 3$ ms^{-1} and Q_a = 50 slm.

Table 5.2 shows that for Case 1, the Sauter mean bubble size was within approximately 6 % of that of the HV1 insert, for all the inserts. Also the ratio of Sauter mean bubble diameter to maximum bubble diameter was between 0.58 and 0.68 for all inserts, which shows a similar bubble size distribution between them. This pattern is followed in Case 2. However, for the A1 and A2 inserts the Sauter mean bubble diameter is reduced when compared to the other inserts. This can be attributed to the ventilated cavity not being allowed to form, where the ventilated cavity was believed by Sotiriadis (2005) to reduce the effect of turbulence on the bubble breakage. Therefore resulting in an increased bubble size when compared to a downcomer, where no ventilated cavity was allowed to form.

The reduction in both the number average and the Sauter mean bubble diameter in case 2, for the A1 and A2 inserts compared to the other inserts will result in an increase in the interfacial area available for mass transfer, according to Equation 5.7. Equation 5.7 calculates the interfacial area based on the Sauter mean bubble diameter, using the assumption of homogeneous air dispersion (Cramers & Beenackers, 2001). However, for the other inserts in Case 2, it is likely that a similar overall interfacial area for mass transfer would be present, within 8 % of each other, based on Equation 5.7. This in conjunction with the ventilated cavity lengths being similar. It can be assumed that all the R_v = 1.5 inserts will have a very similar overall mass transfer performance under the conditions presented in Case 2. This assumption is based on the work by Ohkawa et al (1987) and Mao et al (1993), where it was proven that the flow beneath a ventilated cavity can be considered as a plug flow. Therefore, if the interfacial area for mass transfer is similar due to the similar Sauter mean bubble sizes and a plug flow exists after the ventilated cavity, then the mass transfer variations between R_v = 1.5 inserts under these conditions should be minimal. From the plug flow assumption it can be assumed that when a ventilated cavity is present in the downcomer, the mass transfer rate of the system will then be dependent upon the residence time of the bubbles, which is affected by the length of ventilated cavity.

$$a = \frac{6\varepsilon_G}{d_{32}} \qquad [5.7]$$

Comparing Cases 1 and 2 in Table 5.2 shows that the average bubble diameter deceased with increasing water velocity. The experimental data from this work also showed that the average bubble diameter increased with increasing air flow rate for the same water flow rate when a ventilated cavity was present, which is shown in Table 5.3.

Table 5.3: - Summary of bubble size and cavity length for HV1 insert at $U_w \approx 3$ ms^{-1}.

Q_a (slm)	N_b	L_c (mm)	d_b (mm)	d_{32} (mm)	d_{max} (mm)	d_{32}/d_{max}
50	100	0	2.089 ± 0.14	2.525	3.799	0.66
100	100	220	2.098 ± 0.15	2.632	4.215	0.62
150	100	680	2.274 ± 0.14	2.684	4.268	0.63
200	100	900	2.289 ± 0.16	2.794	4.580	0.61

Table 5.4 shows that when no ventilated cavity was present, the average bubble diameter decreases with increasing air flow rate, at a constant water velocity. The cause of this may be as a result of compression in the downcomer. The static pressure at the point of bubble measurement for Q_a = 300 slm was approximately 1.5 kPa higher than at Q_a = 50 slm. This in conjunction with the reduced coring at the higher flow rates, which may result in an increased mass transfer rate. This in turn would result in a reduced bubble size at the higher air flow rates, due to the lower density of the air bubbles.

Table 5.4: - Summary of bubble size and ventilated cavity length for A1 insert at $U_w \approx 3$ ms^{-1}.

Q_a (slm)	N_b	L_c (mm)	d_b (mm)	d_{32} (mm)	d_{max} (mm)	d_{32}/d_{max}
50	100	0	1.454 ± 0.10	1.805	2.900	0.62
100	100	0	1.479 ± 0.08	1.679	2.271	0.74
150	100	0	1.385 ± 0.07	1.558	2.271	0.68
200	100	0	1.288 ± 0.07	1.517	2.900	0.52
250	100	0	1.288 ± 0.07	1.480	2.303	0.64
300	100	0	1.317 ± 0.06	1.463	1.984	0.73

Despite the ventilated cavity being present in Case 3 for V1 and HV2 inserts, the Sauter mean bubble diameter for the V1 and HV inserts are within 2.5 % of each other. Therefore, under the flow rate conditions of Case 3, as explained above, it would be expected that the A1 and A2 inserts would have a superior mass transfer performance, particularly the A2 insert when compared to the R_v = 1.5 inserts, with the R_v = 1.5 inserts having similar mass transfer performance.

For comparison with other studies in the literature, the results of the Sauter mean bubble diameter were normalised with respect to d_{max}. The average value of d_{32}/d_{max} for all bubble size measurements within this experimental work was found to be 0.63. This is in good agreement with Calabrese et al (1986), Hesketh et al (1987), Evans et al (1992), Zhang et al (1995) and Sotiriadis (2005) who all reported values of between 0.60 and 0.62. Evans et al (1992) conducted experimental work using a plunging jet into a bubble column, where the velocity of the water nozzle is representative of a falling water film. In the work by Evans et al (1992) a series of ID columns were tested from 44 to 95 mm ID. With a typical jet velocity of 11.5 ms^{-1}, for this experimental work the water falling film velocity around the ventilated air cavity was estimated to be between 3 and 6 ms^{-1}. Within the work by Evans et al (1992) air void fractions of up to 65 % were tested. On the other hand Sotiriadis (2005) conducted experimental work on a 105 mm ID pipe with air void fractions of up to only 3 % and the d_{32}/d_{max} ratio was still in the range of 0.60 to 0.62. Therefore, despite the wide range of operating conditions tested within the literature, the d_{32}/d_{max} ratio of approximately 0.6 to 0.62 is consistent.

Comparing the d_{32}/d_{max} for all the experimental data in this work, distinguished by when a ventilated cavity was and was not present in the downcomer. It can be identified, that when a ventilated cavity was present in the downcomer the bubble distributions are similar with a standard deviation of 7.35 %, whereas there was a standard deviation of 12.23 % when no ventilated cavity was present in the downcomer, shown

in Table 5.5. This data can be used to validate the assumption by Sotiriadis (2005), where it was believed that the presence of a ventilated cavity suppresses the turbulence in the downcomer and therefore limits the amount of bubble breakage within it. This in conjunction, with the assumptions by Ohkawa et al (1987) and Mao et al (1993), where it was believed that the flow beneath a recirculating vortex, which is present beneath a ventilated cavity, can be considered as a plug flow. This is in comparison to when no ventilated cavity was present, where the turbulence in the downcomer would lead to the random breakage of the bubbles, potentially leading to a greater range of bubble diameters. These assumptions can be used to explain the scatter of the d_{32}/d_{max} ratio in Table 5.4, where all the flow conditions presented in the table were a full bubbly flow regime and therefore there would be a greater level of scatter of the bubble diameters.

Table 5.5: - Average and standard deviation of d_{32}/d_{max} for the flow regimes present in this experimental work.

Flow regime	Average d_{32}/d_{max}	Standard deviation (%)
Bubbly flow	0.637	12.23
Ventilated cavity	0.626	7.35

Figure 5.9 shows the cumulative frequency curves of the bubble classes for Cases 1 to 3. Figure 5.9 (a) shows that the inserts have a relatively similar bubble size at $U_w \approx 1$ ms^{-1}. However, as the water velocity is increased the A1 and A2 inserts have a considerably smaller mean bubble diameter. This is shown by the respective cumulative frequency curves shifting towards the smaller bubble diameter brackets. Therefore implying a higher number of bubbles in the smaller bubble brackets, this correlates to a smaller overall mean bubble diameter.

(This space is intentionally blank)

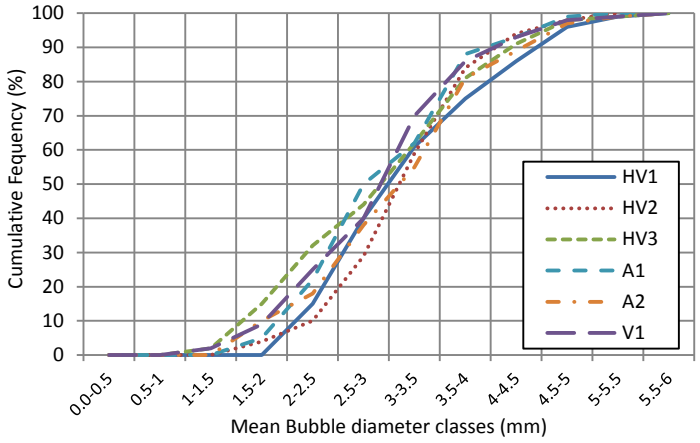

(a)

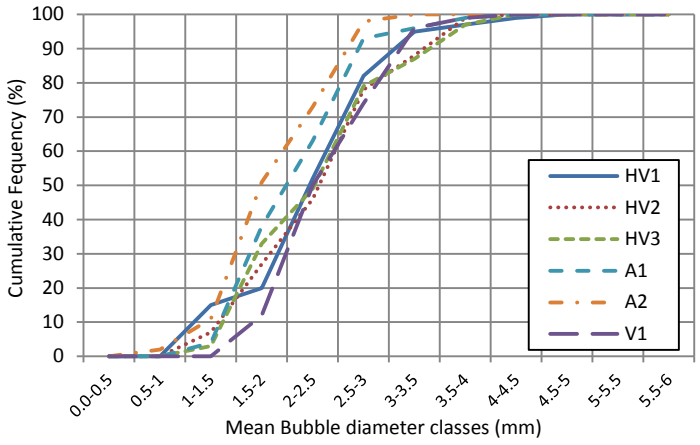

(b)

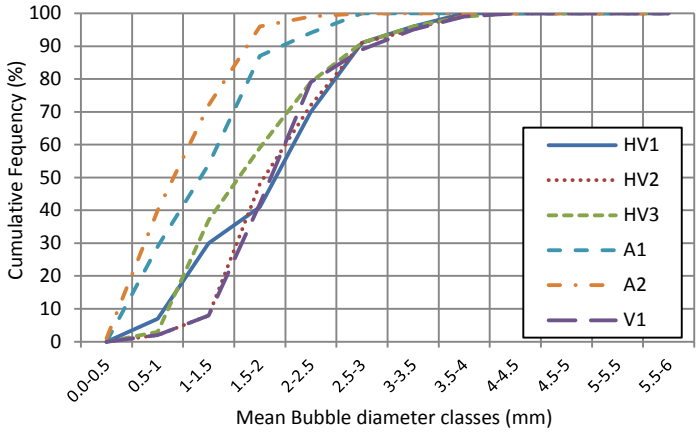

(c)

Figure 5.9. Cumulative distribution curve of the mean bubble diameter (d_b) for (a) Case 1, (b) Case 2 and (c) Case 3.

The significance of the ventilated cavity as well as the venturi ratio is highlighted in Figure 5.10, where Figure 5.10 groups the inserts by venturi ratio. It can be seen in Figure 5.10 (a) that the R_v = 1.5 and 4 inserts have very similar performance, which was when a ventilated cavity was present in the downcomer. However, when there was no ventilated cavity present in the downcomer for the R_v = 4 inserts, but there was with some or all of the R_v = 1.5 inserts, Figures 5.10 (b) and (c), there is a significant difference in the cumulative frequency curves, when distinguished by blockage ratio.

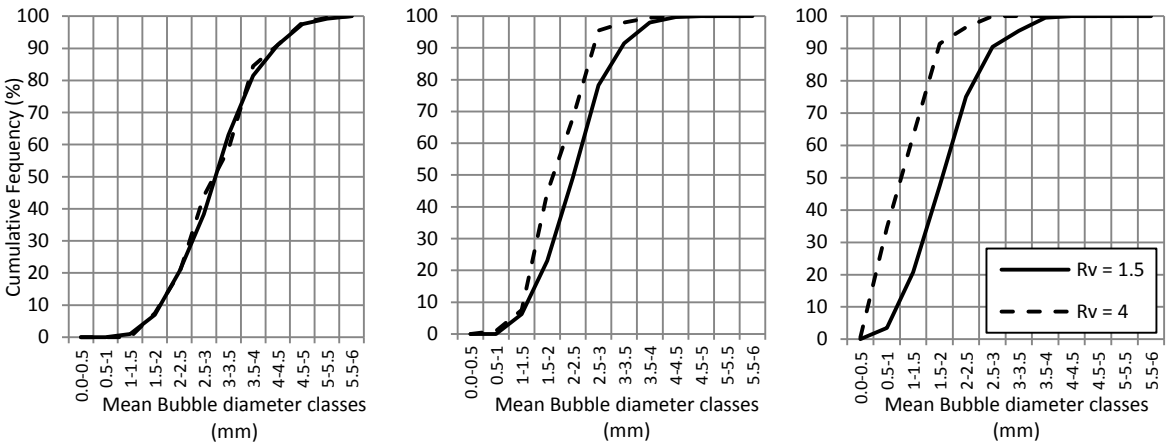

Figure 5.10. Cumulative distribution curve of the mean bubble diameter (d_b) for (a) Case 1, (b) Case 2 and (c) Case 3, when grouped by R_v = 1.5 and R_v = 4.

Figure 5.11 shows the groupings for cumulative frequency curves for the two blockage ratios for Cases 1 to 3. It can be seen in Figure 5.11 that as the water velocity is increased, therefore going from Case 1 to Case 3, the profile moves further to the left and therefore towards the smaller bubbles diameters. It is noticeable in Figure 5.11 that the Case 3 cumulative profile for the R_v = 1.5 inserts is similar to the cumulative profile for Case 2 for the R_v = 4 inserts. Therefore, the performance of the R_v = 4 inserts, in terms of mass transfer, may be similar or even be better than the R_v = 1.5 inserts under these operating conditions. Potentially meaning that the R_v = 4 inserts could deliver the same mass transfer performance for a lower power consumption, due to the lower water flow rate and therefore possibly a lower power requirement.

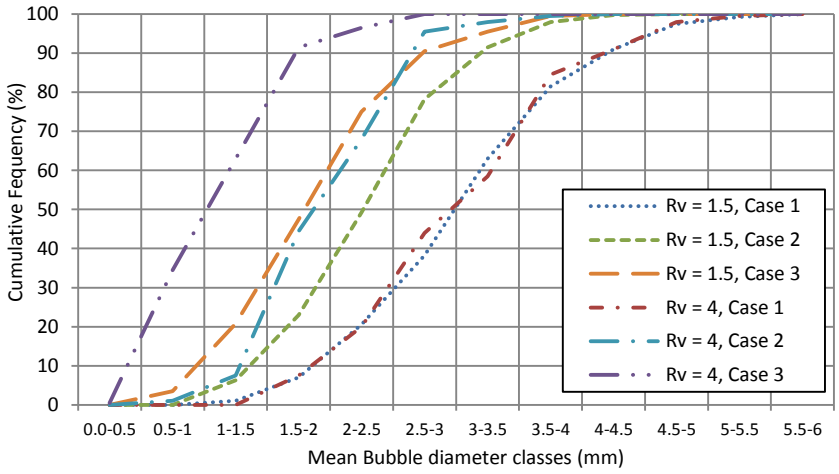

Figure 5.11. Cumulative distribution curve of the mean bubble diameter (d_b) for (a) Case 1, (b) Case 2 and (c) Case 3, when grouped by R_v = 1.5 and R_v = 4.

Within this experimental work a unimodal distribution was identified. Therefore, using the number average bubble diameter with a 95 % confidence level provides a useful and reliable approximation of the bubble distribution and variation. This is because of the low percentage value of the upper and lower boundaries from the mean, which is typically less than 7.5 % for all of the experimental measurements. In conjunction with this the d_{32}/d_{max} values closely conform to the literature. Therefore the sample size of 100

measurements can be considered to be a suitable size for this experimental work.

5.6. Summary

It has been highlighted in this chapter that the A2 insert consistently had the shortest ventilated cavity length and often had a fully developed bubbly flow in the length of the downcomer. This in conjunction with the insert producing a smaller Sauter mean bubble diameter leads to the assumption that the A2 insert would have the greatest $k_L a_{20}$ of all the inserts.

When comparing the R_v = 1.5 inserts, the HV1 insert had the shortest ventilated cavity length at the lower flow rates, with the V1 insert having shorter ventilated cavity length above these lower flow rates, for example above Q_a = 150 slm for $U_w \approx 2$ and 3 ms^{-1}. The produced Sauter mean bubble diameters were similar across all the R_v = 1.5 inserts. This was because a ventilated cavity was present for all the operating conditions for the R_v = 1.5 inserts, except for $U_w \approx 3$ ms^{-1} at Q_a = 50 slm for the HV1 and HV3 inserts. It can therefore be assumed that under these conditions the ventilated cavity length will have a significant effect on the resulting $k_L a_{20}$ values.

When considering the formation of a ventilated cavity. It has been shown that not only does the velocity slip ratio have an effect on the formation of the ventilated cavity, but so does the water velocity at the point of air injection.

CHAPTER 6

ENERGY LOSSES

6.1. Introduction

The energy losses associated with the different inserts has been calculated in the present work. This was achieved through the measurements of static pressure, which were taken upstream of the inserts, at various locations along the length of the insert and at intervals along the length of the downcomer, as is shown later in this chapter in Figure 6.7. In addition to these measurement points, the supply air pressure was also measured. The purpose of this chapter is not only to show the energy losses associated with the inserts, but also the dissipation within the whole aerated volume. The aerated volume consists of the divergent section of the insert from the point of air injection, the ventilated cavity length, the volume of the bubbly flow column and the active tank volume.

The specific power, E, is used as a comparison between the inserts and the results of which are outlined in the following sections, E is calculated using Equation 3.3. Through calculating the specific power of the individual inserts an indication of its performance in terms of aeration efficiency can be gauged, where the initial design parameter of the inserts was to achieve a high oxygen transfer rate. However, this must be achieved whilst having low energy consumption.

6.2. Losses with no air entrained

The pressure loss was calculated across the potential aerated volume for when only water was flowing through the system. Clear differences in pressure loss can be identified between the V1 and the HV, A1 and A2 inserts.

It can be seen in Figure 6.1 that the R_v = 4 inserts are the least efficient in terms of specific power. With the A1 insert having approximately twice the loss of the R_v = 1.5 inserts and the A2 insert having over three times the loss, which is highlighted in Table 6.1. The plotted values in Figures 6.1 are average values, where the standard deviation for all cases was less than 1 %. The HV1, HV2 and HV3 inserts all had very similar losses compared with each other, less than 2 % variation in all cases. Therefore, the data of the HV2 and HV3 inserts are not plotted in Figure 6.1 or listed in Table 6.1.

Figure 6.1 (a) and Table 6.1 shows that at the lower water velocity of $U_w \approx 1$ ms^{-1} the HV1 insert is the most efficient insert. However, as the water velocity is increased the V1 insert becomes the most efficient. Due to the small changes in performance between the V1 and HV1 inserts, less than 10 %. The results can only be considered as an indication of a trend, where as the upstream water flow rate increases, the V1 insert become the most efficient insert and that as the water flow rate is further increased the difference between

the V1 insert and the other inserts is increased. This observation can be explained by considering flow separation. Figures 6.2 and 6.3 show recirculation and therefore flow separation occurring within the HV1 and V1 Inserts at $U_w \approx 3$ ms^{-1}.

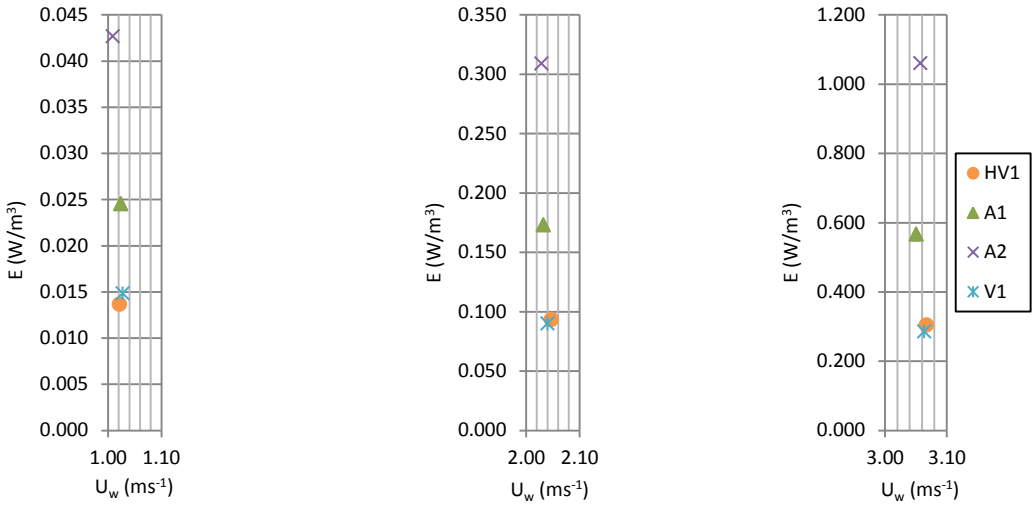

(a) (b) (c)

Figure 6.1: – Pressure losses across the inserts with no air being induced at (a) $U_w \approx 1$ ms^{-1}, (b) $U_w \approx 2$ms^{-1}, (c) $U_w \approx 3$ ms^{-1}.

Table 6.1 – Differences in specific power consumption compared to HV1 insert

Uw (m/s)	Insert	E_{HV1} (W/m3)	Difference[a] V1 (%)	Difference[a] A1 (%)	Difference[a] A2 (%)
1		*0.0137*	*+ 8.76*	*+ 78.83*	*+ 211.69*
2		*0.0933*	*- 3.43*	*+ 85.64*	*+ 231.30*
3		*0.3044*	*- 6.24*	*+ 86.01*	*+ 248.28*

[a] difference is defined as $\frac{E_x - E_{HV1}}{E_{HV1}}$ x 100%,

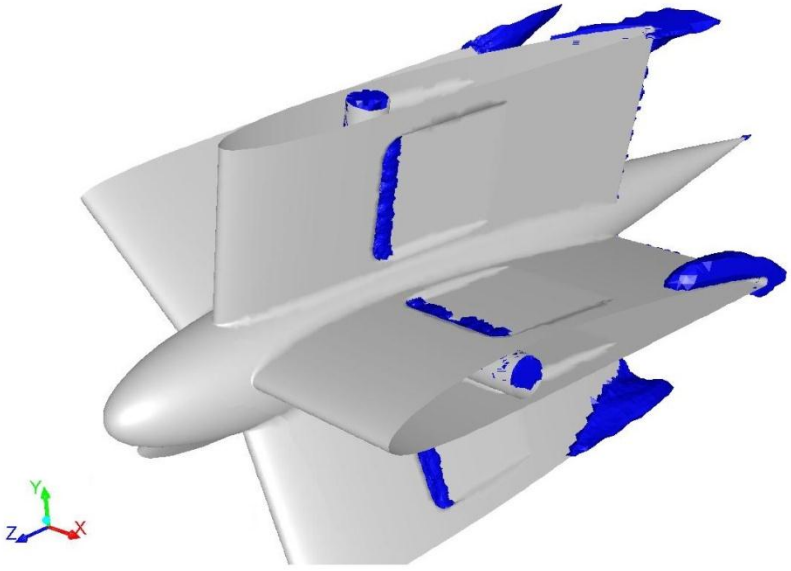

Figure 6.2: - An iso-surface, where the water velocity in the positive z direction is highlighted, for the HV1 insert at $U_w \approx 3$ ms^{-1} with no air flow being injected, the upstream water flow is in the negative Z direction.

Figure 6.2 shows flow separation, with a recirculating vortex occurring at each of the vane tips, next to the pipe wall, as well as along the air orifices and the point of air injection into the water flow at $U_w \approx 3$ ms^{-1}.

These issues will contribute to increased pressure loss, with recirculation velocities of up to 2.48 ms^{-1} at the vane tips. The recirculation regions were less severe at $U_w \approx 1$ ms^{-1} with a maximum recirculation velocity of 0.62 ms^{-1} and at $U_w \approx 2$ ms^{-1} there was a maximum recirculation velocity of 1.72 ms^{-1}.

Figure 6.3 shows flow separation occurring on the V1 insert $U_w \approx 3$ ms^{-1}, however it less than the HV1 insert at the higher water velocities, with the maximum recirculation velocity at $U_w \approx 3$ ms^{-1} of 1.31 ms^{-1}. The recirculation in Figure 6.3 highlights the minor flow separation occurring in the divergent section of the venturi and in the air orifices.

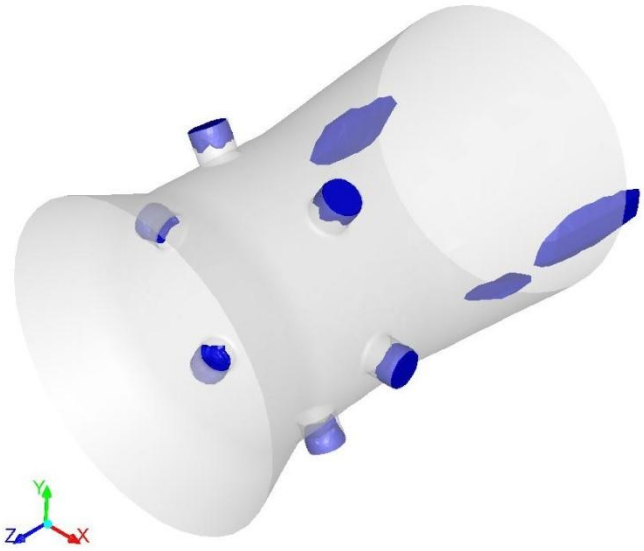

Figure 6.3: - An iso-surface, where the water velocity in the positive z direction is highlighted, for the V1 insert at $U_w \approx 3$ ms^{-1} with no air flow being injected, the upstream water flow is in the negative Z direction.

The influence of the inserts efficiency without air flow on the mass transfer properties will be discussed in Chapter 7.

6.3. Insert energy losses with air flow

A series of measurements were taken across a range of water and air flow rates within this experimental work, as outlined in Chapter 4. Throughout the experimentation two distinct flow regimes were identified, the first was a bubbly flow and the second consisted of a ventilated air cavity that was surrounded by an annular falling water film. In some instances when a ventilated cavity was present, it stretched the entire length of the downcomer. The alternate was that a kinematic shock was observed, below which a bubbly flow was present.

At $U_w \approx 1$ ms^{-1} the V1 insert had the smallest specific power consumption of all the inserts and the A2 insert had the highest, as can be seen in Figure 6.4. This was the case with the A2 insert for all the liquid flow velocities tested, as can be seen in Figures 6.4, 6.5 and 6.6. It is shown in Figure 6.4 that at air flow rates greater than 200 slm there is a levelling off of the specific power consumption across all the inserts at $U_w \approx 1$ ms^{-1}, except for the A2 insert which begins to level off at approximately $Q_a = 250$ slm. This is as a result of

the ventilated cavity stretching the entire length of the downcomer. From this observation it can be taken that any further increase in frictional pressure loss due to an increased liquid film flow velocity, as a result of the increased air flow rate is negligible, when considering a flow where a ventilated cavity stretches the entire length of the downcomer.

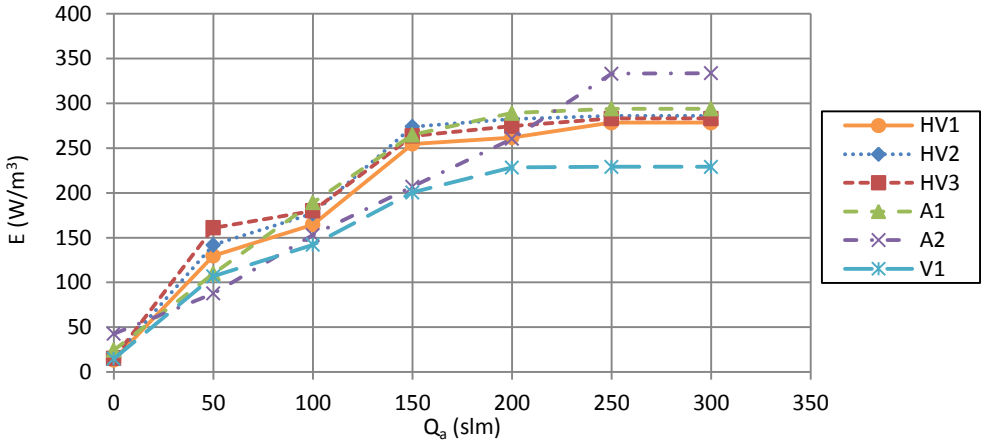

Figure 6.4: – Specific power consumption, for all inserts at $U_w \approx 1$ ms^{-1}.

As can be seen across all of the flow velocities, by comparing Figures 6.4, 6.5 and 6.5, the changes in the location of the air slot openings of the HV1, HV2 and HV3 inserts, only have a minor impact to the specific power of the insert. This is in contrast to changing the blockage ratio, which has a significant effect on the specific power consumption, particularly at higher liquid flow rates, which can be seen in Tables 6.2, 6.3 and 6.4, when comparing the A1 and A2 inserts, as well as the HV1, HV2 and HV3 inserts against the HV1 insert.

Table 6.2: – Specific power differences for all inserts at $U_w \approx 1$ ms^{-1}.

Insert Qa (slm)	HV1 (W/m^3)	Difference[a] HV2 (%)	Difference[a] HV3 (%)	Difference[a] V1 (%)	Difference[a] A1 (%)	Difference[a] A2 (%)
50	62.68	+ 14.10	-2.68	- 20.41	+ 7.95	+ 40.05
100	129.68	+ 9.42	+ 24.17	- 17.57	- 15.21	+ 17.99
150	164.5	+ 7.58	+ 9.40	- 13.65	+ 14.99	+ 25.74
200	254.6	+ 7.60	+ 3.52	- 21.25	+ 3.99	+ 2.64
250	261.67	+ 7.96	+ 4.88	- 12.76	+ 10.45	+ 27.30
300	278.34	+ 2.68	+ 1.66	- 17.72	+ 5.61	+ 19.86

[a] difference is defined as $\frac{E_x - E_{HV1}}{E_{HV1}}$ x 100%

It can be seen however, that having the air inlets on both sides of the wings, HV1, improves the specific power in comparison to the other two orientations, HV2 and HV3. This may be as a result of the air being introduced at a lower velocity, due to the doubling of the open area for the air to travel through or as a result of having shorter ventilated cavity lengths for the same flow rate setting. When comparing the HV2 and HV3, it is shown in Figures 6.4, 6.5 and 6.5 and Tables 6.2, 6.3 and 6.4 that having the air slots on the lower side of the wing, HV2, results in greater power consumption at higher air flow rates, and very similar power consumption at the lower air flow rates.

Figures 6.4, 6.5 and 6.6 show that the V1 insert consistently has a lower E than the HV1 insert. Therefore, for the HV1 insert to be more efficient as an aerator its $k_L a_{20}$ and SOTR must be higher than the V1 insert, to achieve a higher SAE and therefore be a competitive alternative to V1 insert in the aeration market.

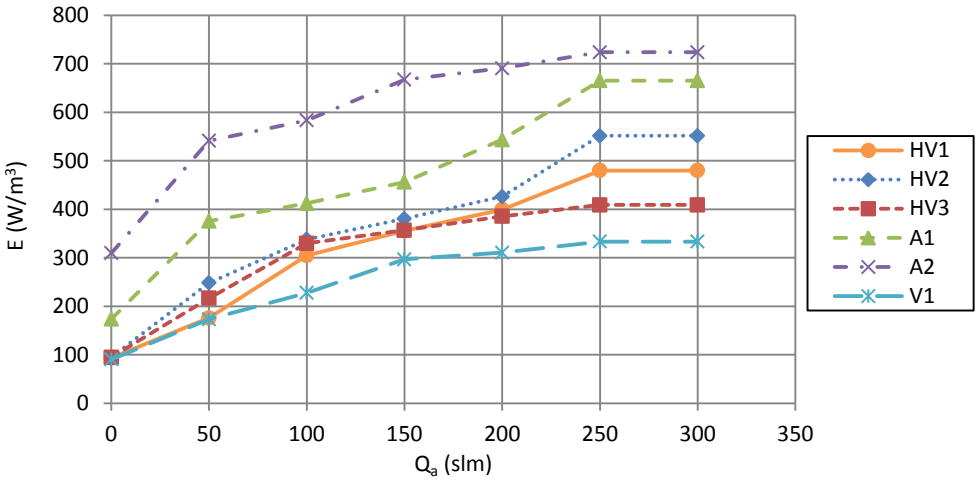

Figure 6.5: – Specific power consumption, for all inserts at $U_w \approx 2$ ms^{-1}.

Table 6.3: – Specific power differences for all inserts at $U_w \approx 2$ ms^{-1}.

Insert Q_a (slm)	HV1 (W/m^3)	Difference[a] HV2 (%)	Difference[a] HV3 (%)	Difference[a] V1 (%)	Difference[a] A1 (%)	Difference[a] A2 (%)
50	135.79	+ 1.89	+ 7.48	- 3.45	+ 126.64	+ 216.55
100	175.78	+ 41.06	+ 23.13	- 1.56	+ 284.39	+ 246.59
150	304.54	+ 10.94	+ 8.19	- 25.30	+ 35.32	+ 91.60
200	355.37	+ 7.04	+0.38	- 16.58	+ 28.37	+ 87.74
250	399.17	+ 6.71	- 3.41	- 22.21	+ 36.13	+ 73.02
300	479.77	+ 14.97	- 14.81	- 30.57	+ 38.66	+ 50.88

[a] difference is defined as $\frac{E_x - E_{HV1}}{E_{HV1}}$ x 100%,

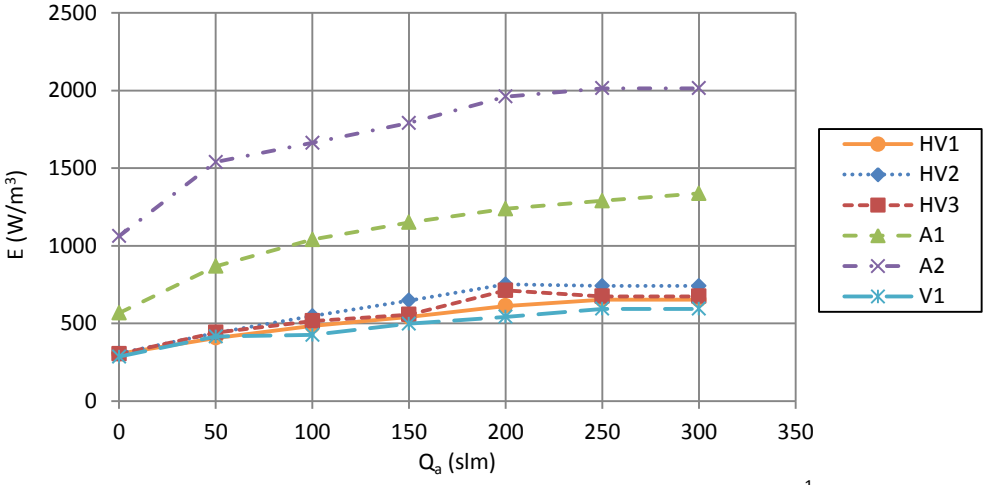

Figure 6.6: – Specific Power consumption for all inserts at $U_w \approx 3$ ms^{-1} all inserts.

Table 6.4: – Specific power differences for all inserts at $U_w \approx 3$ms^{-1}.

Insert Q_a (slm)	HV1	Difference[a] HV2 (%)	Difference[a] HV3 (%)	Difference[a] V1 (%)	Difference[a] A1 (%)	Difference[a] A2 (%)
50	373.7	- 2.16	- 0.50	- 5.21	-132.14	-237.71
100	406	+ 8.18	+ 8.78	+ 2.48	-156.26	-278.93
150	483.4	+ 13.37	+ 6.58	- 11.85	-137.90	-244.02
200	541.8	+ 19.59	+ 0.95	- 7.98	-128.40	-230.50
250	612.8	+ 22.67	+ 16.32	- 11.54	-110.42	-219.88
300	652.9	+ 13.57	+ 3.25	- 9.03	-104.69	-208.60

[a] difference is defined as $\frac{E_x - E_{HV1}}{E_{HV1}}$ x 100%

6.4. Pressure Profile along bubble flow length

The pressure profile along a 10 ID section of pipe, starting 6 ID below the throat of the inserts in the downcomer pipe varied significantly, depending on the length of the ventilated cavity, void fraction and the upstream velocity of the water. Figure 6.7 shows the location of the pressure tappings relative to the throat of the inserts and their associated terms.

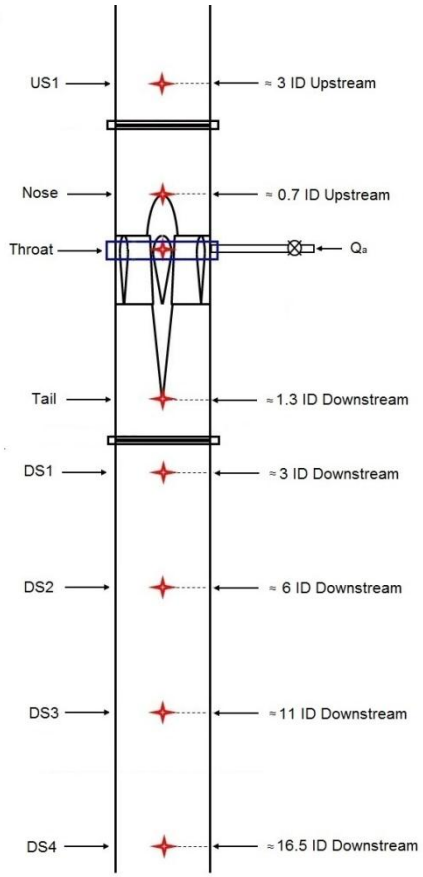

Figure 6.7: - Pressure tapping location along the downcomer and around the insert.

Figure 6.8 shows the pressure profile in the downcomer below the HV1 insert for $U_w \approx 1$, 2 and 3 ms^{-1}. Unfortunately, only 3 data points were possible, due to the number of pressure transducers available within the experimental work. In an ideal scenario more data points would be used, where a pressure tapping location would be approximately every 1 to 2 ID.

Figure 6.8 (a) shows the pressure profiles for the HV1 insert with an upstream water velocity of 1 ms^{-1}. It can be seen that the pressure profile for when no air is flowing follows a straight line, which is also the case in Figures 6.8 (b) and 6.8 (c), when $U_w \approx 2$ and 3 ms^{-1} respectively. When the air flow rate was set to 50 slm at $U_w \approx 1$ ms^{-1}, the ventilated cavity ended 1.2 ID prior to the reference measurement, DS2. Therefore, at the data measurement point, the turbulent mixing region was still present. As a result pressure recovery may have been occurring after the ventilated cavity. This may explain the differential pressure line for Q_a = 50 slm, where the gradient is greater than that for when no air was flowing. Indicating a decreased pressure loss for when Q_a = 50 slm compared to when no air was being injected, by approximately 12.8 %. Lee at al

(2000) suggested that it would be expected for the pressure loss in a two-phase flow to be greater than for when no air was being injected. This is because of the air bubbles in the flow creating increased turbulence and water velocity. As the profile goes past the DS3 data point, the gradient of the line decreases, where there are very similar differential pressures between Q_a = 0 and 50 slm at DS4, where there is only a 2.7 % decrease in pressure loss from Q_a =0 to 50 slm. This is in agreement with Lee et al (2000), where the pressure gradient is less at Q_a = 50 slm, compared to that in Q_a = 0 slm.

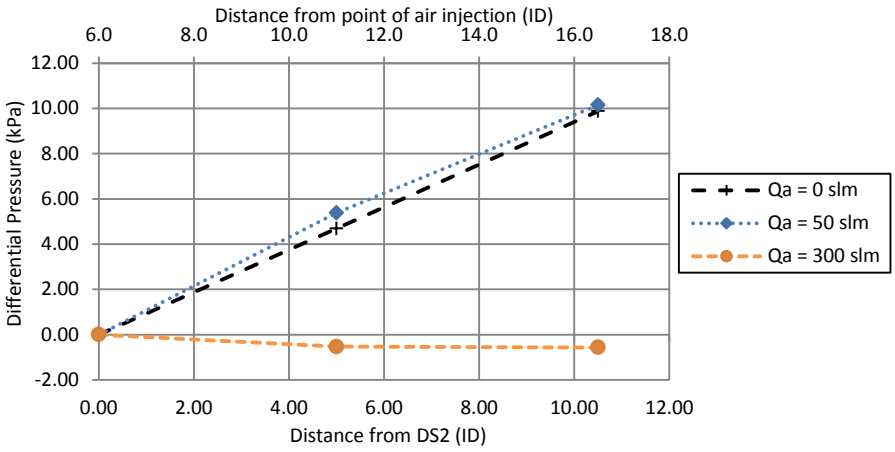

(a)

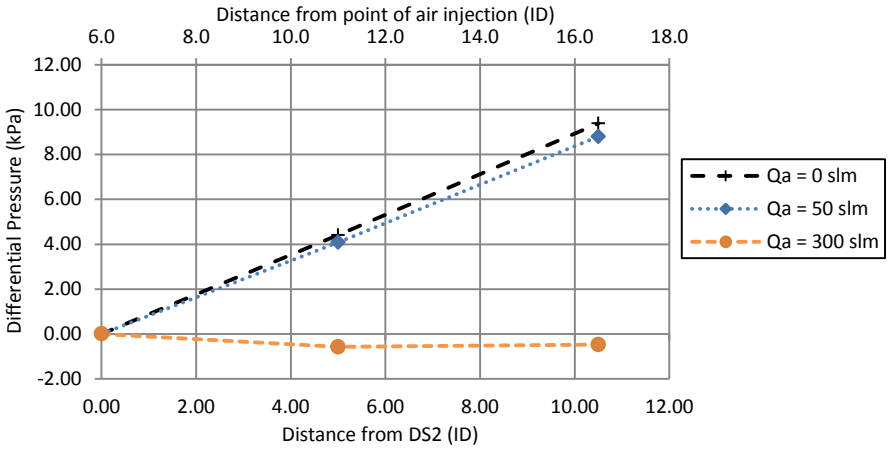

(b)

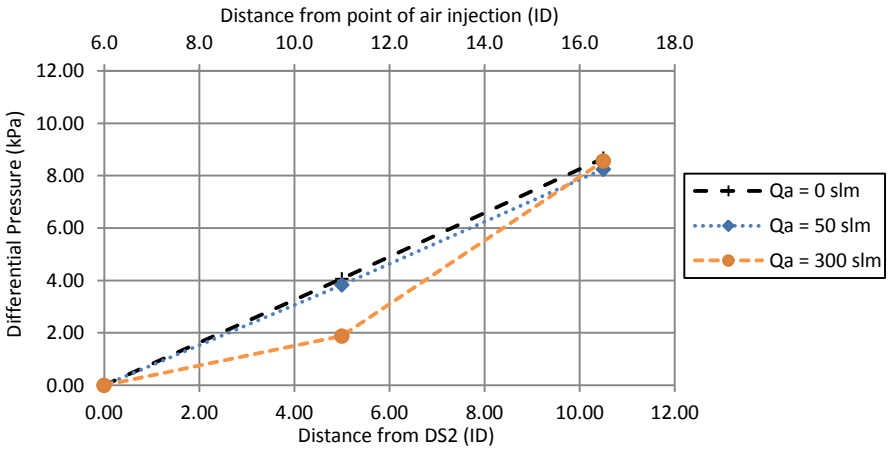

(c)

Figure 6.8: – Pressure Profile along the length of the section of the downcomer, for the HV1 at (a) $U_w \approx 1$ ms^{-1}, (b) $U_w \approx 2$ ms^{-1} and (c) $U_w \approx 3$ ms^{-1}.

A negative pressure differential is observed in Figure 6.8 (a), for the profile of Q_a = 300 slm, where the ventilated cavity length stretches the entire length of the measured profile, which is also shown in Figure 6.8 (b) for a water velocity of $U_w \approx 2$ ms^{-1}. This negative pressure differential at $U_w \approx 1$ and 2 ms^{-1} in the downcomer can be explained by the presence of the ventilated cavity. When the ventilated cavity is present, the density at this point is highly reduced due to the large quantities of air. It is for this reason that Lee et al (2000) considered there to be a constant static pressure along the length of the ventilated cavity. However, under these conditions the accelerated velocity in the liquid film around the ventilated cavity and the frictional losses associated with it must be exceeding the increase in static pressure, due to the reduction in potential energy. As a result a reduction in the static pressure along the length of the downcomer is shown.

It can be seen in Figure 6.8 (b) that for an air flow rate of Q_a = 50 slm, there is a decreased pressure differential when compared to when no air was being entrained. The ventilated cavity at this flow rate setting ended prior to the DS2 pressure measurement location by 3.2 ID, corresponding to a total ventilated cavity length from the point of air injection of 2.8 ID. This decreased pressure differential indicates an increased pressure loss from no air being entrained to an air flow rate of Q_a = 50 slm of 7.6 and 6.7 % at pressure measurements locations DS3 and DS4 respectively. This agrees with the findings of Lee et al (2000), where a two-phase flow was predicted to cause an increased pressure loss, as a result of the dispersed phase increasing the velocity and turbulence in the pipe flow.

Figure 6.8 (c) shows a similar trend as Figure 6.8 (b) for an air flow rate of Q_a = 50 slm. At $U_w \approx 3$ ms^{-1} for an air flow rate Q_a = 50 slm, there was no ventilated cavity present beneath the insert. It is shown in Figure 6.8 (c) that there is a decreased pressure differential of 5.9 and 5.0 % at pressure measurement locations DS3 and DS4 respectively. This indicates an increased pressure loss compared to when no air was flowing. However, the percentage decrease in the pressure loss is less, than it was at $U_w \approx 2$ ms^{-1} for the air flow rate of Q_a = 50 slm, shown in Figure 6.8 (b). This could be attributed to the lower air volumetric void fraction at $U_w \approx 3$ ms^{-1} compared to $U_w \approx 2$ ms^{-1} for the same air flow rate of Q_a = 50 slm. The air volumetric void fractions at $U_w \approx 2$ and 3 ms^{-1} for Q_a = 50 slm are 4.9 and 3.4 % respectively. The decreased volumetric air void fraction would result in a reduced increase in the water velocity.

At $U_w \approx 3$ ms^{-1} for the air flow rate Q_a = 300 slm, the ventilated cavity exceeded the DS3 measured pressure point, where the total length of the ventilated cavity from the air injection point was 12.8 ID. The differential pressure, shown in Figure 6.8 (c) is less than when no air is flowing. However, unlike when the water velocity was 1 and 2 ms^{-1}, Figures 6.8 (a) and (b) respectively, where for these data points the differential pressure was negative. There was an increase in differential pressure at $U_w \approx 3$ ms^{-1} from DS2 to DS3, indicating a change in hydrostatic head despite the presence of a ventilated cavity. This can be explained when considering the change in the liquid film thickness across the length of the ventilated cavity and the frictional losses.

Henstock and Hanratty (1979) provided a correlation for estimating the equilibrium annular film thickness, which is shown in Equation 6.1.

$$\delta\left(\frac{g}{\nu^2}\right)^{\frac{1}{3}} = \left[0.4868\left(\frac{Q_L}{\pi d\nu}\right)^{\frac{5}{2}} + 7.8895\times10^{-8}\left(\frac{Q_L}{\pi d\nu}\right)^{\frac{9}{2}}\right]^{\frac{2}{15}} \quad [6.1]$$

Lee at al (2000) applied a force-momentum balance based on the falling film assumption to determine the falling liquid film area, A_δ, which is shown in Equation 6.1.

$$\int_{A_\delta(z=\infty)}^{A_\delta(z=0)} \frac{dA_\delta}{(gA_\delta^3 - 0.5\pi d C_f Q_L^2)} = \frac{z}{Q_L^2} \quad [6.2]$$

Figure 6.9, shows the predicted liquid film area when calculated using both the Henstock and Hanratty (1979) and Lee et al (2000) correlations. It is shown by the Lee et al (2000) correlation that the flow area decreases quickly, as a result the water film thins and the liquid film is accelerated. The water film thickness eventually settling down to a constant value. The equilibrium film thickness predicted by Equation 6.1 is within 10 % of the stable thickness of the Lee et al (2000) prediction, Equation 6.2, showing good correlation between the two methods. It is shown in Figure 6.9 that the film thickness depends on the inlet boundary condition, such that the stable water film area increases with increasing water velocity. It is also shown that at a slower water velocity, the water film area reduces and achieves a constant closer to the point of air injection.

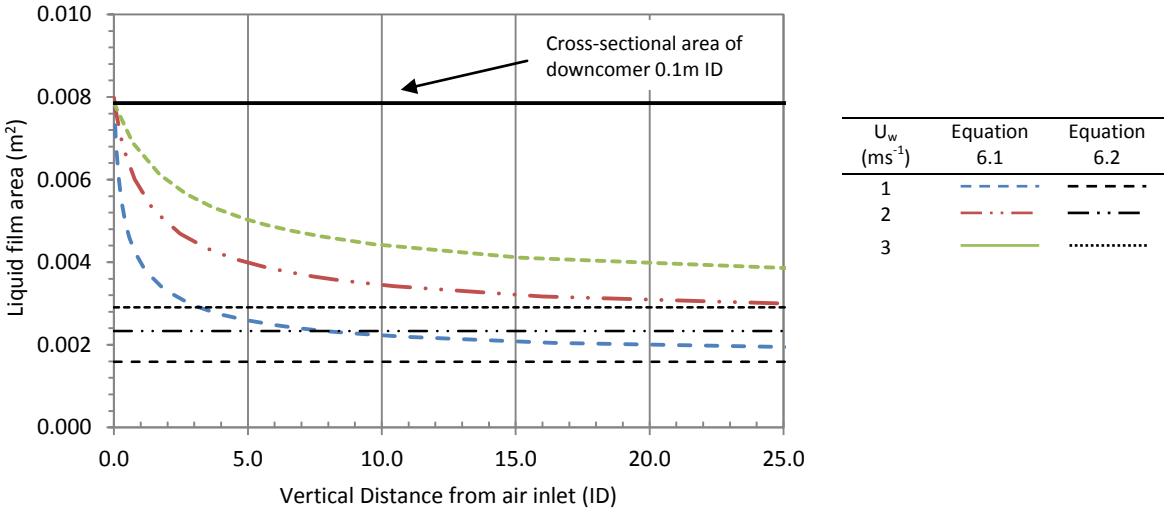

Figure 6.9: – The predicted area of the water falling film around the large ventilated cavity, plotted against the vertical distance from the point of air injection, based on Equations 6.1 and 6.2.

The location of the pressure measurements in the downcomer indicated in Figure 6.8, were 6, 11 and 16.5 ID below the point of air injection and therefore the throat of the inserts.

Figure 6.9 shows that the water film area through the measured pressure locations is approximately double at U_w = 3 ms^{-1} than it is at U_w = 1 ms^{-1}. Therefore, any assumption of a constant hydrostatic head across the length of the ventilated cavity may be invalid, particularly at higher water flow velocities where there is a considerable film thickness. Therefore, the positive pressure differential at U_w = 3 ms^{-1} compared to a fairly

constant pressure differential at U_w = 1 ms^{-1} can be explained, through the increased film thickness when comparing the two water velocities.

For the R_v = 1.5 inserts an approximate relationship can be used for determining the losses associated with a ventilated cavity. Table 6.5 shows the data for the HV1 and V1 inserts, for the test conditions where the ventilated cavity ended between the DS2 and DS4 pressure tapping locations. Due to the ventilated cavity lengths of the A1 and A2 inserts, it was not possible to establish relationships for these inserts because there was either a fully bubbly flow regime or the ventilated cavity lengths were too short be able to provide useful data.

Table 6.5: - Calculation of losses associated with the large ventilated cavity attached to the HV1 and V1 inserts.

Insert	U_w (ms^{-1})	Q_a (slm)	Lc (m)	Losses (m water)	Losses / Lc (m water per unit cavity length)	Average (m water per unit cavity length)	Standard Deviation (%)
HV1							
	≈ 1	50	0.33	0.23	0.71	0.76	5.74
		100	1.02	0.80	0.78		
		150	1.57	1.25	0.79		
	≈ 2	100	0.40	0.26	0.64	0.64	0.00
		150	1.43	0.92	0.64		
	≈ 3	150	0.60	0.24	0.41	0.46	7.51
		200	0.90	0.40	0.45		
		250	1.10	0.54	0.49		
		300	1.24	0.59	0.47		
V1							
	≈ 1	50	0.40	0.28	0.70	0.69	2.05
		100	1.25	0.85	0.68		
	≈ 2	50	0.23	0.16	0.68	0.71	4.98
		100	0.42	0.30	0.70		
		150	0.76	0.54	0.71		
		200	1.32	1.03	0.77		
		250	1.52	1.05	0.69		
	≈ 3	200	0.50	0.22	0.44	0.45	3.37
		250	0.62	0.28	0.45		
		300	0.85	0.40	0.47		

Table 6.5 shows the losses associated with the ventilated cavity, where a ratio of the losses in meters of water, to the ventilated cavity length has been calculated. The calculation of the losses was taken from the throat of the inserts to the DS4 pressure tapping, using the predicted liquid film area based on the Lee et al (2000) calculation and Bernoulli's principle. Table 6.5 shows that for the HV1 insert there is a reducing percentage of the hydrostatic head loss associated with the ventilated cavity from U_w ≈ 1 to 3 ms^{-1}, with 76, 64 and 46 % being lost at U_w ≈ 1, 2 and 3 ms^{-1} respectively. This can be attributed to the reduction in the water falling film area by comparing the change in film area between the three water velocities. The falling film area is approximately 27.5, 42.7 and 56.4 % of that of the open pipe area, at U_w ≈ 1, 2 and 3 ms^{-1} respectively. Therefore, there is a greater expansion of the water film at the base of the ventilated cavity at the lower water flow velocities, representative of a sudden expansion. This greater expansion will cause a greater pressure loss, which can be seen when comparing expansion pressure loss factors, Λ_e as proposed

by Miller (1971), shown in Table 6.6. The data in this table is interpolated from plots by Miller (1971), where the area ratio was plotted against pressure loss coefficient for when water was flowing out of a sudden expansion. The data shows an increase in the Λ_e for a decreasing area ratio. The area ratio is taken as the water film area over the open pipe area. Therefore, a reduced area ratio corresponds to a decreasing water film thickness and an increased pressure loss, which in this experimental work corresponds to the lower upstream water velocities.

Table 6.6: – Pressure Loss coefficients for a sudden expansions interpolated from Miller (1971).

U_w (ms^{-1})	A_{film}/A_{pipe}	Λ_e
≈ 1	≈ 27.5 %	0.58
≈ 2	≈ 42.7 %	0.32
≈ 3	≈ 56.4 %	0.18

When comparing the HV1 and V1 inserts downstream pressure loss to ventilated cavity length ratio, the V1 insert has an average loss of 70% across U_w ≈ 1 and 2 ms^{-1}. However, there is a decreases in the ratio for the HV1 insert between U_w ≈ 1 and 2 ms^{-1} from 76 to 64%. The difference in the pressure loss ratio between the V1 and HV1 inserts at U_w ≈ 1 and 2 ms^{-1} can be attributed to the coalescence behaviour of the individual air streams. Lee et al (1997) identified using a peripheral sparger that significant increases in the length of the ventilated cavity occurred at higher air flow rates, for a small increase in the air flow rate. It was believed that the reason for this was that the individual streams of air from the individual air orifices were coalescing causing a larger bubble. This phenomenon occurred for the HV1 insert at U_w ≈ 2 ms^{-1} between Q_a = 100 and 150 slm, where the ventilated cavity length increased from 0.4 to 1.43 m, corresponding to 4 to 14.3 ID. Whereas for the same operating conditions the V1 insert, there was an increase from 0.42 to 0.72 m, corresponding to 4.2 to 7.2 ID. Having a single large bubble, rather than individual streaks may impact the level of pressure loss across the length of the ventilated cavity. Further investigation would be needed to assess the changes in the geometry of the ventilated cavity and how these changes are affected by the air flow rate, as well as the number of air orifices. There is however, a comparable ratio between HV1 and V1 inserts at U_w ≈ 3 ms^{-1}, where the pressure loss ratio was approximately 45 %. At the water flow rate of U_w ≈ 3 ms^{-1} there is a steady increase in the ventilated cavity lengths for the increasing air flow rates, as shown in Table 6.5.

6.5. Correlation of specific power consumption and bubble size

There are several published correlations in the literature relating the specific power with d_{32}, which are usually in the form of Equation 6.3 (Sotiriadis, 2005). When considering the E it is also important to consider how it relates to the flow regime and the Sauter mean bubble diameter, d_{32}, so that the optimum flow regime, bubble size and therefore the maximum interfacial area for efficient mass transfer can be achieved.

$$d_{32} = C_1(E)^n \quad [6.3]$$

The variation in Sauter mean bubble diameter versus specific power for all inserts were distinguished by the two flow regimes, one with a ventilated cavity present, termed cavity, and the other with no ventilated

cavity present in the downcomer, termed bubbly, were investigated

Figure 6.10, displays the specific power consumption against Sauter mean bubble diameter distinguished by the flow regime present in this experimental work. A strong correlation is shown in Figure 6.10 for when a fully developed bubbly flow existed in the downcomer pipe. Using Equation 6.3, expressions were determined for the two flow regimes, Equations 6.4 and 6.5, which are shown in Table 6.7. When a bubbly flow existed in the downcomer a strong correlation was identified with a R^2 value of 0.99. It can be seen in Figure 6.10 that as the specific power increased the Sauter mean bubble diameter decreased.

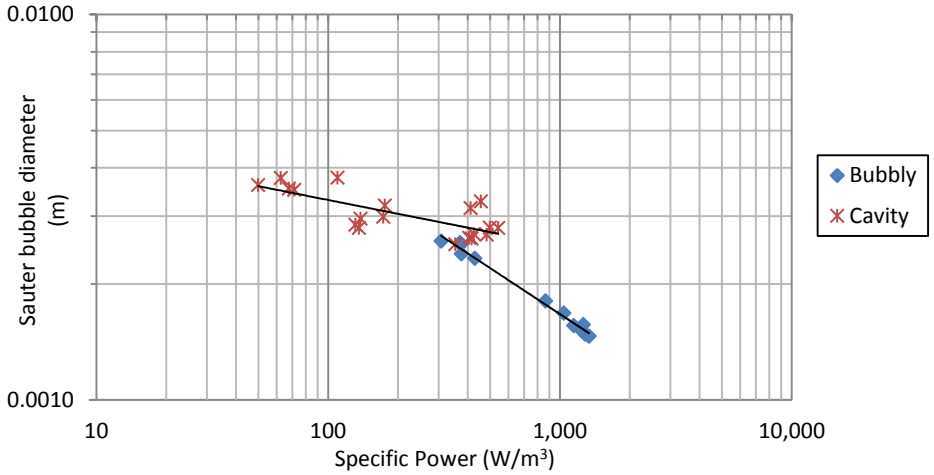

Figure 6.10: - Sauter mean bubble diameter versus specific power consumption for when a ventilated cavity was present and when no ventilated cavity was present.

Table 6.7: – Equations for predicting Sauter mean bubble diameter based on specific power consumption for bubbly and ventilated cavity flow regime using the data from this experimental work.

Flow regime	Expression	Correlation coefficient (R^2)	
Fully Bubbly	$d_{32} = 0.0257(E)^{-0.396}$	0.9901	[6.4]
Ventilated cavity Present	$d_{32} = 0.0057(E)^{-0.119}$	0.564	[6.5]

The order of magnitude of the index of the bubbly flow, n = -0.396, is in good agreement with the literature. Hinze (1955) from turbulence theory deduced that bubble breakage, scales with n = -0.4. A widely accepted empirical correlation presented by Calderbank (1958), shown in Equation 6.6, was developed for a six bladed disk turbine in a baffled tank, where an index of -0.4 is present. This equation was also recommended by Joshi and Sharma (1979) for diffused air systems.

$$d_{32} = 4.15 \frac{\sigma^{0.6}}{\left(\frac{P}{V_{L1}}\right)^{0.4} \rho_L^{0.2}} \sqrt{\varepsilon_G} + 9 \times 10^{-4} \qquad [6.6]$$

where $\left(\frac{P}{V_{L1}}\right)$ is the specific power consumption, E.

Table 6.7 shows that the index of the flow when a ventilated cavity was present in the downcomer, is significantly less than that when the downcomer was bubbly throughout its length. Figure 6.10 also shows a

high level of scatter for when a ventilated cavity was present, with a R^2 value of 0.564. Sotiriadis (2005) found in his experimental work that an index of n = -0.21, gave a good approximation for predicting bubble size with a horizontal sparger. However, measurements were only taken over a limited range of operating conditions, also all the operating conditions tested in the work by Sotiriadis (2005) had a ventilated cavity length of less than 1 ID, where the downcomer was of ID = 105 mm. The lowering of the index suggests that the effect of turbulence on the bubble formation characteristics, such as bubble breakage, may have been reduced by the presence of a ventilated cavity and also the bubble size may have been influenced by coalescence. Therefore, if a ventilated cavity is present in the downcomer, using the data from this experimental work, bubble breakage, scales with n = -0.119.

It can be seen in Chapter 5 with the results from this study that increasing the air flow rate for a constant water flow rate, when a ventilated cavity was present increases the bubble size. This allows for the scatter in Figure 6.10 and the low correlation coefficient of Equation 6.5 because void fraction is not taken into consideration in this form of equation. Despite this there is still an overall relationship that as the specific power is increased the Sauter mean bubble diameter is decreased.

Using the Calderbank (1958) correlation, Equation 6.6, as a basis to develop a correlation that relates the indices from this experimental work (n = -0.396) and the affect of void fraction. Equation 6.6 can be modified to give Equation 6.7,

$$d_{32} = C_2 \frac{\sigma^{0.6}}{\left(\frac{P}{V_{L1}}\right)^{0.396} \rho_L^{0.2}} \sqrt{\varepsilon_G} + C_3 \qquad [6.7]$$

where C_2 and C_3 are empirical constants determined from the data in this experimental work.

The resulting expression which is determined, Equation 6.8, has a standard deviation of < 5 % and a R^2 value of 1, when compared to the experimental data in this study. The experimental data and the results for the Equation 6.8 are shown in Figure 6.11, with a direct comparison of Equation 6.8 against the experimental data being shown in Figure 6.12, where ± 10 % variation lines are also indicated.

$$d_{32} = 0.1098 \frac{\sigma^{0.6}}{\left(\frac{P}{V_{L1}}\right)^{0.396} \rho_L^{0.2}} \sqrt{\varepsilon_G} + 0.002278 \qquad [6.8]$$

(This space is intentionally blank)

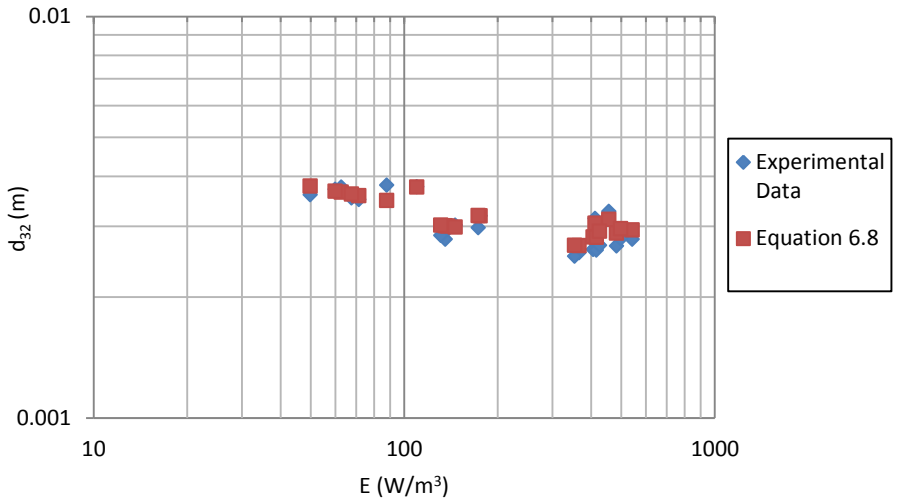

Figure 6.11: - Sauter mean bubble diameter versus specific power consumption for when a ventilated cavity was present, using a modified form of the Calderbank (1958) equation, Equation 6.8.

Equation 6.8 validates the experimental work by showing that the Sauter mean bubble diameter increased with increasing void fraction. Equation 6.8 also suggests a minimum achievable Sauter mean bubble diameter of 2.28 mm, from the empirical constant C_3. The actual minimum achieved in this experimental work with a ventilated cavity present was 2.53 mm, for the HV3 insert at $U_w \approx 3$ ms^{-1} and $Q_a = 50$ slm. The variation in these values in this is due to the range of water velocities tested in this experimental work, a further increase in U_w would result in the predicted minimum Sauter mean bubble diameter being achieved.

The minimum Sauter mean bubble diameter achieved with no ventilated cavity present in the downcomer in this experimental work was 1.26 mm, for the A2 insert at $U_w \approx 3$ ms^{-1} and $Q_a = 300$ slm. Therefore, the interfacial area for mass transfer during a fully developed bubbly flow in the downcomer would be smaller than when a ventilated cavity was present, improving the mass transfer characteristics of the system.

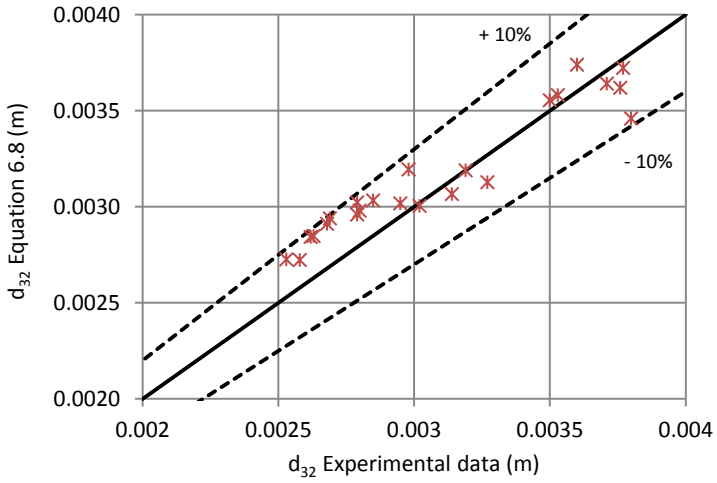

Figure 6.12: - A comparison of the physical Sauter Mean bubble diameter when a ventilated cavity was compared to a modified form of the Calderbank (1958) equation, Equation 6.8.

The bubble sizes were only measured at a fixed point as far down the downcomer as was physically possible in the experimental set up. This location was chosen as it would provide the greatest amount of

photographs possible across the range of inserts and flow rate settings, where the flow regime was a representative of a bubbly flow. In Ohkawa et al (1987), Mao et al (1993) and Evans and Machniewski (1999) the flow beneath a ventilated cavity was assumed to be representative of a plug flow, where after the wake of a ventilated cavity, bubble breakage or coalescence was considered to be negligible. This assumption can be used in this experimental work. This is because despite the various lengths of ventilated cavity and the range in pressures at the point of measurement, shown in Figure 6.13. The generated Sauter mean bubble diameters were within 8 % of each other for the different inserts, under the same operating conditions, when a ventilated cavity was present in the downcomer, as shown Chapter 5, Table 5.2.

The average static pressure at DS4, the location of the bubble measurements, as well as the overall range for all operating conditions is shown in Figure 6.13 for the HV1, V1, A1 and A2 inserts. Despite the pressure range variations of between 4 and 10 %, with ventilated cavity lengths varying between 0.1 and 1.3 m, corresponding to 1 and 13 ID, when the bubbles were measured, variations in the Sauter mean bubble diameter values were small for the same operating conditions, less than 8 %.

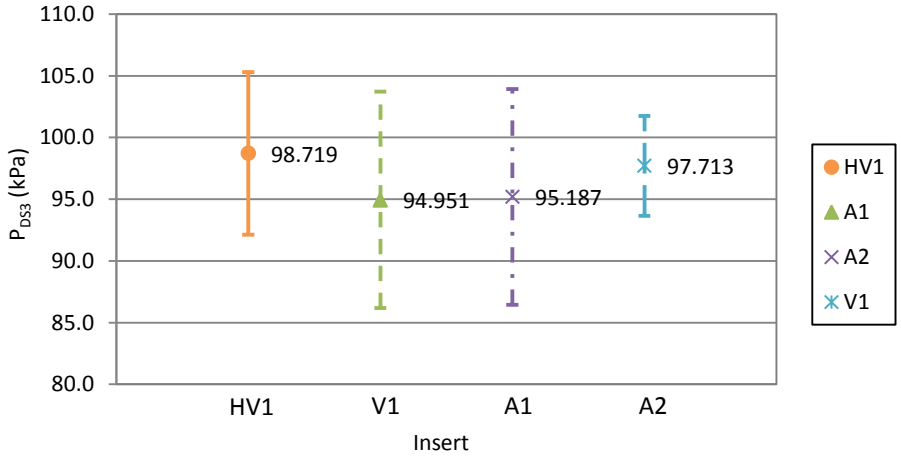

Figure 6.13: - Pressure range at the point of bubble measurements when a ventilated cavity was present for HV1, V1, A1 and A2 inserts.

When considering the same operating conditions, for example $U_w \approx 1$ ms^{-1} and $Q_a = 50$ slm across the inserts there are small changes in d_{32} for the variations in measured static pressure at the point of bubble measurement.

Table 6.8: - Sauter mean bubble diameter, static pressure, ventilated cavity length and mass transfer coefficient for all inserts with a ventilated cavity present in the downcomer at $U_w \approx 1$ ms^{-1}, $Q_a = 50$ slm.

Insert	d_{32} (mm)	P_{DS4} (Pa)	L_c (m)	$k_L a_{20}$ (hr^{-1})
HV1	3.76	-3583	0.48	8.316
HV2	3.50	-3643	0.58	8.208
HV3	3.71	-3514	0.50	7.596
V1	3.60	-4494	0.45	6.264
A1	3.53	-4552	0.32	10.116
Average	3.62	-3957	0.47	8.100
Standard deviation (%)	3.11	13.11	20.34	17.18

Table 6.8 shows that there is no distinct relationship between d_{32}, static pressure and ventilated cavity

length. For example, the smallest d_{32} does not correlate with the highest static pressure and therefore does not conform to the ideal gas law, Equation 6.1. The HV2 and A1 inserts have a similar d_{32} for a pressure change of approximately 1 kPa. However, the A1 insert has a greater bubbly flow length and overall mass transfer coefficient. It therefore could be assumed that the greater mass transfer rate from the bubbles during the A1 experimental could caused the reduced bubble size, which may account for the constant bubble size despite the 1 kPa change in static pressure.

6.6. Comparisons with the literature

The prediction of the Sauter mean bubble size is a valued parameter because it enables the possibility to determine an inserts potential for mass transfer, through the creation of a high interfacial area. Several methods that are found in the literature for predicting the Sauter mean bubble diameter or maximum bubble size and are outlined in this section. These methods are then compared with the determined expressions for this experimental work, Equations 6.4 and 6.8.

The Sauter bubble diameter results for when a ventilated cavity was present in the downcomer are compared in Figure 6.14 with the empirical correlation of Calderbank (1958), Equation 6.6, and the determined equation for this experimental work, Equation 6.8. The results show that Calderbank (1958) over estimates the Sauter mean bubble diameter for the equivalent specific power consumption. This shows that the inserts used in this experimental work are more efficient than the six bladed disk turbine used in the work by Calderbank (1958), in terms of generating a smaller Sauter mean bubble diameter.

Sotiriadis (2005) however, showed good agreement within 20 % of the Calderbank expression. This shows that the designs of spargers used in the experimental work by Sotiriadis (2005) are less efficient that the aerators used in this work. Therefore, compared to the aerators used by Calderbank (1958) and Sotiriadis (2005), the inserts used in this experimental work have the potential to generate a smaller mean bubble size and therefore a greater interfacial area for mass transfer for the same specific power consumption.

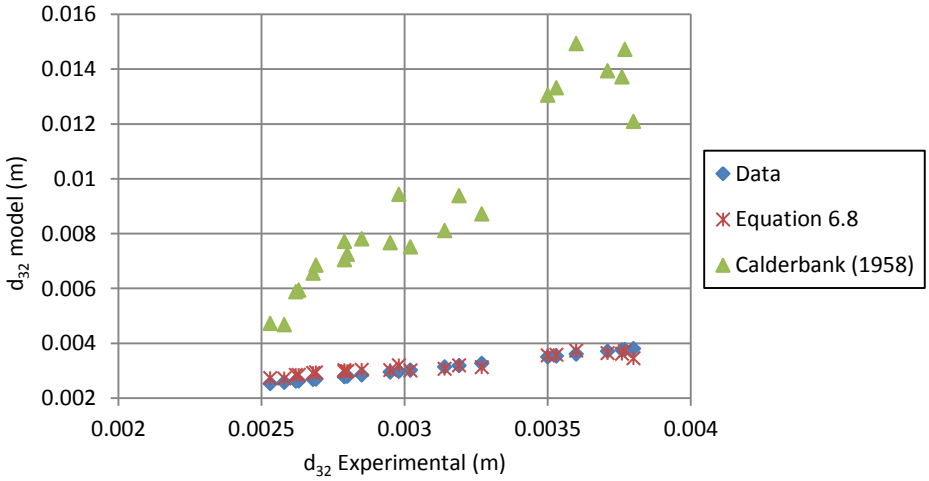

Figure 6.14: - Comparison between measured and the predicted Sauter mean bubble diameters for when a ventilated cavity was present using the Calderbank (1958) correlation and Equation 6.8.

There is a great deal of literature devoted to determining and modelling the breakage rate of bubbles and droplets in turbulent two-phase flows. Much of the published work is based on Hinze (1955), and Sevik and Park (1973), who expanded upon the work of Hinze (1955), for air bubbles in turbulent water jets. The aim of the work by Sevik and Park (1973) was to develop a critical Weber number, We_{crit}, for a bubble for which beyond this value, bubble breakage occurs. Bubble breakage occurs when the local shear forces exerted by the surrounding fluid are greater than the cohesive forces, the surface tension. The non-dimensional critical Weber number, Equation 6.9, is defined by the ratio of shear forces created by turbulent fluctuations, eddies and superficial forces, and is used to characterise bubble breakage.

$$We_{crit} = \frac{\rho_L \langle u'^2 \rangle d_{max}}{\sigma} \qquad [6.9]$$

Hinze (1955) developed a model based on the breakage of a droplet or bubble in viscous shear flow of which a critical Weber number of 1.18 was established. Sevik and Park (1973) developed the Hinze (1955) model using the hypothesis that a bubble would oscillate violently and break up when the characteristic frequency of the turbulence was equal to one of the resonant frequencies of the bubble. From their work by Sevik and Park (1973) produced a critical Weber number of 1.24. However, Lewis and Davidson (1982) found that at a critical Weber number of 4.7, a cylindrical bubble became unstable in an axisymmetric inviscid shear flow. The difference between the values can be attributed to the method of calculation. Typically values quoted of around 1.2 for a critical Weber number are derived from breakage models based on energy dissipation rate. This is in comparison to values of around 4.7, where the critical Weber number is calculated using the velocity profile within the turbulent mixing region beneath the ventilated cavity (Sotiriadis, 2005).

Three different theoretical approaches are found in the literature for predicting the bubble diameter in a bubbly flow beneath a ventilated cavity, in a pipe based on the concept of a critical Weber number. These are outlined below.

The ability to predict the bubble size within a flow will provide an indication for the potential rate of mass transfer, by using the predicted bubble diameter to estimate the interfacial area. Hesketh et al (1987) based their work on the Levich (1962) Weber number expression. Levich (1962) considered the balance of the internal pressure of the bubble with the capillary pressure of the deformed bubble. Levich (1962) hypothesized that a deformed bubble would break up when the internal pressure force overcomes the surface tension force. He obtained the following expression for the critical Weber number,

$$We_{crit} = \frac{\rho_L \langle u'^2 \rangle d_{max}}{\sigma} \left(\frac{\rho_G}{\rho_L}\right)^{1/3} \qquad [6.10]$$

Hesketh et al (1987) calculated $\langle u'^2 \rangle$ from the Kolmogoroff energy distribution law, Equation 6.11, and derived an expression for d_{max} in horizontal fully developed pipe flows, Equation 6.12. Batchelor (1951) found the empirical constant C_1 to be approximately 2.0.

$$\langle u'^2 \rangle = C_1 \left(\frac{e'_{vol} d}{\rho}\right)^{2/3} \qquad [6.11]$$

$$d_{max} = \left(\frac{We_{crit}\sigma}{2}\right)^{0.6} \frac{1}{\left({\rho_L}^2 \rho_G\right)^{0.2}} e_{mass}^{'-0.4} \quad [6.12]$$

where the energy dissipation rate per unit mass defined by Hesketh et al (1987) is defined as,

$$e_{mass}^{'} = \frac{2f{j_L}^3}{D} \quad [6.13]$$

It would be expected that this model would have significant deviations compared to the bubbles measured in this study because the Hesketh et al (1987) model was developed on a horizontal fully developed flow, with measurements taken 220 ID downstream of the air injection point. This is in comparison to this study where the flow was vertically downwards and bubble measurements were taken 15 ID below the air entry point.

Therefore, to check the applicability of Hesketh's model to this experimental work, an alternative definition for the energy dissipation was required, which would account for the difference in geometry and orientation, with the aim to give accurate predictions.

The energy dissipation rate that determines the maximum bubble size in the mixing zone can be found by considering what happens to the entrained air. Initially all of the entrained air enters the mixing zone at the base of the ventilated cavity, the equivalent to the plunge point of a plunging liquid jet. The high energy dissipation in this region results in the generation of a number of very fine bubbles, which are carried downward by the bulk water flow and leave the mixing zone (Evans, et al., 1992). However, a number of larger bubbles are also generated, which re-circulate within the mixing zone, where they are eventually broken up and carried downward by the bulk water flow. Evans et al (1992) showed that the residence time of the larger bubbles in the mixing zone is of the order of 1 s. This length of time is considered by Evans et al (1992) to allow a sufficient number of breakages to occur so that an equilibrium stable bubble size is reached.

According to Hinze (1955), if the flow field is not too homogeneous, the powerful diffusive action of turbulence causes the average size of the largest bubble in the whole field to correspond to the average energy dissipation rate across the field. Therefore, an averaged calculation for the energy dissipation rate across the mixing zone volume at the base of a ventilated cavity would be the most appropriate way to define the energy dissipation rate per unit mass. This can be done by converting the inlet water flow rates for each of the inserts to energy dissipation rates, as shown in Equations 6.14 and 6.15.

$$e_{mass}^{'} = \frac{P_j}{\rho_L L_w A} \quad [6.14]$$

$$P_j = Q_L \rho_L \frac{U_j^2 - j_L^2}{2} \quad [6.15]$$

where the power of the jet, P_j, which is representative of the annular water falling film around the ventilated cavity, is taken from the base of the ventilated cavity. L_w is the length of the recirculation region below the ventilated cavity, which was identified as 2 ID in this experimental work.

Equation 6.14 calculates the energy dissipation per unit mass for the volume of the turbulent wake region beneath the ventilated cavity. Equation 6.15 calculates the power of the liquid falling film or the jet, based on Bernoulli's principle by comparing the open area kinetic energy to the kinetic energy of the liquid falling film. As well as making the assumption that that pressure change across the mixing zone is negligible. Evans (1990) found that the work associated with compressing the air within the mixing zone was less than 1 % of the total work received by the air. Therefore, it is not included in the calculation for determining the energy dissipation per unit mass of the water beneath the ventilated cavity.

Figure 6.15 shows that the model significantly under predicts the maximum stable bubble diameter when using the full range of operating conditions and inserts used in this study, when a ventilated cavity was present. A Weber number for this equation based on the experimental results was calculated to be 14.3 ± 30 %.

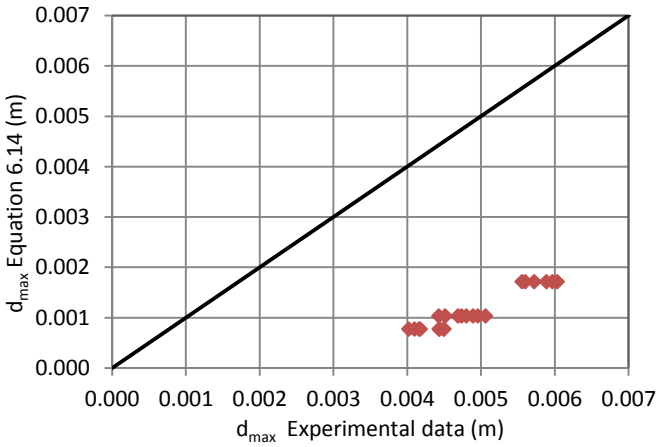

Figure 6.15: - Comparison between the predicted max bubble diameters using the model proposed by Hesketh et al (1987), Equation 6.14, and experimental data in this work, when using a critical Weber number of 1.1.

Evans et al (1992) devised a model for predicting the maximum stable bubble size generated within the mixing zone of a confined plunging liquid jet, CPLJ. They used the Kolmogoroff energy distribution law to calculate $\langle u'^2 \rangle$ and reported a critical Weber number of 1.2. From the experimental work by Evans et al (1992) an expression for the maximum stable bubble diameter was developed,

$$d_{max} = \left(\frac{We_{crit}\sigma}{2}\right)^{0.6} \rho_L^{-0.2} e_{vol}^{'-0.4} \qquad [6.16]$$

$$e_{vol}^{'} = \frac{\rho_L b U_N^3}{2L_W}\left(1 - 2b^2\right) \qquad [6.17]$$

where U_N was the jet velocity at the nozzle exit, representative of the falling film velocity around the ventilated cavity, and *b* is the jet to column area ratio, or for this experimental work the falling film to open pipe area.

The experimental results from Evans et al (1992) were correlated to within 20 % of Equation 6.16, when a critical Weber number of 1.2 was used. In Equation 6.17 the length of the mixing zone was defined as the

point where the wall axial pressure profile became constant with respect to axial distance, which was found to be 3.5 ID in the work conducted by Evans et al (1992).

Figure 6.16 shows that the model proposed by Evans et al (1992) also significantly under predicts the maximum stable bubble diameter across the range of conditions and inserts tested in this experimental work, when a ventilated cavity was present in the downcomer. A Weber number for this equation based on the experimental results was calculated to be 49.4 ± 16 %. When analysing the model, the energy dissipation, when calculated using the Evans et al (1992), is over predicted by approximately 100 times.

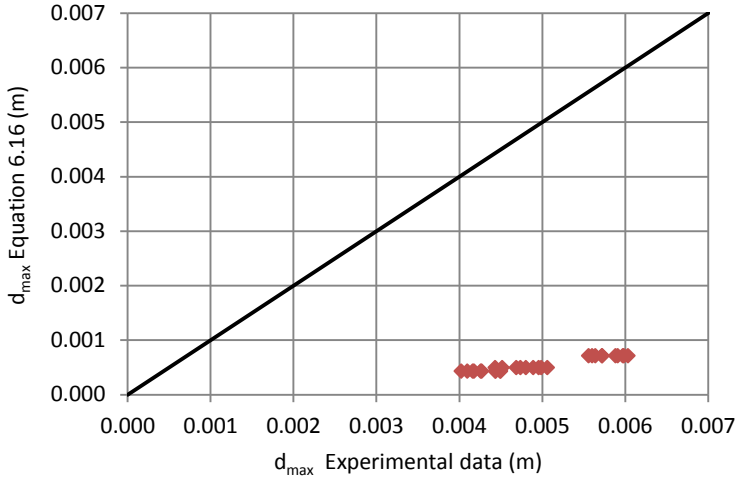

Figure 6.16: - Comparison between the predicted max bubble diameters using the model proposed by Evans et al. (1992), Equation 6.16, and the experimental data in this work, using a critical Weber number of 1.2.

If Equation 6.14 is used instead of Equation 6.17 for calculating the energy dissipation in this experimental work. The resulting predictions form good agreement with the experimental data as shown in Figure 6.17, where the calculated d_{max} is approximately within 20 % of the measured values in this study. Using Equation 6.14, with the correlation proposed by Evans et al (1992), Equation 6.16, a critical Weber number of 1.3 ± 30 % was determined, based on the experimental data from this study, for the maximum bubble diameter. This critical Weber number despite the large variation conforms closely with the typical values for critical Weber number of 1.2 quoted in the literature, such as Hinze (1955), and Sevik and Park (1973) and Evans et al (1992).

(This space is intentionally blank)

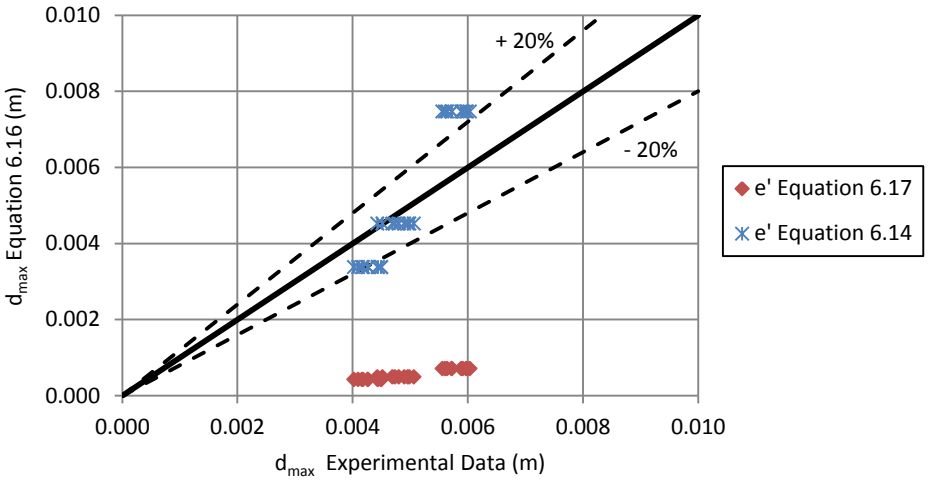

Figure 6.17: - Comparison between the predicted maximum bubble diameters using the model proposed by Evans et al. (1992), Equation 6.16, when using both Equations 6.14 and 6.17 to calculated energy dissipation, and the experimental data in this work, when using a critical Weber number of 1.2.

Thorpe et al (2001) modelled the recirculation region beneath a ventilated cavity as a Hill's Vortex, which is when the vorticity is distributed within a sphere, but the internal symmetry of the flow is however, still annular. Thorpe et al (2001) defined the critical Weber number using Equation 6.18.

$$We_{crit} = \frac{\rho_L \Delta u^2 d_{max}}{\sigma} \qquad [6.18]$$

where Δu^2 is the square of the velocity difference across the diameter of the bubble.

Thorpe et al (2001) found that the prediction of the maximum stable bubble diameter was in good agreement with their experimental data, when a critical Weber number of 4.7 was used. From this, Thorpe et al (2001) determined an equation to estimate d_{max},

$$d_{max} = 3.\sqrt[3]{\frac{We_{crit}\sigma(R-\delta)^4}{128\rho_L(KU_F)^2}\frac{1}{\left(R-\delta-\frac{d_{max}}{2}\right)^2}} \qquad [6.19]$$

In Equation 6.19, K is the proportionality constant given by Equation 6.20 and $U_{Z(max)}$ is the maximum axial velocity inside the vortex beneath a ventilated cavity. In Thorpe et al (2001) a K value of 0.38 was quoted and it was stated in Thorpe et al (2001) that in the literature, typical values for K of 0.4 to 0.55 were found. It was proposed that the axial component was directly proportional to the velocity of the falling film, U_{film}, which plunged at the base of the ventilated cavity, such that,

$$K = \frac{U_{z(max)}}{U_{film}} \qquad [6.20]$$

The model proposed by Thorpe et al (2001) under predicts the maximum stable bubble diameter, when comparing it to the data in this experimental study. However, the model by Thorpe et al (1992) is considerably better than Calderbank (1958), Hesketh et al (1987) and Evans et al (1992). The Thorpe et al (2001) model was based on data from a horizontal and central sparger, shown in Figure 2.11, and was deemed not to be applicable for a plunging jet sparger, shown in Figure 2.11, in the work by Sotiriadis

(2005). The horizontal and central spargers are a significantly different system, in comparison to the inserts in this experimental work, where no significant channelling and constriction of the flow occurs. However, the plunging jet sparger closely resembles the V1 insert, although it does not consist of a steady divergent section. The plunging jet sparger also has a resemblance to the HV, A1 and A2 inserts, as it channels the flow into a constriction, although not into a number of discrete channels.

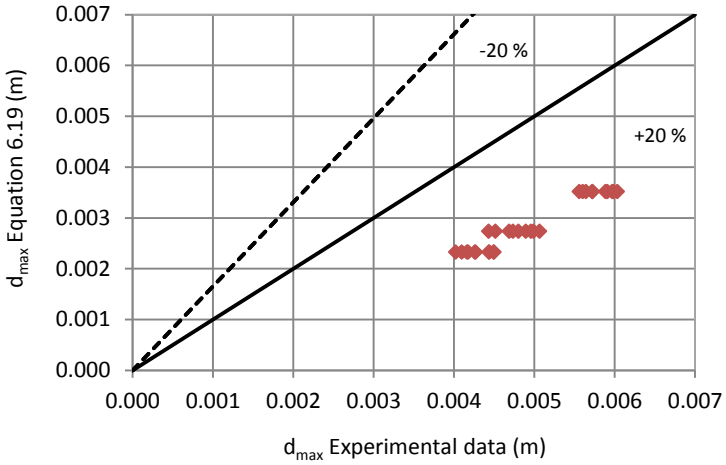

Figure 6.18: - A comparison between the predicted maximum bubble diameters using the model proposed by Thorpe (2001), Equation 6.19 and the data from this experimental work, when a critical Weber number of 4.7 is used.

The conclusion, this section shows that the models found in the literature for predicting bubble size, Hesketh at al (1987), Evans et al (1992) and Thorpe et al (2001) all significantly under predict the resulting bubble size significantly. Despite the closer conformity of the modified Evans at al (1992) correlation method, using Equation 6.14 to calculate the energy dissipation, compared to the others. It can be seen due to the wide scatter of the correlations that the geometry of the aerator used in a contained flow, when a ventilated cavity is present has a significant effect on the formed bubbles in the downcomer.

6.7. Summary

Despite the qualities of the A2 insert in terms of generated bubble size and distribution, its significantly higher specific power consumption, particularly at higher liquid flow rates, where it was regularly three times the power consumption of the R_v = 1.5 inserts. It is expected that it will have low mass transfer efficiencies overall. The V1 insert however, has similar Sauter mean bubble diameters, in comparison to the other R_v = 1.5 inserts, under identical test conditions. However, it typically has up to 20 % less specific power consumption. Therefore it could be expected that the V1 insert would have a higher SAE than all other inserts.

It has also been shown that the upstream velocity of the water has a significant impact on the resulting pressure losses associated with a ventilated cavity. With the higher upstream water velocities having a reduced pressure loss.

CHAPTER 7

MASS TRANSFER TESTING

7.1. Introduction

For the mass transfer section of this experimental work, the overall oxygen transfer coefficient at standard conditions, $k_L a_{20}$, for each of the inserts is calculated over a range of operating conditions, which are identical to those tested during the hydrodynamic efficiency phase of the study. During this section of work the mass transfer testing was conducted in accordance with the procedure outlined by ASCE (2007). In 1977, under the sponsorship of the US Environmental Protection Agency, EPA, a committee organised by the American Society of Civil Engineers, ASCE, conducted a study into the methods for measuring oxygen transfer rates in wastewater treatment. The aim was to propose a method for establishing uniform and repeatable test conditions. As well as estimating clean water parameters from re-aeration data and translating clean water performance to in-process conditions. The result was the publishing of the 1984 version of the ACSE Standard for the measurement of Oxygen transfer in clean water, which was subsequently improved, updated and republished in 1999 and 2007.

The method proposed was an unsteady state method, which is outlined in this chapter and in Appendix B. The process involves the re-aeration of clean water that has previously been depleted of DO. During the unsteady state method a number of steps are followed in order to calculate the $k_L a_{20}$ and the performance characteristics for an experiment.

The first step was to deoxygenate the water to almost a zero concentration of DO through nitrogen sparging. A zero DO concentration was not always achievable in this experimental work, due to time constraints and a limited supply of nitrogen. If a zero DO concentration was not achievable, deoxygenating continued until a stable DO of less than 2 mg/L was present in the water. Nitrogen sparging is used mainly in laboratory experiments because it avoids the use of harmful chemicals, which therefore increases safety (Chawla & Pourhashemi, 2004). The method is also low cost and avoids chemical interference in oxygen determination, (Wang, et al., 1973). Once a stable DO level was reached the nitrogen was then stopped, the nitrogen bubbles were then allowed to rise from the tank and then the airflow was injected into the downcomer. During this re-aeration step, measurements were taken of DO at regular intervals, every 5 s. These measurements were taken at a location in the in-active tank, details on this location and the choosing of it are found in Appendix B.

After the data was collected the Non Linear Regression Analysis, NLRA, technique was used to determine the $k_L a$ and all other performance characteristics. Upon determining the $k_L a$ using the NLRA technique it was converted to standard conditions, $k_L a_{20}$, using methods described by ASCE (2007) and Chapter 3, by

using Equation 3.54.

The NLRA method initially plots a curve of time against DO concentration. The aim of NLRA is to get the best fit of all data points with respect to curve y so that R^2 is as close to 1 as possible. The basic equation for the conducted NLRA is Equation 7.1, where values of the initial and saturation DO concentration were estimated based on the data curve. Equation 7.1 is derived by integrating Equation 3.44, in Chapter 3, and rearranging. The Solver method in MS Excel was utilised so it was possible to gain an accurate value for the slope, $k_L a$ and therefore $k_L a_{20}$. Further details of the calculation are found in Appendix B.

$$DO_{NLRA} = C_\infty - (C_\infty - C_0)e^{-k_L a(t-t_0)} \quad [7.1]$$

Prior to conducting the full experimental programme a series of experiments were undertaken to determine the oxygen transfer from the atmosphere to the water through its surface. This was done by initially sparging the nitrogen into the water and then running the system with no air being entrained. There was no significant change in DO during these experiments. Therefore any transfer from the atmosphere to the system at the water surface can be considered negligible.

To evaluate the $k_L a_{20}$ from the individual DO concentration curves from the experiments, a number of assumptions were made. The evaluation assumed that: -

a) The oxygen transfer coefficient, $k_L a$ was controlled by the liquid phase resistance as shown by Boyle et al (2002) and detailed in Chapter 3.
b) The active liquid tank was well mixed.
c) The system can be divided into two zones, the first zone is considered for active mass transfer, V_{L1} and the second zone, V_{L2}, which included the recirculation loop, is in-active due to the complete separation of the bubbles from the liquid stream in this volume.
d) There was no change in the composition of the air.

When the unsteady state measurement method is used, care is taken to keep the hydrodynamics constant and hence the void fraction independent of time. The air was assumed to establish quickly on admitting it to the system and consequently the aerated volume was considered to be constant with time.

During the experimentation only a single DO probe was used, which could lead to inaccuracies and anomalies if the tank was not fully mixed. For example, a small amount of bypassing within the tank could result in a modification in the measured DO history, which would be reproduced in the fitted $k_L a$ value and subsequently $k_L a_{20}$. Therefore, the quality of the mixing in the tank on the measurements had to be checked. A number of tests were run with the probe in different locations within the in-active tank to show if there is a measureable difference in DO concentration with probe position. There were no significant differences between the response curves and the calculated $k_L a_{20}$ values of the different locations. The $k_L a_{20}$ values were within ± 6 % of each other, as shown in Appendix B.

Chisti (1989) stated that if calculated $k_L a_{20}$ values were within ± 10 % of each other across various locations

within an aeration system, then the system can be assumed to be fully mixed. This assumption was said by Chisti (1981) to be even more pronounced where systems had low $k_L a_{20}$ values of ≤ 0.1 s^{-1} (360 hr^{-1}), as was the case with this study. The surface of the tanks were also seen to be turbulent, therefore the flow systems in the tanks were never quiescent. With this and the presence of the baffles within the aerated volume, acting as crude mixers and a high rate of recirculation of the water volume, the validity of the assumption for a fully mixed system is confirmed.

7.2. Mass transfer coefficients

The $k_L a_{20}$ is an important indicator of how an aerator performs. The results of $k_L a_{20}$ against air flow rate for all the inserts at U_w ≈ 1, 2 and 3 ms^{-1}, are shown in Figure 7.1. It can be seen in Figure 7.1 that the HV inserts performs comparatively with the V1 insert throughout the experimental range, with performance being within ± 20 % for the vast majority of cases. However, as can be seen when comparing the R_v = 1.5 inserts in Figures 7.1 (a), (b) and (c), as the air flow rates are increased, the V1 insert typically outperforms all the HV inserts. There are noticeable transition points where this occurs, for example when Q_a > 200 slm at U_w ≈ 1 and 2 ms^{-1} and for all air flow rates at U_w ≈ 3ms^{-1}.

The A1 and A2 inserts have similar performances to the R_v = 1.5 inserts at U_w ≈ 1 ms^{-1}, as can be seen in Figure 7.1 (a). However, at U_w ≈ 2 ms^{-1} it can be seen in Figure 7.1 (b) that the A2 insert begins to outperform all other inserts, particularly at the mid-range of air flow rates, Q_a = 100 to 250 slm. Then at U_w ≈ 3 ms^{-1}, this trend is exaggerated, with the A2 insert significantly having a higher $k_L a_{20}$ value than the Rv = 1.5 inserts, especially at the higher air flow rates. The A1 insert also follows a similar trend of performance as the A2 insert. This increased performance is especially noticeable at in Figure 7.1 (c) for Qa > 100 slm, which was when the A1 and A2 inserts had a bubbly flow throughout the downcomer, whereas the R_v = 1.5 inserts had a ventilated cavity present.

In Figure 7.1 (a) it can be seen for the majority of the inserts, the $k_L a_{20}$ begins to plateau around the air flow rates of 250 to 300 slm. This is the point at which the ventilated cavity stretched throughout the entire length of the downcomer. This $k_L a_{20}$ profile is in contrast to Figure 7.1 (c), where the relationship between air flow rate and $k_L a_{20}$ for the inserts is fairly linear and still increasing at Q_a = 300 slm. This is because the ventilated cavity at the higher water flow rates did not stretch the entire length of the downcomer, as was discussed in Chapter 5. Therefore, the presence of a ventilated cavity in downcomer cannot only be seen to increase the pressure loss within it, as was identified in Chapter 6, but can also cause a reduction in $k_L a_{20}$, which is emphasised in Figure 7.1 (c). At Q_a = 50 slm in Figure 7.1 (c), there was no ventilated cavity present for the HV1, HV3, A1 and A2 inserts, at these operating conditions the A1 and A2 inserts had an increased $k_L a_{20}$ compared to the other inserts by 10 and 20 % respectively. However, at Q_a = 300 slm there was no ventilated cavity present with the A1 and A2 inserts, but there was with the all other inserts. At this air flow rate, the A1 and A2 inserts had an increased $k_L a_{20}$ compared to the other inserts by approximately 30 and 50 % respectively.

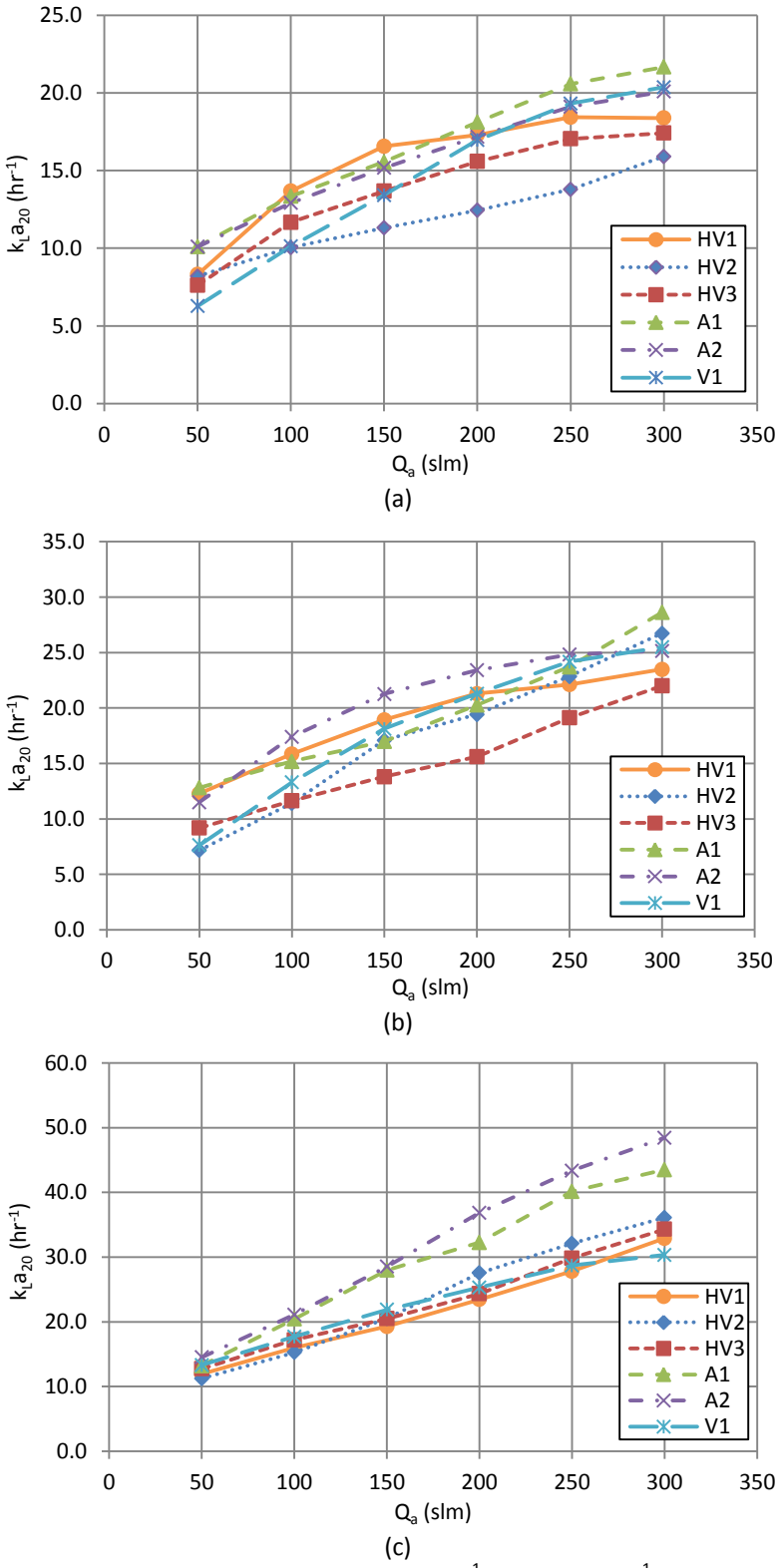

Figure 7.1: – k_La_{20} for all inserts for (a) $U_w \approx 1$ ms^{-1}, (b) $U_w \approx 2$ ms^{-1} and (c) $U_w \approx 3$ ms^{-1}.

When comparing the HV inserts it can be seen in Figure 7.1, that the HV1 insert has the highest k_La_{20} at $U_w \approx 1$ and 2 ms^{-1}. However, at $U_w \approx 3$ ms^{-1}, all the HV inserts have very similar performances within ± 5 %. However, the HV2 insert does have the best performance at the higher air flow rates, Q_a = 200 to 300 slm at $U_w \approx 3$ ms^{-1}. This variation could be caused by the distribution of air from the air orifices, where at the higher

flow rates the pressure profile at the throat, due to the vanes could have an impact on the distribution of the air through the orifices. At the higher flow rates, enhanced negative pressure on the top side of the vanes might cause the air injection in the HV1 insert to be primarily entrained through the orifice on this top side. As a result of the negative pressure, the air could then travel closely down the surface of the vane, minimising its overall distribution. This could be in comparison to the HV2 insert, where the significant negative pressure on the top side of the opposite vane could cause the air to be 'pulled' across the water flow. As a result this would generate a greater and more even distribution of the air in the downcomer, therefore improving mass transfer.

Figure 7.2 shows the air void fraction distribution for $U_w \approx 3$ ms^{-1} at Q_a = 200 slm, for the HV1 and HV2 inserts. There are clear differences in the air distribution between the inserts at the tips of the vanes and just downstream of the insert. The HV1 insert appears to have a very narrow core of air with a distribution of the air in-line with the vanes, whilst the HV2 insert also has this core of air. However, the distribution is much greater across the cross-section of the downcomer, which could result in improved mass transfer.

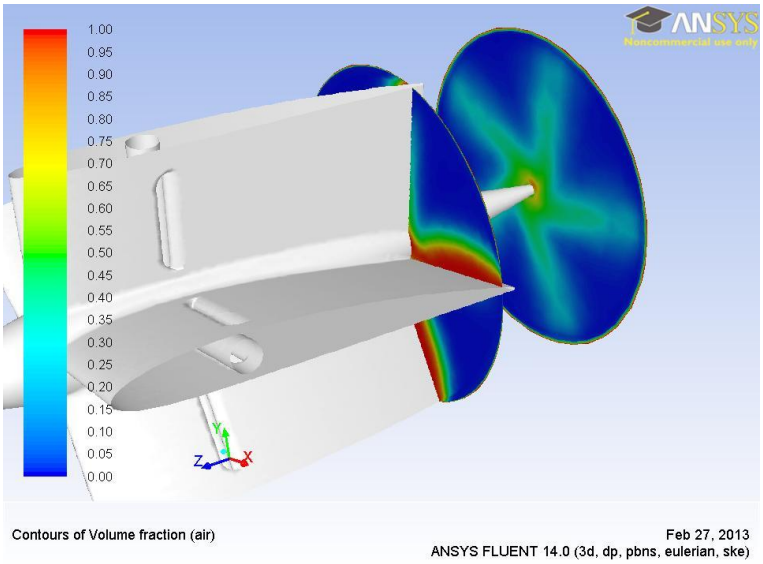

(a)

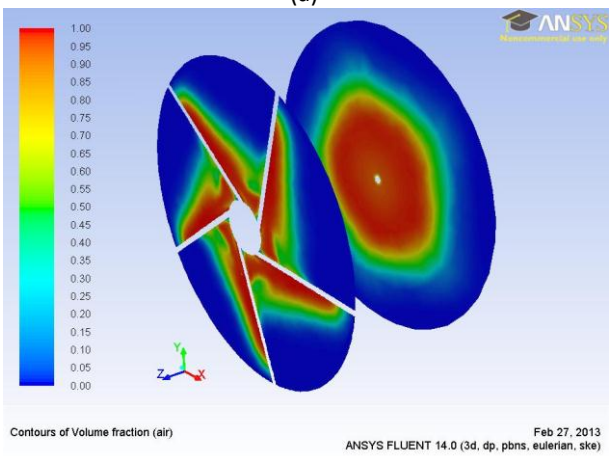

(b)

Figure 7.2: - Air void fraction distribution for the (a) HV1 and (b) HV2 inserts at $U_w \approx 3$ ms^{-1} at Q_a = 200 slm, the planes highlighted are at the vane tips and 0.05m, 0.5 ID, further downstream.

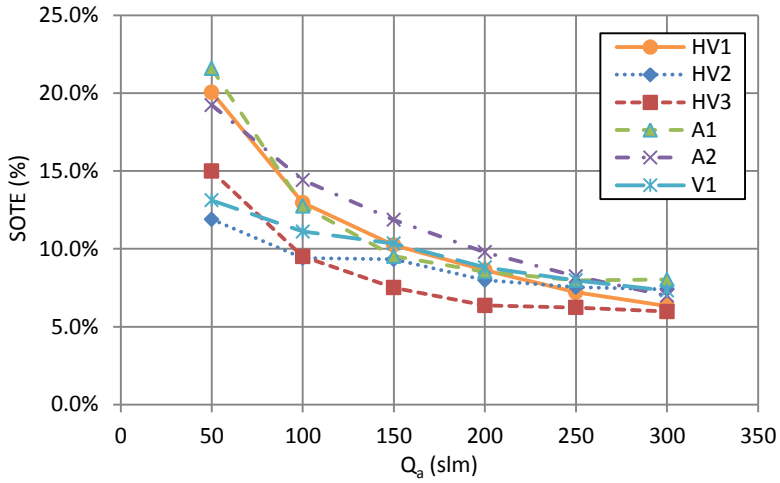

Figure 7.3: – Standard oxygen transfer efficiency against air flow rate for all inserts at $U_w \approx 2$ ms^{-1}.

Plotting SOTE, which is calculated using Equation 3.60, against volumetric air flow rate, Figure 7.3, gives an appreciation for the level of oxygen absorbed as a percentage of what is supplied. Figure 7.3 shows that at the lower air flow rates a higher rate of oxygen is absorbed into the water. Figure 7.3 shows that between Q_a = 100 and 250 slm the A2 insert has the highest SOTE, which coincides with the results for $k_L a_{20}$, shown in Figure 7.1 (b). As well as the bubble size measurements, where below Q_a = 250 slm the flow in the downcomer of the A2 insert was entirely bubbly. However, above 250 slm a ventilated cavity was present in the A2 insert and therefore it had a similar d_{32} as the other inserts, under these operating conditions. This is also the case when comparing the HV1 and V1 insert, where below Q_a = 150 slm at $U_w \approx 2$ ms^{-1} the HV1 Insert had a shorter ventilated cavity length than V1 and therefore outperforms the V1 Insert below an air flow rate of 150 slm, in terms of SOTE and $k_L a_{20}$. Figure 7.3 shows the data for $U_w \approx 2$ ms^{-1} however, similar trends and comparisons between L_c and SOTE are identified for all water flow rates.

7.3. Mass transfer and bubble size

As discussed throughout this experimental work the interfacial area for mass transfer is an important parameter when comparing aerator designs. When comparing bubble size and overall mass transfer coefficient it is possible through this experimental work to develop relationships between d_{32} and therefore interfacial area and $k_L a_{20}$. The basis of the relationships can be determined from the equation for liquid mass transfer coefficient, k_L as described by the penetration theory, Higbie (1935) which is outlined in Chapter 3, where k_L is given by, (Boyle, et al., 2002)

$$k_L = 2\sqrt{\frac{D_L}{\pi t}} \qquad [7.2]$$

where t, is the gas-liquid contact time, or for this study the air-water contact time.

The interfacial area for mass transfer, a, is approximated by, (Boyle, et al., 2002)

$$a = \frac{6\varepsilon_G}{d_{32}} \qquad [7.3]$$

Multiplying Equation 7.2 and 7.3, gives Equation 7.4, which can be used to approximate the $k_L a_{20}$ using the penetration theory.

$$k_L a_{20} = 12.\frac{1}{d_{32}}.\varepsilon_G.\sqrt{\frac{D_L}{\pi t}} \quad [7.4]$$

In this experimental work the air-water contact time can be defined by Equation 7.5 (Calderbank, 1958).

$$t = \frac{L_B}{U_W} \quad [7.5]$$

where L_B is the bubbly flow length.

The assumption has been made that the vast majority of the mass transfer occurs in the downcomer and that mass transfer from a ventilated cavity is negligible. This assumption has been validated by The Newton Group (2011) where they considered that 90 % of the all mass transfer occurred within the first 1.25 m of a bubbly flow in a downcomer. Jackson and Collins (1964) also believed that a high percentage of the mass transfer occurred immediately downstream of a venturi.

Therefore, the equation for $k_L a_{20}$ for this experimental work can be shown as,

$$k_L a_{20} = \frac{12}{\sqrt{\pi}}.\frac{1}{d_{32}}.\varepsilon_G.\frac{1}{\sqrt{\frac{L_B}{U_W}}}.\sqrt{D_L} = C_1.\frac{1}{d_{32}}.\varepsilon_G.\frac{1}{\sqrt{\frac{L_B}{U_W}}}.\sqrt{D_L} \quad [7.6]$$

where C_1 is an empirically derived constant from this experimental work.

Using the experimental data in this study, Equations 7.7 and 7.8 were determined using Equation 7.6 as the basis for their development. Equation 7.6 includes important parameters in mass transfer, such as the bubbly flow residence time, void fraction, the diffusion coefficient of oxygen into water (2.1 x 10^{-9} m^2s^{-1}) and d_{32}. Equations 7.7 and 7.8, shown in Table 7.1 were established for determining $k_L a_{20}$, these equations are distinguished by whether or not a ventilated cavity was present in the downcomer.

Figures 7.4 and 7.5 show how Equations 7.7 and 7.8 compare to the experimental data. It is shown in Figures 7.4 and 7.5 and in Table 7.1 that there is a good correlation between determined equations and the experimental data, where standard deviations of less than 17 % was observed in both cases and R^2 values of 1 and 0.99 were determined for Equations 7.7 and 7.8 respectively.

Table: 7.1: - $k_L a_{20}$ correlations for when there was and was not a ventilated cavity present in the downcomer, using the experimental data for all inserts.

Flow Regime	Correlation	Standard Deviation	
Bubbly	$k_L a_{20} = 1685.2.\frac{1}{d_{32}}.(\varepsilon_G)^{0.3}.\frac{1}{\sqrt{\frac{L_B}{U_W}}}.\sqrt{D_L}$	± 16.5 %	[7.7]
Cavity present	$k_L a_{20} = 1769.3.\frac{1}{d_{32}}.(\varepsilon_G)^{0.3}.\frac{1}{\sqrt{\frac{L_B}{U_W}}}.\sqrt{D_L}$	± 16.7 %	[7.8]

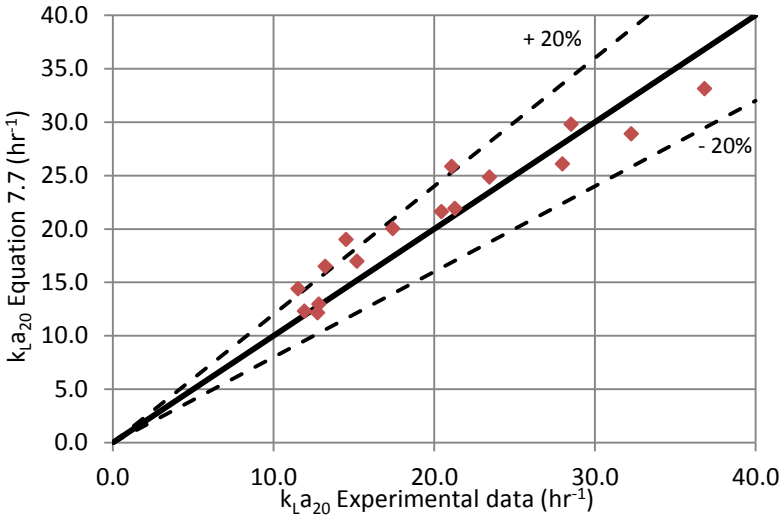

Figure 7.4: - Experimental k_La_{20} against derived k_La_{20} from Equation 7.7 for all inserts under fully bubbly flow regime.

It can be seen when comparing Equations 7.6, with Equations 7.7 and 7.8 that the air void fraction within this experimental set up has a greater impact on k_La_{20}, when compared to the Penetration Theory using the Calderbank (1958) equation for air residence time, Equation 7.5. This is because, in Equations 7.7 and 7.8 air void fraction has an index of n = 0.3, whereas in Equation 7.6 air void fraction has an index of n = 1. This means that for the same air void fraction and under the same operating conditions, Equations 7.7 and 7.8 predicts a higher k_La_{20} than Equation 7.6. This means that for the same air void fraction, there is greater mass transfer in this experimental work than what is predicted using the Penetration Theory. This could be as a result of an increased interfacial area for mass transfer, which would result from a decreased d_{32} for the same void fraction. In Chapter 6, Section 6 the Calderbank (1958) equation, Equation 6.9 was shown to over predict that the Sauter mean bubble diameter for this experimental work.

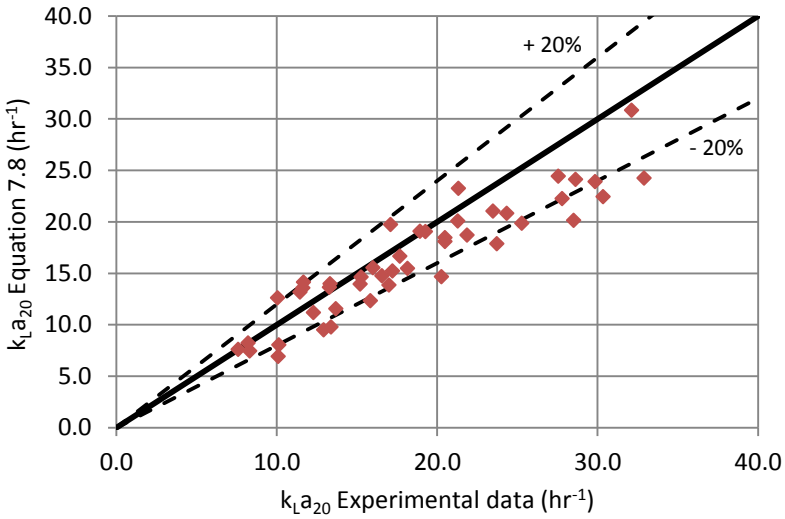

Figure 7.5: - Experimental k_La_{20} against derived k_La_{20} from Equation 7.8 for all inserts under fully bubbly flow regime.

From Chapter 6, it was identified that the experimental Sauter mean bubble diameters from this study were approximately 36 % of the values that were predicted using the Calderbank (1958) equation, Equation 6.9. Therefore, it is not a surprise that the $k_L a_{20}$ equation, Equation 7.6, which was based on the Calderbank (1958) equation for the air-water contact time, Equation 7.5, would under predict the $k_L a_{20}$ by over a third based on the indices of the air void fraction. Also Equation 7.3 shows that if the d_{32} is a third, then the interfacial area for mass transfer will be three times the size for the same air void fraction, hence vastly improving the potential for oxygen transfer. Therefore, the Calderbank (1958) equations for Sauter mean bubble diameter, Equation 6.9, in conjunction with the Penetration theory, Higbie (1935), Equations 7.2 and 7.5, gave a good first approximation for determining correlations for aerators. However, adaption was required to determine accurate design correlations for the inserts used in this experimental work.

7.4. Standard Aeration Efficiency, SAE

The measure of performance which can be used to directly compare various aerators is SAE, is calculated using Equation 3.57. SAE combines the SOTR, Equation 3.56, and the specific power consumption, E, for the total aerated volume, Equation 3.3. The SAE for this experimental data is presented in Figure 7.6.

It can be seen in Figure 7.6 that for the lower water and air flow rates, the HV1 and A1 inserts surpass the V1 insert. However, as the flow rates increase the V1 insert surpasses the others as the most efficient insert. The transition air flow rates for this are identified in Table 7.2.

Table 7.2: - Operational change over points for V1 insert, where it then outperforms all other inserts.

U_w (ms^{-1})	Q_a (slm)
1	> 150
2	100 - 150
3	All

In Figure 7.6 (a) it can be seen that there is a steadily decreasing SAE for all inserts, as the air flow rate is increased. This is because of a number of issues, for example, at the lower velocities a ventilated cavity is present and therefore as the air flow rate is increased there is a decrease in the bubbly flow length within the downcomer. The presence of a ventilated cavity in the downcomer has been shown in Chapter 6 to cause an increased power consumption, which would negatively impact the SAE values. Also when there was a ventilated cavity present, there is an increase in bubble size with increasing air flow rate, as shown in Chapter 5. Thus reducing the interfacial area and therefore the potential for mass transfer. The levelling off or slight increases in the SAE at air flow rates greater than 200 slm can be attributed to the ventilated cavity stretching the entire length of the downcomer. It is under these conditions where a similar pressure drop occurs for a constant water flow rate, despite any further increase in air flow rate.

(This space is intentionally blank)

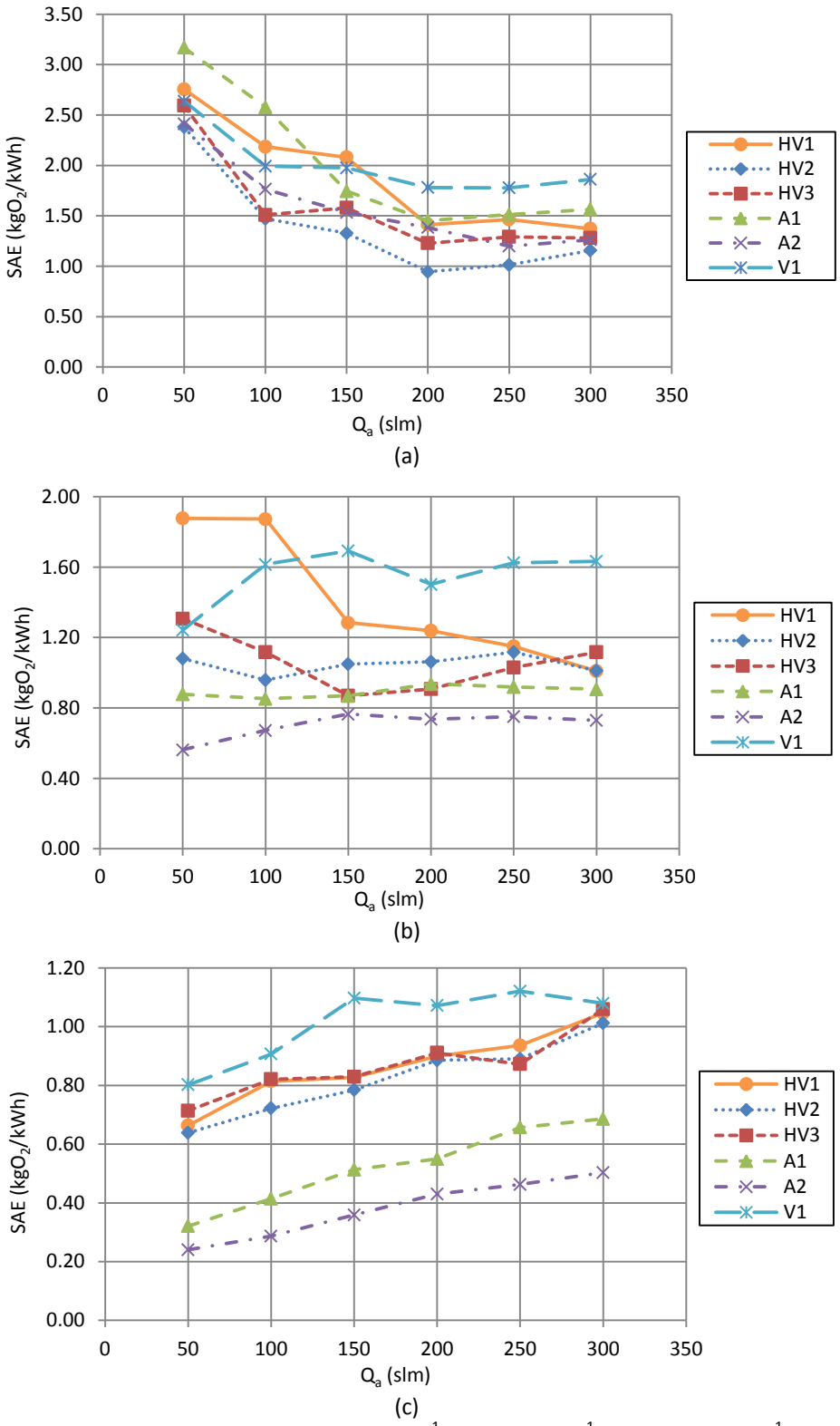

Figure 7.6: – Air flow rate against SAE for (a) $U_w \approx 1$ ms^{-1}, (b) $U_w \approx 2$ ms^{-1} and (c) $U_w \approx 3$ ms^{-1} for all inserts.

At $U_w \approx 2$ ms^{-1}, Figure 7.6 (b), most of the inserts maintain a fairly stable SAE, within ± 0.15 kgO_2/kWh of their respective average values, for all air flow rates or for Q_a > 100 slm. However, Figure 7.6 (b) shows that the V1 insert has a rise in SAE up to Q_a = 100 slm, the SAE profile then achieves a constant average value of 1.62 kgO_2/kWh ± 3 %. This is a result of its improved $k_L a_{20}$ and L_c, when compared to the other inserts. For

example, at $U_w \approx 2$ ms^{-1} and $Q_a > 150$ slm, the V1 insert has a shorter ventilated cavity than the other $R_v = 1.5$ inserts and therefore had an improved mass transfer performance, shown in Figure 7.1 (b). The increasing values of SAE can explained due to its ventilated cavity lengths, which displayed a steadily increasing length for an increased air flow rate. This is in comparison to the other $R_v = 1.5$ inserts, which had a significantly increasing ventilated cavity length for air flow rates greater than 100 slm, shown in Figure 5.1.

The V1 insert contradicts the profile of the HV1 Insert, in Figure 7.6 (b), which follows a more similar SAE profile to that of the inserts at $U_w \approx 1$ ms^{-1}, which is initially a quickly decreasing SAE which then settles. The reasons for this can be attributed again to the ventilated cavity length, where between an air flow rate of 50 and 100 slm the HV1 insert had a fairly constant ventilated cavity length, However, above $Q_a = 100$ slm there was a significant increase in L_c and therefore a reduced mass transfer performance. This significant increase was caused by the individual air streams coalescing, causing a sudden increase in L_c. This phenomenon was also seen within the experimental work by Lee at al (1997) on spargers in downward two-phase flow.

At $U_w \approx 3$ ms^{-1} all the SAE profiles for the inserts rise with air flow rate. It can be seen that the blockage ratio is the most important factor in determining the SAE. At the higher water velocities the A1 and A2 inserts significantly underperforms in comparison to the HV and V1 inserts. The increasing SAE across all of the inserts can be attributed to the ventilated cavity, where for the vast majority of the cases there is a ventilated cavity but it is significantly shorter than at the lower water flow rates. In most cases there was an amount of bubbly flow within the downcomer. It is clear to see in Figure 7.6 that in terms of SAE, the V1 insert out performs all the other inserts at $U_w \approx 3$ ms^{-1}. Comparing the $R_v = 1.5$ to inserts to the A1 and A2 inserts, the significant difference in the performance is due to the specific power requirements of the A1 and A2 inserts, which typically used 2 to 3 times the power of the $R_v = 1.5$ inserts, shown in Figure 6.6 and Table 6.4.

It can be seen in Figure 7.6 that the HV1 insert is the optimum insert of the three HV inserts, for water flow velocities of 1 and 2 ms^{-1}. However at $U_w \approx 3$ ms^{-1} the HV1 and HV3 inserts become very comparable, with the HV2 insert being the least efficient of the three orientations. Figure 7.7 shows that the air void fraction at the operating conditions of $U_w \approx 3$ ms^{-1} and $Q_a = 200$ slm, at the trailing edge of the vanes of the HV1 and HV3 inserts. Figure 7.7 shows that the air distribution is very similar for both the inserts. However, there is still some of the air being entrained through the lower side of the vanes on the HV1 insert, which will provide a reduced velocity slip ratio, as discussed in Chapter 6, and therefore will result in a shorter ventilated cavity length, when compared to the HV3 insert. Therefore, the HV1 insert will have a lower specific power requirement and an increased oxygen transfer than the HV3 insert, at the higher air flow rates at $U_w \approx 3$ ms^{-1}, which is shown in Figure 7.6 (c).

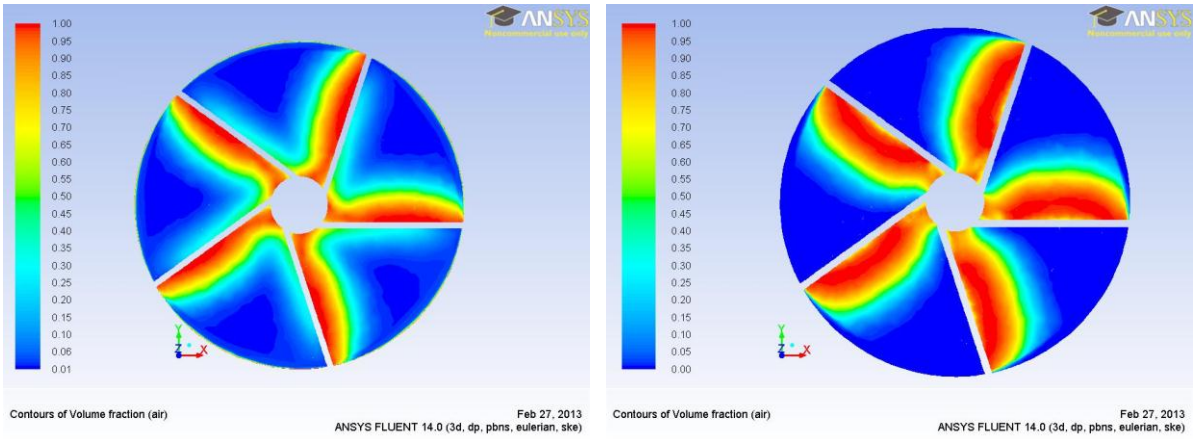

(a) (b)

Figure 7.7: - Air void fraction distribution for the (a) HV1 and (b) HV3 inserts at $U_w \approx 3$ ms^{-1} at Q_a = 200 slm, the plane highlighted are at the trailing edge of the vanes.

The distribution of SAE varied greatly between the upstream water velocities as can be seen in Table 7.3.

Table 7.3: – Range of SAE's achieved at each upstream water flow velocity for all inserts.

U_w (ms^{-1})	SAE (kgO_2/kWh)	Range (kgO_2/kWh)
1	0.95 – 3.20	2.25
2	0.56 – 1.87	1.31
3	0.22 – 1.15	0.93

It has been identified in Figure 7.6 that the HV1 insert had a slightly improved SAE over the V1 insert at the lower water and air flow rates. It was also shown in Figure 6.1 that when no air was being entrained the HV1 insert was the most efficient at the lower water flow rates, $U_w \approx 1$ ms^{-1}. However, at $U_w \approx 2$ and 3 ms^{-1} the V1 insert had the lowest power consumption with no air being entrained. This was replicated with the SAE values, where the HV1 insert had the best performance at the lower flow rates but was then surpassed by the V1 insert. Therefore, conducting physical experimentation or developing CFD simulations with no air being entrained could give an indication of an aerators performance, when establishing prototypes for development, where a new design would have to surpass the performance of the V1 insert for a range of water flow rates, when no air was being entrained.

Looking at an overall comparison between the V1 And HV1 inserts there appear to be two distinct regions of performance when plotting specific power against $k_L a_{20}$, as shown in Figure 7.8. For upstream water velocities of 1 and 2 ms^{-1} there is a constant trend for each of the individual inserts. There is then however, a step change in performance at $U_w \approx 3$ ms^{-1}. This may be as a result of frictional losses being a function of the flow velocity squared, as shown by the Darcy Weisbach equation, Equation 3.6. Therefore, as the water velocity is increased linearly the resultant frictional loss and therefore power consumption increases at a greater rate. Despite this, Figure 7.8 shows that for a $k_L a_{20}$ value ≥ 16.92 hr^{-1}, the V1 insert outperforms the HV1 insert and therefore all other inserts, in this experimental setup. The region below $k_L a_{20}$ ≤ 16.92 hr^{-1} corresponds to low mass transfer and air flow rates, which is when the HV1 insert had shorter ventilated cavity lengths and therefore greater operational stability, with a reduced risk of stall in the downcomer.

Therefore, the results indicated that there may be a level of operational benefit for using the HV1 insert in comparison to the V1 insert at the lower air flow rates.

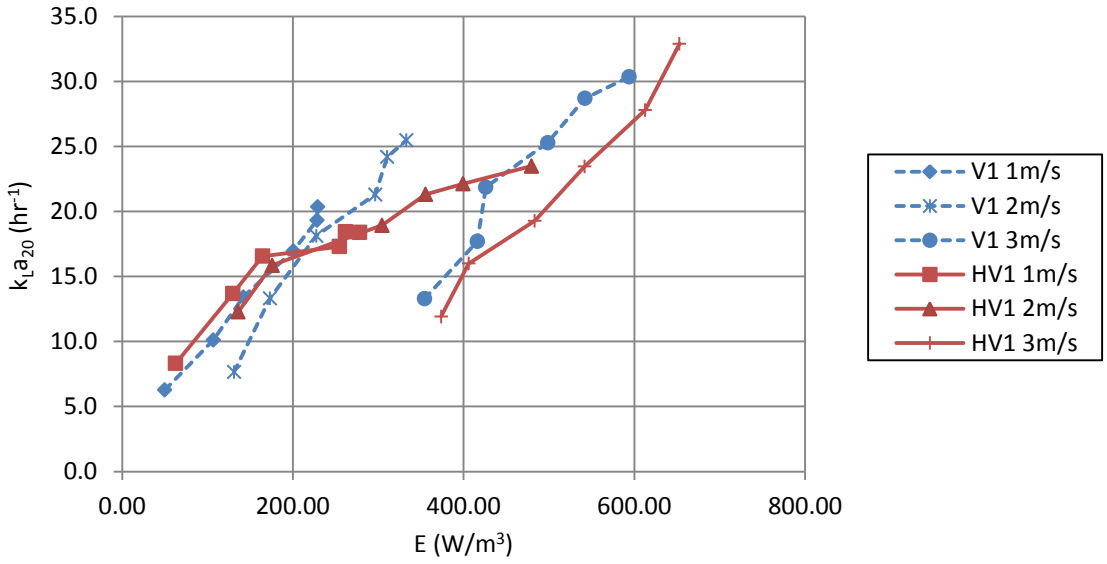

Figure 7.8: – Specific power, E, against overall mass transfer coefficient, k_La_{20}, for the V1 and HV1 inserts across the range of upstream water velocities, 1, 2 and 3 ms^{-1}.

7.5. Mass transfer and energy dissipation

Within the literature there have been a number of studies with gas-liquid ejectors, which have generated equations for predicting the mass transfer performance for an ejector based on energy dissipation per unit mass, for example Changfeng et al (1991), Dirix and Van de Wiele (1990) and Cramer and Beenackers (2001). These proposed equations are outlined below in Table 7.4.

Table 7.4 – Correlation of ejector systems from literature.

Authors	Correlations	Flow regime
Changfeng et al (1991)	$k_La_{20} = 0.7206(\epsilon)^{0.492}(\varepsilon_G)^{0.88}$	Down flow ejector coalescing system
Dirix and Van de Wiele (1990)	(1) $k_La_{20} = 5.4 \times 10^{-3}(\epsilon)^{0.66}\varepsilon_G\left(\frac{d_N}{d_M}\right)^{0.88}$ (2) $k_La_{20} = 8.5 \times 10^{-4}(\epsilon)^{0.66}\varepsilon_G\left(\frac{d_N}{d_M}\right)^{0.88}$	Down flow ejector Coalescing system (1) Bubble flow regime (2) Jet flow regime
Cramer and Beenackers (2001)	(1) $k_La_{20} = C_6(\epsilon)^{0.65}\varepsilon_G\left(\frac{1+0.2\varepsilon_G}{1+\varepsilon_G}\right)^{1.2}\left(\frac{\rho_L^2\rho_G}{\sigma^3}\right)^{0.2} \times \left(\frac{L_M}{d_M}\right)^{0.42}\left(\frac{d_N}{d_M}\right)^{0.65}$ (2) $k_La_{20} = C_7(\epsilon)^{0.65}(1-\varepsilon_G)\left(\frac{d_N}{d_M}\right)^{0.65}$ (3) $k_La_{20} = C_5(\epsilon)^{0.65}\varepsilon_G\left(\frac{1+0.2\varepsilon_G}{1+\varepsilon_G}\right)^{1.2}\left(\frac{\rho_L^2\rho_G}{\sigma^3}\right)^{0.2} \times \left(\frac{L_M}{d_M}\right)^{0.42}\left\{1-0.55\left(0.38-\frac{d_N}{d_M}\right)^2\right\}$	Down flow ejector Coalescing system (1) Upstream induced swirl – Bubble (2) Upstream induce swirl – jet annular (3) No swirl induced

Table 7.4 shows two important characteristics for improving the mass transfer performance of ejectors.

a) Improving the amount of energy dissipated per unit mass.

b) Increasing the volumetric air void fraction.

Further to this, Dirix and Van de Wiele (1990) showed that higher $k_L a_{20}$ values are obtainable when the nozzle to mixing tube diameter is increased in a plunging jet reactor, which would equate to reducing the blockage ratio of an insert.

There is a significant range of variations to the ejector configurations in the studies. Therefore, it is not surprising that there is a degree of variation in the reported correlations. Dirix and Van de Wiele (1990) obtained their data with a swirl device placed in the upstream section of the nozzle, so did Cramers and Beenackers (2001) for some of their study, indicated in Table 7.4. Whereas in Changfeng et al (1991) no spinner was present. This is similar to the range of inserts tested in this experimental work, where some inserts, HV and A1 imposed a swirl into the flow and the V1 and A2 inserts did not. Therefore a good comparison between the presented literature and this experimental work can be made.

Using the basic format of the equations in Table 7.4, where $k_L a_{20}$ is a function of energy dissipation and air void fraction such that,

$$k_L a_{20} = C_1(\in)^n(\varepsilon_G)^m \quad [7.9]$$

where C_1 is an empirically determined constant for this experimental work.

The energy dissipation is taken through the entire aerated volume as is calculated by Equation 7.10.

$$\in = \frac{E}{\rho_{2ph}} \quad [7.10]$$

Using Equations 7.9 and 7.10, Equations 7.11 and 7.12 have been determined for the experimental data in this study, which are presented in Table 7.5. The data is distinguished for when the downcomer was in a fully bubbly flow regime and when a ventilated cavity was present.

Table 7.5 – Correlation from experimental work.

Flow Regime	Correlation	Standard Deviation	
Bubbly	$k_L a_{20} = 46.535(\in)^{0.48}(\varepsilon_G)^{0.3}$	± 14.5%	[7.11]
Cavity present	$k_L a_{20} = 55.944(\in)^{0.48}(\varepsilon_G)^{0.3}$	± 14.7 %	[7.12]

As can be seen, in Table 7.5 that the determined equations for the data in this experimental study for when a ventilated cavity was and was not present in the downcomer are very similar, except the empirical constant, C_1. The air void fraction index is also the same as in Equations 7.7 and 7.8. When comparing the Changfeng at al (1991) equation to Equations 7.11 and 7.10 for this experimental work. It can be seen that the air void fraction has less of a role in determining the overall volumetric mass transfer coefficient in the Changfeng at al (1991) equation, than in this experimental work. However, energy dissipation per unit mass has a similar degree of importance with an indices of n = 0.492 compared to n = 0.48.

Figures 7.9 and 7.10 show the resulting correlations, Equations 7.11 and 7.12, compared to the experimental data from this study.

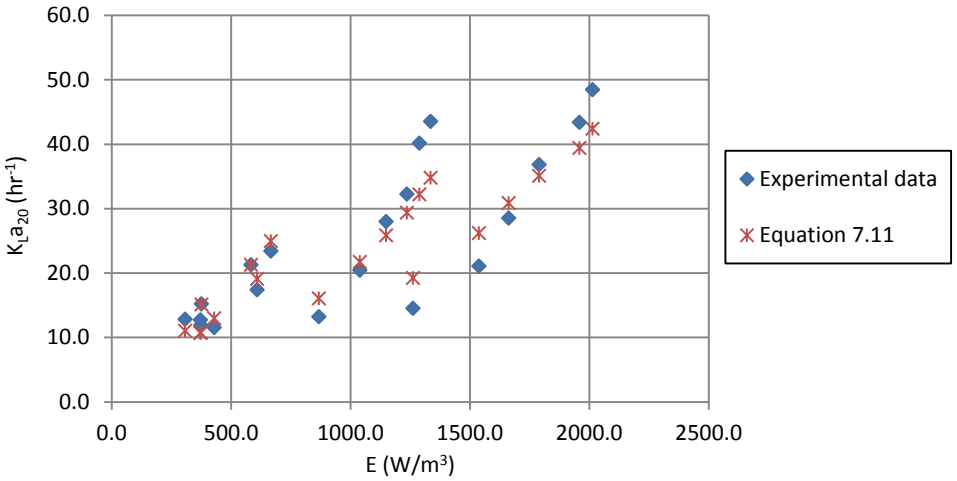

Figure 7.9: - Specific energy input against overall mass transfer coefficient for when a bubbly flow was present in the entire downcomer, comparing the experimental data with Equation 7.11.

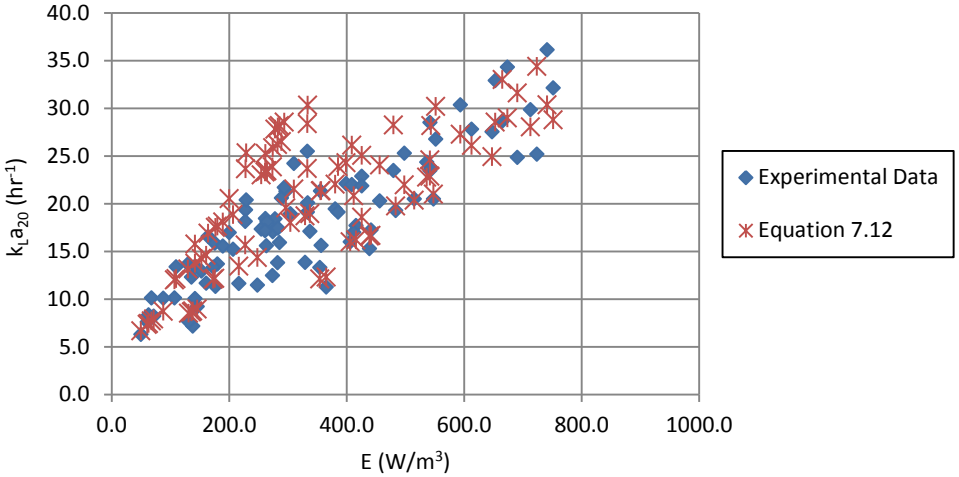

Figure 7.10: - Specific energy consumption against overall mass transfer coefficient for when a cavity was present in some of the downcomer, comparing the experimental data with Equation 7.12.

7.6. Summary

When considering mass transfer, the ventilated cavity has a significant effect on k_La_{20} as well as the E and d_{32}. This is highlighted in Figure 7.1 (b) for the A2 insert, which outperforms all other inserts when a full bubbly flow was present in the downcomer in terms of the k_La_{20}. However, as soon as a ventilated cavity forms in the downcomer the performance begins to match the other inserts. It was also shown that the presence of a ventilated cavity also affects the oxygen transfer efficiency of the inserts, with reduced percentage absorption at the higher air flow rates, which is indicative of a ventilated cavity being present.

Throughout this Chapter correlations have been identified with good agreement in principle with those found in the literature, with k_La_{20} being closely related to d_{32} and energy dissipation. These correlations can be used as a set of design equations for potential design improvements of the inserts, with the correlations having a suitably low standard deviation when applied across the full range of inserts, as well as flow conditions tested in this study.

When taking into consideration the experimental findings, it is clear to see that the HV1 insert is the optimum of the aerofoil inspired venturi designs. However, it potentially has a limited range of operating conditions in which it would be superior to a regular venturi in terms of SAE. Potential areas for improvement would be to improve the velocity slip ratio in the throat by increasing the open area for air injection, with the aim in preventing the formation of a ventilated cavity. Also there would be a number of benefits from increasing the length of the channels. Firstly, there will be a reduction in the merging and coalescence of the individual air streams. Also increasing the length of the channels is said to reduce the level of turbulence which leads to vorticity and increased energy dissipation (West, 2009). Reducing the recirculation patterns from vortical motions will tend to reduce the level of coalescence between the air bubbles (West, 2009). In addition to the reduced turbulence, the increased channel lengths will also increase the extent of the flow experiencing strong strain, which is beneficial for bubble breakage. Therefore there are a number of initial design changes that can be made, so that the HV insert can be improved.

CHAPTER 8

COMPUTATIONAL FLUID DYNAMICS ANALYSIS

8.1. Introduction

In this chapter, a review of various techniques for simulating two-phase flows using computational fluid dynamics, CFD, is given. In particular, the discussion involves different multiphase and turbulent modelling approaches used, followed by the handling of interphase force that is largely responsible for accurate predictions of dispersed phase distribution and other system parameters. Moreover, an introduction to CFD is given including application, advantages and methodology, as well as the CFD analysis procedure, the discretisation methods and the governing equations.

Within the simulations the HV1, A1 and A2 inserts were modelled at U_w = 3 ms^{-1}, Q_a = 50 slm. This was the operating conditions where both the higher and lower blockage ratio inserts, the A1 and A2 and the HV1 respectively, exhibited a fully bubbly flow through the entire downcomer. As described through Chapters 5, 6 and 7, the bubbly flow regime is the ideal operating condition for the insert and it is for this reason that modelling this flow regime accurately will provide the greatest benefit. From the validation between CFD and experimental findings, it is possible to determine the effects of geometric scaling on interfacial area, specific power consumption and therefore the aeration efficiency.

8.2. Definition, history and application of CFD

CFD is an engineering tool based on a computer simulation that is used to assess the system performance, including fluid flow, and heat and mass transfer. It has become a useful design and analysis tool for many industries (Versteeg & Malalasekera, 1996). The setup of CFD simulations can be divided into two steps. The first is a numerical model which is created by a set of mathematical equations that express the flow. The second step is when these mathematical equations are solved by a computer program in order to gain the flow variables through the domain.

Since the invention and development of the digital computer, CFD has been given comprehensive attention and has been used extensively in the engineering industry to contemplate different aspects of fluid dynamics. During the 1980's computers developed into a sufficiently powerful tool for the general application CFD software to become accessible.

The earliest users of CFD were the nuclear, aerospace and automotive industries (Bakker, et al., 2001). Further improvements have been made in CFD and its capability to model complicated phenomena, such as evaporation, condensation and two-phase flow in process engineering. This in conjunction with the fast development in computer power has increased the range of CFD applications. For a wide range of process

industries CFD techniques have been utilised to gain information about various flow phenomenon, such as mass transfer, to investigate the design of different equipment or to evaluate the performance under various operating conditions.

In general, CFD models require validation to examine the accuracy of the computational model. The validation process is carried out by comparing CFD results with the available experimental, theoretical or analytical data.

Some of the benefits of using CFD codes are,

a) It can be used to study any system numerically when it is too complicated to do through experimentation.
b) CFD is able to provide different kinds of information, which can be difficult to obtain through experimentation because of limitations with equipments and techniques.
c) The complex physical interactions that take place in a flow conditions can be modelled simultaneously since no limiting assumptions are usually required.
d) CFD enables the visualisation of the flow behaviour of a system and it is commonly used in industry as a flow visualisation tool (Gaylard, 2001).

8.3. Motivation for the use of CFD for aeration technology development

The design process traditionally relies on experimental pilot scale studies and empirical correlations. Pilot scale studies are carried out at a smaller scale, often at ambient operating conditions which may differ from the in-process operating conditions and using convenient fluids, for example, tap water instead of wastewater as well as using materials like clear acrylic, so that flow regimes can be observed. Going from prototypes to a full-size plant requires the use of scaling laws, but they may not always be established for the particular application that the engineer is looking at.

The design optimisation process usually requires several iterations until the performance criteria are reached. This iterative process is long, difficult and expensive in terms of man hours, materials, the purchase and maintenance of buildings and testing equipment. At the same time global market pressures, force the companies to shorten the design process drastically. In summary, the primary objectives for the design process of a new technology include,

a) Getting the product quickly to market,
b) Providing a more reliable product,
c) Reducing the costs in product development,
d) Providing significant technical innovation.

From these objectives, it becomes clear that the development of an additional methodology able to complement the experimental studies and empirical correlations is desirable. Such a methodology should be flexible, for example, it should be applicable to various engineering systems and designs, cost-effective,

accurate and capable of predicting in detail the behaviour of complicated flow problems, such as the case in this experimental work. CFD modelling is just such an approach. Broadly speaking, this is the analysis of engineering systems involving fluid flow, heat transfer and associated phenomena such as oxygen transfer, by means of computer-based simulations.

CFD can be an integral step in the design process where the goals are to,

a) Provide insight into the physical fluid process occurring,
b) Understand flow patterns and the relative importance of some parameters compared with others,
c) Reduce the number of prototypes by defining a good design earlier,
d) Minimise the time spent in the verification and testing phase of product development,
e) Avoid unnecessary changes after design release,
f) Reduce the overall costs of the product design stage.

8.4. The CFD analysis procedure

All numerical methodologies consist of a model which is a simplified mathematical representation of the physical and/or chemical process to be predicted. Such a model consists of a set of equations, where less important or less influential phenomena, or effects, are neglected. They also consist of a solution procedure, which specifies the details of how to obtain an approximate solution to the set of equations to be solved.

In the last few decades, CFD has received interest from industry. This has led to the development of a variety of CFD codes that are available commercially, for instance FLUENT and CFX. CFD codes are structured around the numerical algorithms which will solve the governing equations of the physics of the problem. There are three main elements to CFD codes these are the pre-processor, the solver and the post processor.

The pre-processor is where the flow problem inputs are specified. The step involves the creation of the geometry and mesh, termed the grid. After that, the flow model, fluid properties and control parameters of the solver are specified, and then the boundary conditions are applied. The grid is where the computational domain is subdivided into a finite number of smaller, non-overlapping sub-domains which are termed cells. These are where each equation will be numerically solved. It follows that the accuracy of the simulation is influenced by the grid resolution. In general, the larger the number of cells, the better the solution accuracy. However, calculation time is dependent on the fineness of the grid. In order to balance computational times and data accuracy, meshes are often non-uniform such that they are finer in areas where large flow variations are expected and coarser in regions with relatively little change. Further details about the pre-processor and the steps involved will be discussed later in this chapter.

The solver is used to discretise and solve the numerical transport equations based on specified data. This is achieved by the integration of the equations over all of the cells within the computational domain. Then discretisation is used to convert the integral equations and boundary conditions into an algebraic system.

From this, the solution is determined for the algebraic equations by an iterative method. This process is fully integrated within modern CFD packages and as such, it is non-interactive from the user's point of view as it requires only machine time.

The post-processor records and displays all relevant information about the flow, for example velocity and pressure profiles across two-dimensional cross-sections, as well as shear rates, vector plots, line and shaded contour plots, three-dimensional plots, particle tracking and so on.

Once the solution is achieved, the results are subsequently analysed to find out the accuracy of the solution. If these results are not accurate, the source of the error has to be identified which could be an incorrect definition of the flow specification, or a poor quality grid or a conceptual error in the specification of the problem.

8.5. Numerical techniques

The governing equations are typically presented by partial differential equations, PDE's, such as the Navier-Stokes equations. These equations cannot be solved directly using computers that are able to identify and operate with numerical data (Mahmud, 2012). The PDE's have to be converted into numerical equations that include only numbers and no derivatives. This process is called Numerical Discretisation. There are various approaches used for solving the numerical equations, these include the finite difference method, FDM, the finite element method, FEM and the finite volume method, FVM.

The FLUENT CFD software which has been used in this work uses the FVM. The FVM is a versatile technique that incorporates parts of both the FEM and FDM. It is a similar mode of application of the FDM, while some of its implementation is driven on characteristics based on the FEM approach. Further details of the FEM and FDM can be found in Mahmud (2012).

The FVM takes into account the discretisation of the spatial domain into finite control volumes. A control volume usually covers many grid elements that can be divided into sectors which belong to a different grid element. The differential governing equations are integrated over individual control volumes. The result of this integration ensures the accurate conservation of related properties in individual finite volumes. Each integral term is transformed to a discrete term that results into discretised equations at the nodal or centroids points of the control volumes. This method is similar to the FDM method, where the numerical equations at a particular point are derived from the values at neighbouring points (Versteeg & Malalasekera, 1996).

8.6. CFD modelling approaches for multiphase flow

The modelling of multiphase flow is an enormous topic and includes a wide range of industrial processes (Mahmud, 2012). The following sections review the multiphase modelling aspects of bubbly flow, which is

the most desirable flow state to enhance two-phase flow mass transfer. In reality, most of the fluids flow is turbulent due to the nature of the operating conditions. Later in this chapter will also discuss the various turbulence modelling features in two-phase flow systems. Particular attention is given to the treatment of the interface forces that play an important role in the prediction of the parameters.

It is important to understand the need for modelling flow fields and turbulence in order to resolve them directly. A special technique which provides for an exact computation of the instantaneous flow fields and their turbulent fluctuations without resorting to any kind of modelling is discussed. This method has some limitations that are emphasised and therefore the requirement for modelling is demonstrated.

8.7. Dispersed multi-fluid flow modelling

Within FLUENT there are three recognized methods to modelling dispersed multiphase flows, the Volume of Fluid method, termed VOF, the Eulerian - Eulerian method, termed E-E, and the Mixture method. The E-E and Mixture method are both present within FLUENT. However, for more complex models with a greater desire for accuracy the E-E model is recommended (ANSYS Inc, 2011a). When looking at the experimental results as shown in Chapters 5, 6 and 7, especially with HV and V1 inserts having percentage differences of less than 5 % across a significant range of performance characteristics. It is for this reason that the E-E method will be chosen over the Mixture method, as a result the Mixture method will not be discussed here.

The VOF method tracks the motion of a distinct phase in each cell through the domain. In the VOF model, a single set of conservation equations are shared by the two-phase flow using mixture properties, when both the phases share the same control volume. In addition, if the control volume is occupied by one of the phases, its properties are utilised. The benefit of this is to avoid any unexpected changes in the physical properties of the fluid through a thin interface.

Usually, when the shape and flow processes taking place close to the interface are of interest, the VOF method is beneficially utilised because it is able to simulate the profile deformation of the dispersed phase particles, for example droplets and bubbles, as a result of the surrounding fluid flow (Delnoij, et al., 1999). When the system is characterised by a great fraction of the dispersed phase, for example in a bubbly flow, it requires substantial computational resources around every dispersed entity to determine the flow field. It is appropriate to use as an application that focuses on simple flow pattern problems as seen in pipelines, such as slug flows (ANSYS Inc, 2011a).

The E-E model is the most complex of the multiphase models in FLUENT. The flow of all phases is modelled by an Eulerian framework. Therefore, the E-E method is based on the assumption that all phases share the domain and may interpenetrate as they move all the way through it. It solves a set of momentum and continuity equations for each phase where every phase is described by velocity and volume fraction. The interface forces such as drag, lift and virtual mass must be specified in order to effectively handle the

coupling among the phases. Coupling is achieved through the pressure and interphase exchange coefficients. Comparison between the VOF and the E-E approach, demonstrates that the E-E approach is well accommodated to modelling systems which account for high gas volume fractions, for example greater than 10 % of the dispersed phase, such as bubbly flow pipes and bubble columns (ANSYS Inc, 2011a; Mahmud, 2012). It is for this reason that the E-E approach will be utilised in this work and will be discussed further.

8.8. E-E governing equations

The governing equations for the E-E method are derived by averaging all of the conservation equations for each one of the phases as mentioned by Drew (1983) and Lopez de Bertodano et al (1990). The equation of volume average continuity for i^{th} interpenetrating phase is provided by, (Ranade, 2002).

$$\frac{\delta}{\delta t}(\alpha_i \rho_i) + \nabla.(\alpha_i \rho_i \vec{u}_i) = \sum_{j=1}^{n} \dot{m}_{ji} \qquad [8.1]$$

where α, ρ, u are expressed as the macroscopic volume fraction, density and the velocity of the phase i respectively, while $\dot{m}_{ji}$ is the mass transfer from the j^{th} phase to the i^{th} phase.

The momentum equation of the phase i is given by the Navier-Stokes equation as follows, (Mahmud, 2012)

$$\frac{\delta}{\delta t}(\alpha_i \rho_i \vec{u}_i) = -\nabla.(\alpha_i \rho_i \vec{u}_i \vec{u}_i) - \alpha_i \nabla p - \nabla.(\alpha_i \tau_i) + \alpha_i \rho_i \vec{g} + \alpha_i \rho_i \left(\vec{F}_i + \vec{F}_{lift,i} + \vec{F}_{ji}\right) \qquad [8.2]$$

where $p, g, F_i, F_{lift,i}$ and F_{ji} are expressed as hydrodynamic pressure, gravity, external body force, lift force and virtual mass force respectively, while τ_i represents the viscous stress tensor for i^{th} phase, which can be expressed by, (ANSYS Inc, 2011a)

$$\tau_i = \alpha_i \mu_i \left(\nabla \vec{\mathrm{u}}_\mathrm{i} + \nabla \vec{\mathrm{u}}_\mathrm{i}^{\,\mathrm{T}}\right) + \alpha_i \left(\lambda_i - \frac{2}{3}\mu_i\right) \nabla.\vec{u}_i I \qquad [8.3]$$

In the Eulerian multiphase application, the energy conservation equation can be expressed by the enthalpy equation of each phase as,

$$\frac{\delta}{\delta t}(\alpha_i \rho_i h_i) = -\nabla.(\alpha_i \rho_i h_i \vec{u}_i) - \alpha_i \frac{\delta P_i}{\delta t} + \tau_i : \nabla.\vec{\mathrm{u}}_\mathrm{i} - \nabla.\vec{\mathrm{q}}_\mathrm{i} + \mathrm{S}_\mathrm{q} + \sum_{j=1}^{n} \left(\vec{\mathrm{Q}}_\mathrm{ji} + \dot{m}_{ji} h_{ji}\right) \qquad [8.4]$$

Where h_i, q_i, S_i, Q_{ji} and h_{ji} represent the specific enthalpy of the i^{th} phase, the heat flow, the source term that takes into account sources of enthalpy due to chemical reaction or radiation, the intensity of heat exchange between two phases and the interphase enthalpy respectively.

8.9. Lift force

Generally in multiphase systems, FLUENT has the ability to take into account the effect of lift force on a spherical object, for example a droplet, bubble, or particle. The influence of this force on a bubble is mainly as a result of velocity gradients in the primary phase flow. The lift force on large particles is considered to be more significant, although the FLUENT model assumes that the inter-particle spacing is greater than the particle diameter. The enclosure of lift forces, therefore, is not suitable for very small particles and closely

packed particles, as recommended in ANSYS Inc (2011a).

The influence of the lift force on the dispersed phase, j, in a primary phase, i, is obtained as,

$$\vec{F}_{lift,i} = -C_L \rho_i \alpha_j \left|\vec{\mathrm{u}}_\mathrm{i} - \vec{\mathrm{u}}_\mathrm{j}\right| \times (\nabla \vec{\mathrm{u}}_\mathrm{i}) \quad [8.5]$$

where F_{lift} is the lift force that will be added to the right hand side of the momentum equation, which is Equation 8.2. C_L is typically around 0.5 for inviscid flow. However, values in the range of $0.01 \leq C_L \leq 0.15$ have been found as a good fit with experimental data for a vertical gas-liquid flow in a pipe (Mahmud, 2012).

In most of the situations, the lift force is not important in contrast to the drag force, but if the lift force is significant, such as in the case of two–phase separation, where both phases might be quickly separated. In that situation, it could be appropriate to take into account the effect of this term. By default, the lift force is not included, but if it is required for multiphase system, the lift coefficient can be specified.

8.10. Virtual mass force

For multiphase flows, FLUENT includes the virtual mass effect that occurs when a secondary, dispersed phase j accelerates relative to the primary phase or continuous phase i. The inertia of the continuous phase mass encountered by the accelerating droplets or bubbles exerts a virtual mass force upon them.

$$\vec{F}_{ji} = \frac{1}{2}\, \alpha_j \rho_i \left(\frac{d_i \vec{\mathrm{u}}_\mathrm{i}}{dt} - \frac{d_j \vec{\mathrm{u}}_\mathrm{j}}{dt} \right) \quad [8.6]$$

The virtual mass force $\vec{F}_{ji}$ will be added to the right hand side of the momentum equation, Equation 8.2 for both phases.

The virtual mass effect is significant when the secondary phase is much smaller than the primary phase density, for example in an air and water bubbly flow pipe.

8.11. Momentum exchange term

In multiphase gas-liquid flows, the secondary phase is assumed to form droplets or bubbles, in the case where the gas is the sparser fluid. It is the gas, which is more likely to form droplets or bubbles. Whereas the more predominant liquid is modelled as the primary fluid. The momentum exchange between the phases is based on an exchange coefficient which can be written in the following form,

$$K_{ji} = \frac{\alpha_i \alpha_j \rho_j f}{\tau_j} \quad [8.7]$$

where f is the drag function and τ_j is the particulate relaxation time and is defined as,

$$\tau_j = \frac{\rho_j d_j^2}{18 \mu_i} \quad [8.8]$$

where d_j is the diameter of the bubbles or droplets of phase$j$.

Nearly all definitions of f include a drag coefficient, C_D, that is based on the relative Re_{ji}. For the model of Schiller and Naumann (1935) f is defined as,

$$f = \frac{C_D Re_{ji}}{24} \quad [8.9]$$

where C_D is defined using Equation 8.10.

$$C_D = \begin{cases} \frac{24\left(1 + 0.15 Re_{ji}^{0.687}\right)}{Re_{ji}} & Re_{ji} \leq 1000 \\ 0.44 & Re_{ji} > 1000 \end{cases} \quad [8.10]$$

The drag function and drag coefficient can be modelled by different formulates of which some are available by default in the FLUENT code, such as the one outlined by Schiller and Naumann (1935), further correlations can be found in ANSYS Inc (2011a). The Re_{ji} is the relative Reynolds number and is obtained by Equation 8.11 for the primary phase, i and the secondary phase, j.

$$Re_{ji} = \frac{\rho_i \left|\vec{u}_i - \vec{u}_j\right| d_j}{\mu_i} \quad [8.11]$$

8.12. Modelling turbulence

Turbulence is the pseudo-random and apparently unpredictable state of a fluid. It is one of the most challenging problems in fluid dynamics. Its appearance causes radical changes to the flow which can range from favourable, such as efficient mixing to detrimental, for example friction and high energy losses. The ability to predict these mechanisms is of great importance in practical engineering applications.

Turbulence is essentially characterised by unsteadiness, three-dimensionality, unpredictability, a broad spectrum of time, length scales and strong vorticity. Typical turbulent flows are separated into regions containing strong coherent vorticity or little vorticity. The fluctuations between the two zones are significant and vortex interactions dominate the flow. These interactions lead to smaller and smaller length scales being generated and the spreading of the large scale motions to fill the flow.

The scientists Stokes (1851) and Reynolds (1883) tried to quantify the onset of the turbulence. They showed that a flow regime changes from an orderly laminar state to a turbulent one. Another important discovery was the energy cascade theory, where turbulent flows incorporate a hierarchy of eddies ranging from large to very small scales in size, and energy is transferred from the larger to the smaller eddies. This process lasts until finally the smallest scales are dissipated into heat by molecular viscosity. At the end of the 20th century, the Russian physicist A. N. Kolmogorov formulated this theory into physical laws for the various scales present in a turbulent flow (Massey, 2006).

The wide range of length and time scales of motion makes turbulence very difficult to tackle mathematically. There are few analytical approaches to the turbulence because of the stochastic and strongly non-linear nature of the phenomenon. Experiments remain of fundamental importance for the research in this field. In particular, the introduction of novel advanced measuring techniques such as laser-

Doppler velocimeters, and multiple wire anemometers have allowed single and multi-point sampling of flow characteristics. This consequently has significantly increased the utility and range of experimental measurements.

In the meantime, computational simulation techniques have become well established as a means to study turbulent flows. The most straightforward approach to simulate the turbulence is a direct numerical simulation, DNS, which directly discretises and solves the governing equations of the fluid dynamics. DNS attempts to compute all scales of motion in the fluid, from the largest coherent structures to the smallest dissipative eddies. The great advantage is that DNS resolves fully the flow, there is neither averaging nor smoothing of the solution field (ANSYS Inc, 2011a). Thus no turbulent modelling assumptions or empirical correlations are introduced in the solving procedure. In theory, the only difference between the results from the simulations and the experimental findings are due to errors introduced by numerical discretisations. Consequently, the DNS modelling procedure is expected to deliver an almost exact three-dimensional, time-dependent solution, providing a sufficiently fine grid and highly accurate, high order numerical schemes are used. Unfortunately, for these reasons and given the current state of computational capacity, the DNS is largely limited to simple geometries, such as flat plates, homogeneous turbulence and channels at relatively low Reynolds numbers (Versteeg & Malalasekera, 1996).

The trade-off of simulating the turbulence accurately is to reduce the amount of turbulent scales to be resolved. To do so, the governing equations of the fluid mechanics are simplified and turbulence models are introduced to supply the information lost during the simplification process. These models are expressed under the form of algebraic or differential equations that approximate the complex behaviour of the turbulent flows. They are based upon empirical information derived from experimental observations and DNS data.

A wide variety of turbulence models exist. They differ by their attempt to represent the turbulent eddies using various levels of approximation. They have their advantages and drawbacks, such as any flow quantity can be sampled at any point in the field and instantaneous field values can be obtained for the whole domain. However, they are still unable to guarantee accuracy under all conditions. Results of simulations are currently best presented in combination with experimental data to confirm their validity.

Large eddy simulations, LES, capture the large scales while averaging the small scales and modelling their effects. This approach sounds logical because the large eddies carry much more information, they contain most of the energy, do most of the transporting of the conserved properties and vary most from case to case (ANSYS Inc, 2011a). LES is showing great promise in the calculation of traditionally difficult turbulent problems, such as unsteady and recirculating flows. Unfortunately, this modelling procedure comes at a considerable computational cost because large scale structures are three-dimensional and time-dependent. Although LES much less computationally expensive than DNS.

A popular alternative in the industry is to use the steady-state Reynolds averaged Navier-Stokes, RANS, turbulence models (Versteeg & Malalasekera, 1996). The idea lies in applying an averaging operator to the governing fluid flow equations. From a practical point of view, this is equivalent to an infinite set of experiments being sampled at the same time, the average of all the flow fields representing the ensemble average. The averaging of the non-linear terms of the flow equations introduces additional variables. Therefore, the system has more unknowns than equations. Therefore closure models must be introduced. There is a broad variety of RANS turbulence models ranging from various levels of difficulties, for example from the simple mixing length model to the commonly used k-ε models, or on to full Reynolds stress closures. The turbulence in RANS models is mainly assumed to be isotropic. However, the RSM model is the most elaborate type of RANS turbulence model that FLUENT provides (ANSYS Inc, 2011a). Abandoning the isotropic eddy-viscosity hypothesis, the RSM model closes the RANS equations by solving transport equations for the Reynolds stresses, together with an equation for the dissipation rate, therefore modelling anisotropic turbulence. The RANS computational technique is largely employed to model flows in complex geometries and at high Reynolds numbers. However, when any description of any phenomenon is simplified, accuracy is lost and/or range of applicability.

The detached eddy simulation, DES, approach has been suggested for three-dimensional unsteady separated flows as a hybrid method capable to providing the advantages of both RANS and LES, while avoiding their disadvantages, for example errors in RANS in massively separated flows and the computational cost of LES in the whole computational domain. In this approach, RANS is used in regions where the grid is not too fine, such as the attached boundary layer and LES is applied in the zone where the mesh is fine enough, for example the free shear flow resulting from separation, as illustrated in Figure 8.1. The RANS and LES regions are separated by an interface dictated by the grid. This requires some means of producing the initial conditions for the LES in the separation region and this is a difficult.

Figure 8.1: - Schematic of DES Turbulence model.

8.13. Turbulence models based on RANS

In the RANS approach, the instantaneous value of any flow variable, φ, is decomposed into a mean, $\overline{\varphi}$ and a fluctuating component, φ', such that,

$$\varphi = \bar{\varphi} + \varphi' \qquad [8.12]$$

The mean value can be found by averaging over an appropriate time interval, where the Reynolds averaging obeys the following properties,

$$\overline{\overline{\varphi}} = \overline{\varphi} \; and \; \overline{\varphi'} = \varphi' \qquad [8.13]$$

Equation 8.12 is substituted in the basic governing equations for the flow variable, for example the velocity

of the phase, which is followed by time averaging, subject to the conditions listed in Equation 8.13, in order to yield governing equations for the mean quantities. When simplified the equation is led to a new averaged equation featuring an extra term which takes into account the turbulent transport of φ. As the fluctuation of time averaged quantities takes place at much larger scales, resolving the smaller spatial and temporal scales is not needed in the RANS based approach (Mahmud, 2012).

The variation of fluid velocity with time is shown in Figure 8.13 and also demonstrates a comparison between RANS based approach with the DNS and LES approaches.

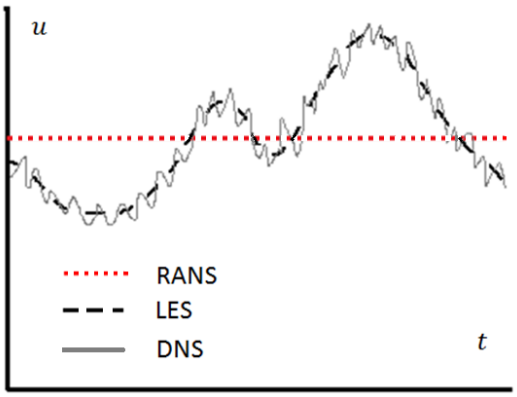

Figure 8.2: - A comparison of RANS, DNS and LES, adapted from Ranade (2002).

The averaging of RANS approach requires considerably less computational power compared to the LES or DNS methods. However, time averaging the basic governing equations results in the creation of new terms which lead to a closure difficulty. These new expressions might be integrated as apparent stress gradients and have the mass fluxes associated with turbulent motion (Ranade, 2002). The governing equations for these new expressions can be derived theoretically. However, these obtained equations would also have more unknown expressions. Therefore, it becomes very important to establish a turbulence model, which relates these unidentified terms to known ones, in order to complete the set of governing equations. During the last three decades, several turbulence models have been developed and utilised in simulations that have confirmed different degrees of achievement.

There is no single turbulence model universally accepted as being the most appropriate for all classes of problems. The choice of turbulence model depends on considerations such as the physics of the flow, the level of accuracy required, the available computational resources and the amount of time available for the simulation. To make the most appropriate choice of turbulence model for the specific application, an understanding of the turbulence models capabilities and limitations is required. The next section offers an overview of the issues related to the turbulence models provided in FLUENT.

RANS models offer the most economic approach for computing complex turbulent industrial flows. Typical examples of such models are the k-ε or the k-ω models, in their different forms. These models simplify the problem to the solution of two additional transport equations and introduce an eddy viscosity sometimes

referred to as a turbulent viscosity, to compute the Reynolds Stresses. More complex RANS models are available which solve an individual equation for each of the six independent Reynolds Stresses directly known as the Reynolds Stress Models, RSM, plus a scale equation, either the ε or ω equation. RANS models are suitable for many engineering applications and typically provide the level of accuracy required.

8.14. k-ε models

Two-equation models are historically the most widely used turbulence models in industrial CFD (ANSYS Inc, 2011b). They solve two transport equations and model the Reynolds Stresses based using the eddy viscosity approach. The two transport equations are expressed by two terms, which are the turbulent kinetic energy, k and its dissipation rate, ε. The standard k-ε model in FLUENT falls within this class of models and has become the workhorse of practical engineering flow calculations in the time since it was proposed by Launder and Spalding (1974). The k-ε models presents robustness, economy, and reasonable accuracy for a wide range of turbulent flows which explains its popularity in industrial flow and heat transfer simulations. The draw-back of all k-ε models is their insensitivity to adverse pressure gradients and boundary layer separation (ANSYS Inc, 2011b). They typically predict a delayed and reduced separation relative to observations. This can result in overly optimistic design evaluations for flows, which separate from smooth surfaces, for example aerodynamic bodies, and diffusers. The k-ε model is therefore not widely used in external aerodynamics. It is recommended to use the k-ε model in combination with the Enhanced Wall Treatment, EWT. In EWT the whole domain is subdivided into a viscosity affected region and a fully turbulent region based on the turbulent Reynolds number, Re_y which is defined as,

$$Re_y = \frac{\rho y \sqrt{k}}{\mu} \qquad [8.14]$$

where y is the wall normal distance calculated at the mesh cell centres and k is the turbulent kinetic energy.

For cases of separating flows under adverse pressure gradients from smooth surfaces, such as airfoils the k-ε models are generally not recommended. This is also the case for swirl flows or high turbulence, for example increasing anisotropy. It is for these reasons that the k-ε will not be investigated in this experimental work, due to the nature of the inserts, which incorporate aerofoil geometries and induce swirl into the flow.

8.15. k-ω models

The ω equation offers several advantages relative to the ε equation, where ω is the specific dissipation rate which can be evaluated as the ratio of ε and k. The most prominent one is that the equation can be integrated without additional terms through the viscous sub-layer (ANSYS Inc, 2011b). Furthermore, k-ω models are typically better in predicting adverse pressure gradient boundary layer flows and separation. The downside of the standard ω equation is a relatively strong sensitivity of the solution depending on the free stream values of k and ω outside the shear layer. The use of the standard k-ω model is, for this reason, not generally recommended in FLUENT (ANSYS Inc, 2011b).

The Shear Stress Transport, SST, k-ω model has been designed to avoid the freestream sensitivity of the standard k-ω model, by combining elements of the ω-equation and the ε-equation. In addition, the SST model has been calibrated to accurately compute flow separation from smooth surfaces. Within the k-ω model family, it is therefore recommended to use the SST model (ANSYS Inc, 2011b). The SST model is one of the most widely used models for aerodynamic flows and as with all ω equation based models it uses EWT as default. Therefore, the k-ω model will be used as the basis for the CFD simulations.

8.16. Reynolds stress models

RSM's include several effects which are not easily handled by the two-equation eddy viscosity models, such as k-ε and k-ω. The most important effect is the stabilisation of turbulence due to strong rotation and streamline curvature as observed, for example in cyclone flows. RSM requires a significant increase in computing time, due to the additional equations but also due to reduced convergence (ANSYS Inc, 2011b). This additional effort is not always justified by increased accuracy. The usage of RSM is therefore not recommended and should be restricted to flows for which their superiority has been established, especially flow with significant swirl and rotation. If wall boundary layers are important, the combination of RSM and the ω equation is more accurate than the combination with the ε equation. Due to the increased swirl in the A1 insert, as shown with the coring of the air in Chapter 5, at the high water and low air flow rates. RSM may be required to establish greater accuracy for these flow conditions.

8.17. Numerical simulation

Prior to running the solver a number of conditions and parameters are specified to define the fluid flow problem, such as the initial conditions, the boundary conditions and turbulence parameters.

The initial conditions are required to be specified for all dependent variables for the flow phase solution before using the CFD solver, in order to obtain unique solution for the governing equations. Moreover, the initial solution has to be taken carefully into consideration in order to provide a desired ultimate solution and abstain from numerical difficulties. Usually the initial pressure field is initialised using gravity forces, resulting in a pressure drop at the fluid phase being equal to atmospheric pressure. Two different techniques are used in the existing CFD codes to initialise the solution, which are initialising the whole flow field or patching values in selected zones for chosen flow variables (ANSYS Inc, 2011b).

Boundary conditions are used to identify the flow and thermal variables on the system boundaries under consideration and are significant factors of dynamic simulations. The boundary conditions for two-phase pipe flow simulations, which are typically employed are inlet and outlet boundary conditions, as well as wall boundaries at solid surfaces.

To obtain a reliable solution for the simulation, appropriate specification of inlet and outlet boundaries are required. Various boundaries are possible for inlet and outlet boundaries such as, mass flow inlet, velocity

inlet, and inlet and outlet pressure.

In this simulation for a two-phase vertically downward flow, the mass flow inlet condition is specified at the inlets. A mass flow inlet is often used when it is more important to match a pre-described mass flow rate than to match the total pressure of the inflow stream. In this experimental work the upstream water flow rate was defined, as was the air flow rate at standard conditions. The mass flow rate could therefore be replicated in the CFD simulation. This in conjunction with the simulation being validated based on pressure drop comparisons between the CFD simulation and the experimental work. It was therefore deemed that mass flow rate was the most appropriate inlet condition for both the water and air inlets. While at the outlet of the pipe, the pressure outlet condition was specified due to the convergence improvements (Mahmud, 2012).

Wall boundary conditions can be applied using different terms that depend on the situation, such as symmetry and periodic axis. In the case of viscous flows, the wall boundary condition can be specified as a no-slip boundary or by describing shear. Within the wall boundary conditions, the pipe wall roughness can be specified and in this work, an equivalent roughness of 0.0025 mm was specified as a typical value for plastic and Perspex pipes, using the Moody diagram in Massey (2006), with a no-slip boundary condition imposed.

8.18. Turbulence parameters

When using the k-ω model, two turbulence properties have to be provided for the two phases. The combinations given within the FLUENT code to identify these values are,

a) Turbulence intensity, TI, and length scale, l
b) Turbulence intensity and viscosity ratio, $\frac{\mu_t}{\mu}$
c) Turbulence intensity and hydraulic diameter, d_H

The turbulence intensity term can be calculated by,

$$TI = 0.16Re^{\frac{-1}{8}} \quad [8.15]$$

Usually the turbulence intensity for fluid simulations is specified as being between 1 and 10 % (ANSYS Inc, 2011b), for this experimental work with $U_w \approx 1$ and 3 ms^{-1}, TI was approximated to be between 3.5 and 4 %.

In the situation of fully developed pipe flows, turbulent length scales is limited by the flow path length because turbulent eddies cannot be greater than the conduit length. The turbulent length scale as recommended by ANSYS Inc (2011b) can be approximated by,

$$l = 0.07d \quad [8.16]$$

where 0.07 is an empirical constant based on the maximum value of the mixing length in a fully developed turbulent flow (ANSYS Inc, 2011b).

ANSYS Inc (2011b) recommends using turbulence intensity and length scale for the turbulence parameters when the physical length scale is not known, therefore specific dissipation rate, ω, cannot be calculated, where ω is approximated by Equation 8.17.

$$\omega = \frac{k^{\frac{1}{2}}}{C_{\mu} l} \qquad [8.17]$$

where $C_{\mu}$is an empricially derived constant and is approximated to be 0.09 (ANSYS Inc, 2011b).

The turbulent kinetic energy, k, is given by Equation 8.18.

$$k = (TI.u_{inlet})^2 \qquad [8.18]$$

8.19. Development of the multiphase flow model

Gas-liquid two-phase flow in a pipe is a complex multiphase and turbulent flow, governed by mass and momentum conservation, turbulence transport and interphase momentum transport. Therefore, the following assumptions were made in developing a theoretical model that characterises the air and water flow in this experimental work,

a) The two-phase pipe system temperature is constant, at an ambient temperature of 20 ˚C and the outlet pressure is at 101.325 kPa, which conforms to the standard conditions of the mass transfer testing, and each phase is isothermal and incompressible. It is recommended that for small pressure variations and for Mach numbers of less than 0.3 that incompressible flows can be assumed (ANSYS Inc, 2011b). In this experimental work Mach numbers are predicted to be considerably less than 0.3.

b) The two-phase flow is assumed to be a bubbly flow, where the operating conditions simulated were ones that displayed a full bubbly flow for the respective inserts in the physical experimentation. Therefore, the water will be treated as the continuous phase and the air will be treated and the dispersed phase.

c) Initially all bubbles sizes will be treated as uniform in size and exhibit a spherical shape, where the size will be based on the experimental measurements and bubble coalescence and breakage will be considered as negligible. However, the influence of bubble coalescence and breakage will be investigated later in this chapter using the Population Balance model, PBM, which will also be discussed later in this chapter.

d) Drag force and surface tension from the water acting on the air bubbles will be included in the interphase momentum exchange and interactions.

e) Lift force is considered to be negligible in the operating conditions where a bubbly flow is present. This is because the velocity slip ratio in the flow will be less than 1 for a full bubbly flow whose void fraction is less than 0.4 (Bhagwat & Ghajar, 2012). ANSYS Inc (2011a) recommends only including the lift force when there is a large slip velocity ratio or when flow separation is present. This in conjunction with the high computational expense associated with including the lift force, it was chosen to not include the lift force in the following simulations.

8.20. Domain description

In order to study the validity of the simulations against the experimental data, 3D simulations were performed with air and water as the dispersed and continuous phase respectively. The geometry consisted of dimensions similar to that in the experimental set up with a 0.1 m ID pipe, a 10 ID upstream section from the start of the inserts to the inlet boundary and a section of 22 ID downstream from the throat, which is representative of the distance to the surface of the water in the tank and therefore atmospheric conditions.

A grid with tetrahedral cells was generated using ANSYS Meshing software. All meshes were constructed to a maximum cell skewness of 0.95 and a minimum of 5 cells across any flow boundary, with inflation used from the walls and solid surfaces within the domain, as recommended by ANSYS Inc (2011b). To optimise the gird size it was necessary to carry out a grid-independence study. This was done by performing a number of simulations with different mesh sizes, starting from a coarse mesh and refining it until the results were no longer dependent on the mesh size. The results of which will be discussed later in Section 8.27.

8.21. Solution procedure

One of the FLUENT turbulence models is used to simulate the pressure drop and gas void fraction in a vertical pipe. In the FLUENT's E-E models, as described earlier in the Chapter, the gas-liquid volume fraction in each cell is equal to unity. The phases are assumed to share the space in proportion to their volume fractions, so as to satisfy the continuity relationship,

$$\sum_{i=1}^{n} \alpha_i = 1 \qquad [8.19]$$

where n is the number of phases.

The mass conservation equation for any phase can be written as,

$$\frac{\delta \rho_i}{\delta t} + \nabla . (\rho_i \vec{u}_i) = 0 \qquad [8.20]$$

and the momentum conservation equation, Equation 8.2, is solved through the whole domain.

Within this work the turbulence models k-ω SST and RSM with ω will be utilised where appropriate to simulate the turbulence eddies and to model the turbulence in the domain.

In order to solve the modelling equations the type of solver, number of phases, fluid properties, and operating and boundary conditions have to be specified.

Both segregated and coupled solvers are available with FLUENT. Using either method will solve the integral equations for conservation of mass and momentum and other scalar equations. The segregated solver has traditionally been used for incompressible flows, while the coupled formulation has a performance advantage over the segregated solver for high speed compressible flows. Furthermore, the segregated

solver normally takes a shorter time to converge solutions and requires less memory (Versteeg & Malalasekera, 1996). Therefore the segregated solver was selected for all models.

The Phase Coupled SIMPLE, PC-SIMPLE, segregated solver is an extension of the SIMPLE algorithm to multiphase flows. The SIMPLE algorithm uses a relationship between velocity and pressure corrections to enforce mass conservation and to obtain the pressure field. In PC-SIMPLE the velocities are solved, coupled by phases in a segregated fashion. Fluxes are reconstructed at the faces of the control volume and then a pressure correction equation is built based on total continuity. The coefficients of the pressure correction equations come from the coupled per phase momentum equations. This method has proven to be robust and is the only segregated solver usable across all of the multiphase models.

The operating conditions specified within FLUENT include gravity, operating pressure and density. A gravitational acceleration of 9.81 m/s^2 was applied in the appropriate direction. An operating pressure of 101.325 kPa was specified and an operating density equal to that of the lightest phase, which was air and therefore a density of 1.225 kg/m^3. Using the lightest phase density is said to improve convergence behaviour (ANSYS Inc, 2011b).

The boundary and initial conditions were specified as outlined in Section 8.17. The bubble size was initially specified as a fixed spherical bubble diameter. However, to improve the accuracy of the simulations the Population Balance Model, PBM, was used to predict the parameters of the air-water, two-phase downward flow.

8.22. Population balance model, PBM

In reality, during two-phase flow application, bubbles can break and aggregate due to interaction between other bubbles and with the liquid phase. Under these conditions a constant bubble size model may not be suitable for the simulation of a two-phase flow model. A single droplet size cannot properly describe the interfacial interactions that take place between the phases, such as mass transfer and the interfacial forces. Therefore, in order to develop a system design tool where the bubble diameter is important, as is the case in aeration. New simulation tools are required to take into account the bubble size distribution, which results from breakage and coalescence phenomena in the flow, where coalescence is also termed as aggregation. In FLUENT this can be performed using the PBM framework for illustrating the populations of the bubble sizes.

This section presents the PBM and available techniques to solve it, as well as demonstrating the available aggregation and breakage kernels. A two fluid Eulerian approach is used as the framework for this model and a population balance equation, PBE, is used to obtain the dispersed air droplet diameter distribution, pressure drop and air void fraction. A review of the population balance approaches can be found in Jakobsen et al (2005).

The PBE is a simple continuity statement and it can be derived as a balance for droplets in some fixed sub-region of internal-coordinate and physical space. Based on the PBM, the dispersed phase is expressed for a number density function, $n(\vec{x}, \phi, t)$, where $\vec{x}$ is a set of external coordinates which denote the spatial vector position of the bubble, ϕ is the internal coordinates of the bubble which could include volume, area or mass and t is time. Therefore, the average number of bubbles in the infinitesimal volume, $dV_{\vec{x}}dV_{\phi}$ is $n(\vec{x}, \phi, t)dV_{\vec{x}}dV_{\phi}$. Under these conditions the volume of a particle in state ϕ is given by $V(\phi)$ (ANSYS Inc, 2011c). Assuming that ϕ is the particle volume, the transport equation for the number density function is given by Equation 8.21, (ANSYS Inc, 2011c), where V is the particle volume.

$$\frac{\delta[n(V,t)]}{\delta t} + \nabla.[\vec{u}\, n(V,t)] + \nabla_v.[G_v\, n(V,t)] = \frac{1}{2}\int_0^V a(V-V',V)n\,(V-V',t)n(V',t)dV' - \int_0^\infty a(V',V)n\,(V,t)n(V',t)dV' + \int_{\Omega_V} pg\,(V')\beta\left(\frac{V}{V'}\right)n(V',t)dV' - g(V)n(V,t) \quad [8.21]$$

In Equation 8.21, $a(V', V)$ is the aggregation rate between bubbles of size V and V', $g(V)$ is the break up rate of bubbles of size V, $pg(V')$ represents the number of fragments, or daughter droplets which are generated from the breakage of a bubble of size V' and $\beta\left(\frac{V}{V'}\right)dV$, is the fraction of daughter bubbles having a size between V and $(V + dv)$, generated by the breakage of bubbles of size V'.

The first, second and third terms on the left hand side of Equation 8.21 are the accumulation, convection and growth rate terms. Whilst the first and second terms on the right hand side of Equation 8.21 accounts for the birth and death events related to aggregation and the third and fourth term relates to the birth and death events due to breakage processes.

8.23. Particle birth and death due to breakage

The breakage rate expression, or kernel consists of a breakage frequency, g, that describes the droplets splitting function per unit time and β which is the distribution of the daughter bubbles from the splitting mother bubble (Christian, et al., 2009).

$$g(V')\beta\left(\frac{V}{V'}\right) \quad [8.22]$$

Different models of the breakage rate of bubbles have been developed by several authors, Alpoaeus et al (2002), Andersson and Andersson (2006), Coulaloglou and Tavarides (1977), Hagesaether (2002), Lehr et al (2002), Luo and Svendsen (1996), Martinez-Bazan et al (1999) and Prince and Blanch (1990). The breakup expression accounts for the interaction of a single bubble with the turbulent continuous phase in which the bubble undertakes breakage if the turbulent kinetic energy transmitted to the droplet is higher than its surface energy (Coulaloglou & Tavlarides, 1977).

In most models, the researchers made an assumption that bubble deformation and breakup occurs under the influence of local pressure fluctuations in a locally isotropic flow field, or due to the arrival of turbulent

eddies to the surface of the bubbles. The new bubble diameter is mainly dependent on the turbulent energy dissipation. To obtain the daughter bubble distribution it is necessary to specify the number of daughter bubbles. Valentas et al (1966) utilised a normal density function for the daughter bubble distribution that assumes binary breakage. For binary breakage the breakage kernel must by symmetrical with respect to, (ANSYS Inc, 2011c).

$$\frac{V}{V'} = 0.5 \qquad [8.23]$$

As an alternative to using the binary breakup assumptions in the other models, a distribution as proposed by Bahmanyar and Slater (1991) can illustrate more than two daughter droplets. Other PDF's have been developed by Martinez–Bazan et al (1999) or Diemer and Olson (2002). However, binary breakup is more appropriate for bubbles (Mahmud, 2012).

The Luo model is commented in ANSYS Inc (2011c) as being the most widely used model for determining bubble breakage and therefore will be used as a starting point in this experimental work. The Luo model is an integrated kernel which encompasses both the breakage frequency and the PDF of breaking bubbles, where the general breakage rate per unit volume is given by Equation 8.22. Further details of the Luo model can be found in Luo and Svendsen (1996).

8.24. Particle birth and death due to aggregation

The process of bubble aggregation takes place due to the interaction between two bubbles and the turbulent continuous phase. The aggregation process among the bubbles is expected to occur if the intervening liquid film has sufficient contact time to be drained out (Chatzi & Lee, 1987). The aggregation source expression takes into account the aggregation kernel that considers the probability of successful collisions between two bubbles, V and V'. It is usually defined as a product of two quantities, the first is the frequency of the collisions, h, between bubbles of volume, V and V'. The second is the efficiency of the collisions, λ, the efficiency of the collisions is the probability that the bubble of volume V, will coalesce with a bubble of volume V'. The aggregation kernel is expressed as,

$$a(V', V) = h(V', V) \times \lambda(V', V) \qquad [8.24]$$

ANSYS Inc (2011c) comments that in gas-liquid dispersion the aggregation kernels are primarily a function of the local liquid phase turbulent dissipation, it is for this reason that the turbulent aggregation kernel within the FLUENT software will be used in this experimental work.

During the mixing processes, mechanical energy is supplied to the fluid. This energy creates turbulence within the fluid. This turbulence creates eddies which in turn help dissipate the energy. The energy is transferred from the largest eddies to the smallest eddies in which it is dissipated through viscous interactions. The size of the smallest eddies is the Kolmogorov micro scale, η, which is expressed as a function of the kinematic viscosity and turbulent energy dissipation rate, shown in Equation 8.25.

$$\eta = \left(\frac{\nu^3}{\varepsilon}\right)^{\frac{1}{4}} \qquad [8.25]$$

In the turbulent flow field, aggregation can occur by two mechanisms, the first is a viscous sub-range mechanism which is applied when bubbles are smaller than the Kolmogorov micro scale, where the collision of the bubbles is influenced by the local shear within the eddy (ANSYS Inc, 2011c). The second mechanism is when the bubbles are bigger than the Kolmogorov micro scale or smallest eddy in this instance an inertial sub-range mechanism is applied. In this case the bubbles assume independent velocities and are therefore dragged via these velocity fluctuations (ANSYS Inc, 2011c). Further information about the turbulent aggregation kernel can be found in ANSYS Inc (2011c).

8.25. PBM numerical methods

In FLUENT there are three solution methods to the PBE, the discretised population balance method, termed discrete, the standard methods of moments, termed SMM, and the quadrature method of moments, termed QMOM.

The discrete method was developed by Ramkrishna (2000), in this method the bubble population is discretised into a finite number of size intervals. This approach has the advantage of computing the bubble size distribution directly. This approach is also particularly useful when the range of particle sizes is known and does not span more than two or three orders of magnitude. In this case, the population can be discretised with relatively small number of size intervals and the size distribution that is couple with fluid dynamics can be computed. The disadvantage of the discrete method is that it is computationally expensive if a large number of intervals are needed. However, due to the importance of being able to accurately predict the bubble sizes and therefore be able to determine the interfacial area for mass transfer. The discrete method is a suitable starting point, where the outlet bubble size will be the measured bubble size for the experimental work and the inlet bubble size will be equal to that of the air inlet orifice.

The SMM is an efficient alternative to the discrete population balance approach and was developed by Randolph and Larson (1971). In this approach the PBE is transformed into a set of transport equations for moments of distribution. The ith moment is defined by integrating the number density throughout the bubble space, weighted with the bubble property raised to the ith power (ANSYS Inc, 2011c). Typically 3 to 6 moment equations are solved, which lowers the computational requirements compared to the discrete method (ANSYS Inc, 2011c). The first four moments are generally used, the zeroth moment represents the total number density, the first moment represents the total length, the second moment represents the total surface area per unit volume and the third moment represents the total mass density (Randolph & Larson, 1971). In the SMM approach, no assumptions are made about the size distribution and the moment equations are formulated in a close form involving only functions of the moments themselves. The disadvantage is that exact closure of the right hand side of Equation 8.21 is only possible in cases of constant aggregation and size-independent growth, also bubble breakage modelling is difficult because it cannot be described as a function of moments (Mahmud, 2012).

The closure constraint however, is overcome through QMOM which has similar advantage to the SMM in terms of computational costs but replaces the exact closure needed by SMM with an approximate closure. The approach was developed by Marchisio et al (2003) to include the aggregation and breakage processes. In the QMOM model the ith moment is described by integrating the function of the population number density with respect to specific population property, such as bubble size, weighted with this property to its ith power.

It is for the reasons described above that the discrete method will be used to generate a CFD simulation for the experimental work. Especially, due to the importance of being able to accurately predict the bubble sizes and therefore be able to determine the interfacial area for mass transfer, which is paramount in designing an aerator.

8.26. Validation of CFD model

To achieve validation of the CFD simulations used in this study, the pressure drop across various sections of the pipe were compared to experimental data measurements. The objective was to attempt to validate the CFD models and therefore establish confidence in the numerical results. Various stages of the validation process are described below.

Initially, simulations were established for the HV1 insert with just the water phase, for U_w = 1, 2 and 3 ms^{-1}. In this work an assessment of the three turbulence models, k-ε, SST and RSM were used. The calculated pressure differential from US1 to the throat and from the throat to the DS3 pressure measurement location, as well as their associated pressure loss factor, Λ, calculated using Equation 3.23 are shown in Table 8.1, where the pressure measurements locations are shown in Figure 8.3 for all the CFD simulations in the following sections.

Table 8.1: - Comparison of the experimental data to the CFD simulations for the three turbulence models, k-ε, SST and RSM conducted using the HV1 insert for U_w = 1, 2 and 3 ms^{-1}.

		US			DS3		
U_w (ms^{-1})		ΔP (Pa)	Λ_{US}	Difference* (%)	ΔP (Pa)	Λ_{DS3}	Difference* (%)
≈ 1	k-ε	64.3	0.06	100.0	347.3	0.34	17.2
	SST	96.3	0.09	200.0	341.3	0.33	13.7
	RSM	100.3	0.10	233.3	374.3	0.36	24.1
	Experimental data	29.53	0.03	-	293.1	0.29	-
≈ 2	k-ε	281.2	0.07	75.0	1293.2	0.31	- 16.2
	SST	251.2	0.10	51.2	1539.1	0.37	0.0
	RSM	115.2	0.03	- 25.0	1153.2	0.28	- 24.3
	Experimental data	166.1	0.04	-	1561.6	0.37	-
≈ 3	k-ε	655.6	0.07	- 36.4	2813.6	0.30	- 21.0
	SST	1138.6	0.12	9.1	3347.6	0.36	- 5.3
	RSM	468.6	0.05	- 54.5	2635.6	0.28	- 26.3
	Experimental data	1036.8	0.11	-	3582.6	0.38	-

* difference is defined as $\frac{\Lambda_x - \Lambda_{experimental}}{\Lambda_{experimental}}$ x 100 %

Only the Throat to DS3 pressure differential location is shown in Table 8.1 because there was a similar trend across the downstream measurement locations. The percentage difference between the Λ for the CFD simulations and the experimental data is also highlighted in Table 8.1.

As can be seen in Table 8.1, the SST turbulence model has a good correlation with the experimental data, for the DS3 pressure loss factor with errors of less than 15 %. The correlation improves as U_w increases and therefore as turbulence increases. However, there is a significant difference between the Λ_{US} for the experimental data and all CFD simulations for the vast majority of cases. On closer inspection, it can be seen that the SST turbulence model closely conforms to the experimental data at U_w = 3 ms^{-1}, which is the flow rate of interest for the following CFD simulations. This is because U_w = 3 ms^{-1} was the only water flow rate where a bubbly flow was present across multiple inserts. The accuracy of the CFD simulations increased with the refinement of the grid, as will be shown in Section 8.27.

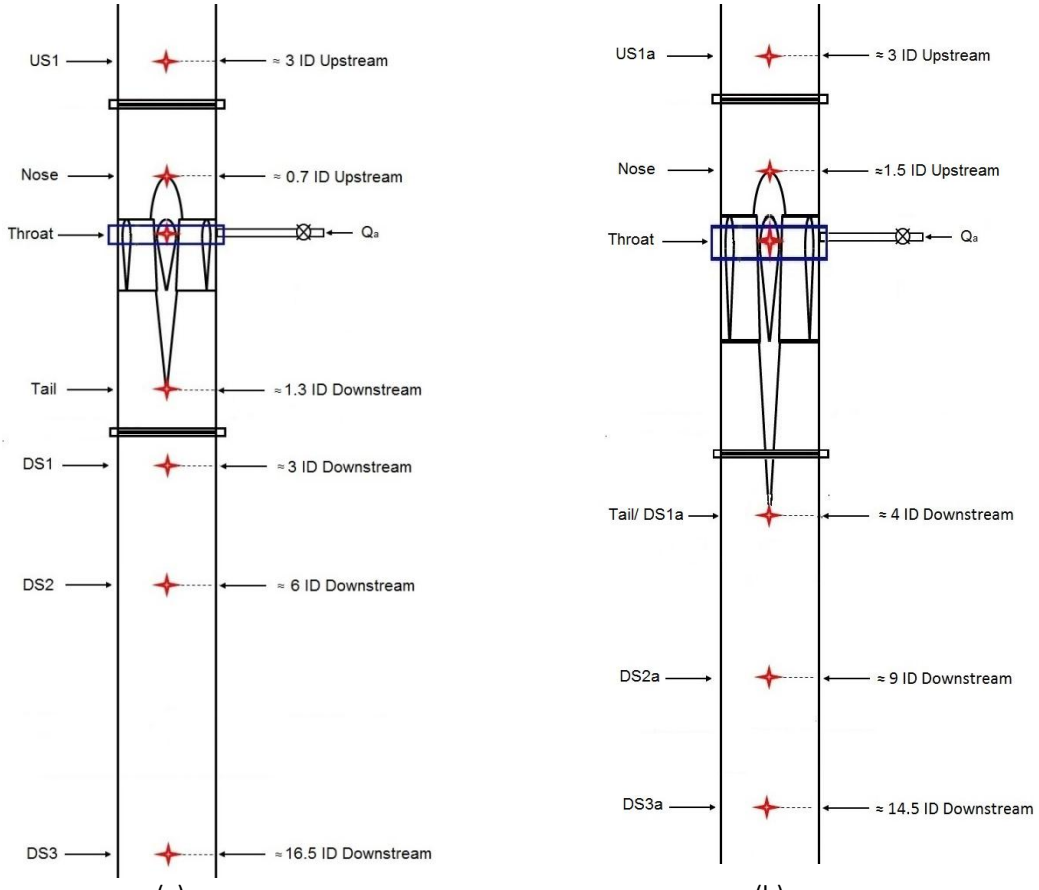

(a) (b)

Figure 8.3: - Pressure tapping locations for CFD simulations of (a) HV1 insert and (b) A1 and A2 inserts.

Figure 8.3 shows the pressure tapping locations and positions considered from the CFD simulation for the HV1, and the A1 and A2 inserts, where the datum is at the throat of the inserts. As can be seen the locations of the measurements vary between the HV1 insert, and A1 and A2 inserts. This is because of the A1 and A2 inserts are considerably longer than the HV1 insert. Due to the extended length of the A1 and A2 inserts, the Tail pressure tapping location in the experimental work and therefore the CFD simulations is in the same location as the DS1a measurement location, which is shown in Figure 8.3 (b).

To achieve validation of the multiphase simulations, several turbulence and multiphase models were used along with various specifications of the air bubble size. Each of the models has advantages, disadvantages, limitations and appropriate flow regimes for which they should be used to predict. An abundance of turbulence models exists in the literature, for example ANSYS Inc (2011a) and Mahmud (2012). However, there are no quantitative guidelines for choosing an appropriate turbulence model for a multiphase flow (Mahmud, 2012). In this section of the work an assessment of two turbulence models, SST and RSM were used because of the recommendations in ANSYS Inc (2011a), outlined in Sections 8.15 and 8.16, and the results in Table 8.1. In conjunction with these turbulence models, two multiphase models, VOF and E-E along with a number of bubble size specification techniques were used because of the recommendations in ANSYS Inc (2011a) and outlined in Section 8.7. For example, a fixed bubble diameter specification was used, where 3 or 5 mm was specified. In addition to this, the PBM method was investigated for predicting the bubble size. Also the turbulence intensity, TI, at the air inlet was adjusted from 4 % as recommended by Equation 8.15, to a significantly higher value of 30 % to assess its impact on the pressure loss in the system.

Figure 8.4 shows the range of the models used to simulate the operating conditions of U_w = 3 ms^{-1} and Q_a = 50 slm for the HV1 insert. Figure 8.4, illustrates the pressure profile along the downcomer and across the insert at the measurement points illustrated in Figure 8.3 (a) for U_w = 3 ms^{-1} and Q_a = 50 slm, for the HV1 insert, for the various turbulence and multiphase models, and bubble specification methods.

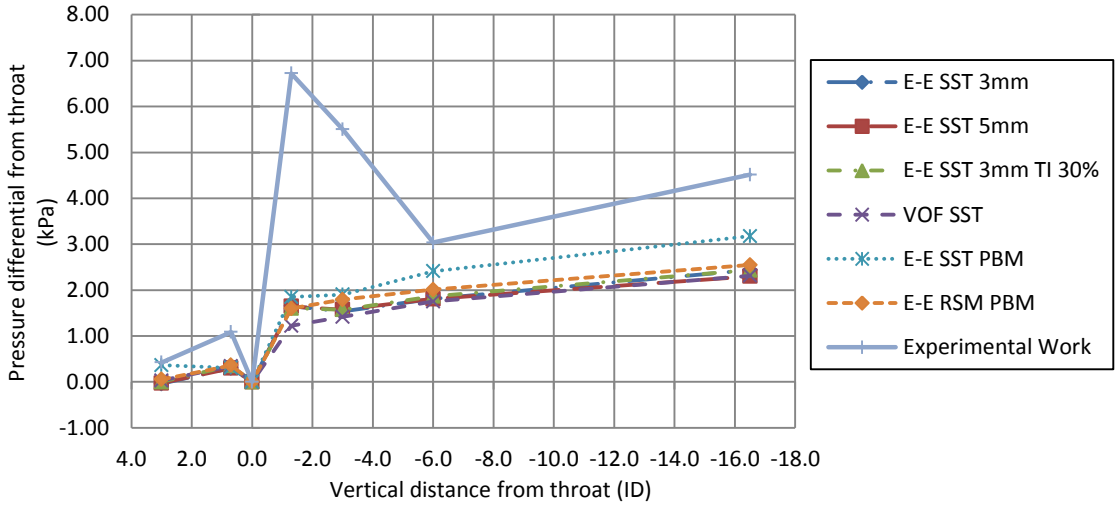

Figure 8.4: - Shows the comparison of pressure gradient between the experimental data and different simulation models.

It can be seen in Figure 8.4 that there is considerable differences between the experimental data and the CFD simulations for the pressure locations of the Tail and DS1 measurements, which are - 1.3 and - 3 ID from the throat respectively. However, the trend is comparable to the experimental data, where there is an increased pressure differential to the Tail location, which then reduces to the DS1 location, which is 3 ID below the throat. There is then a steadily increasing gradient from DS1 to DS3, which is 16.5 ID downstream of the throat. However, overall the CFD simulations do underestimate the pressure differential across all locations, which is more significant at the Tail and DS1 measurement locations.

From the various bubble diameter specification simulations, it can be seen in Figure 8.4 that increasing the bubble diameter or the TI of the air inlet, did not significantly affect the overall pressure drop downstream of the insert. However, coupling the PBM method with the E-E and SST simulation significantly affected the downstream pressure drop, where the E-E SST PBM simulation had a steeper gradient, which was more representative of the experimental data. In contrast to the other simulations, where they all had a similar gradient between 6 and 16.5 ID downstream of the insert.

The gradient of the pressure profile of the experimental work, in Figure 8.4, is significantly increased compared to the CFD simulations, which represents an increased pressure loss in the downstream section of the experimental data compared to the simulations. This could be caused by the surface of the pipe, in the physical experiments there were several channels around the circumference of the pipe, which were approximately 4 mm in width and depth. These channels were as a result of the various lengths of pipe being connected, as can be seen in Figure 4.1. These channels could result in turbulent eddies forming within them, which would result in flow separation and therefore an increased pressure loss. Overall it can be seen in Figure 8.4, that the E-E SST PBM simulation has the closest agreement with the experimental data in terms of the pressure gradient and predicted pressure losses, when compared to the other simulations tested. Therefore, this model has been chosen of further sensitivity analysis.

8.27. Grid independence test

The aim of the grid independence test was to determine the minimum grid resolution required to generate a solution using the E-E SST PBM model, which was shown to give the best prediction in Figure 8.4. Due to the complex nature of the HV1 insert, a number of element sizing techniques were utilised in order to a achieve the required standard of, a maximum cell skewness of 0.95, a minimum of 5 cells across any inlet and the use of inflation on the solid surfaces. As a result of the geometry of the insert, the maximum cell sizes possible to achieve the maximum skewness of 0.95 was 1.4 mm on the body of the insert and 0.6 mm on the air inlet faces and around the air slot location. Along with these specifications, a minimum and maximum domain face sizing of 0.01 mm and 10 mm respectively were defined to ensure the above criteria. This initially produced a grid size of approximately 2.6 million cells. This grid was used as the basis for the lower level of the grid independence test. From this, the size of the face sizing across the surface of the insert was reduced to 1 mm, and the air inlets and their associated faces were reduced to 0.4 mm in size. Producing a grid size of approximately 3.6 million cells. From this, a third grid was established using a insert face size of 0.6 mm, and an air inlet and associated face sizing of 0.4 mm was used which generated a grid size of approximately 5.5 million.

Figure 8.5, shows comparison between the CFD grid sizes with respect to the pressure profile along the downcomer and across the insert, against the experimental data for U_w = 3 ms^{-1} and Q_a = 50 slm. The errors between the CFD simulations and the experimental data are shown in Table 8.2. Also shown in Table 8.2 is the amount of time steps required to achieve a stable solution along with the computing time per time step.

In general it can be seen that the specification method of an insert cell size of 1.0 mm and air inlet size of 0.4 mm is acceptable for the meshing of the insert and downcomer.

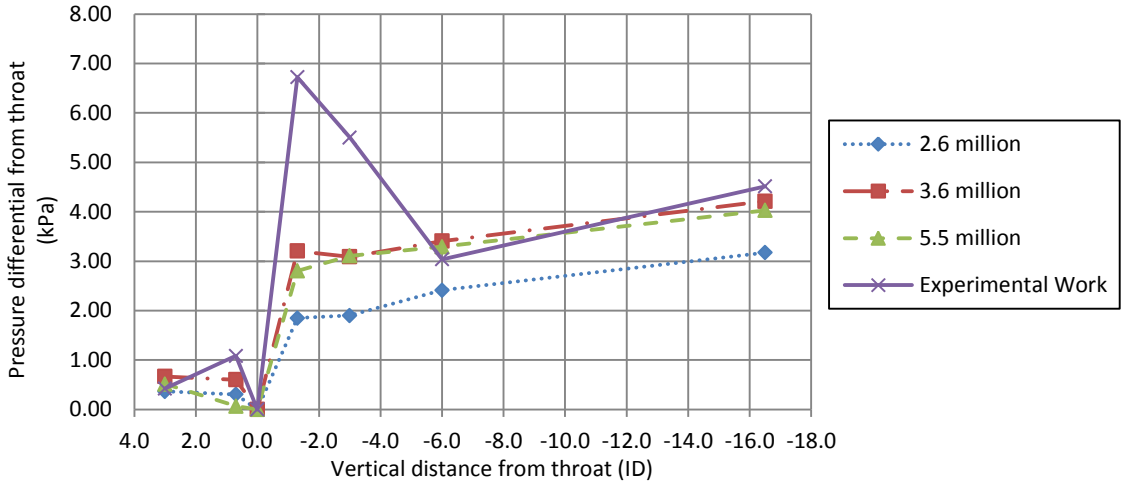

Figure 8.5: - Effect of grid size on pressure drop using the E-E SST PBM model at U_w = 3 ms^{-1} and Q_a = 50 slm for the HV1 insert.

Table 8.2: - Percentage error from experimental data showing the effect of grid size on pressure drop using the E-E SST PBM model at U_w = 3 ms^{-1} and Q_a = 50 slm for the HV1 insert.

			% Differential from experimental data					y^+ at Tail on	
Grid Size (x 10^6)	Time steps	Time per step (hh:mm)	US	Tail	DS1	DS2	DS3	Insert	Pipe wall
≈ 2.6	200	≈ 00:21	- 14.10	- 72.51	- 65.43	- 20.54	- 29.68	< 20	< 60
≈ 3.6	200	≈ 00:30	22.36	- 52.31	- 43.51	12.16	- 6.68	< 12	< 30
≈ 5.5	200	≈ 00:56	21.52	- 58.29	- 43.49	8.44	- 10.7	< 10	< 30

Despite the higher difference between the predicted numerical simulation results and the experimental data around the insert of the Tail and DS1 pressure measurement locations. The close approximation upstream and further downstream of the insert at the DS2 and DS3 pressure measurement locations shows that despite the initial errors, the predicted pressure drop across the insert and further downstream in the downcomer is in good agreement with the experimental data. When analysing the overall pressure drop from the US to DS3 location of the CFD simulations, it can be seen in Figure 8.5 that overall they CFD simulations closely conform to the experimental results, within approximately 28 %, 1 % and 8 % for the 2.6, 3.6 and 5.5 million grids respectively.

The reason for the variation in the pressure measurements of the CFD simulations compared to the experimental results, which are shown in Figures 8.4 and 8.5, could be due to the fineness of the grid. Table 8.2, shows the average y^+ values on the pipe wall and the insert at the location of the Tail pressure measurement, where y^+ is a non-dimensional wall distance for a wall-bounded flow and can be defined by,

$$y^+ = \frac{u^* y}{\nu} \qquad [8.26]$$

For the SST turbulence model, it is recommended by ANSYS Inc (2011a) that each wall-adjacent cell's centroid should be located within the log-law layer, 30 < y^+< 300. A y^+ value close to the lower bound y^+ = 30 is most desirable (ANSYS Inc, 2011a). The results in Table 8.2 show that y^+ values of the simulations are

close to 30 for the 3.6 and 5.5 millions cell grids, and there is still a high level of variation in the pressure measurements at the Tail compared the experimental data, by up to 60 %. Therefore, other turbulence models which are more accurate in modelling turbulence in the near wall region, such as LES, would need to be investigated, to more accurately model the turbulence along the insert and the pipe wall, and therefore capture all the information in terms of velocity and pressure profiles in the near wall region. Despite this, the overall pressure loss from the US to DS3 pressure location for the 3.6 million grid simulation closely conforms to the experimental data, approximately within 1 %.

8.28. A1 Insert simulation

Along with the HV1 insert the A1 insert displayed a fully developed bubbly flow in the downcomer at U_w = 3 ms^{-1} and Q_a = 50 slm. The A1 insert displayed considerably higher pressure loss and showed significant coring of the air under these operating conditions. Therefore, by running a simulation of this insert will show the validity of the E-E SST PBM model across a wide range of insert characteristics and profiles, such as higher blockage ratios and an increased swirl. Using the same grid specification techniques as for the HV1 insert, which included a face sizing of 1.0 mm on the surface of the insert and a 0.4 mm face sizing on the air inlets and their associated faces. This generated a grid of approximately 4.2 million cells for the A1 insert.

Figure 8.6 shows the comparisons of an E-E SST PBM simulation and an E-E RSM with EWT PBM simulation, against the experimental findings for the A1 insert. The usage of RSM is recommended for flows which are predicted to have swirl and rotation, which has been identified for the A1 insert in Chapter 5, with the coring of the air. Therefore, the RSM turbulence model may be required to establish greater accuracy for these flow conditions, which exhibited swirl. Table 8.3 highlights the percentage error of the simulations.

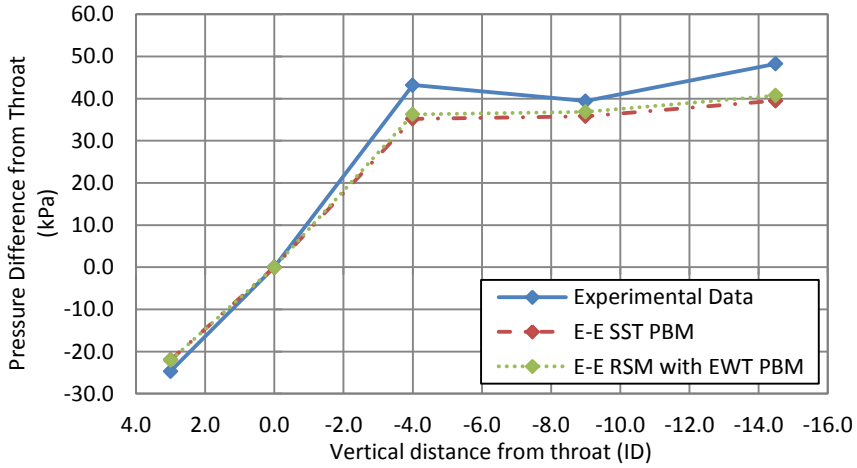

Figure 8.6: - Effect of turbulence model on predicted pressure drop, using the E-E PBM with SST and RSM with EWT simulations, at U_w = 3 ms^{-1} and Q_a = 50 slm for the A1 insert.

Figure 8.6 and Table 8.3 show good agreement between the CFD simulation and the experimental data, with the RSM EWT simulation having the lowest percentage error when compared to the experimental data, less than 16 %. However, the RSM EWT simulation took approximately twice the time, when compared to the SST simulation, for only marginally improved results, where the percentage difference of the SST simulation

was typically less than 19 %. The overall percentage difference in pressure loss between the SST and RSM EWT simulations and the experimental data from the US to DS3a pressure measurement locations, were approximately - 26 and - 21 % respectively.

Table 8.3: - Percentage error from experimental data showing the effect of turbulence model on pressure drop, using the E-E PBM with SST and RSM with EWT at U_w = 3 ms^{-1} and Q_a = 50 slm for the A1 insert.

	US1		TAIL/ DS1a		DS2a		DS3a	
	ΔP (kPa)	Difference* (%)	ΔP (kPa)	Difference* (%)	ΔP (kPa)	Difference* (%)	ΔP (kPa)	Difference* (%)
E-E SST PBM	-21.97	- 11.04	35.19	- 18.54	35.80	- 9.14	39.49	- 18.18
E-E RSM EWT PBM	-22.04	- 10.74	36.49	- 15.54	37.05	- 5.97	40.88	- 15.31
Experimental Data	-24.69		43.20		39.40		48.26	

* difference is defined as $\frac{\Delta P_x - \Delta P_{experimental}}{\Delta P_{experimental}}$ x 100 %

Figure 8.7 shows the air distribution at the DS3a location, for the SST and RSM EWT simulations with a photograph from the experimental work. Figure 8.7 (c) shows the significant coring of the air in this experimental work, with a peaked distribution at the centre of the downcomer spanning approximately 40 to 50 mm across the centre of the pipe, 0.4 to 0.5 ID respectively.

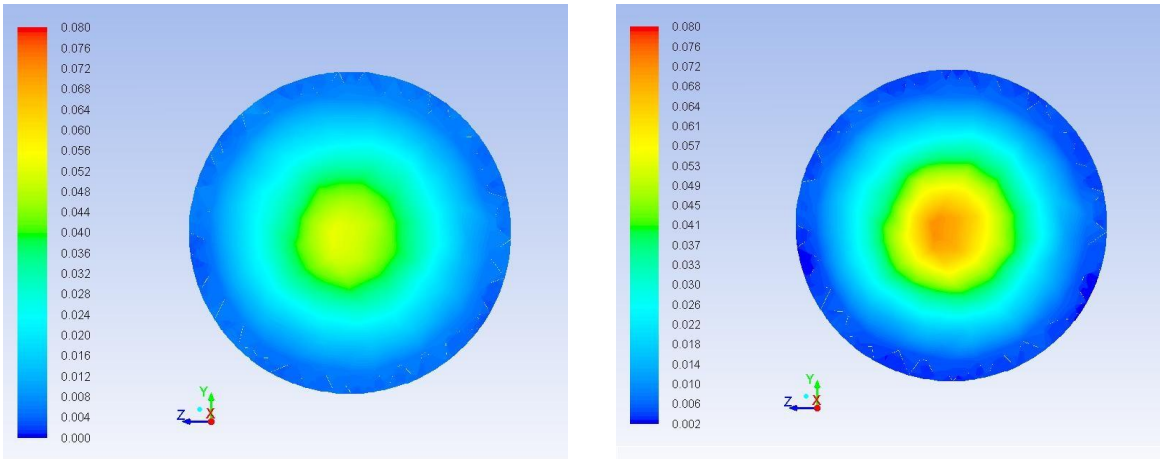

(a) (b)

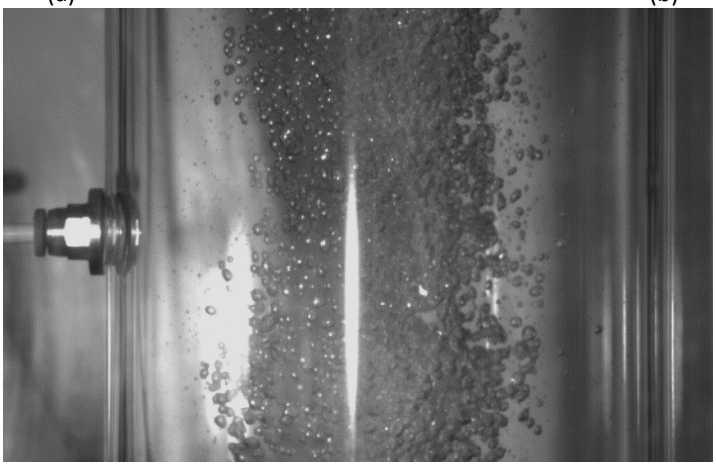

(c)

Figure 8.7: - The air distribution in the downcomer at DS2 which is - 1.45 m, 14.5 ID from the point of air injection for (a) the E-E RSM EWT PBM and (b) the E-E SST PBM simulations, and (c) the experimental data.

Figure 8.7 (a) and (b) show that the RSM with EWT and SST CFD simulations both predict coring, with a peaked central air distributions and a void fraction of < 1 % near the pipe wall. This is a similar pattern to

what is shown for the experimental work, Figure 8.7 (c). The peaked air void fraction in the centre of the pipe for the SST and RSM with EWT simulations were approximately 6 and 8 % respectively, where the void fraction for the specified flow rates is 3.42 %. The SST model predicted a peak distribution of 43 mm in diameter, whereas the RSM model predicted 32 mm in diameter, 0.43 and 0.32 ID respectively. The increased peak distribution of the RSM can be attributed to the RSM's improved handling of anisotropic turbulence, where the anisotropy of the turbulence in the downstream flow of the A1 insert has a dominant effect on the mean flow. This is in comparison to the SST model, which assumes an isotropic turbulent viscosity (ANSYS Inc, 2011a). Despite this, the SST simulation predicts a coring, which is closer in diameter to the experimental data, with a diameter of 43 mm.

Despite the differences in the modelling of turbulence between the SST and RSM simulations, they both produce a similar level of error between them and the experimental data. Therefore, considering the extended time required for the RSM EWT model for only minor improvements in the results. In conjunction, with the SST simulation better predicting the coring of the air, the SST simulation will provide a suitable approximation for predicting the pressure loss for the range of inserts tested in this study.

8.29. A2 insert simulation

Along with the HV1 and A1 inserts, the A2 insert displayed a fully developed bubbly flow in the downcomer at U_w = 3 ms-1 and Q_a = 50 slm. The A2 insert along with the A1 insert displayed a considerably higher pressure loss than the HV1 insert. The A2 insert did not induce a swirl into the flow, due to the symmetry of its vanes. This in conjunction with the findings in Section 8.28, the RSM model was not used for the simulation of the A2 insert. Again using the same grid specification techniques for the A2 insert as for the HV1 insert, which included a face sizing of 1.0 mm on the surface of the insert and a 0.4 mm face sizing on the air inlets and their associated faces. This generated a grid of approximately 4.5 million cells for the A2 insert.

Figure 8.8 and Table 8.4 show the comparison of the E-E SST PBM simulation against the experimental findings for the A2 insert, as well as the percentage error from the simulation to the experimental results.

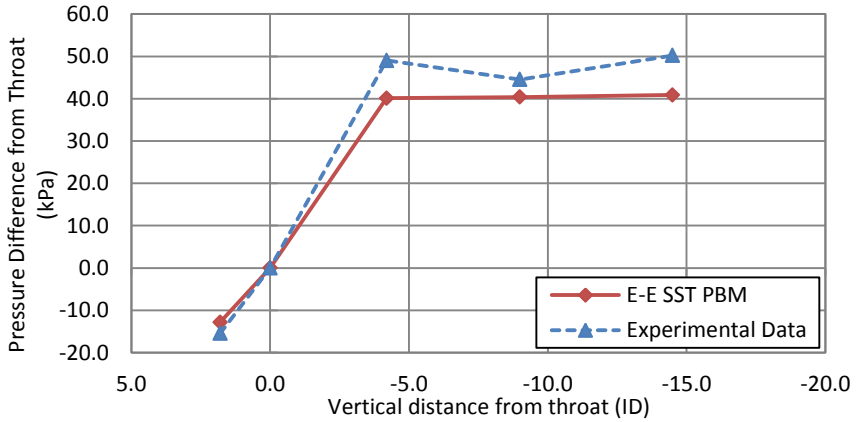

Figure 8.8: - Effect of turbulence model on pressure drop, using the PBM coupled with E-E SST at U_w = 3 ms^{-1} and Q_a = 50 slm for the A2 insert.

Table 8.4: - Percentage error from experimental data showing the effect of turbulence model on pressure drop using the E-E PBM with SST at U_w = 3 ms^{-1} and Q_a = 50 slm for the A2 insert.

	US1		TAIL/ DS1a		DS2a		DS3a	
	ΔP (kPa)	Difference (%)	ΔP (kPa)	Difference* (%)	ΔP (kPa)	Difference* (%)	ΔP (kPa)	Difference* (%)
E-E SST PBM	-12.83	- 16.94	40.12	- 18.17	40.39	- 9.32	44.18	- 17.44
Experimental Data	-15.45		49.02		44.54		53.51	

* difference is defined as $\frac{\Delta P_x - \Delta P_{experimental}}{\Delta P_{experimental}}$ x 100 %

Figure 8.8 and Table 8.4 shows a good agreement between the CFD simulation and the experimental data, with the E-E SST PBM simulation for the A2 insert, with percentage errors at the individual pressure measurement locations of approximately 18 %. The overall pressure loss between the US and DS3a pressure measurement location was found to be approximately - 19 %, when compared to the experimental data.

In summary, Figures 8.6 and 8.8 shows that the CFD simulations under predict the pressure losses for the A1 and A2 inserts. However, the predicted pressure losses for the CFD simulations are within 20 % of the experimental findings for the individual pressure measurement locations and up to 26 % across the length of the downcomer, from the US to DS3a pressure measurement location. Chapter 7 identified that the A1 and A2 inserts had the smallest overall aeration efficiencies, due to their higher blockage ratio. Therefore, it would be unlikely that any design improvements to the inserts would involve increasing the blockage ratio of the HV1 insert. As a result the increased errors between the A1 and A2 inserts CFD simulations and the experimental results, is not of a huge concern. This is because the CFD simulation errors for the HV1 insert with the SST model were shown in Table 8.2 for the 3.6 million cell grid to be within 10 % of the experimental results for the individual pressure measurement locations, with an error across the entire length of the downcomer, US to DS3, of approximately 1 %. Therefore, the SST E-E model coupled with the PBM method provides a suitable simulation for predicting the pressure losses and air core size involving an insert in a downward two-phase flow.

8.30. Predicted interfacial area and overall oxygen transfer coefficients

The discrete method was used in the CFD simulations for predicting the bubble size distribution. In this method the bubble size population is discretised into a finite number of size intervals, which are identified in Table 8.5.

Table 8.5: - List of size intervals used for Discrete PBM simulations.

Bin	Size interval (mm)
0	25.398
1	16.0
2	10.079
3	6.35
4	4.0
5	2.52
6	1.587
7	1.0

The intervals are achieved by defining a minimum bubble size, the required number of intervals and the

ratio exponent, which in the ratio between the bubble size intervals, for example Bin 7 to Bin 6. The default value in FLUENT is 1.587, which was found to give a range of bubble sizes that spanned the measured bubble sizes in the laboratory scale experimental work. The Discrete approach is useful when the range of particle sizes is known and they do not span more than two or three orders of magnitude. The outlet bubble size was specified as the measured bubble size within the experimental work and the inlet bubble size specified was set as equal to that of the inlet orifice.

Figure 8.9 shows the bubble size distribution of the HV1, A1 and A2 inserts at U_w = 3 ms^{-1} and Q_a = 50 slm.

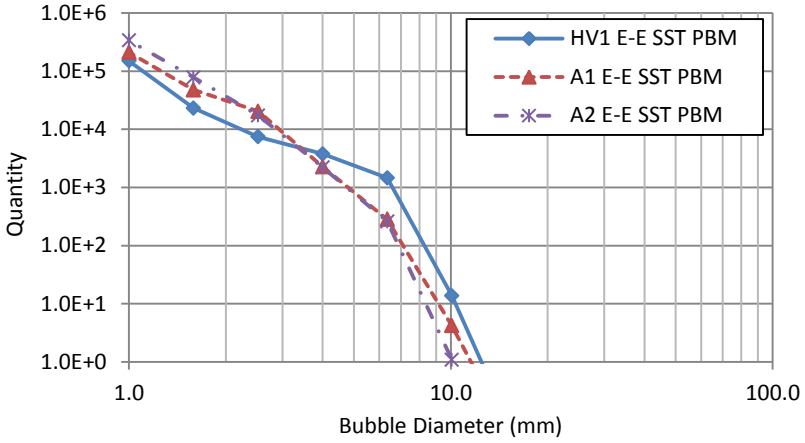

Figure 8.9: - Bubble size distribution through the downcomer at U_w = 3 ms^{-1} and Q_a = 50 slm, for the HV1, A1 and A2 inserts modelled using PBM coupled with E-E and SST.

Figure 8.9 shows that the A1 and A2 inserts have a significantly high quantity of bubbles at the lower bubble size interval, below 2.52 mm, than the HV1 insert. In contrast, the HV1 insert has a considerably higher number of bubbles above 2.52 mm. Therefore, it is predicted that the A1 and A2 inserts will have a smaller Sauter mean bubble diameter, than the HV1 insert.

The calculated Sauter mean bubble diameter from the simulations and experimental work are shown in Table 8.6, along with the percentage difference between these predicted values and the experimental values.

Table 8.6: - Details of the predicted Sauter mean bubble diameter from the CFD simulations and the experimental work at U_w = 3 ms^{-1} and Q_a = 50 slm.

Insert, Simulation	Simulation d_{32} (mm)	Experimental d_{32} (mm)	Difference (%)
HV1 E-E SST PBM	2.63	2.53	3.95
A1 E-E SST PBM	1.87	1.80	3.89
A2 E-E SST PBM	1.65	1.57	5.10
Average: -	2.05	1.97	4.3
St Dev (%): -	± 25.28	± 25.49	15.8

Table 8.6 shows that the predicted Sauter mean bubble diameter in the simulations for HV1, A1 and A2 inserts are in good agreement with the experimental work. The predictions of all three simulations were within 6 % of their respective experimental values. However, the predicted values are slightly higher than the experimental values, which would correlate to a decreased interfacial area and therefore a decreased prediction of mass transfer. It was identified in Sections 8.27, 8.28 and 8.29 that the pressure loss in the

simulations of the HV1, A1 and A2 inserts were under predicted compared to the experimental results, by between 1 and 26 %. Therefore, as a result of this reduced pressure loss and therefore lower levels of turbulence, it is expected that there would be a decreased level of bubble breakage in the downcomer, compared to the experimental work. As a result, it is expected that the simulations would over predict the Sauter mean bubble diameter, as because bubble breakage is a function of shear stress and turbulence (Martin, et al., 2009).

In addition to extracting the Sauter mean bubble diameters from the CFD simulations it is also possible to predict the Sauter mean bubble diameter from the determined specific power of the simulations. The Specific power can be calculated using the predicted pressure loss in the simulations, which are shown in Figures 8.5, 8.6 and 8.8, in conjunction with Equation 3.3. Using the specific power consumption in combination with Equation 6.7, which was established for determining the Sauter mean bubble diameter from this experimental work based on the specific power, will give an alternate prediction of the Sauter mean bubble diameter.

The calculated specific power consumption from the CFD simulations is presented alongside the experimental values in Table 8.7.

Table 8.7: - Details of the predicted Specific power consumption from the CFD simulations and the experimental results, at U_w = 3 ms^{-1} and Q_a = 50 slm.

Insert, Simulation	Simulation E (W/m^3)	Experimental E (W/m^3)	Difference (%)
HV1 E-E SST PBM	254.5	274.1	7.15
A1 E-E SST PBM	752.0	867.0	15.29
A2 E-E SST PBM	1102.2	1262.0	14.49
Average: -	0.7049	0.8010	
St Dev (%): -	± 59.98	± 62.07	

As expected the results in Table 8.7 show a similar reduction in the specific power of the simulations as a percentage, compared to the pressure loss predictions. The pressure loss predictions are shown in Tables 8.2, 8.3 and 8.4, with a reduced prediction in the specific power consumption by approximately 7 to 15 %.

Table 8.8 shows the calculated Sauter mean bubble diameters, using Equation 6.7, alongside the experimental values. It is shown that the A1 and A2 insert simulations have a good agreement with the experimental findings, with differences of less than 4 %. However the result of the HV1 simulation does not have as close agreement with a difference of over 12 %. Leading to nearly a 91 % standard deviation in the differences of the three simulations.

Table 8.8: - The predicted Sauter mean bubble diameter using Equation 6.7, for the CFD simulations compared to the experimental values for U_w = 3 ms^{-1} and Q_a = 50 slm.

Insert, Simulation	Simulation d_{32} (mm)	Experimental d_{32} (mm)	Difference (%)
HV1 E-E SST PBM	2.84	2.53	12.25
A1 E-E SST PBM	1.87	1.80	3.89
A2 E-E SST PBM	1.60	1.57	1.91
Average: -	2.10	1.97	6.0
St Dev (%): -	± 31.0	± 25.5	91.2

Tables 8.6 and 8.8 show that the Sauter mean bubble diameter has been over predicted in the CFD simulations. Extracting the Sauter mean bubble diameters from the CFD simulations, Table 8.6, is shown to have the closest agreement across the three simulations, with an average percentage difference value of 4.3 %. This is compared to an average value of 6.0 % in Table 8.8. Table 8.8, does show a closer agreement for the A1 and A2 insert simulations. However, there is a greater standard deviation across the three simulation difference values, with a value of 91.2 %. This is in comparison to a standard deviation value of the differences of 15.8 % in the results shown in Table 8.6. Therefore, there is a greater level of confidence with the values predicted in Table 8.6, the extracted Sauter mean bubble diameter. In comparison to calculating the Sauter mean bubble diameter using the specific power, in conjunction with Equation 6.7.

It is stated in Mahmud (2012) that the Luo bubble breakage model can under predict bubble breakage for bubble sizes greater than 0.1 mm, when compared to experimental data. The experimental investigation and modelling of breakage phenomena and daughter bubble distribution in gas and liquid, two-phase flow systems is a current research area (Andersson & Andersson, 2006; Mahmud, 2012). Thus, it is to be expected that there would be some variations in the results between the experimental findings and the CFD simulations. However, the predicted values in the CFD simulations within this experimental work have an acceptable level of error between them and the experimental results, typically around 4.3 %.

Table 8.9 shows the overall oxygen transfer coefficient, $k_L a_{20}$, from the experimental work, the predicted interfacial area from the CFD simulations and then the calculated liquid film coefficient, k_L. As well as the predicted Sauter mean bubble diameter. Table 8.9 shows that the predicted interfacial area from the simulations increases with increasing $k_L a_{20}$, as would be expected. It is also shown that as the interfacial area for mass transfer increases, the liquid film coefficient, k_L decreases, where k_L is defined by Equation 8.27.

Table 8.9: - The overall oxygen transfer coefficient from the experimental study, the predicted interfacial area from the CFD simulations and the calculated liquid film coefficient, as well as the predicted Sauter mean bubble diameter, at U_w = 3 ms^{-1} and Q_a = 50 slm.

Insert, Simulation	$k_L a_{20}$ (hr^{-1})	a $\left(\frac{m^2}{m^3}\right)$	k_L (ms^{-1})	d_{32} (mm)
HV1 E-E SST PBM	11.922	2277.8	0.0052	2.63
A1 E-E SST PBM	13.196	3210.8	0.0041	1.87
A2 E-E SST PBM	14.509	3645.1	0.0040	1.65
	Average: -	2985.1	0.0044	2.05
	St Dev (%): -	± 19.52%	± 15.52 %	± 25.28 %

Equation 8.27 is a combination of the Penetration theory, liquid film coefficient equation, Equation 3.36, and the Calderbank (1958) equation for gas-liquid contact time for a bubble travelling through a liquid, Equation 3.37.

$$k_L = 2\sqrt{\frac{D_L u_b}{\pi d_b}} \qquad [8.27]$$

Equation 8.27 shows that k_L is dependent upon the relative slip velocity of the air to the flowing liquid, as

well as the bubble diameter.

Table 8.10 shows the average air and water velocities, and the relative slip velocity along the length of the downcomer. As well as the standard deviation of the slip velocities.

Table 8.10: - The average air and water velocities at various lengths along the downcomer for the various CFD simulations, at U_w = 3 ms^{-1} and Q_a = 50 slm.

Insert, Simulation	U_w (ms^{-1})	U_a (ms^{-1})	S (ms^{-1})	Standard Deviation (%)
HV1 E-E SST PBM	3.322	3.100	0.231	± 13.85
A1 E-E SST PBM	3.342	3.150	0.162	± 0.37
A2 E-E SST PBM	3.229	3.097	0.133	± 2.01

Using the data presented in Table 8.9, it can be determined that there is a decrease in the Sauter mean bubble diameter from the HV1 insert to the A1 and A2 inserts of 28.9, and 37.3 % respectively. There is also a significant decrease in slip velocity from the HV1 insert to the A1 and A2 inserts simulations of 28.8 and 42.4 % respectively, using the slip velocity ratios shown in Table 8.10. Therefore, using Equation 8.27 with a constant diffusivity, it would be expected that there would be an increase in the k_L for the HV1 insert compared to the A1 and A2 insert simulations of 1.4 and 7.2 % respectively. The actual predicted results from the CFD simulations shown in Table 8.9, showed a 21.2 and 23.1 % increase in the k_L values from the HV1 insert to the simulations of the A1 and A2 inserts respectively. Therefore, there is a significant variation in the k_L values between the CFD simulations and the experimental data, according to the Penetration theory. However, the CFD simulations predict the correct trends with the k_L increasing, with increased slip velocity.

Table 8.11, shows the experimental $k_L a_{20}$ values from this study for the HV1, A1 and A2 inserts at U_w = 3 ms^{-1} and Q_a = 50 slm. Along with the calculated $k_L a_{20}$ values, using Equations 7.7 and 7.11, using the calculated Sauter mean bubble diameters and specific power from the CFD simulations, shown in Tables 8.6 and 8.7 respectively. Table 8.11 shows that the CFD simulations predicted $k_L a_{20}$ values vary from the experimental data by ± 28 %. This high value of standard deviation is somewhat expected due to standard deviations of the Equations 7.7 and 7.11 to experimental data, of ± 16.5 and ± 14.5 % respectively. These inherent variations in the determined equations for this experimental work, in conjunction with the variations of the CFD simulations for the Sauter mean bubble diameter and specific power of 5.1 % and 15.3% respectively, contribute the level of variation between the experimental data and the CFD simulations.

Table 8.11: - The overall oxygen transfer coefficient from the experimental study and the predicted overall oxygen transfer coefficient using Equations 7.7 and 7.11, at U_w = 3 ms^{-1} and Q_a = 50 slm.

Insert, Simulation	Experimental $k_L a_{20}$ (hr^{-1})	Equation 7.7 $k_L a_{20}$ (hr^{-1})	Difference (%)	Equation 7.11 $k_L a_{20}$ (hr^{-1})	Difference (%)
HV1 E-E SST PBM	11.922	11.61	-2.58	8.97	-24.80
A1 E-E SST PBM	13.196	16.33	23.78	14.91	13.02
A2 E-E SST PBM	14.509	18.51	27.59	17.92	23.49
	Average: -	15.49		13.93	
	St Dev (%): -	± 22.77		± 32.70	

Table 8.12 shows the predicted SOTR and SAE for HV1, A1 and A2 insert CFD simulations and the experimental values along with the percentage difference between them. In Table 8.12, Equation 7.7 was used to calculate the $k_L a_{20}$. This is because the range of the percentage differences between the experimental and CFD simulation values for Equation 7.7 are smaller than the percentage differences of Equation 7.11, where the variations in Equation 7.7 range from - 2.6 to 27.6 %, a range of 30.2 %. Whereas the percentage differences in Equation 7.11 range from - 24.8 % to 23.5 %, a range of 48.3 %. The SOTR and SAE presented in Table 8.12 are calculated using Equations 3.56 and 3.57 respectively.

Table 8.12: - The predicted SOTR and SAE for HV1, A1 and A2 insert CFD simulations and the experimental values, along with the percentage difference between them.

	Experimental		CFD simulation		Difference	
Insert	SOTR (kgO_2/hr)	SAE (kgO_2/kWh)	SOTR (kgO_2/hr)	SAE (kgO_2/kWh)	SOTR (%)	SAE (%)
HV1	0.164	0.663	0.160	0.626	-2.59	- 5.53
A1	0.184	0.321	0.234	0.311	27.13	- 3.00
A2	0.201	0.240	0.265	0.240	32.08	0.02

Table 8.12 shows that there is a higher level of variation between the values of experimental and CFD simulation SOTR for the A1 and A2 inserts, up to 32 %, when compared to the HV1 insert simulation. The HV1 simulation conforms closely to the experimental data, in terms of SOTR, with a difference value of less than 3 %. Despite the variations in the SOTR values of the A1 And A2 insert simulations, the SAE predicted values for all the CFD simulations conforms closely with the experimental data, with all the simulation values falling within ± 6 % of the experimental values.

The results in Tables 8.6, 8.7, 8.12 have shown that the despite some errors in the predicted results for the Sauter mean bubble size, specific power and overall oxygen transfer coefficient. The trends between the inserts in terms of the performance in the experimental findings have been replicated in the CFD simulations. For example, the A2 insert was shown to have a significantly higher specific power than the HV1 and A1 inserts, with a higher interfacial area for mass transfer. It is therefore expected that for future designs and geometrically scaled models, CFD simulations can be used to predict the Sauter mean bubble diameter as well as the specific power in the system. Using this predicted specific power, in conjunction with the extracted Sauter mean bubble diameter from the simulations, in conjunction with Equations 7.7 and 7.11, the $k_L a_{20}$ can also be predicted. Therefore, SOTR and SAE can be estimated using Equations 3.56 and 3.57 respectively, as shown in Equation 8.12.

8.31. Geometric scaling

When considering geometric scaling, the CFD simulations generated using the Discrete PBM numerical method for the laboratory scale experiments were shown to give a good approximation of the experimental results. Therefore, the same numerical model and grid specification techniques can be used to approximate the performance of a larger geometrically scaled insert.

For this section of work a 190 mm ID geometrically scaled equivalent of the HV1 insert was be generated,

termed $HV1_{190}$. The grid specification of this model was the same as the laboratory scale CFD simulations with the faces of the insert having a 1 mm face sizing applied to them and then the air inlets and all their associated faces have a 0.4 mm face sizing applied, which generated a grid size of over 7.2 million cells. The simulation was run using the PBM method coupled with the SST turbulence and E-E multiphase models. The bubble size intervals for this simulation were the same as in Table 8.5 and the air bubbles at the air inlets were specified to be the same size as the diameter of the orifices, which was the same specification technique as the laboratory scale CFD simulations.

The geometrically scaled size of 190 mm ID was chosen because large scale experiments were conducted using a 190 mm ID geometrically scaled equivalent of the HV2 insert. Therefore through further experimentation, the pressure loss and mass transfer characteristics could be comprehensively validated and therefore geometric scaling laws could be established. However, during the large scale experimentation the Sauter mean bubble size was not determined, and the mixture outlet was shown to be undesirable, causing bubble coalescence and increased pressure losses, which will be discussed in Chapter 9. Therefore, a direct comparison between the large scale experimental work and the CFD simulations cannot currently be made at this stage. The CFD simulation will be run using the same mass flux flow rate settings as the CFD simulations of the laboratory scale experiments of $\left(\frac{\dot{m}}{A}\right)_W$ = 3081 kg/s.m^2 for the water, corresponding to a flow rate of 85.5 L/s and a mass flux of $\left(\frac{\dot{m}}{A}\right)_W$ = 4.06 kg/s.m^2 for air, which corresponds to an air flow rate of 180 L/min. Therefore there is a constant velocity of the air and water, between the HV1 and $HV1_{190}$ CFD simulations, as per the recommendations in Chapter 2 Section 3. The geometric scale from 100 mm to 190 mm ID corresponds to a volumetric capacity increase of 3.61 for the geometric scaling factor of 1.9.

Figure 8.10 shows the pressure distribution across the length of the downcomer of the $HV1_{190}$ simulation compared to the simulation of the HV1 and Table 8.13 shows the pressure loss of the two simulations and the difference between them, where the measurements in length are from the throat and are presented in ID, where the terminology of the locations are the same as that shown in Figure 8.3 (a)

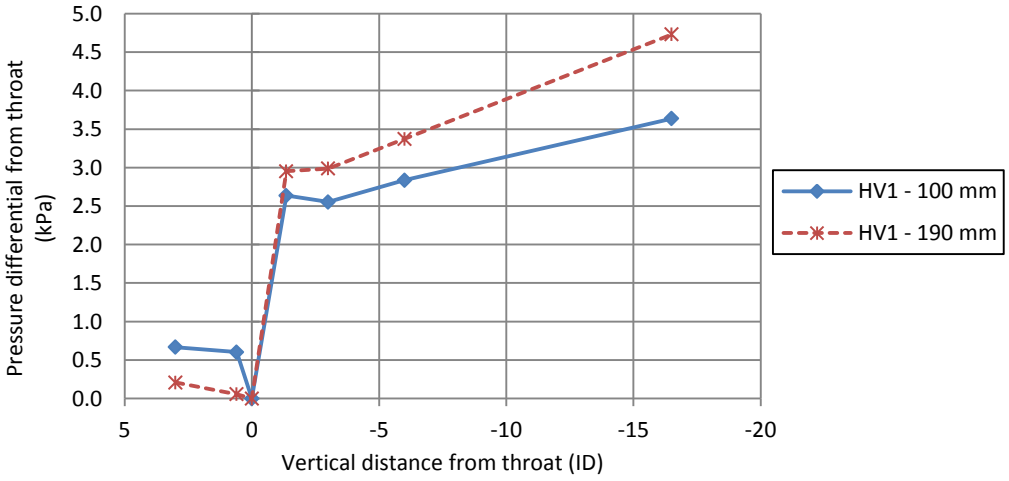

Figure 8.10: - Effect of geometric scale on pressure drop using for the HV1 and $HV1_{190}$ inserts.

Table 8.13: - Effect of geometric scale on pressure drop using the E-E SST PBM for the HV1 and $HV1_{190}$ inserts.

Terminology	US1	Nose	Tail	DS1	DS2	DS3	
Distance from throat	+ 3 ID	+0.6 ID	- 1.3 ID	- 3 ID	- 6 ID	- 16.5 ID	Total
	ΔP (kPa)	ΔP (kPa)	ΔP (kPa)	ΔP (kPa)	ΔP (kPa)	ΔP (kPa)	ΔP (kPa)
HV1	0.67	0.60	2.64	2.55	2.84	3.64	4.30
$HV1_{190}$	0.21	0.06	2.95	2.99	3.37	4.73	4.94
Difference (%): -	- 68.93	- 90.65	11.96	17.10	18.98	30.08	14.73

It is shown in Figure 8.10 that there is a similar pressure loss pattern between the two geometric scales along the downcomer. However, It can be seen in Figure 8.10 and Table 8.13 that the $HV1_{190}$ has an increased total pressure loss by approximately 15 %, when considering the entire length of the downcomer, from + 3 ID to - 16.5 ID, US1 to DS3.

Figure 8.11 shows the cumulative distribution of the bubble sizes in the downcomer and Table 8.14 highlights the predicted interfacial area for mass transfer and Sauter mean bubble diameter.

In Figure 8.11 a cumulative percentage of below 1 % has been omitted from the plot, such that there is an improved visibility of the results, where the cumulative frequency of all bubbles above 10 mm for both the HV1 and $HV1_{190}$ simulations amounted to less than 1 %.

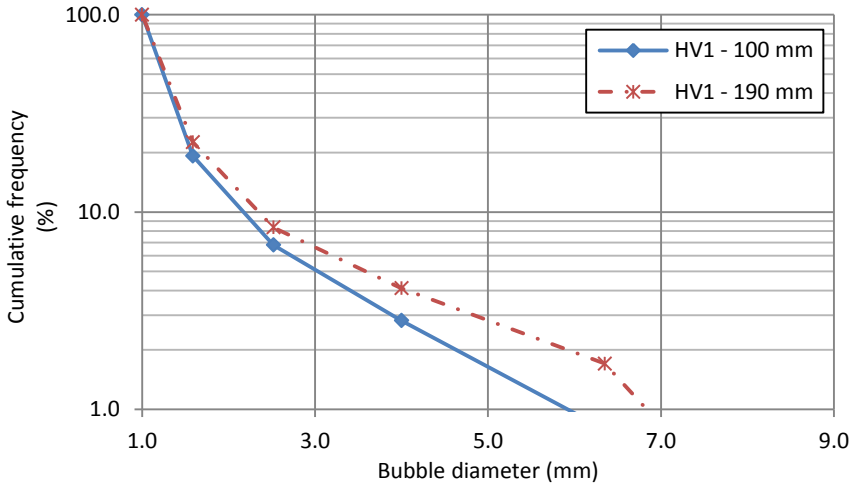

Figure 8.11: - Effect of geometric scale on predicted air distribution for HV1 and $HV1_{190}$ simulations.

Table 8.14: - Effect of geometric scale on Sauter mean bubble diameter, interfacial area for mass transfer and overall oxygen transfer coefficient for HV1 and $HV1_{190}$ simulations.

	d_{32} (mm)	a $\left(\frac{m^2}{m^3}\right)$	Equation 7.7 $k_L a_{20}$ (hr^{-1})
HV1	2.63	2277.8	11.61
$HV1_{190}$	3.35	1853.2	6.75
Difference (%): -	27.38	- 18.64	- 41.86

The results in Figure 8.11 show that there are more bubbles in the larger bubble diameter range of the $HV1_{190}$ simulations, which is highlighted in Table 8.14 with the predicted Sauter mean bubble diameter of the $HV1_{190}$ simulation being 27.38 % larger than the HV1 simulation. Therefore, the interfacial area in the HV_{190} insert is 18.64 % smaller than the HV1 simulation, as shown in Table 8.14.

Hinze (1955) considered that the breakage of bubbles occurs if the kinetic energy transmitted to the bubbles by the turbulent eddies is greater than its surface energy, and that bubble breakage, scales with an index of n = - 0.4, as described in Chapter 6 Section 5. Figure 8.12 shows a plot of turbulent kinetic energy, TKE, along the length of the downcomer for the HV1 and $HV1_{190}$ CFD simulations.

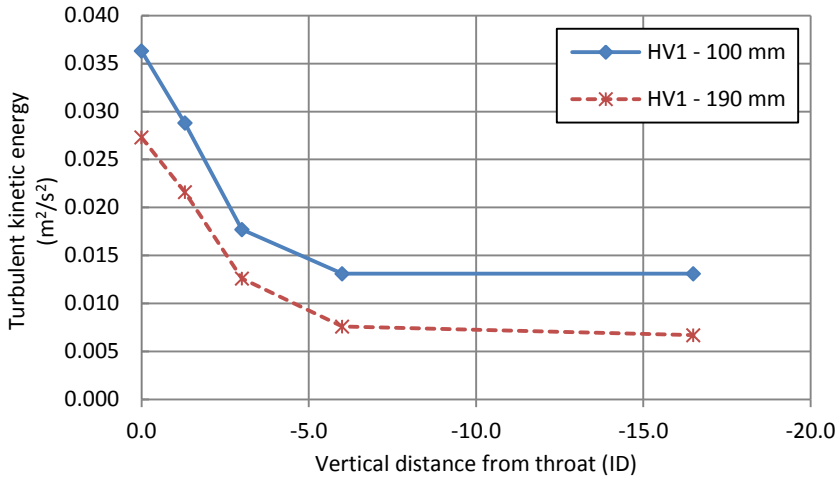

Figure 8.12: - Vertical distance from the throat of the insert against turbulent kinetic energy for the HV1 and $HV1_{190}$ CFD simulations.

As can be seen in Figure 8.12 the TKE along the length of the downcomer in the HV1 simulation is significantly higher than the $HV1_{190}$ CFD simulation by between 24 and 49 % for each of the individual measurement points.

Table 8.15 displays the weight average TKE along the length of the downcomer, the extracted Sauter mean bubble diameter of the CFD simulations, as well as the predicted Sauter mean bubble diameter using Equation 8.28.

Equation 8.28 was used as the basis for determining the Sauter mean bubble diameter based on the TKE and the Hinze (1955) bubble breakage scaling factor of n = - 0.4, where for these CFD simulations C_1 was found to be 0.51. This correlation was found to give a close prediction of the Sauter mean bubble diameter predicted within the CFD simulations, with a variation of ± 2 %. In Table 8.15 the weighted average TKE was found to be 40.3 % higher in the HV1 than $HV1_{190}$ simulation.

Table 8.15: - Sauter mean bubble diameter, the weighted average TKE and the predicted Sauter mean bubble diameter using Equation 8.28, with an empirical constant of 0.51.

	$\overline{TKE}$ (m^2/s^2)	d_{32} (mm)	Equation 8.28 d_{32} (mm)	Difference* (%)
HV1	0.0159	2.63	2.68	1.72
$HV1_{190}$	0.0095	3.35	3.29	- 1.86

* difference is defined as $\frac{d_{32\,x}-d_{32\,experimental}}{d_{32\,experimental}}$ x 100 %

$$d_{32} = C_1.\overline{TKE}^{-0.4} \quad [8.28]$$

Table 8.16 shows the calculated specific power consumption from the simulations, the predicted SOTR and SAE values for the $HV1_{190}$ and HV1 simulations, as well as the differences between them. It is shown in Table

8.16 that the predicted $k_L a_{20}$ is nearly 42 % smaller in the $HV1_{190}$ simulation compared to the laboratory scale simulation. Therefore, there is only a predicted increase in SOTR by 10.5 % from the $HV1_{190}$ to HV1 simulations, despite the 3.6 times increase in the volume of air being entrained into the simulation. As a result the predicted SAE in the $HV1_{190}$ geometric scale is nearly 7 % smaller than the HV1 CFD simulation. Some degree of caution is required when considering the $k_L a_{20}$ and as a result the SOTR and SAE. This is because it is currently unknown the effect of geometric scale on the empirical constant C_1 in Equation 7.7. An empirical constant C_1 of approximately 2975 gives a $k_L a_{20}$ for the $HV1_{190}$ simulation of 11.92, which is the value for the laboratory scale experimental work. However, the resultant SAE is then 1.03 kgO_2/kWh, which is 65 % greater than the HV1 value. Therefore, large scale experimental work is required using a similar set up to validate the results of the CFD simulations and examine the effect of geometric scale on C_1 on the $k_L a_{20}$. As will be discussed in Chapter 9, the geometric set up, in terms of upstream of the insert and the mixture outlet can have a significant impact on the mass transfer performance of a set up. However, it has been shown in the geometrically scaled up model that the Sauter mean bubble diameter increased by over 27 % resulting in a decreased interfacial area by over 18 %.

Table 8.16: - Effect of geometric scale on Sauter mean bubble diameter, E, $k_L a_{20}$, SOTR and SAE.

	d_{32} (mm)	E (W/m^3)	Equation 7.7 $k_L a_{20}$ (hr^{-1})	SOTR (kgO_2/hr)	SAE (kgO_2/kWh)
HV1	2.63	254.85	11.61	0.160	0.626
$HV1_{190}$	3.35	301.90	6.75	0.176	0.584
Difference (%): -	27.38	18.46	- 41.86	10.47	- 6.75

8.32. Summary

As a result of the physical experimentation, CFD simulations were validated and it was found that a population balance model coupled with the Eulerian-Eulerian multiphase and k-ω shear stress transport turbulence model resulted in the most accurate solution. The average bubble size, specific power consumption and mass transfer coefficients are found to be within 6, 15 and 25 % of the laboratory scale values respectively. With the SOTR and SAE values being within 32 and 6 % of the laboratory scale experimental values.

Geometric scaling was investigated using the geometric scaled up equivalent of the HV1 insert from 100 mm to 190 mm ID, therefore a geometric scaling factor of 1.9 and a volumetric capacity increase of 3.61 times compared to the laboratory scale experimental work. It was predicted that the larger scale HV1 insert had an increased Sauter mean bubble diameter by over 27 %, resulting in a decreased interfacial area for mass transfer of over 18 %. The geometrically scaled up HV1 insert was predicted to have an increased specific power compared to the laboratory scale experiment of 18.5 %. Therefore it has been shown that geometrically scaling up the insert is shown to have a negative impact in terms of generated bubble size and specific power consumption, it is therefore predicted that the geometrically scaled up insert would have decreased aeration efficiency when compared to the laboratory scale experimental work. Although large scale experimentation is required to validate the CFD simulation results. It was also found when comparing the HV1 and $HV1_{190}$ simulations that the Sauter mean bubble diameter scaled with TKE to the power of - 0.4.

CHAPTER 9

EXPERIMENTAL CASE STUDIES

9.1. Introduction

Within this study, an in-process case study and a series of large scale experimentation was conducted. In both scenarios hydrodynamic and mass transfer testing was conducted. The in-process case study was conducted on a Farm in Devon, where the aim of the project was to remove an odour problem that was currently being experienced on the farm due to the recirculation of farm sourced liquids, which were used to wash the floors of various areas at the farm. Therefore, this experimentation was conducted on wastewater and gave an indication of the performance on an insert on in-process conditions. The large scale testing was conducted at the HydroVenturi Ltd office using clean water. The large scale testing gave an indication of performance issues that may be encountered at a larger scale, which were not present in the laboratory scale experiment. The results of the in-process case study and the large scale experimentation will be presented in the following sections, with comparisons made in terms of performance to the laboratory scale.

9.2. Case study 1 – Hethenhill Farm project - February 2011

A case study was undertaken at Hethenhill Farm, Devon where an analytical study was conducted to assess the mass transfer potential and hydrodynamic efficiencies of the HV2 insert at a geometric scale of 150 mm ID.

Hethenhill dairy farm operates a flushed slurry system, which utilises farm sourced liquids to wash cubicle passages, milking parlours, and collection and handling areas. The system circulates underground in the farm via a reception and separated slurry pit, before being released from two flush tanks that sit above the cattle yard. These flushes are computerised and scheduled to run up to four times a day depending on milking times. The advantage of having this flush system is a reduced cost. However, the consequence of having the system is a serious odour problem at the farm, which occurs during these scheduled flushes over the yards. As a result of complaints from neighbouring properties, HydroVenturi Ltd was approached to trial its aeration technology within the farm's existing flush system, with the anticipation of it reducing this offensive odour.

After conducting research via consultants Wastewater Management and the internet, it was uncertain whether aeration technology would assist in reducing the odour or even increase the farmer's problem. Although aeration can be and has been used for slurry odour reduction in certain circumstances. The slurry on the farm was being stored underground in anaerobic conditions with likely high concentrations of odorous substances, which would be released when disturbed through aeration. Beyond this, prolonged

aeration encourages the establishment of aerobic conditions, which is conducive to wastewater treatment. Such an approach is used in most municipal wastewater treatment works. Correctly designed aeration systems can treat slurry in a relatively short period of time, between 3 to 10 days, to achieve the objectives of reduced or complete removal of offensive odour and reduction in biological oxygen demand, BOD (Boyle, et al., 2002). There has been significant interest in using aeration on animal wastewater as a method of tackling the problem of offensive odour. This is because the relatively strong oxidising environment, resulting from aeration leads to a more intensive breakdown of organic compounds (Burton, 1992; Zhang & Zhu, 2005). Biodegradation of organic compounds related to odour emissions, such as volatile fatty acids, alcohols, volatile amines and skatols (Westerman & Zhang, 1997; Zhu, 2000; Zhang & Zhu, 2005), is an attractive feature of the aeration process.

Regardless of the outcome in terms of odour treatment, the farm project would provide the potential to learn a substantial amount about the technology, through the various stages of its process.

The flush system layout contained two holding or flush tanks upstream of the cattle yards and parlours. At various stages in the day these tanks are emptied to clean the yards and parlours. This liquid is then collected in a reception pit and pumped to a series of slurry separators and solid screens. The resulting separated slurry is then pumped into a separated liquid slurry pit, which in turn is pumped back up to the flush tanks at various points in the flushing cycle.

After a site visit and advice from Wastewater Management it was perceived that the process would run efficiently in an underground separated liquid slurry pit, which maintains a fairly consistent and stable level, with a fixed content for significant periods of time, where the level could also be controlled. Therefore, the content within the tank could be kept at a constant depth, where there is no input or output of liquid at set times. Therefore forming a steady state system. Figure 9.1 shows the separated liquid slurry pit, where a manhole cover is highlighted, which is where the pump and pipe work was fitted through for the system.

Figure 9.1: - Photograph above the separated liquid slurry pit.

Figure 9.2 is a schematic of the separated slurry pit, where the manhole is located in the bottom right of the figure and an example of the slurry level is indicated.

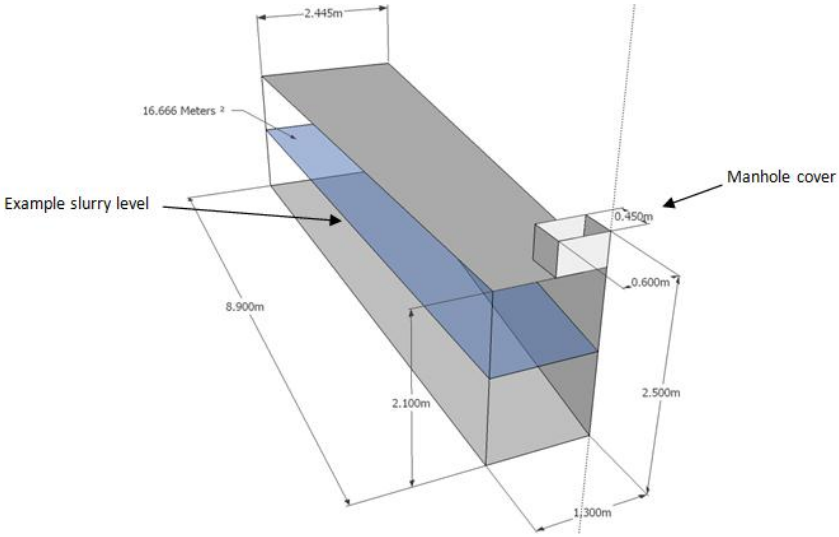

Figure 9.2: - Schematic of the separated liquid slurry pit.

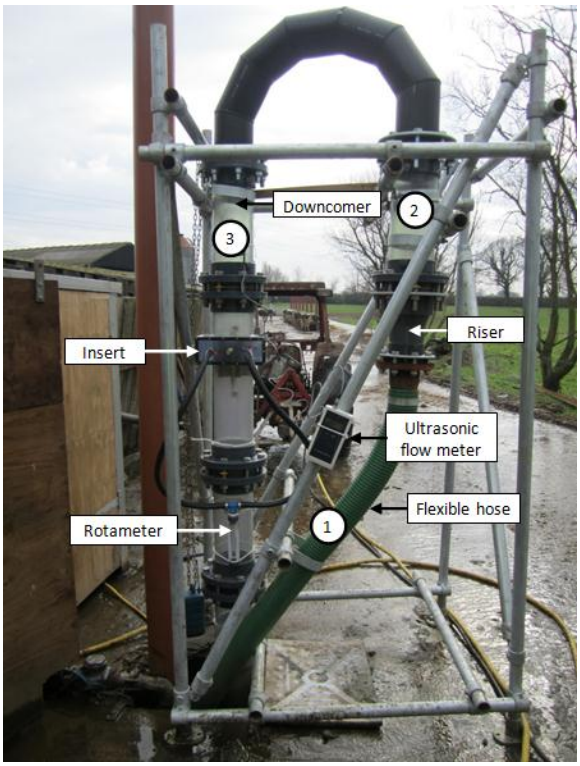

Figure 9.3: - Farm project experimental set up.

Figure 9.3 shows the section of the system above ground level, with the downcomer and the insert on the left of the figure, and the upstream section and the riser on the right hand side. Due to the size of the small opening and the dimensions of the U-bend, required at the top of the structure to minimise pressure losses, the project was unable to use 150 mm ID PVC pipe work for the entire process. This meant that the upstream pipe work would not fit back into the chamber, due to its size. Therefore an expansion in conjunction with a flexible hose was used for this section of the system, from the pump to the U-bend. This would result in losses due to the surface of the hose, the expansion and any resulting vibrations in the flexible hose. At the base of the downcomer was a 7˚ expanding diffuser directed towards the centre of the chamber.

The liquid flow rate was measured using an Omega portable ultrasonic flow meter with an accuracy of ± 2 % full scale (9 ms^{-1}). The sensor was placed at three locations to determine the average velocity during the tests. The three locations are indicated by 1, 2 and 3 in Figure 9.3. The first was on the flexible hose, the second was just prior to the U-bend and the final location was just upstream of the insert, which proved to be the most reliable and repeatable point of measurement. The air entrainment rate was measured using an Omega rotameter, which was connected to two 1 inch ID air hoses which were connected to a collar that was located around the HV2 insert, in a similar arrangement to the laboratory scale testing.

9.3. Observations from Case study 1

As a result of the discoloured nature of the liquid it was impossible to distinguish any bubble sizes or distributions. However, It could be seen that under certain flow conditions that a ventilated cavity was present on the upper side of the wing, as shown in Figure 9.4. This was shown in Test 7, details of the test conditions are outlined in Table 9.1. Unfortunately, it was not possible to accurately measure the length of the ventilated cavity. However, it was approximated as being between 250 and 300 mm, corresponding to 1.67 to 2 ID in length, which is at the very low end of the lengths of ventilated cavity in the laboratory experiments. Test 7 had an upstream water velocity of 1.6 ms^{-1} and a void fraction of 15.8 %, which under these conditions during the laboratory scale testing, a ventilated cavity length of over 10 ID was typical.

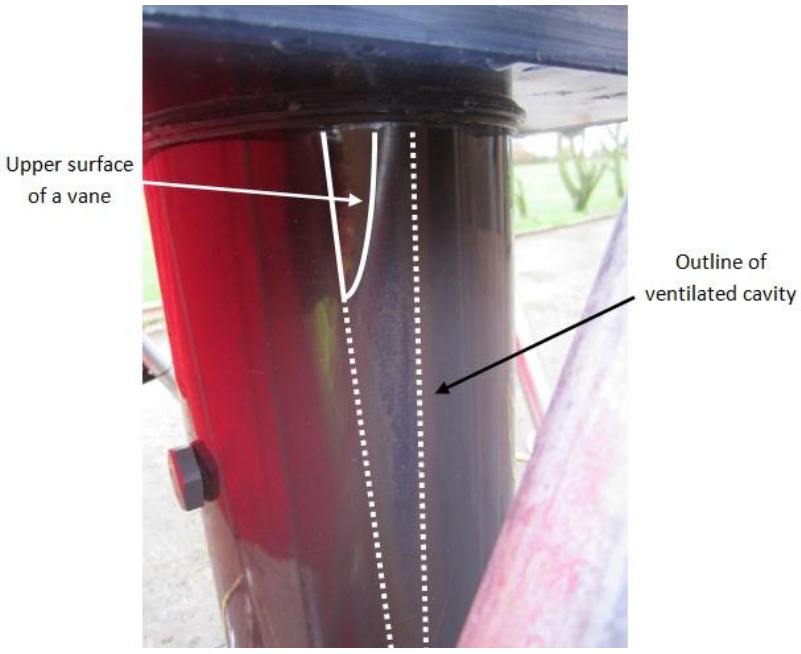

Figure 9.4: - Ventilated cavity upper side of wing, during test 7.

9.4. Pressure loss from Case study 1

A series of eight pressure loss and oxygen transfer tests were conducted over a three day period. The tests were conducted at four different pump frequencies. Table 9.1 shows the operating test conditions that were tested across the three days. As can be seen in Table 9.1 the vast majority of the tests were conducted at a depth of approximately 2.10 m ± 0.05 m, with some supplementary tests conducted to look at comparisons between depths at a constant pump frequency.

Table 9.1: - Test conditions for farm project.

Test No.	Date	Time	Freq (Hz)	Q_w (l/s)	Q_a (l/s)	Pump Power (kW)	Void (%)	Volume (m^3)	Depth (m)	P_{ATMOS} (mbar)
1	23-Feb	10:20	29	30.4	4.3	1.24	12.27	41.8	≈ 2.50	1014
2	23-Feb	14:05	49	49.5	8.0	5.60	13.94	32.2	≈ 1.90	1013
3	23-Feb	15:55	49	49.5	8.0	5.60	13.94	32.2	≈ 1.90	1013
4	24-Feb	10:45	44	44.2	6.7	4.10	13.17	34.2	≈ 2.10	1021
5	24-Feb	13:15	39	38.9	6.4	2.90	14.13	34.2	≈ 2.10	1020
6	24-Feb	15:15	34	33.6	5.9	1.90	14.94	34.2	≈ 2.10	1022
7	25-Feb	10:00	29	28.3	5.3	1.20	15.79	34.6	≈ 2.10	1021
8	25-Feb	11:45	49	48.7	7.2	5.60	12.88	34.6	≈ 2.10	1021

Calculating specific power consumption, E, for the two-phase section of the system, enables comparisons to be made between the overall system specific power consumption and specific power consumption of the two-phase section of the system. The overall system and two-phase specific power consumption are shown in Figure 9.5, where the specific two-phase power consumption is calculated using Equation 3.3.

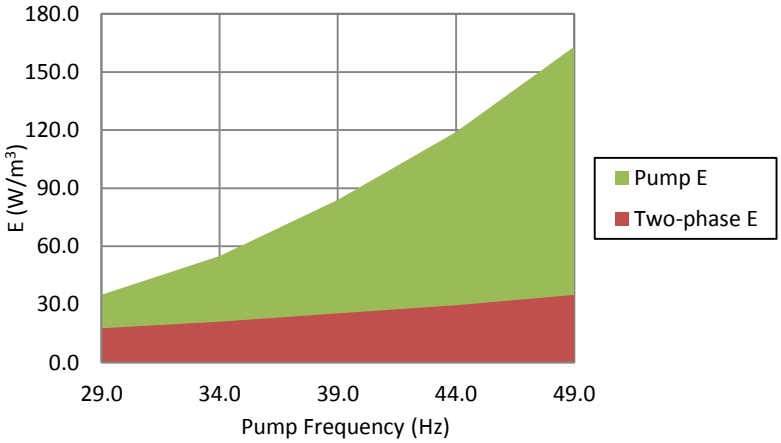

Figure 9.5: - Comparison of two-phase specific power consumption, calculated consumption using Equation 3.3, and pump power for a liquid depth of ≈ 2.10 m.

Table 9.2: - Two-phase and system specific power consumption, for a liquid depth of ≈ 2.10 m.

Pump Frequency (Hz)	E_{2ph} (W/m^3)	E_{pump} (W/m^3)	$\frac{E_{2ph}}{E_{pump}}$
29	17.7	34.92	50.81%
34	21.1	55.30	38.11%
39	25.4	84.40	30.04%
44	29.6	119.32	24.77%
49	34.9	162.98	21.45%

Figure 9.5 and Table 9.2 shows that the overall specific power consumption of the system is significantly more than that required to overcome the pressure loss across the insert and in the two-phase flow in the downcomer. It is shown in Table 9.2 that as the pump frequency is increased, the ratio between the insert and system power becomes smaller. Therefore, the losses upstream of the insert to the pump have a greater significance. This could be caused by the upstream bend, the expansion or the flexible hose that was required to connect the pump to the rest of the system, which was seen to have significant vibration.

It can be seen in Table 9.1 that at 29 Hz, decreasing the water depth from approximately 2.50 m to 2.10 m increased the entrained air by 1.0 L/s which is a 24.7 % increase. A similar trend was shown with an increase of 11.4 % by decreasing the liquid depth from approximately 2.10 to 1.90 m at a pump frequency of 49 Hz,

the significance of which will be discussed in the following section.

9.5. Mass transfer from Case study 1

A single DO probe was situated in the tank directly beneath the small opening, 1 m below the water free surface. Wastewater Management were commissioned to attend the site and conduct the oxygen mass transfer testing to ensure the independence of the measurements.

Two methods were used to determine the aeration efficiencies of the system. The first used the equations proposed by Andersson, as described in Boyle et al (2002), which takes into account the respiration rate of the bacteria present in the process water. The second method is described in Chapter 3, which is the ASCE standard (ANSI/ASCE 2-06) for determining in-process aeration performance using the NLRA method, as per the laboratory scale clean water testing done within this study. The experiments were run in a steady state system, where the chamber was closed with no in or out flow during the individually conducted tests. The formula used in the Andersson calculation is,

$$OTRf = \frac{R_O \; x \; C_{s20} \; x \; V}{(\beta C_\infty^* - C_O) x \; 1.024^{(T-20)}} \; x \; 10^{-3} \qquad [9.1]$$

where R_0 is the endogenous respiration of bacteria (mgDO/L per hr) and is calculated by Equation 9.2, where H is the height of the DO probe from the water free surface, which was kept at 1 m. The β factor, which was described in Chapter 3, was taken as 0.99.

$$R_0 = \frac{\Delta DO . H}{t} \qquad [9.2]$$

Tables 9.3 and 9.4 show the calculated mass transfer characteristics for the two calculation methods, for the tests conducted in this case study.

Table 9.3: - Mass transfer results using the Andersson method.

Test No.	C_o (mg/l)	C_∞^* (mg/l)	Water temp (°C)	R_o (mgDO/l/hr)	$\dot{m}_{o2}$ (kgO_2/hr)	$SOTR_f$ (kgO_2/hr)	SAE_f (kgO_2/kWh)	$SOTE_f$ (%)	$SOTE_f$ (%/m)
1	1.26	11.01	11.06	32.65	4.54	1.59	1.28	34.93	13.97
2	6.61	10.88	11.48	32.65	8.57	2.81	0.50	32.77	16.98
3	6.05	10.78	11.88	32.65	8.57	2.50	0.45	29.23	15.14
4	5.18	10.86	11.88	34.14	7.16	2.31	0.56	32.23	15.72
5	3.92	10.75	12.33	34.14	6.84	1.89	0.65	27.67	13.50
6	2.15	10.64	12.75	34.14	6.30	1.50	0.79	23.83	11.62
7	1.04	10.79	12.18	35.84	5.66	1.40	1.17	24.78	11.97
8	3.77	10.70	12.51	35.84	7.69	1.97	0.35	25.58	12.36

Table 9.4: - Mass transfer results using the ASCE non linear regression method.

Test No.	$(C_o)_{20}$ (mg/l)	$k_L a_{20f}$ (hr^{-1})	$\dot{m}_{o2}$ (kgO_2/hr)	$SOTR_f$ (kgO_2/hr)	SAE_f (kgO_2/kWh)	$SOTE_f$ (%)	$SOTE_f$ (%/m)
1	1.26	3.21	4.54	1.35	1.09	29.72	11.89
2	6.61	7.05	8.57	2.23	0.40	26.05	13.50
3	6.05	7.21	8.57	2.28	0.41	26.64	13.80
4	5.18	1.97	7.16	0.67	0.16	9.30	4.54
5	3.92	6.91	6.84	2.33	0.81	34.16	16.66
6*	NA	NA	6.30	NA	NA	NA	NA
7	1.04	4.30	5.66	1.47	1.22	25.94	12.53
8	3.77	5.39	7.69	1.84	0.33	23.94	11.56

**it was not possible to analyse the data from test 6 using the NLRA method due to the quality of the data. Therefore it was not possible to determine the mass transfer coefficient.*

All the data in Tables 9.3 and 9.4 have been corrected to standard conditions, using the methods described in Chapter 3. It should also be noted that the average filtered chemical oxygen demand, COD, in the system across the period of testing was just below 8,000 mg/l, which is a high strength wastewater. Unfortunately, during the testing an alpha factor was not determined and therefore it is not possible to compare the results to clean water testing.

Tables 9.3 and 9.4 shows the results from the oxygen transfer testing and it is shown there is a wide range of efficiencies, with the highest at the lower pump speeds. Part of the reason for this may be caused by the air intake set up. In order to measure the air intake, a rotameter was used, which may have restricted the air intake at the higher pump speeds. Also as can be seen in Section 9.3 the losses associated with the upstream section of the system at the higher flow rates were considerable and would therefore have lowered the aeration efficiencies at these higher liquid flow rates.

When comparing the results between the two methods, they were generally similar. However, the results of the $SOTR_f$ from the NLRA method were lower than the Andersson method. The Andersson method gave a more consistent result, when looking at a comparison between pump power and the $SOTR_f$, where any variations at a constant pump power were caused by the various depths of slurry, as shown in Figure 9.6.

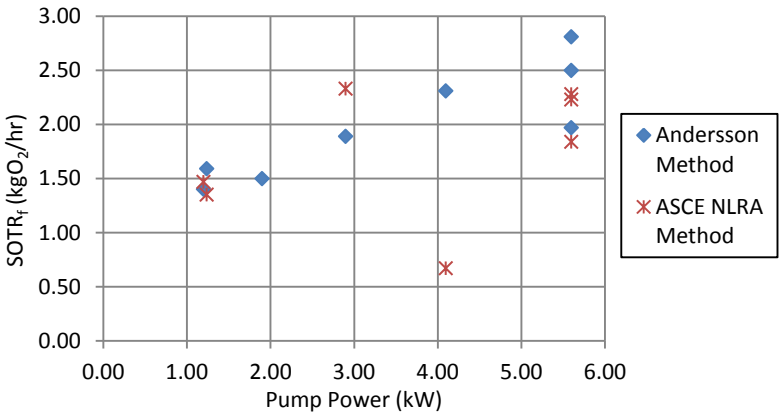

Figure 9.6: - Pump power against standard oxygen transfer rate when calculated using the Andersson and ASCE NLRA method.

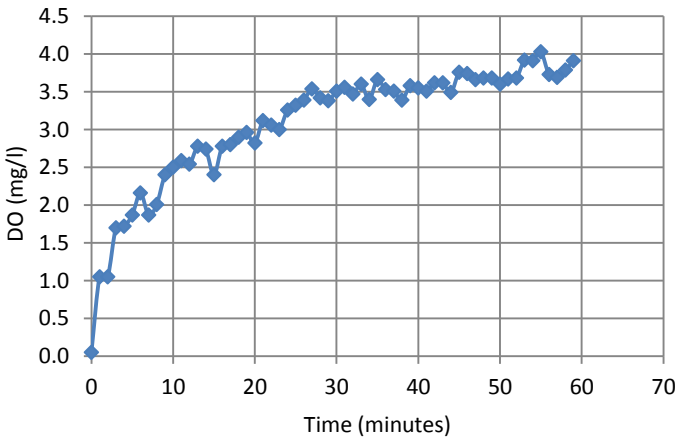

Figure 9.7: - DO versus time for test 8.

The main problem with calculating the $SOTR_f$ when using the NLRA method in this work is caused by some of the tests having a high degree of scattered and unclear curve DO curves, as shown in Figure 9.7. It is for this reason that the results determined by the Andersson method are used for the following discussion.

Figure 9.6 shows the $SOTR_f$ results range from 1.4 to 2.8 kgO_2/hr for the Andersson method at a test depth of approximately 2.10 m. This was achieved with an SOTE of between 23 and 33 %, as shown in Figure 9.8. The SAE_f across these experimental results was between 0.35 and 1.17 kgO_2/kWh, as shown in Figure 9.8. With the lowest efficiencies occurring at the highest pump frequency. When considering just the two-phase specific power consumption for ≈ 2.10 m depth test results, therefore using the values in Table 9.2 to calculate SAE_f, the range changes to 1.64 to 2.30 kgO_2/kW, as shown in Table 9.5. This shows that in future system designs and orientations, a high level of consideration has to be placed in the upstream design of the system, to ensure the highest possible aeration efficiencies of the system.

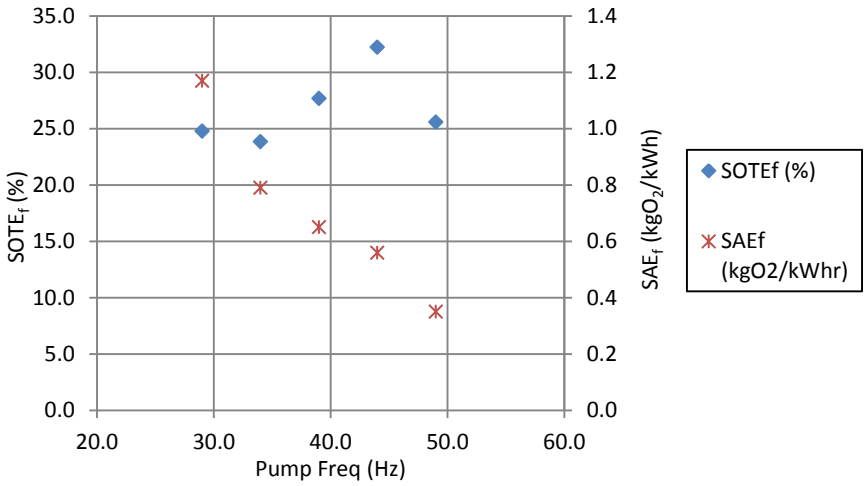

Figure 9.8: - Oxygen transfer efficiency and aeration efficiency for a test depth of ≈ 2.10 m, Tests 4 – 8.

Table 9.5: - SAEf when calculated using either E_{pump} or E_{2ph}, for a liquid depth of ≈ 2.10 m.

Test	Pump Frequency (Hz)	E_{pump} (W/m^3)	SAE_f E_{pump} (kgO2/kWh)	E_{2ph} (W/m^3)	SAE_f E_{2ph} (kgO2/kWh)
4	44	119.32	0.56	29.6	2.27
5	39	84.40	0.65	25.4	2.17
6	34	55.30	0.79	21.1	2.07
7	29	34.92	1.17	17.7	2.30
8	49	162.98	0.35	34.9	1.64

Comparing the two tests conducted at a pump frequency of 29 Hz. It can be seen in Table 9.6 that reducing the depth of the water by 17.6 % resulted in an increase in air flow rate by at least 25 %. Despite this, the operational efficiencies of the system were higher at an increased liquid depth. With $SOTR_f$ and SAE_f increasing by approximately 10 %. More noticeably, there was a significant increase the $SOTE_f$ by nearly 30 %. These results suggest that the system as a whole operates more efficiently at greater water depths, although this suggestion is based on only two measurements. To validate this suggestion more measurements would be needed to potentially find an optimum depth of tank for the greatest mass transfer and also the height of the throat of the inserts above the liquid surface for most efficient air entrainment.

Table 9.6: - Comparison of test results 1 and 7 where a common pump frequency of 29 Hz is used at 2 separate depths.

Test No.	Depth (m)	Q_w (l/s)	Q_a (l/s)	Pump Power (kW)	Q_a/Q_w (%)	$SOTR_f$ (kgO_2/hr)	SAE_f (kgO_2/kWh)	$SOTE_f$ (%)
1	≈ 2.50	30.4	4.25	1.24	14	1.59	1.28	34.9
7	≈ 2.10	28.3	5.3	1.20	18.7	1.4	1.17	24.8
Difference (%)	- 17.6%	- 7.0%	24.7%	- 3.2%	33.6%	- 12.0%	- 8.6%	- 29.1%

In summary, based in the above case study at Hethenhill farm, the most efficient results were obtained by running the pump at a lower frequency and running the system using a greater water depth. With efficiencies decreasing as pump speed is increased. However, it is suspected that the air intake on the venturi began to throttle the air entrainment rate at the higher pump frequencies, therefore limiting performance. The results displayed are all in-process conditions and as the alpha factor for the wastewater was unknown, it was not possible to translate the results into clean water test data. Wastewater Management commented that the strength of the wastewater was very high and had a high solids concentration in excess of 30,000 mg/l for all the tests, which is higher than what would be expected in a typical activated sludge plant, therefore hampering oxygen transfer.

9.6. Comparisons of Case study 1 with the laboratory scale experimental work

Comparing the laboratory scale experimentation with the farm project case study, a comparative measurement of performance can be made when considering how the $k_L a_{20}$ relates to energy dissipation and therefore specific power consumption. Using Equations 7.11, where a bubbly flow was entirely present in the downcomer, as the basis for a design correlation for the farm project case study testing, Equation 9.3 can be established,

$$k_L a_{20}\ (hr^{-1}) = 1.775(\in)^{0.48}(\varepsilon_G)^{0.3} \qquad [9.3]$$

Equation 9.3 has an R^2 of 0.95 and a standard deviation of ± 13.3 %, a graph of the farm project case study experimental data against Equation 9.3 is plotted in Figure 9.9.

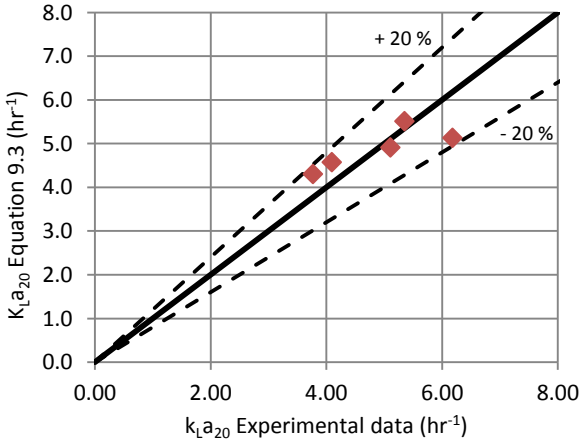

Figure 9.9: - The farm project case study experimental $k_L a_{20}$ against derived $k_L a_{20}$ from Equation 9.3.

The main noticeable difference between Equation 9.3 and 7.11 is the empirical constant, where in Equation 7.11 it was 46.535, compared to 1.775 in Equation 9.3. Therefore, under the same operating conditions in the laboratory experiment there is a greater overall oxygen transfer for the same specific power input than

in the farm project case study. This is caused by the inefficiencies of the upstream section of the system and as a result of the wastewater itself. From this it can be clearly seen that the characteristics of the wastewater and the system geometry can have a significant effect on the performance and efficiencies of the system.

9.7. Large scale testing

A series of tests were conducted on the HV2 insert, geometrically scaled up to 190 mm ID scale. Hydrodynamic and mass transfer testing was conducted across a wide range of depths and flow rates. Wastewater management conducted the mass transfer testing to again ensure the independence of the measurements. The tests were conducted in accordance with the methods stated in the ASCE standard 'Measurement of Oxygen Transfer in Clean water' ANSI/ACSE 2-06.

The test tank is shown in Figure 9.10, which has an ID of ≈ 4.3 m with a total height of 6.3 m. The HV2 insert was placed in an external section of pipe work and a centrifugal pump was used to circulate water through the insert. The HV2 insert was installed in a 190 mm ID pipe work, where the throat of the insert was located at ≈ 6 m above the base of the test tank. At the base of a downcomer was a 6 degree conical diffuser, where the exit area is twice that of the inlet area. During the mass transfer testing water depths of ≈ 4.5 and 5.0 m were tested.

Figure 9.10: - Large scale testing experimental set up.

The air flow was measured using a TSI Velocicalc thermal anemometer with temperature, humidity and

pressure correction, and an accuracy of ± 3 %. The air flow measurements were taken in an inlet pipe connected to the insert. The inlet pipe of 100 mm ID and 10 ID in length. The probe was located 7 ID downstream of the entrance to the inlet pipe, which was open to the atmosphere, and 3 ID upstream of the insert pipe work section. This met the manufacturers' requirements for the position the probe. The probe was calibrated for the pipe work using a pre-calibrated Omega mass flow meter.

The test tank was filled with potable water and a sample was taken at the start of the testing when the water was filled to ≈ 4.5 m and again when the water was raised to ≈ 5.0 m, the samples were analysed for total dissolved solids, TDS. The requirement for the ASCE standard is that the TDS is less than 2000 mg/l for clean water testing. In both samples the TDS were less than 240 mg/l.

During the testing, the water flow rate was controlled using a variable speed drive and was measured using a pre-calibrated Magflow meter, which was installed in the riser, as shown in Figure 9.10. Water velocities were set to approximately 1, 1.5, 2, 3 and 4 ms^{-1} during the mass transfer testing. Power drawn from the pump was measured using an Elcomponent Microvip 3 plus power monitor, which was installed on the incoming power supply to the control panel.

9.8. Observations of the large scale testing

It was not possible to measure any of the entrained air bubbles because there was no portable high speed camera available so therefore, the bubbles were only visually inspected. Despite this it was identified that the bubbles in the downcomer were larger at the bottom of the downcomer compared to closer to the insert. The bubbles were also not uniformly spherical and their elongation increased as they moved further downstream. This suggests the likelihood of high shear rates, or that the bubbles were colliding with each other due to the increase in slip ratio in the lower stages of the downcomer. Figure 9.11 shows typical bubble distributions and sizes at various points down the length of the pipe.

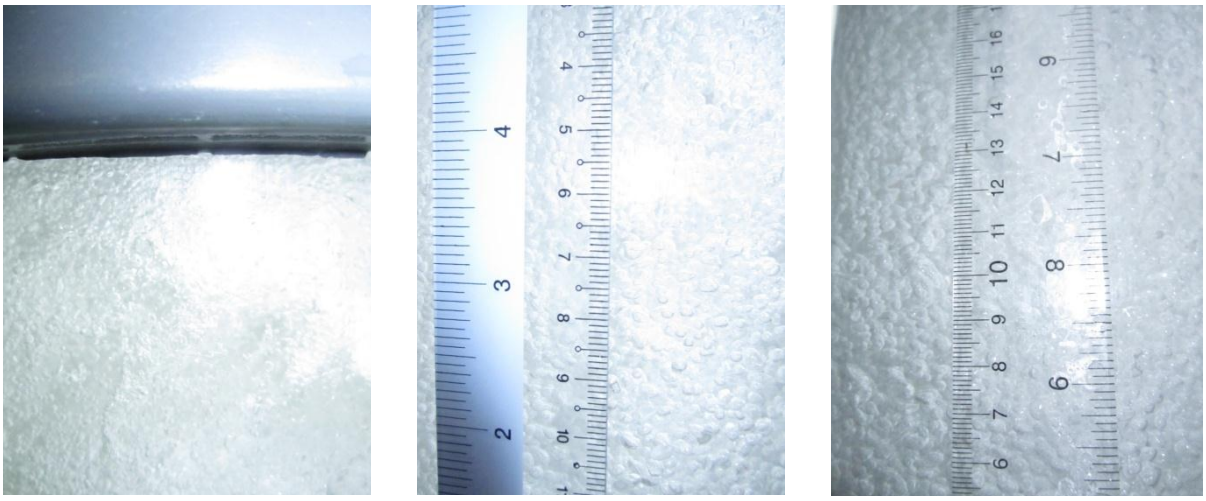

(a) (b) (c)

Figure 9.11: - Bubble density at different pipe sections, (a) bubbly flow just after the mixing zone, d_B <1mm, (b) the mid-section of pipe, d_B ≈ 1-2 mm and (c) the bottom-section of pipe, d_B ≈ 3-4mm.

Table 9.7 displays the operating conditions of the tests conducted during the oxygen transfer testing. A number of tests were conducted at a water depth of ≈ 4.5 m. To ensure the reproducibility of the experimental work, three tests being conducted at $U_w \approx 2$ ms^{-1}. The results at a depth of ≈ 4.5 m were then compared with results at a tank depth of ≈ 5.0 m.

Table 9.7: - Oxygen transfer efficiency testing, operating conditions for the large scale experiments.

Test	Date	VSD (Hz)	Water Depth (m)	Q_w (l/s)	U_w (m/s)	Q_a (Sm^3/hr)	Power (Elcomp) (kW)	P_{ATMOS} (mbar)
1	31-Aug	28	≈ 4.5	57.4	2.02	42.07	1.87	1018
2	31-Aug	37	≈ 4.5	84.5	2.98	77.03	3.83	1017
3	31-Aug	47	≈ 4.5	114.1	4.02	91.68	7.47	1017
4	01-Sep	24	≈ 4.5	43.1	1.52	28.94	1.20	1017
5	01-Sep	20.9	≈ 4.5	27.5	0.97	17.02	0.54	1016
6	01-Sep	28	≈ 4.5	57.4	2.02	40.78	1.85	1014
7	01-Sep	28	≈ 4.5	56.7	2.02	45.28	1.79	1013
8	02-Sep	26	≈ 5.0	57.0	2.01	30.18	1.57	1014
9*	02-Sep	23.5	≈ 5.0	57.2	2.02	17.43	1.21	1014
10*	02-Sep	43.5	≈ 5.0	112	3.95	44.35	5.88	1014

* represents test conditions where the air was throttled to obtain a fully developed bubbly flow in the entire length of the downcomer.

A series of photographs were taken of the bubble pattern on the surface of the water at various water and air flow rates, as shown in Figure 9.12.

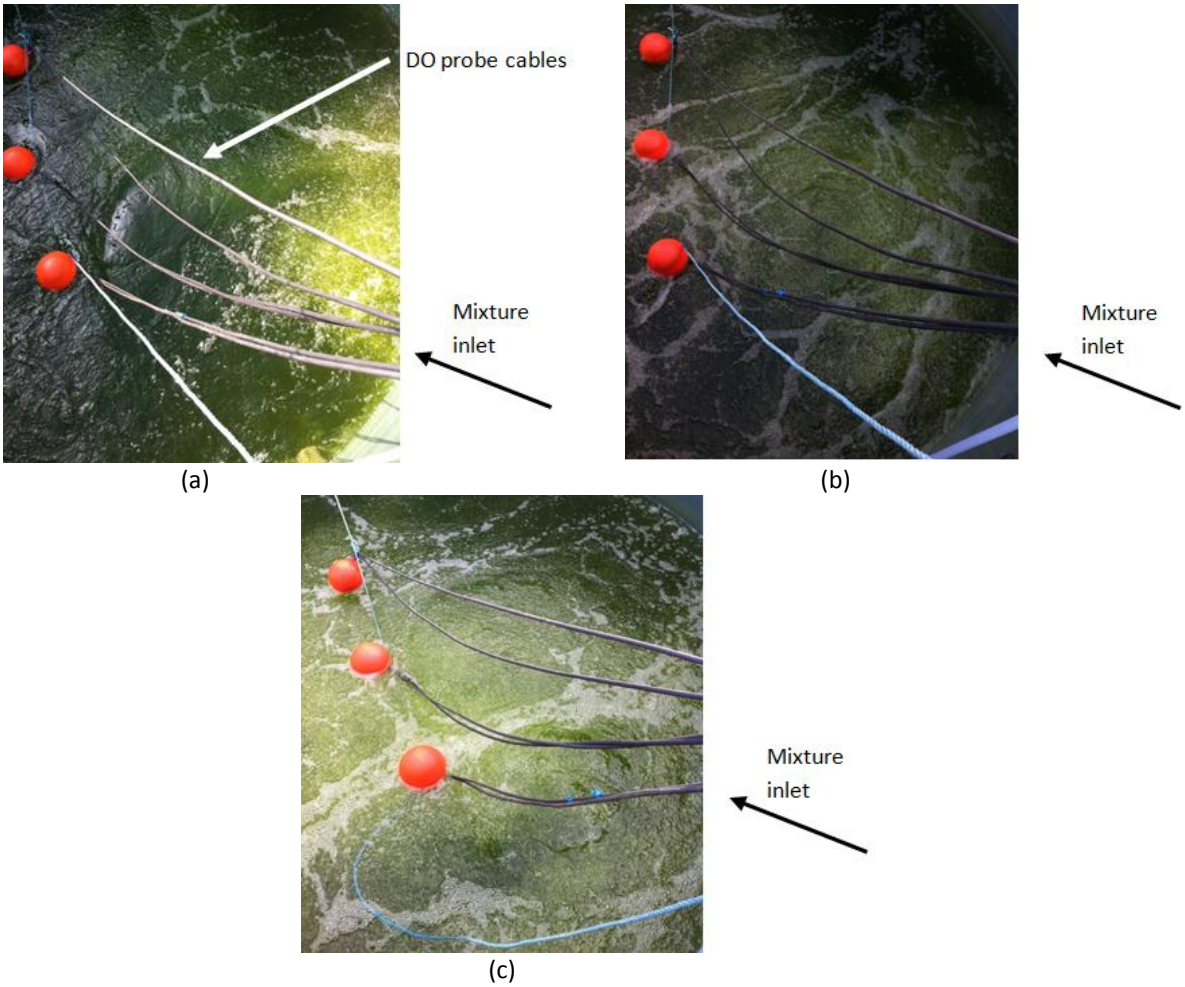

Figure 9.12: - Bubble pattern on the tank surface at (a) $U_w \approx 1$ ms^{-1}, (b) $U_w \approx 2$ ms^{-1} and (c) $U_w \approx 4$ ms^{-1} at a depth of ≈ 4.5 m.

It was noticed during the experimental work that at the lower water flow rates, Figure 9.12 (a), the air bubbles had a tendency to surface against the tank wall adjacent to the inlet pipe work, which is at the bottom right of the photos in Figure 9.12. However, as the water velocity was increased the bubble surface pattern improved, with a greater distribution across the surface of the water, as shown in Figure 9.12 (c).

It was determined that by throttling the air flow rate, it was possible to achieve a bubbly flow throughout the length of the downcomer, therefore eliminating the presence of the ventilated cavity. The benefit of this was that the bubbles in the downcomer visually appeared smaller than when a ventilated cavity was present. This was also the case in the laboratory scale testing, where operating without a ventilated cavity in the downcomer enabled smaller air bubbles to be generated, as highlighted in Chapter 5.

9.9. Pressure loss from large scale testing

It can be seen in Figure 9.13 that the power requirements for the insert and the downcomer are approximately 60 to 70 % of the overall system. Figure 9.13 and Table 9.8 show that as the water velocity is increased, the ratio between the two-phase and system power becomes smaller. At $U_w \approx 1$ ms^{-1} the two-phase pressure loss in the system almost equates to the entire system. When comparing these values to the Hethenhill farm case study in Figure 9.5, it can be seen that the loses in the farm project case study upstream of the insert were considerably higher than those experienced in the large scale testing. This emphasises the undesirable nature of the Hethenhill farm set-up.

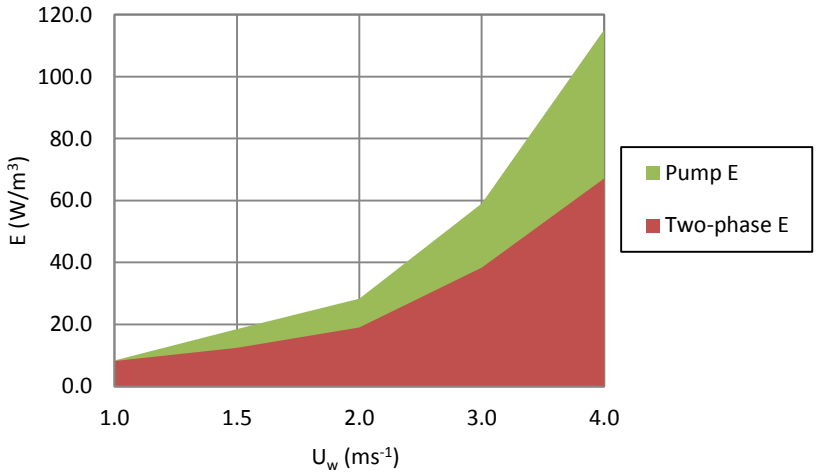

Figure 9.13: - Comparison of two-phase specific power consumption, calculated consumption using Equation 3.3, and pump power for a liquid depth of ≈ 4.5 m.

Table 9.8: - Two-phase and system specific power consumption, for a liquid depth of ≈ 4.5 m.

U_w (ms^{-1})	E_{2ph} (W/m^3)	E_{pump} (W/m^3)	$\frac{E_{2ph}}{E_{pump}}$
≈ 1.0	8.19	8.37	97.89 %
≈ 1.5	12.45	18.50	67.30 %
≈ 2.0	19.03	28.31	67.22 %
≈ 3.0	38.35	59.05	64.95 %
≈ 4.0	67.13	115.16	58.29 %

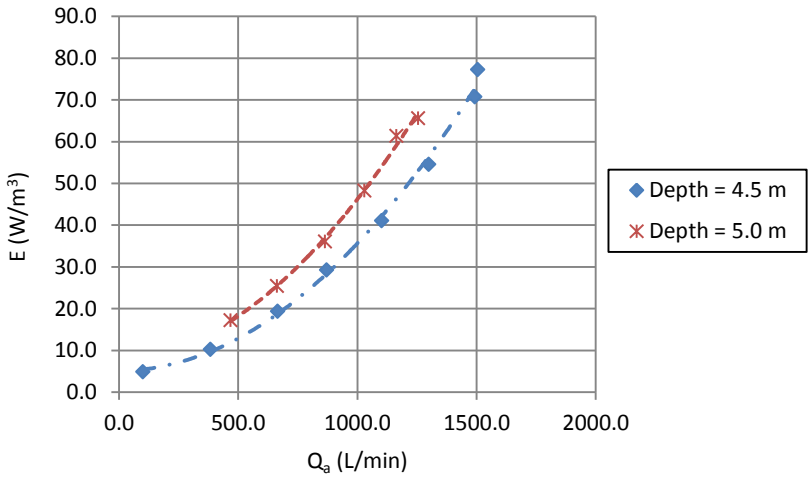

Figure 9.14: - Air entrainment against specific power consumption for depths of ≈ 4.50 and 5.0 m.

From the experimental work it can be seen in Figure 9.14, that as the water depth is increased, the specific power required in order to entrain the same amount of air as at a lower depth of water is also increased, in most cases by approximately 25 %.

9.10. Mass transfer of large scale testing

During the mass transfer testing six DO probes were used in the test tank, exceeding the minimum requirement outlined by the ASCE standard (ANSI/ASCE 2-06). The DO probes were recalibrated prior to the testing programme by Wastewater Management. The DO probes used were WTW CellOx 325 probes with Oxi240i handsets. The DO probes were positioned along the centre of the tank in three positions at depths of 1.5, 2.5 and 3.5 m, as shown in Figure 9.15.

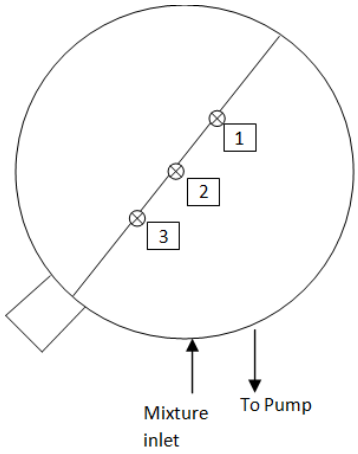

Figure 9.15: - DO probe positions from large scale testing.

The ASCE (2007) requirements for spatial variation are that for an individual test, 75 % of the $k_L a_{20}$ values are within ± 10 % of the mean value for that test. When looking in terms of the reproducibility of the results, it is recommended by ASCE (2007) that for three replicate tests the $k_L a_{20}$ values of an individual determination point shall not vary by more than ± 15 % from the mean value of the determination point.

Initially during the mass transfer testing three tests were conducted at the $U_w \approx 2$ ms^{-1} at a depth of ≈ 4.5 m.

The purpose for this was to provide three replicate tests at one set point, thus demonstrating and confirming the reproducibility of the data. Table 9.9 shows that the results display a good level of reproducibility, with standard deviations being less than 3 % for the $k_L a_{20}$. The requirements for the individual tests were also easily met. Any data shown for this experimental work for $U_w \approx 2$ ms^{-1} at a depth of ≈ 4.5 m will be the average value of the three tests.

Table 9.9: - Test results for $U_w \approx 2$ ms^{-1} at a depth of ≈ 4.5 m.

Test	$C_{sat}20$ (mg/l)	$k_L a_{20}$ (hr^{-1})	SOTR (kgO_2/hr)	SOTE (%)	SAE (kgO_2/kWh)
1	11.73	3.26	2.505	21.6	1.34
6	11.60	3.14	2.387	21.2	1.29
7	11.62	3.31	2.522	20.2	1.41
Average	11.65	3.24	2.471	21.0	1.35
Standard Deviation (%)	± 0.60	± 2.70	± 2.98	± 3.43	± 4.46

Figure 9.16 shows the SOTR against pump power at a water depth of ≈ 4.5 m. The figure shows a rapidly increasing SOTR up to a pump power output of 4 kW, above this the slope of the curve reduces, the SOTR ranged between 1 and 5.5 kgO_2/hr. Figure 9.16 also shows that as the upstream water velocity is doubled from approximately 2 to 4 ms-1, which corresponds to a pump power of 1.87 to 7.47 kW respectively, the SOTR is more than doubled from 2.47 to 5.53kgO_2/hr.

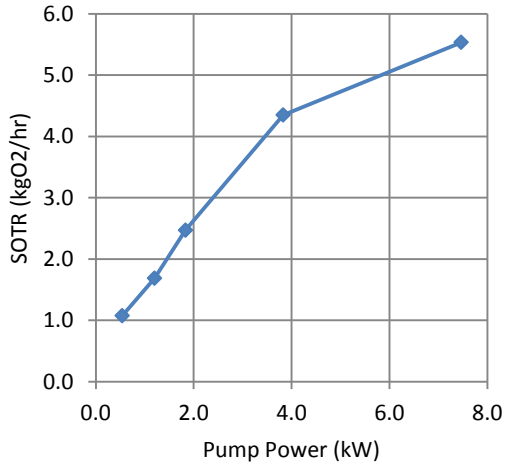

Figure 9.16: - Pump power against standard oxygen transfer rate when calculated using the ASCE NLRA method for a tank depth of ≈ 4.5 m.

Figure 9.17 shows the oxygen transfer efficiency, SOTE and the aeration efficiency, SAE for a test depth of approximately 4.5 m. The results show that the HV2 insert is capable of achieving a SAE of between 0.75 and 2 kgO_2/kWh with an oxygen transfer efficiency of between 20 to 23 %, as can be seen in Figure 9.17. It can also be seen in Figure 9.17 that as pump power becomes greater than 4 kW, corresponding to $U_w > 3$ ms^{-1}, the trend of a reducing SOTE is reversed. This is likely to be because of the better bubble distribution within the tank, shown in Figure 9.12. Operating at higher water velocities increases the specific power consumption, (W/m^3) which is required to bring about homogeneity, bubble dispersion and micro-mixing, in the tank and as such, the rate of oxygen transfer can improve.

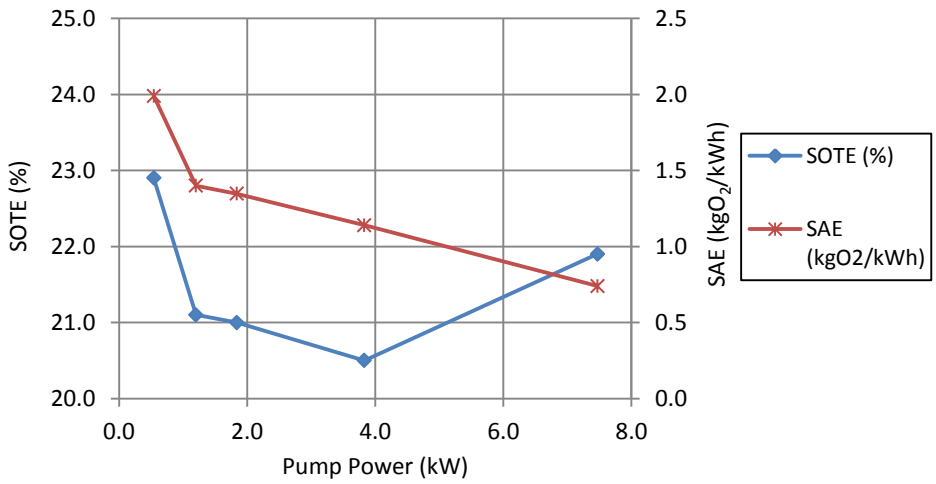

Figure 9.17: - Oxygen transfer efficiency and aeration efficiency for a test depth of ≈ 4.5 m, Tests 1 – 7 using the average value at $U_w \approx 2$ ms^{-1}.

The final three tests, Tests 8, 9 and 10 respectively, were conducted at a liquid depth of ≈ 5.0 m. Initially with $U_w \approx 2$ ms^{-1} and the air inlets open to the atmosphere. During this test a ventilated cavity was noticeable at the base of the insert, approximately 1.5 ID in length. The second and third test, Tests 9 and 10 respectively, at $U_w \approx 2$ ms^{-1} were conducted with the air inlet restricted so that no ventilated cavity was present in the downcomer and therefore a bubbly flow regime was present throughout the entire length of the downcomer, from this any changes in the overall aeration efficiency with regards to the changing flow regime could be assessed.

Table 9.10 shows the data for $U_w \approx 2$ ms^{-1} at a depth of ≈ 4.5 and ≈ 5.0 m with the air inlets unrestricted, it can be seen that by raising the depth of the water. The mass transfer characteristics were reduced with the overall mass transfer coefficient, SOTR and SAE reducing at the higher water level. The SOTE increased due to in increased depth. This is in contrast to the results for the Hethenhill farm case study, shown in Table 9.6.Potentially in this experimental set up a depth of ≈ 5.0 m may be above the optimum water level, where the impact of the reduced amount of entrained air, exceeds the benefit of a greater depth of liquid for mass transfer to take place.

Table 9.10: - Experimental data for $U_w \approx 2$ ms^{-1} with a tank depth of ≈ 4.5 and 5.0 m.

Test	U_w (ms^{-1})	Depth (m)	Q_a (Sm^3/hr)	C_{s20} (mg/l)	$k_L a_{20}$ (hr^{-1})	SOTR (kgO_2/hr)	SOTE (%)	SAE (kgO_2/kWh)
1, 6 & 7 (avg)	2.02	≈ 4.5	42.92	11.65	3.24	2.471	21.0	1.35
8	2.01	≈ 5.0	30.18	11.94	2.28	1.978	23.8	1.26
	Difference (%)	11.06	- 29.69	2.49	- 29.63	- 19.95	13.33	- 6.67

Tests 9 and 10 were conducted at ≈ 5.0 m water depth, were an attempt to improve the bubbly flow immediately downstream of the insert. The first eight tests all experienced a ventilated cavity immediately downstream of the insert and the bubbly flow commenced after this ventilated cavity. The bubbles produced were visibly larger when this ventilated cavity was present. Unfortunately, it was not possible to accurately photograph or measure the bubbles.

When comparing test 8 and 9, shown in Table 9.11. The pump power consumption was reduced from 1.57 to 1.21 kW between the tests, shown in Table 9.7. However, the void fraction reduced significantly from 12.8 to 7.8 %, again shown in Table 9.17, with a 4 2% reduction in the entrained air, shown in Table 9.11. It was considered the reduction in performance was partially down to the poor bubble distribution experienced at the lower flow rates.

Table 9.11: - Experimental data for $U_w \approx 2$ ms^{-1} with a tank depth of ≈ 5.0 m with air inlet unrestricted and restricted to ensure full bubbly flow in the downcomer.

	U_w (ms^{-1})	Depth (m)	Q_a (Sm^3/hr)	C_{s20} (mg/l)	$k_L a_{20}$ (hr^{-1})	SOTR (kgO_2/hr)	SOTE (%)	SAE (kgO_2/kWh)
Test 8	2.01	5.02	30.18	11.94	2.28	1.978	23.8	1.26
Test 9*	2.02	5.02	17.43	11.86	1.23	1.058	22.0	0.87
	Difference (%)		- 42.25	- 0.67	- 46.05	- 46.51	- 7.56%	- 30.95

Therefore, a final test was conducted at a water depth of ≈ 5.0 m with an $U_w \approx 4$ ms^{-1} again restricting the air intake to the insert, in order to create a fully developed bubbly flow regime throughout the downcomer. The improvement in the SOTE, shown in Tables 9.11 and 9.12, when comparing the results between Tests 9 and 10, shows that the better bubble distribution on the surface of the tank, resulted in improved oxygen transfer efficiency by 34 %. This is also the case when comparing tests 7 and 10, shown in Table 9.12, where increasing the depth of the water and ensuring no ventilated cavity was present in the downcomer improved the SOTE by approximately 32 %. This improved SOTE however, came at and expense with a reduced SAE.

Table 9.12: - Experimental data for $U_w \approx 4$ ms^{-1} with a tank depth of ≈ 4.5 and 5.0 m with air inlet unrestricted at ≈ 4.5 m and restricted at depth of ≈ 5.0 m to ensure full bubbly flow in the downcomer.

	U_w (ms^{-1})	Depth (m)	Q_a (Sm^3/hr)	C_{s20} (mg/l)	$k_L a_{20}$ (hr^{-1})	SOTR (kgO_2/hr)	SOTE (%)	SAE (kgO_2/kWh)
Test 7	2.02	≈ 4.5	91.68	11.9	7.09	5.534	21.9	0.74
Test 10*	3.95	≈ 5.0	44.35	11.9	4.07	3.523	28.8	0.60
	Difference (%)		- 51.63%	0.00%	- 42.60%	- 36.34%	31.51%	- 18.92%

* represents test conditions where the air was throttled to obtain a fully developed bubbly flow in the entire length of the downcomer.

A CFD analysis study by MMI Engineering identified the possibility of air accumulating at the exit diffuser section suggesting that a high proportion of the fine bubbles, which are produced by the insert are lost due to bubble coalescence. This may explain the reason behind the possible hindered performance of the aeration system.

Consultants MMI Engineering were employed by HydroVenturi Ltd to undertake CFD work on the existing tank intake set up, which included the short bend and the conical diffuser design. The work focused on operation at a pipe velocity of 1.5 ms^{-1}, which was deemed as being at the lower limit of what would be acceptable in practice and denoting the point that coalescence is likely to be most pronounced.

An Eulerian- Eulerian two-phase model was used so that the transport of air and water were solved using a momentum equation for each phase. The coalescence and breakup of air bubbles was not calculated and a constant bubble size of 2.5 mm was specified, in conjunction with an air void fraction of 20 % at the inlet.

The distribution of air within the bend and diffuser based on this volume fraction was not dissimilar to a case, where aggregation and breakage were calculated. Therefore, aggregation and breakage modelling was not considered to be fundamental to resolving the distribution of air. The k-ω Shear Stress Transport, SST, turbulence model was used. This is a two equation turbulence model and is generally used for industrial applications. This model solves a transport equation for turbulent kinetic energy and one for dissipation. The Reynolds stresses are not solved because turbulence was assumed to be isotropic.

The modelling output confirmed that air was coalescing in the conical diffuser section, immediately after the bend. The CFD simulations also showed that air tended to rise close to the tank inner wall, corresponding to what had been observed in practice, shown in Figure 9.12.

Figure 9.18 shows the distribution of air through the diffuser and tank. The air within the diffuser is not well mixed. Consequently, there is a bubble plume of air within the tank as shown by the iso-surface at 1 % void fraction. The results show a concentrated plume of air rising up the wall of the tank and therefore hampering the potential for mass transfer.

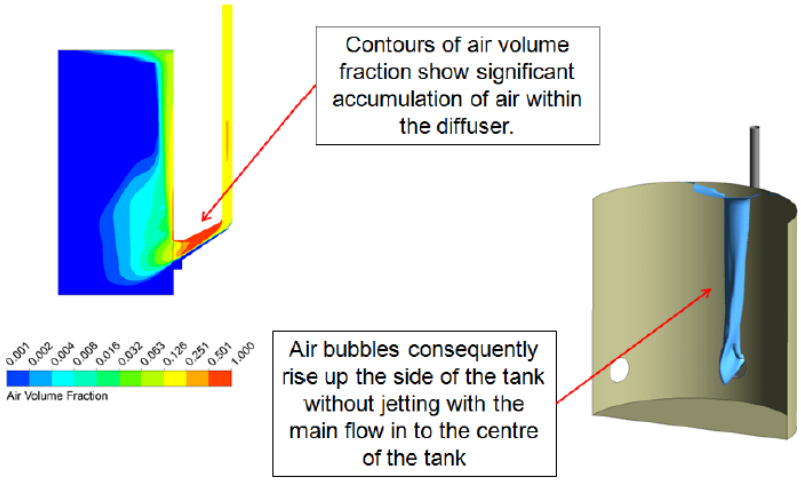

Figure 9.18: - Air distribution in the diffuser of the large scale experimental set-up at U_w = 1.5 ms^{-1} with an air void fraction of 2 %.

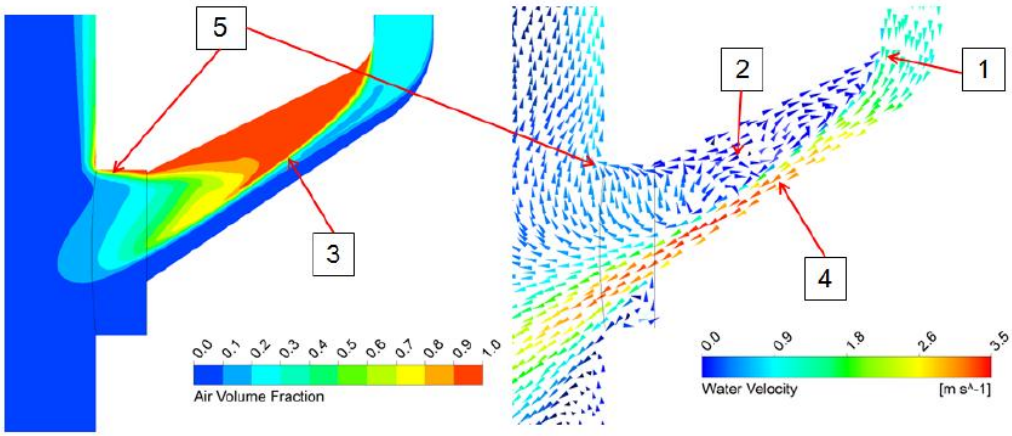

Figure 9.19: - Air distribution and velocity vectors in diffuser of the large scale experimental set-up at U_w = 1.5 ms^{-1} with a air void fraction of 2 %.

Figure 9.19 shows contours of volume fraction and velocity vectors through the diffuser. Due to the buoyancy of air there is separation of the air within the diffuser or bend, as the flow turns away from the vertical. As can be seen in Figure 9.19, the flow separates from the bend at (1) and due to the air accumulation within the recirculation zone (2 and 3) the water flow jets beneath the region in which the air accumulates (4). A high volume fraction of air passes to and rises up the side wall of the tank (5). Therefore the discharge in to the receiving tank needs to be optimised in order to develop a highly efficient and competitive system.

9.11. Comparisons of the large scale testing with the laboratory scale experimental work

Comparing the laboratory scale and large scale testing, a comparative measurement of performance can be made when considering how $k_L a_{20}$ relates to energy dissipation and specific power consumption. Using Equation 7.11, where a bubbly flow was present in the downcomer, as the basis for a design correlation for the large scale testing, Equation 9.4 can be established,

$$k_L a_{20}\ (hr^{-1}) = 10.0(\in)^{0.48}(\varepsilon_G)^{0.3} \qquad [9.4]$$

Equation 9.4 has an R^2 of 0.997 and a standard deviation of ± 16.9 %, a graph of the large scale experimental physical data against Equation 9.4 is plotted in Figure 9.20.

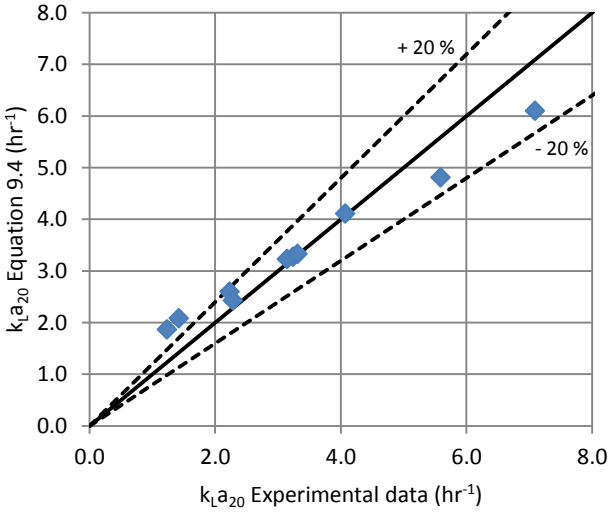

Figure 9.20: - The large scale experimental $k_L a_{20}$ against derived $k_L a_{20}$ equation for large scale experimental work, Equation 9.4.

The main noticeable difference between Equations 9.4 and 7.11 is the empirical constant, where in Equation 7.11 it was 46.535, compared to 10.0 in Equation 9.4. To note the empirical constant from Equation 9.3, from the farm project case study was 1.775. Therefore, under the same operating conditions in the laboratory experiment there is a greater $k_L a_{20}$ for the same specific power input than the large scale set-up. This could primarily be caused by the bubble coalescence in the large scale experiment, which would have not been present in the laboratory scale testing due to the straight pipe for the mixture outlet. Hence, a better air distribution would be needed at the large scale to provide a comparison to the laboratory scale experimental work and therefore, to be able to investigate the effects of geometric scaling accurately.

9.12. Summary

When analysing the farm project case study and large scale experiment a number of key parameters have been seen to affect the system performance, when comparing the results to the laboratory experiments. Firstly, the upstream system set-up and the fraction of the overall system power it contributes to, can have a significant effect on the overall performance of the aeration system, which is shown when comparing Figures 9.5 and 9.13.

Secondly, the effect of the receiving tank water depth on mass transfer performance. It was seen in the Hethenhill farm project, where a lower depth of water was used that increasing the water depth improved the mass transfer performance and aeration efficiency despite and reduced air entrainment, Table 9.6. However, in the large scale testing where a greater depth of water was used, increasing the water depth reduced the overall aeration efficiency, Table 9.10. Therefore, to optimise the aeration system considerations have to be made towards the depth of the receiving tank and the height of the throat above the water surface, so that the optimum depth can be found, where the reducing air entrainment is outweighed by the increased efficiency of the mass transfer.

As was identified in the empirical constants of Equation 9.3 and 9.4, the characteristics of the water, in terms of viscosity, density, TDS, BOD and COD as well the geometric effects of the system with regards to the upstream conditions, as well as the discharge geometry can all have a significant effect on the mass transfer performance and aeration efficiency of the system. Therefore, consideration is needed to how the two-phase mixture is discharged into the receiving tank. Further investigation into this is conducted and discussed in Chapter 10.

CHAPTER 10

DISCUSSION AND IN-PROCESS CONSIDERATIONS

10.1. Introduction

During the designing process for a new aerator to be used within the municipal and industrial wastewater industry, or any other potential industries, where there is a requirement for aeration. There must be considerations towards the primary requirement of the aerator, for example whether it is the oxygen transfer rate or the aeration efficiency.

This chapter aims to bring the information and results outlined in this experimental study together, to give an assessment of all the inserts for the primary performance characteristics of aeration, SOTR, SAE and d_{32}. Therefore, a direct comparison of how the inserts performed against the V1 insert can be made. Also in this chapter considerations will be made towards the overall system and support structure, including insert placement and mixture outlet geometry. In addition to this any potential problems with the existing insert designs will be discussed, alongside methods or design changes to alleviate the problem.

The following sections discuss the performance characteristics of the inserts as well as a number of design considerations and approaches to negating any negative effects and promoting the positive attributes of the inserts.

10.2. Standard oxygen transfer rate, SOTR

The SOTR is a hypothetical mass of oxygen transferred per unit of time in water at zero DO concentration, water temperature of 20˚C and barometric pressure of 101.325 kPa under specified air rate and power conditions. Table 10.1 displays the average and maximum SOTR of all the inserts across the full range of operating conditions tested in this study, whilst Figure 10.1 shows the average and standard deviations.

Table 10.1: - SOTR average and maximum values for all inserts across the range of operating conditions tested in the laboratory scale experiments.

Insert	Average	± (%)	Max	at
V1	0.259	37.42	0.42	U_w = 3 ms^{-1}, Q_a = 300 slm
HV1	0.257	31.36	0.45	U_w = 3 ms^{-1}, Q_a = 300 slm
HV2	0.244	47.39	0.50	U_w = 3 ms^{-1}, Q_a = 300 slm
HV3	0.240	39.64	0.47	U_w = 3 ms^{-1}, Q_a = 300 slm
A1	0.306	42.60	0.61	U_w = 3 ms^{-1}, Q_a = 300 slm
A2	0.316	46.49	0.67	U_w = 3 ms^{-1}, Q_a = 300 slm

As can be seen in Table 10.1 the maximum SOTR occurred for all the inserts at the highest water velocity and air flow rate, U_w = 3 ms^{-1} and Q_a = 300 slm. It is also noticeable in Table 10.1 that the V1 insert had the smallest maximum SOTR, in comparison to the inserts. The A2 insert had the highest maximum and average SOTR and when comparing the HV1, HV2 and HV3 inserts it can be seen that the HV1 insert had the highest average SOTR. However, the HV2 insert had the highest maximum value of the R_v = 1.5 inserts.

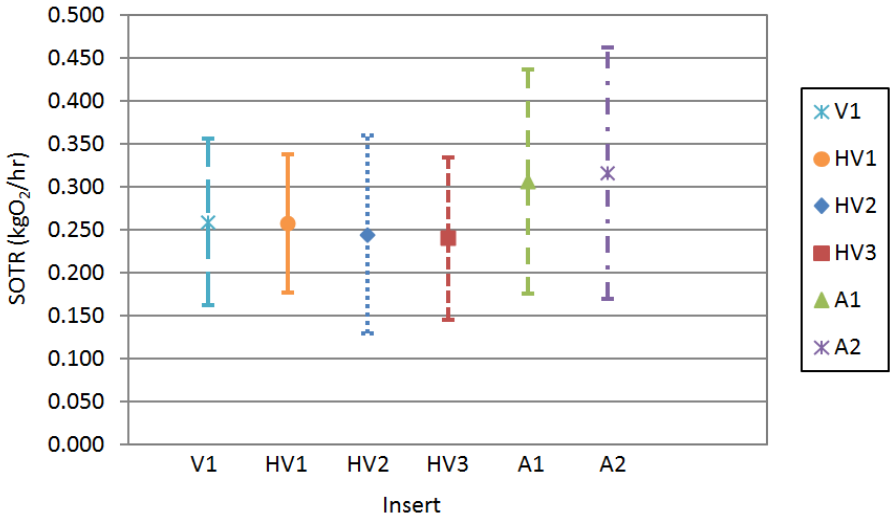

Figure 10.1: - SOTR average and standard deviation for all inserts across the range of operating conditions tested in the laboratory scale experiments.

10.3. Standard aeration efficiency, SAE

The SAE is the ratio between the amount of oxygen transferred to the water and the energy required to do so, with water at a temperature of 20˚C and barometric pressure of 101.325 kPa. Table 10.2 displays the average and maximum SAE of all the inserts across the range of operating conditions, whilst Figure 10.2 shows the average and standard deviations.

Table 10.2: - SAE average and maximum values for all inserts across the range of operating conditions tested in the laboratory scale experiments.

Insert	Average	± (%)	Max	at
V1	1.52	30.62	2.64	U_w = 1 ms^{-1}, Q_a = 50 slm
HV1	1.38	40.86	2.76	U_w = 1 ms^{-1}, Q_a = 50 slm
HV2	1.08	34.99	2.38	U_w = 1 ms^{-1}, Q_a = 50 slm
HV3	1.17	36.87	2.59	U_w = 1 ms^{-1}, Q_a = 50 slm
A1	1.14	66.30	3.17	U_w = 1 ms^{-1}, Q_a = 50 slm
A2	0.89	65.65	2.41	U_w = 1 ms^{-1}, Q_a = 50 slm

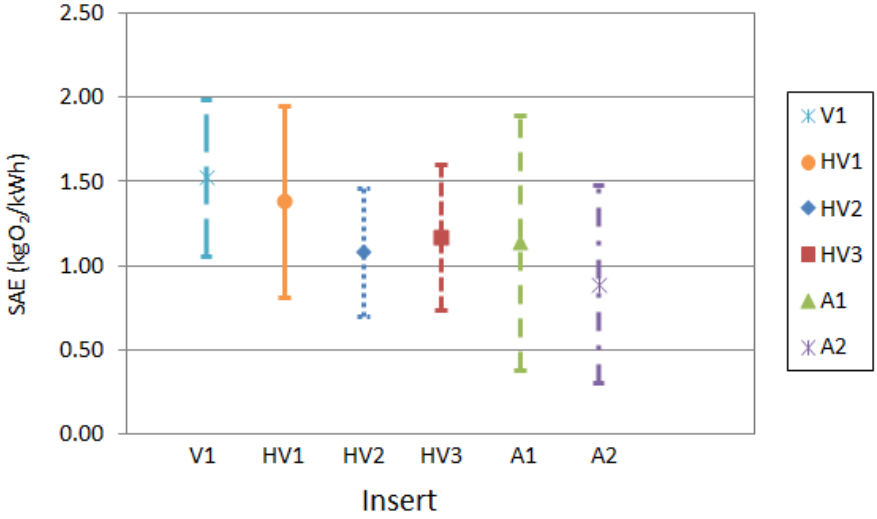

Figure 10.2: - SAE average and standard deviation for all inserts across the range of operating conditions tested in the laboratory scale experiments.

As can be seen in Table 10.2 the maximum SAE occurred for all the inserts at the lowest water velocity and air flow rate, U_w = 1 ms^{-1} and Q_a = 50 slm. It is also noticeable in Table 10.1 that the A1 insert had the highest maximum SAE, in comparison to the other inserts and the HV1 insert had the highest maximum of the R_v = 1.5 inserts. The V1 insert however, had the highest average SAE of all the inserts. When comparing the HV1, HV2 and HV3 inserts it can be seen that the HV1 insert had the highest average SAE and the highest maximum value.

10.4. Sauter mean bubble diameter, d_{32}

The Sauter mean bubble diameter in fluid dynamics is an average of the bubble size. It was originally developed by German scientist J. Sauter in the late 1920's (Sauter, 1926) and it is defined as the diameter of a sphere that has the same volume to surface area ratio as a particle of interest.

Table 10.3 displays the average and maximum SAE of all the inserts across the range of operating conditions, whilst Figure 10.3 shows the average and standard deviations.

Table 10.3: - d_{32} average and maximum values for all inserts across the range of operating conditions tested in the laboratory scale experiments.

Insert	Average	± (%)	Min	at
V1	2.87	12.45	2.53	U_w = 3 ms^{-1}, Q_a = 50 slm
HV1	2.91	14.76	2.53	U_w = 3 ms^{-1}, Q_a = 50 slm
HV2	2.91	11.59	2.58	U_w = 3 ms^{-1}, Q_a = 50 slm
HV3	2.94	13.79	2.56	U_w = 3 ms^{-1}, Q_a = 50 slm
A1	2.35	37.54	1.46	U_w = 3 ms^{-1}, Q_a = 300 slm
A2	2.02	45.55	1.26	U_w = 3 ms^{-1}, Q_a = 300 slm

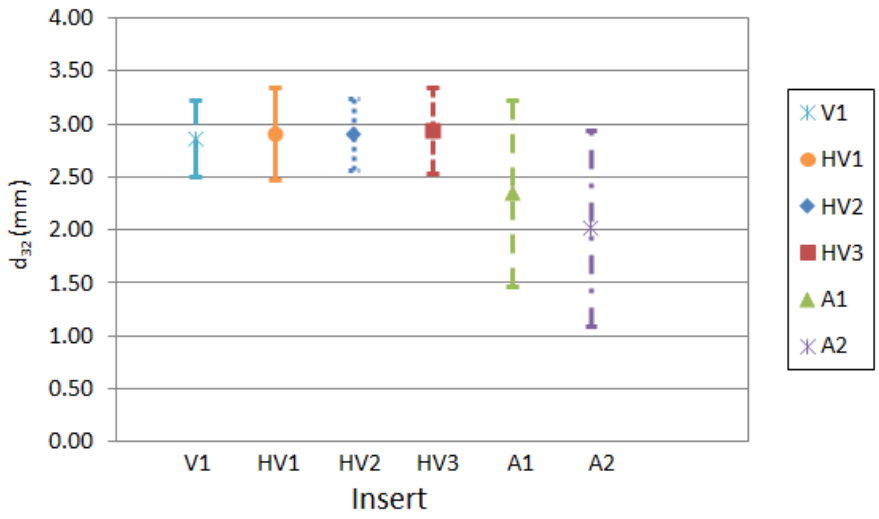

Figure 10.3: - d_{32} average and standard deviation for all inserts across the range of operating conditions tested in the laboratory scale experiments.

As can be seen in Table 10.3 the minimum d_{32}, which is the most desirable to achieve the maximum interfacial area for mass transfer, occurred for all the inserts at the highest water velocity and either at the highest or lowest air flow rate, U_w = 3 ms^{-1} and Q_a = 50 or 300 slm. The reason for the range in the air flow rate to achieve the minimum d_{32} is because of the formation of the ventilated cavity, as was discussed in

Chapter 5, where the A1 and A2 inserts did not have a ventilated cavity present for all air flow rates at U_w = 3 ms^{-1}. However, the R_v = 1.5 inserts had a ventilated cavity present for all air flow rates of above 50 slm. It is noticeable in Table 10.3 that the A2 insert had the smallest minimum d_{32}, in comparison to the other inserts and the HV1 and V1 inserts had the smallest minimum of the R_v = 1.5 inserts. The V1 insert also had the smallest average d_{32} of the R_v = 1.5 inserts. When comparing the HV1, HV2 and HV3 inserts it can be seen that the HV1 insert had very similar performance between all three of the inserts. Again, this is because of the formation of the ventilated cavity, which as highlighted in Chapter 5, reduces the turbulence in the flow associated with bubble breakage and therefore limits the formation of a small Sauter mean bubble diameter. Throughout all of the water and air flow rates for the R_v = 1.5 inserts had a ventilated cavity present, except for the HV1 and HV3 inserts at U_w = 3 ms^{-1} and Q_a = 50 slm.

10.5. Upstream structure

Considering the overall system of the aerator system, including upstream and downstream of the insert it was shown in case studies outlined in Chapter 9, that the upstream section of the overall structure requires considerable thought and planning to minimise the upstream losses associated with the pipe work. Careful consideration is required so that additional fittings that can cause additional pressure losses, such as expansions and pipe bends, are minimised.

If pipe bends are required then a larger, pipe bend radius to pipe diameter ratio, $r_{pipe}/_{d}$ would be more beneficial in terms of losses. Based on the performance charts from Miller (1971) a ratio of 3 for 90 and 180˚ bends are the most efficient. Above a $r_{pipe}/_{d}$ ratio of 3 the resulting length of the bend and the additional frictional losses begin to outweigh the benefits of an increased ratio.

When a flow travels round a bend the fluid near the wall of the outside of the bend has a higher momentum than its neighbours that are nearer to the inner wall of the bend. This is because the fluid nearer to the outer wall has a higher velocity and the centrifugal force on the fluid acts to displace it further towards the wall. There is an enhancement of the turbulent energy being transferred towards the outer wall and energy dissipation is increased. This results in the velocity gradient close to the wall to be steep. The fluid approaching the outer wall sees an adverse pressure gradient and the energy deficient near wall fluid at the outer wall cannot pass through the adverse pressure gradient. Instead the fluid moves around the walls towards the low static pressure region on the inside of the bend. This flow from the outer to the inner wall region is termed a secondary flow. Increasing the radius ratio is seen to increase the strength of the secondary flow which re-energises the inner wall regions, thus preventing flow separation at the inner wall and increased pressure losses.

Therefore when considering an in process design structure a considerable amount of thought is required with the aim to minimising upstream pressure losses, thus maximising the efficiency of the system.

10.6. Mixture outlet

Chapter 9 showed that careful consideration is required into the design of how the outlet geometry of the two-phase mixture. The CFD simulations conducted by MMI Engineering showed significant coalescence of the air on the inside of the outlet bend in to the receiving tank. These CFD simulations were validated with the visual observations of the large scale experiments were the air was seen to rise against the tank wall above the mixture outlet. From these observations it is clear that careful consideration is needed to the geometry of the outlet and considerable investigation is required into determining the optimum design of outlet.

Within the wastewater industry there are two main types of aeration tanks or containers. The first are aeration lanes which are primarily used in municipal wastewater treatment. Aeration lanes can span 10's of meters in width and 100 m in length (Boyle, et al., 2002). Within these aeration lanes there is a steady and slow flow of the wastewater from one side to the other. The second kind of aeration basin is a cylindrical tank or a submerged pit, which are typically used in industrial wastewater treatment (Boyle, et al., 2002).

The type of aeration volume used would have a significant impact on the outlet geometry of the downcomer. For example, with an aeration lane it may not be practical to have a vertical discharge into the volume. For this to be the case, pipes would have to span the width of the aeration lane so that a sufficient amount of air was distributed throughout the volume of wastewater. In this instance it may be more suitable to have the aerator at the edge of the aeration lane and use a pipe bend to direct the two-phase mixture towards its centre. A $r_{pipe}/_{d}$ ratio of 3 could be recommended to prevent the separation of the two phases flowing through the bend. Alternatively, if a cylindrical tank were to be used a vertical discharge in conjunction with a cylindrical baffle could be used. The vertical outlet would prevent bubble accumulation and the use of the baffle to constrict the aerated liquid would promote mixing. This is similar to the set up within a bubble column, which incorporates a draft tube. In a bubble column recirculation occurs when the denser non-aerated liquid at the outer vessel wall recirculates at the bottom of the draft tube into the less dense and lower pressure aerated liquid within the draft tube. Or vice versa, if the aerated liquid was on the outside of the draft tube. In conjunction with this, if a diffuser were to be used then it could allow the two-phase mixture to begin to disperse within the diffuser outlet, encouraging a greater dispersion in the tank, as a result of the increased angular momentum.

Figure 10.4 and 10.5 shows the air distribution and the air plume in the aeration tank used in the large scale experiment, where the CFD simulations shown in Figures 10.4 and 10.5 used the mixture outlet from the large scale experiment and a mixture outlet of $r_{pipe}/_{d}$ ratio of 3, respectively. Figures 10.4 (a) and 10.5 (a) shows the air distribution on a vertical plane through the tank, downcomer and the mixture outlet. The air plume in Figures 10.4 (b) and 10.5 (b) is for an air void fraction of greater than 1 %. It is shown in Figure 10.5 (a) that for a $r_{pipe}/_{d}$ ratio of 3 there is still bubble accumulation in the upper side of the pipe bend.

However, when compared to Figure 10.4 (a) it can be seen there is a greater dispersion of air towards the middle of the tank and less of a concentrated stream of air at the tank wall, all of which is highlighted by comparing Figures 10.4 (b) and 10.5 (b). Despite the improvement in air distribution in the tank. If the air coalescence in the pipe bend was great enough, then due to the buoyancy of the air the large accumulated bubble could then rise up the downcomer. The air would either vent through the air inlets or accumulate in a bend, if present prior to the downcomer. This would cause significant back pressure and as result greater energy requirements. Examples of an upstream bend are shown in the experimental set ups of the farm project and large scale experiments, which are outlined in Chapter 9, shown in Figures 9.3 and 9.10. If the system was located in a siphon arrangement this could cause the siphon arrangement to break and the system to stall. This is in addition to the negative impacts of bubble coalescence, such as increased back pressure and reduced interfacial area for mass transfer. These negative impacts have been shown with the presences of a ventilated cavity in the downcomer of the laboratory scale experimental work.

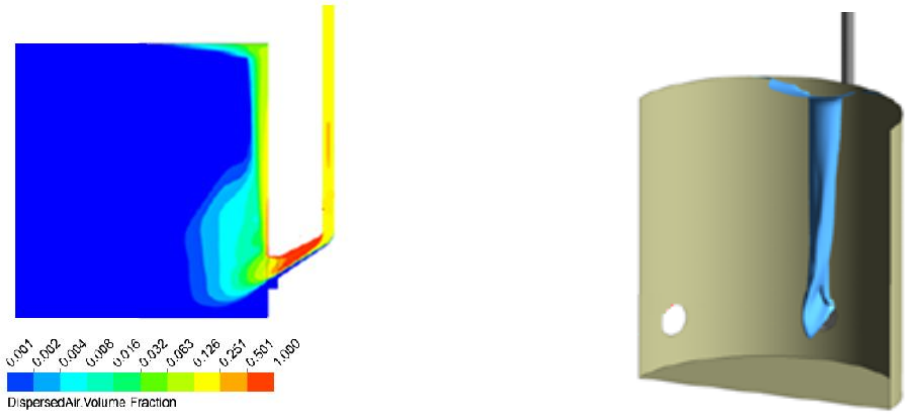

(a) (b)

Figure 10.4: - Air distribution (a) through a slice in the diffuser and (b) the air distribution in the tank for the mixture outlet for the large scale case experimental set up.

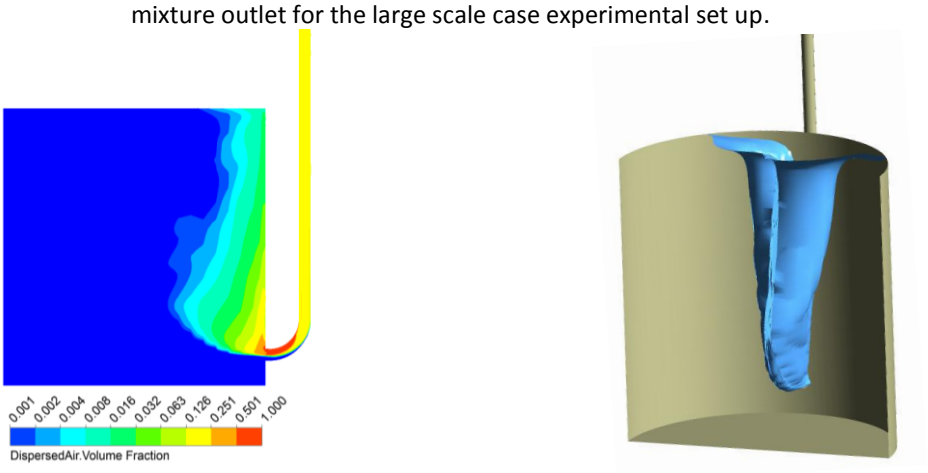

(a) (b)

Figure 10.5: - Air distribution (a) through a slice in the diffuser and (b) the air distribution in the tank for the mixture outlet of a $^{r_{pipe}}/_{d}$ ratio of 3.

An alternative approach to using a side entry into the mixing tank would be to us a vertical discharge which would prevent bubble accumulation at the outlet. The air distribution through a slice of the domain and a bubble plume of air within the tank, which is shown by an iso-surface, where a void fraction of greater that

1 % is present, for a vertical discharge, a vertical discharge with a diffuser as well as the use of the baffle are shown in Figures 10.6, 10.7 and 10.8 respectively. The angle of the diffuser shown in Figure 10.7 is 7˚ and has a outlet to inlet area ratio of 4

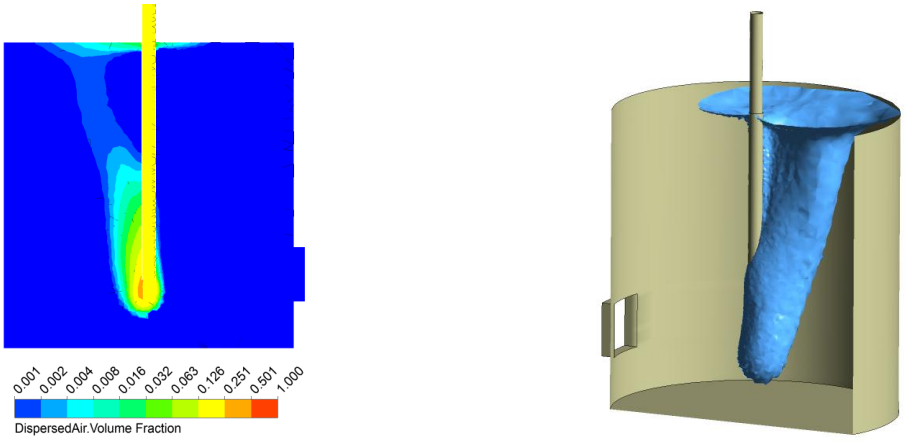

(a) (b)

Figure 10.6: - Air distribution (a) through a slice in the diffuser and (b) the air distribution in the tank for a vertical mixture outlet.

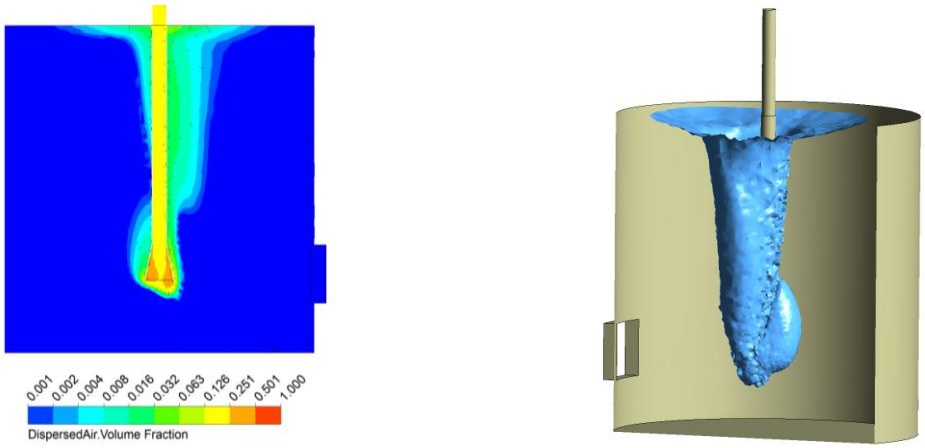

(a) (b)

Figure 10.7: - Air distribution (a) through a slice in the diffuser and (b) the air distribution in the tank for a vertical mixture outlet with a conical diffuser of 7˚.

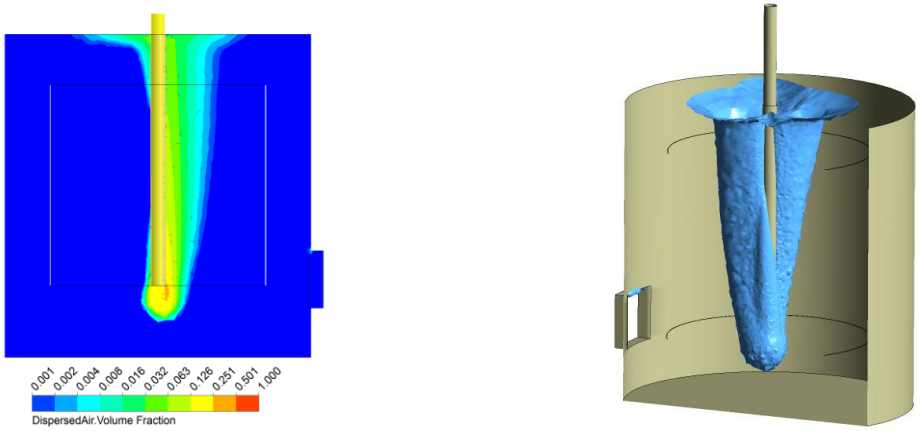

(a) (b)

Figure 10.8: - Air distribution (a) through a slice in the diffuser and (b) the air distribution in the tank for a vertical mixture outlet with a baffle of 3 m diameter.

Figures 10.6, 10.7 and 10.8 all show a relatively similar air distribution of with a vertical air column surrounding the downcomer. However, the dispersion of the air with a diffuser present, Figure 10.7, or

when a baffle was used, Figure 10.8, were slightly greater than when neither of them were used, Figure 10.6. Figure 10.7 (a) shows there is a level of air accumulation within the walls of the diffuser. Figure 10.9 shows the velocity of the water in the diffuser and it can be seen that flow reversal and separation is occurring at the outlet of the diffuser, which would lead to increased pressure losses along with the bubble accumulation leading to a reduced interfacial area. It was for these reasons that a baffle was investigated with a vertical outlet with no diffuser present.

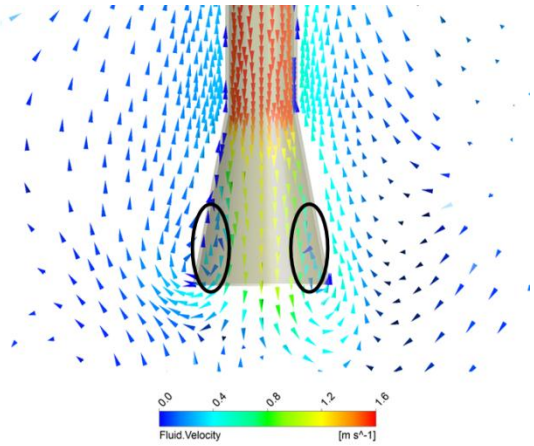

Figure 10.9: - The velocity vectors of the water at the diffuser outlet.

When choosing the location of the baffle for the vertical outlet, a velocity vector plot for the water with the vertical outlet was obtained, as shown in Figure 10.10 (a). Figure 10.10 (a) shows a clear level of recirculation occurring in the tank, which has been highlighted by the dashed lines. This natural recirculation occurred at approximately a diameter of 3 m. Figure 10.10 (b) shows the velocity vectors of the water with a 3 m baffle in situ.

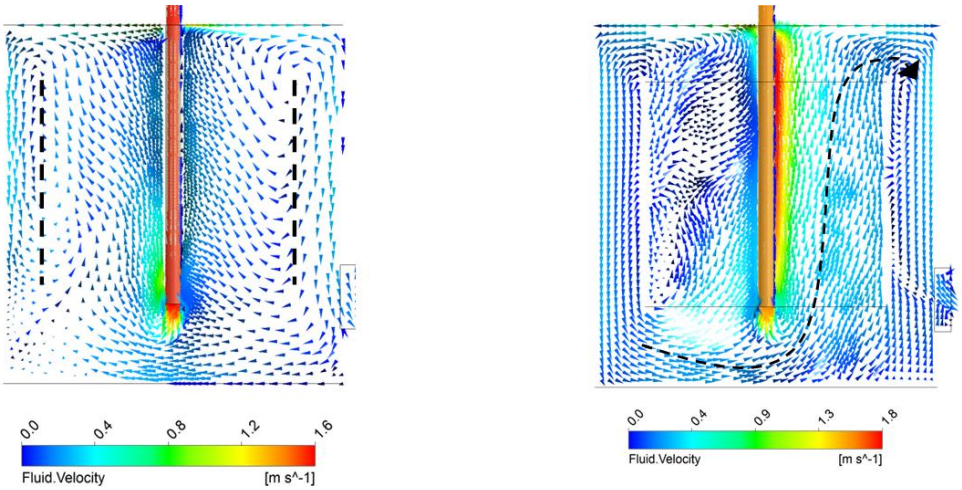

(a) (b)

Figure 10.10: - Velocity vectors of the water across a slice of the domain for (a) when a vertical outlet was used and (b) when a baffle was used with a 3 m diameter in conjunction with a vertical outlet.

Figure 10.10 (b) shows a significant amount of turbulent mixing and recirculation within the baffle geometry, which would improve mass transfer. Then outside of the baffle there is a less turbulent and linear falling liquid film, which then flows back into the baffle geometry. It can also be seen that some of the

flow from the left hand side of the figure, which is furthest away from the pump inlet flows along the base of the tank into the right hand side of the baffle and then down the right hand side falling film near the pump inlet, illustrated by the dashed line. Therefore, this set up has indicators of high levels of mixing, where all the water would come into contact with the entrained air.

From these numerical simulations it has been identified that a number of issues need to be considered when designing the outlet of the mixture into the receiving tank. It has been identified that using a pipe bend to promote a horizontal flow into the pipe to improve the distribution of air can lead to bubble accumulation at the top side of the pipe. This would affect the mass transfer performance of the system, lead to higher pressure losses and potentially result in stall conditions. Further investigation could be conducted into inducing a swirl upstream of the pipe bend. The aim of the swirl would be to reduce flow separation by encouraging secondary flows to occur in the bend, where the heavier density water would flow around the outside of the pipe to the lower pressure region at the inside of the pipe. Therefore preventing bubble accumulation at the upper wall of the pipe bend. It has however been shown that using a vertical discharge in conjunction with a baffle to form a loop reactor set up has a number of benefits. These include the prevention of flow separation and significant turbulent mixing within the tank, which in turn would enhance mass transfer. However, this type of system would be limited to relatively small diameter receiving tanks, which are typically used in the industrial wastewater industry compared to aeration lanes, which are used for municipal wastewater treatment.

10.7. Insert location

Using the insert in a vertical orientation requires consideration into the height of the throat above the water level and how is can have a significant impact on the efficiency of the system, as will be discussed in this section. Increasing the height of the throat above the surface of the water will reduce the static pressure in the throat of the insert, according to Bernoulli's principle, where the reduction in the static pressure will be equal to the mixture frictional losses in the downcomer subtracted from the mixture hydrostatic head difference (Soo, 1967). Provided the increased frictional losses are less than the hydrostatic head, there will be a resulting increase in the suction pressure at the throat. This increase in suction pressure will result in an increased air entrainment, which can have an impact on the resulting flow regime. As shown in Chapter 5, increasing the air entrainment can result in a ventilated cavity forming from the points of air injection, which in turn causes an increase in pressure drop, which would lead to an increased back pressure and therefore reduced entrainment.

A series of experiments were conducted with the air inlets of both the HV1 and V1 inserts open to the atmosphere, which was followed by lowering the HV1 insert by 12 ID and retesting, which is termed by HV1L. The distance of 12 ID was chosen because it was the lowest possible location within the experimental set up, due to the tank walls, the support structure and the existing lengths of pipe work. Lowering the insert as much as possible would enable the extremes of the heights available for the inserts within the

laboratory scale set up to be studied and compared. As was detailed in Chapter 4, the current insert location was chosen to be as close as possible to the pipe bend above the downcomer, to maximise the visible length of the two-phase flow. The results of $k_L a_{20}$, E, SAE and SOTR are shown in Figure 10.11.

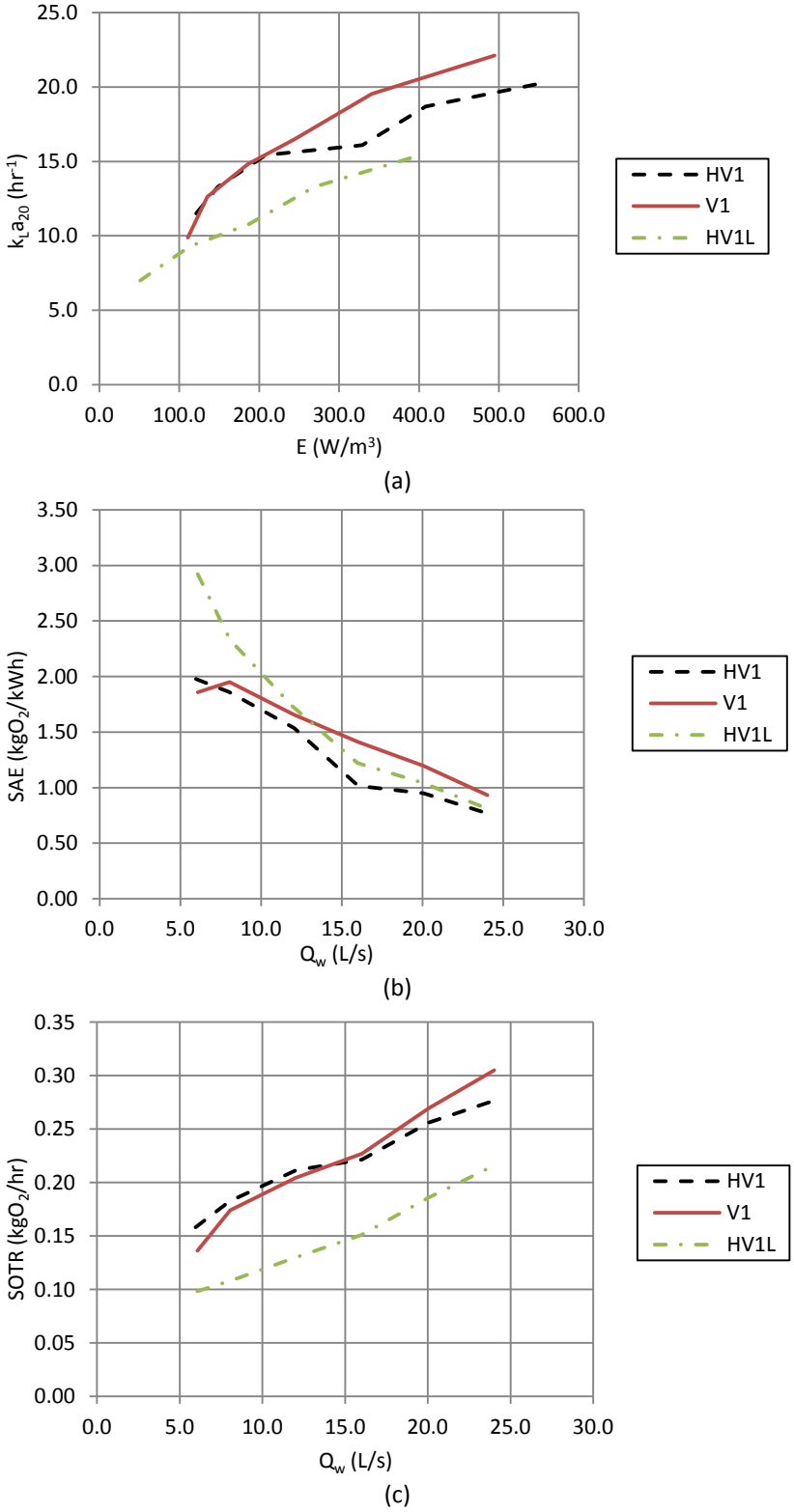

Figure 10.11: - A comparison of (a) specific power against $k_L a_{20}$, (b) water flow rate against SAE and (c) water flow rate against SOTR, for the HV1, V1 and HV1L inserts with the air inlets open to the atmosphere.

Figure 10.11 (a) shows that the V1 insert typically has the highest SOTR for the same specific power, especially at the higher specific power values, correlating to higher air and water flow rates. This is despite the HV1 and V1 inserts having similar air entrainment, shown in Table 10.4 (a), and bubbly flow length values within ± 5 % of each other. However, it can be seen that at the lower E values of less than 150 W/m^3 the HV1 insert out performs the V1 insert, which was a similar trend when the air was being imposed into the water flow, as was shown in Chapter 7.

It is observed in Figure 10.11 (b) that below water flow rates of 7 L/s the HV1 insert has a higher SAE than the V1 insert. It is also shown in Figure 10.11 (b) that below 13 L/s the HV1L insert has the superior performance in terms of SAE than the HV1 and V1 insert. However, when analysing Figure 10.11 (c) it can be identified that the HV1L experiment had a significantly reduced SOTR compared to the other two experiments. This can be attributed to the reduced air entrainment or because of the shorter length of two-phase bubbly flow in the downcomer, due to the lowering of the insert closer to the mixture outlet at the base of the downcomer.

Table 10.4: - Mass transfer characteristics and performance for the (a) HV1 and V1 and (b) HV1 and HV1L, inserts with the air inlets open to the atmosphere.

(a)

Q_w (L/s)		Q_a (slm)		$k_L a_{20}$ (hr^{-1})		SOTR (kgO_2/hr)		SOTE (%)		E (kgO_2/kWh)	
HV1	V1	HV1	V1	HV1	V1	HV1	V1	HV1	V1	HV1	V1
5.96	6.08	121.0	125.0	11.51	9.88	0.16	0.14	7.79%	6.51%	121.0	110.8
8.02	8.06	142.0	145.0	13.30	12.63	0.18	0.17	7.60%	7.15%	148.3	135.1
12.06	12.02	166.0	165.0	15.42	14.83	0.21	0.20	7.55%	7.37%	208.2	186.3
16.01	16.02	171.0	185.0	16.10	16.46	0.22	0.23	7.70%	7.30%	329.1	243.4
20.08	20.06	192.0	197.0	18.68	19.54	0.26	0.27	7.92%	8.12%	408.4	340.8
24.07	24.02	205.0	202.0	20.17	22.12	0.28	0.30	7.95%	8.96%	546.8	494.6

(b)

Q_w (L/s)		Q_a (slm)		$k_L a_{20}$ (hr^{-1})		SOTR (kgO_2/hr)		SOTE (%)		E (kgO_2/kWh)	
HV1	HV1L	HV1	HV1L	HV1	HV1L	HV1	HV1L	HV1	HV1L	HV1	HV1L
5.96	6.08	121.0	75.0	11.51	7.01	0.16	0.10	7.79%	7.93%	121.0	50.9
8.02	8.08	142.0	88.0	13.30	7.73	0.18	0.11	7.60%	7.42%	148.3	70.3
12.06	11.95	166.0	105.0	15.42	9.30	0.21	0.13	7.55%	7.44%	208.2	113.3
16.01	15.97	171.0	112.0	16.10	10.79	0.22	0.15	7.70%	8.11%	329.1	186.8
20.08	20.01	192.0	130.0	18.68	13.29	0.26	0.19	7.92%	8.68%	408.4	269.0
24.07	23.98	205.0	144.0	20.17	15.43	0.28	0.22	7.95%	8.99%	546.8	402.2

Table 10.4 shows the associated values of E, $k_L a_{20}$, SOTR, SOTE and air entrainment for the various water flow rates tested for the inserts. Table 10.4 (b) shows that the SOTE values of the HV1 and HV1L were very similar, this indicates that the length of the downcomer beneath the point of air injection did not significantly affect the percentage of oxygen transferred, where the length of the downcomer below the HV1L was 10 ID, in comparison to 22 ID for the HV1 experimental work. It is not possible with this experimental work to comment on whether reducing the length of the downcomer to less than 10 ID would begin to reduce the percentage of oxygen transferred and at what point this would occur. But from this it is possible to make the assumption that the vast amount of the oxygen transfer occurs immediately downstream of the insert, or if a ventilated cavity is present. The mass transfer occurs immediately

downstream of this. This assumption is validated by the work of Mao et al (1993) and Evans and Machniewski (1999), where it was found that the contribution to mass transfer of the mixing zone beneath a plunging liquid jet was significantly greater than that in the pipe flow zone beneath it. This is also similar to the work of Jackson and Collins (1964) were they discovered that the vast majority of the mass transfer in a horizontal venturi aerator occurred immediately downstream of the venturi.

As was shown in Chapter 7, the HV1 insert had the superior performance to the V1 insert at the lower water and air flow rates. This was also the case when the air was being induced into the flow. Also when considering the design of a system the location of the aerator can have a significant impact on its performance, where lowering the aerator closer to the water can improve the aeration efficiency of the system. However, this comes at a cost of a reduced air entrainment, which may cause the water to be treated to become septic, if the required oxygen demand was not met.

10.8. Design for purpose

Due to the wide variety of industries that use aerators for the purpose of mass transfer, fouling of the aerator may be an issue. Issues regarding fouling and clogging can be resolved on an individual basis and come under three main categories. The first is inside fouling, this can be where the aerator can foul from the inside, such that the air inlets become blocked with debris from the external environment. Internal fouling can also occur, where the system may be switched off for maintenance or because of a decreased requirement for mass transfer, due to low loading. In the case of fine bubble diffusers this could cause the wastewater to flow into the orifices and as result block them. This should not be a problem for the inserts, which have been considered in this experimental work. This is because the insert itself would be located above the water free surface and as such, if the system were to be turned off then the water within the pipe work would flow back into the receiving tank, preventing blockage of the air inlets.

The second issue is biological fouling can occur when the surface of the insert is rough in texture which can be support biological growth (Environmental Dynamics Inc, 2013). Biological fouling can become a problem when on and off operations are employed or when the system is operated at very low air flows. At low air flows the distribution across the surface of the inserts will be reduced. Under these conditions flooding of the air inlets can occur, which in turn will cause clogging and/or biological fouling in the regions of the air inlets where there may be no flow, due to the reduced air flow rate. Therefore, design considerations are required to minimise or remove the affect of biological fouling. If it is allowed to persist then high pressure hosing or similar maintenance systems may be used to remove the formation of any biological film. Alternatively, the surface of the insert could be designed to be a smooth as possible, thus preventing biological build up and also reduce frictional pressure losses across the surface of the insert.

Industrial and municipal wastewater treatment plants can contain fibrous solids for example hair, lint, paper, leaves and plastic bags. Effective screening plays an important role in minimising the amount of

fibrous solids within the treatment plant. However, it is not possible to exclude all of this material and it must therefore be considered when designing an efficient aerator.

The effect of this fibrous material over time on a aerator can cause a third issue, when a small amount of this material clings to the leading edge of the vanes or to the hub and then weaves together with other fibres, growing larger and larger until a significantly sized clump of fibrous, rope-like material becomes securely fixed to the insert. This process is termed as ragging and is shown in Figure 10.12 for an impellor used within a stirred vessel. Ragging would not be a problem with the V1 insert or other types of venturi because there is no leading edge for the fibrous material to cling to and therefore cause problems. This added mass can great significant issues such as,

a) The efficiency of the flow generated through the system can be severely reduced, resulting from increased back pressure due to the ragging potentially on the leading edge of the vanes, creating blockage to the flow.
b) An increased back pressure can cause increased pressure on the pump, resulting in motor overload as well higher wear on gearing and bearings with subsequent premature failure.
c) The increased velocity through the insert due to the blockage would cause increased losses due to friction which can lead to problems with mechanical integrity of the pipe work of the system (Hill & Wood, 1994).

Figure 10.12: - Ragging on an impeller within a municipal wastewater treatment plant taken from Glass (2010).

Typically with impellors the only way to effectively deal with the problem of ragging is to periodically remove the build up by either draining the tank of raising the mixer and then manually removing the mass from the impellor. In terms of the inserts in this experimental work it could be possible to monitor ragging using condition monitoring, which would incorporate a series of pressure monitors through the insert, looking to identify an increase in back pressure. An accessible hatch around the insert could be used to manually remove blockages. A more automated approach could be to use a series of air jets at the leading

edges of the vanes, to eject a high pressure air jet out on to the tips of the vanes and hub in such a way to remove any potential blockages. Alternatively a redesign of the insert could be undertaken. This could be done to assess the performance of an insert with the hub removed, in such a case the leading edges of the vanes would taper to the middle of the pipe preventing the build up of material along its edge.

10.9. Summary

As has been summarised in this chapter the highest maximum and average SOTR achieved was with the A2 insert, when comparing the R_v = 1.5 inserts, the HV1 and V1 inserts had a very similar performance, in terms of both the average and maximum SOTR achieved. Therefore, the primary aim of an aeration system would need to be established, such that if the primary focus was oxygen transfer rather than efficiency then the A2 insert would be the optimum insert. This primary focus could be present if there was a restricted size of aeration basin, thus a high SOTR would be required. However, if efficiency was the overall aim then a different conclusion may be arrived.

The SAE values from this experimental work across the inserts showed that the highest achieved was with the A1 insert. However, this was at a considerably low water and air flow rate, corresponding to low mass transfer rates. Therefore, the oxygen demand of the aeration system would need to be established to determine the applicability of these lower flow rates. If a higher overall mass transfer was required then the V1 insert had the highest overall SAE across the range of the operating conditions. Due to its lower specific power consumption. Therefore, for the inserts to be competitive, there would to be a redesign with the aim of reducing the specific power consumption. This can be achieved through preventing the formation of a ventilated cavity, thus significantly reducing pressure losses.

A long structure separates the flow for a longer time, thus encouraging a greater distribution of the air in the pipe, therefore preventing bubble coalescence. Extending the flow channels also increases the extent of the flow experiencing strong strain, which is beneficial to bubble breakage (West, 2009). However, there is an increased resistance to flow in the constricted region, potentially leading to a greater pressure loss, although this increased pressure loss could be offset by preventing the formation of a ventilated cavity. To prevent the formation of a ventilated cavity the velocity slip ratio between the air and the water at the throat also needs to be optimised, as identified in Chapter 5.

The formation of a ventilated cavity also hampers the generation of a small Sauter mean bubble diameter. It has been shown in Table 10.3 and Figure 10.3, that the smallest minimum and average Sauter mean bubble diameter was achieved with the A1 and A2 inserts, resulting in a higher interfacial area for mass transfer. The A1 and A2 inserts consistently had the shortest ventilated cavity lengths and at the higher water flow rates, they regularly had a full bubbly flow throughout the length of the downcomer, as shown in Chapter 5.

In summary there are a number of design issues with regards to both an in-process set up as well as the design of the insert. It has been shown in this chapter that the upstream section of the system requires careful design such that the losses associated with it are minimised. This can be achieved through removing any unnecessary fittings. This is also the case with the mixture outlet, where bubble accumulation needs to be prevented and turbulent mixing in the receiving volume of water can be enhanced by using a cylindrical baffle within the tank to promote mixing and recirculation.

With regards to the insert and its location within the system it has been shown that lowering the insert closer to the water surface can increase aeration efficiency. However, it comes at the cost of a reduced air entrainment and SOTR. For this series of experimental work it has been hypothesised that the vast majority of the mass transfer in the downcomer occurs within a relatively short distance beneath the point of air injection or below a ventilated cavity.

To maximise on the range of industrial application that would be able to use venturi insert that incorporates the use of aerofoils. A redesign may be required such that the insert could be used in wastewater that has not been as heavily filtered or would contain a higher level of dissolved solids and fibrous material. This could be done by using a 'hubless' insert, which would prevent ragging.

CHAPTER 11

CONCLUSIONS AND FUTURE WORK

11.1. Introduction

This final chapter of this thesis presents the main contribution of the present work and provides some suggestions for further research. The main conclusions of the study are outlined in the first section, followed by some suggestions for future work with both experimental and theoretical extensions of the current work.

11.2. Conclusions

The conclusions of the present work can be summarised in the following considerations of, flow regime and bubble size, hydrodynamic and mass transfer efficiencies, CFD simulations and geometric scaling, as well as in-process design. The main conclusions are briefly mentioned and discussed below,

Throughout this study two flow regimes were identified, firstly a bubbly flow and the second is when a ventilated cavity forms at the point of air injection. It has been shown that,

a) Reducing the air and water velocity slip ratio at the throat, by increasing the blockage ratio and amount of air orifices, reduces the length of a ventilated cavity (Chapter 5, Section 2).
b) Inducing a swirl in combination with a high blockage ratio resulted in coring of the air at the higher flow rates, (Chapter 5, Section 4).
c) For a fixed flow rate, a bubbly flow produces a smaller average bubble size than when a ventilated cavity was present, when a ventilated cavity was present average bubble sizes were similar across the inserts for fixed flow rate conditions (differences within ± 10 %), (Chapter 5, Section 5).

Throughout this study, the geometry of the insert, flow regime and the flow rate settings, have a significant effect on the hydrodynamic and mass transfer efficiencies of an insert, for example,

a) Increasing the blockage ratio significantly increasing the specific power consumption, (Chapter 6, Section 3) and $k_L a_{20}$, (Chapter 7, Section 2), which results in a low SAE, (Chapter 7, Section 4).
b) Increasing the water flow rate reduced the specific power consumption associated with the ventilated cavity. However, a ventilated cavity has significantly higher specific power consumption than a bubbly flow, (Chapter 6, Section 4).
c) Mass transfer is a function of ventilated cavity length when one is present, where a reduced length of ventilated cavity results in an increased rate of mass transfer, (Chapter 7, Section 2).
d) The regular venturi consistently had the lowest specific power consumption, (Chapter 6, Section 3).
e) The HV1 insert has the highest SAE at the lower flow rates. However, V1 surpasses the performance of the HV1 insert at the higher flow rates, (Chapter 7, Section 4).

As a result of the physical experimentation, CFD simulations were validated and it was found that,

a) A population balance model coupled with the Eulerian-Eulerian multiphase and k-ω shear stress transport model resulted in the most accurate solution, (Chapter 8, Section 30).
b) The average bubble size, specific power consumption and mass transfer coefficients are found to be within 6, 15 and 25 % of the laboratory scale values, (Chapter 8, Section 30).
c) Geometric scaling found that the larger scale HV1 insert had an increased Sauter mean bubble diameter and specific power consumption when compared to the laboratory scale experiment by over 27 % and 18.5 % respectively, (Chapter 8, Section 31).

In addition to the laboratory scale experimental work, a case study and large scale experimental work was conducted, using the HV2 insert. The case study was conducted using wastewater at 150 mm ID scale and the large scale experimental work was conducted using clean water at 190 mm ID scale. It was found that,

a) The upstream conditions were seen to have a significant impact of the system performance and design consideration is required to minimise the losses associated with this section of the system, through removing any unnecessary pipe fittings, (Chapter 9, Sections 4 and 9).
b) The mixture outlet was seen to impact on the aeration efficiency, where pipe bends resulted in flow separation and bubble coalescence, leading to reduced mass transfer, (Chapter 9, Section 10)
c) The design of the inserts could be a cause for concern with the issue of ragging on the leading edge of the vanes, which would not be a problem with the V1 insert, (Chapter 10, Section 8).

11.3. Future work

The main conclusions of the present study have been presented. The next paragraphs give a few suggestions for further research for both theoretical and experimental extensions of this work. Based on the current work the following areas of research are identified,

a) It has been shown in this experimental work that the formation of the ventilated cavity is an undesirable flow state, which can be alleviated through reducing the air to water velocity slip ratio in the throat of the insert. It has also been shown that ragging can be a significant problem in the aeration industry and it could potentially occur on the leading edge of the vanes of the inserts. Therefore, an alternate design of insert to counteract these problems needs to be investigated. The problem of bubble coalescence and therefore ventilated cavities can also be lessened by elongating the channels. This allows the air bubbles to become more dispersed within the flow and increases the extent of the flow that experiences strong strain, which is beneficial to bubble breakage. In conjunction with this, removing the central hub would alleviate any potential problems with ragging on the leading edges of the vanes. This redesign would initially be assessed for improvements using the CFD simulations, which would be used to determine the average bubble size, specific power and the $k_L a_{20}$.

b) Chapters 9 and 10 identified that there are potential problems with coalescence and phase separation in the mixture outlet of the large scale experimental set up, which could be overcome by using a vertical discharge into the bulk liquid of the aeration tank. Conducting both hydrodynamic and mass transfer testing on the large scale set up with a vertical discharge would decrease the coalescence of the air, which in turn will result in a reduced the pressure loss and increased mass transfer, and therefore an improved the SAE.

c) It is important to directly compare the technology studied in this thesis against the leading technology in the aeration market, such as fine and coarse bubble diffusers, through testing in both clean and wastewater. The large scale experimental set up could be retrofitted with a series of fine or coarse bubble diffusers. Hydrodynamic and mass transfer testing could then be conducted using both clean and wastewater. As a result, a direct comparison on the same system between an insert and a competitor within the aeration market could be made.

d) It is important in the development of a product, to test its performance within the market place. Therefore, designing and constructing a large scale in-process demonstration project would be of importance. A large scale demonstration project constructed on a functioning wastewater treatment plant would enable the technology to be brought to the market place after being successfully trialled. During the design stage of the demonstration project, decisions will have to be made so that the technology can display its effectiveness, based on the characteristics and requirements associated with the insert, such as the rate of oxygen transfer. Decisions will also have to be made on factors, such as the number, location and arrangement of inserts in operation, the required pump capacity and the air to water ratio that should be provided. Other decisions will involve water sampling and analysis procedures, which will be aimed at providing accurate monitoring of the power consumption and DO levels. Prior to the construction, the final design of the insert, assembly procedures and construction costs will have to be finalised. Consultations with manufacturers will be useful, both for estimating the cost to produce the insert and in the long term to identify ways to make the insert cheaper, easier and quicker.

e) It is important to continue building up a theoretical knowledge and understanding of the processes involved with the insert. An understanding of bubble breakage, coalescence and the velocity profile of the flow beneath the insert will enable the future designs of the insert to generate a smaller average bubble size and therefore promote a higher rate of mass transfer. Also measuring the $k_L a_{20}$ and the resulting bubble size in different liquids would provide a better assessment of the effects of the liquid physical properties on the system's mass transfer performance. This can be achieved by conducting bubble measurements using photography at more locations along the flow axis and closer to the insert, therefore generating a bubble size gradient for the downcomer. Using a high-speed video camera at the point of air injection will also enable a greater understanding of

the distribution of the air in the throat. The velocity profile of the air and the water can be accurately measured using LDA, as shown in Sotiriadis (2005). Therefore, the air to water velocity slip ratio will be established, which is important because the liquid mass transfer coefficient is a function of the air to water velocity slip ratio, as shown in Calderbank (1958) and in this experimental work.

f) From this greater understanding of the bubble formation and velocity profile, as well as the effects of different liquid properties. The applicability of the breakage and aggregation models in FLUENT could be established and in the long term, hydrodynamic efficiencies and mass transfer performance could be established using CFD for a range of in-process conditions, provided the liquid properties of the wastewater were known.

REFERENCES

ABS Group UK, 2013. *ABS Group UK.* [Online]
Available at: http://www.absgroupuk.com/default.asp?iAreaId=2794 [Accessed 17 02 2013].

Alleman, J., 1996. *The genesis and evolution of activated sludge technology - Enhancing the design and operation of activated sludge plants,* WI, USA: ASCE.

Alpoaeus, V., Koskinen, J. & Keskinen, K., 2002. Simulation of the population balances for liquid-liquid systems in a nonideal stirred tank. *Chemical engineering science,* 57(24), pp. 1815-1825.

American Public Health Association, 1995. *Standard methods for the examination of water and wastewater.* 22nd ed. Chicago: APHA, AWWA, WEF.

Andersson, R. & Andersson, B., 2006. Modeling the breakup of fluid particles in turbulent flows. *AIChE Journal,* 52(6), pp. 2031-2038.

ANSYS Inc, 2011a. *ANSYS FLUENT Theory Guide.* V14.5 ed. Canonsburg, PA: ANSYS Inc.

ANSYS Inc, 2011b. *ANSYS FLUENT Users Guide.* V14.5 ed. Canonsburg, PA: ANSYS Inc.

ANSYS Inc, 2011c. *ANSYS FLUENT Population Balance Module Manual.* V14.5 ed. Canonsburg, PA: Ansys Inc.

Aragaki, T., Nakayama, S., Suzuki, M. & Toyama, S., 1987. Characteristics of a falling film on a vertical tube. *International Chemical Engineering,* 27(1), pp. 326-333.

ASCE, 2007. *Measurement of oxygen transfer in clean water. ASCE Standard No. ASCE/EWRI 2-06,* Virginia: American Insitute of Civil Engineers.

Asher, W. & Pankow, J., 1991. *The effect of surface films on concentration fluctuations close to a gas/liquid interface, in Air-Water Mass Transfer.* New York, American Society of Civil Engineering, pp. 68-80.

Bacon, R., 1995. *Large bubbles in downwards two phase flow, PhD Thesis.* Cambridge, UK: Department of Chemical Engineering.

Bacon, R., Scott, D. & Thorpe, R., 1995. Large Bubbles attached to sparged in downwards two-phase flow. *International Journal of Multiphase Flow,* 21(5), pp. 949-959.

Bagatur, T., 2005. Technical note: Minimal conditions for a venturi aeration of water flows.. *Proceedings of the ICE - Water Management,* 158(3), pp. 127-130.

Bahmanyar, H. & Slater, M., 1991. Studies of drop-break up in liquid-liquid systems in a rotating disc contactor. *Chemical engineering technology,* 14(2), pp. 79-89.

Bakker, A., Haidari, A. & Oshinowo, L., 2001. Realize greater benefits from CFD, fluids/solids handling. *American Institute of Chemical Engineers: CEP magazine,* 3(1), pp. 45-53.

Baroczy, C., 1968. A Systematic correlation for two phase pressure drop. *Chem. Engin. Prog. Symp. Series,* 64(62), pp. 232-249.

Batchelor, G., 1951. *Pressure fluctuations in isotropic turbulence.* Cambridge, Proc. Camb. Phil. Soc.

Baylar, A. & Emiroglu, M., 2003. Air entrainment and oxygen transfer in a venturi. *Proceedings of the ICE - Water and Maritime Engineering,* 156(3), pp. 249-255.

Baylar, A., Ozham, F. & M.Unsal, 2007. Determination of the optimal location of the air hole in venturi aerators. *Clean-soil Air Water,* 35(3), pp. 246-249.

Baylar, A., Ozkan, F. & M.Ozturk, 2005. Influence of venturi cone angles on jet aeration systems. *Proceedings of the ICE - Water Management,* 158(1), pp. 9-16.

Baylar, A., Ozkan, F. & Tugal, M., 2006. The Performance of two phase flow systems in pond aeration. *International Journal of Science & Technology,* 1(1), pp. 65-74.

Benson, B. & Krause, D., 1984. The concentration and isotopic fractionation of oxygen dissolved in freshwater and seawater in equilibrium with the atmosphere. *The american society of lumnology and occanography,* 29(3), pp. 620-632.

Benzing, R. A. & Mayers, J. E., 1955. Low-frequency bubble formation at horizontal circular orifices. *Ind. Eng. Chem,* 47(10), pp. 2087 - 2090.

Bhagwat, S. & Ghajar, A., 2012. Similarities and differences in the flow patterns and void fractions in vertical upward and downward two-phase flow. *Experimental Thermal and Fluid Science,* 39(1), pp. 213-227.

Binder, J. & Hanratty, T., 1991. A diffusion model for droplet deposition in gas/liquid annular flow. *International Journal of Multiphase Flow,* 17(1), pp. 1-11.

Blasius, H., 1913. Das Aehnlichkeitsgesetz bei Reibungsvorgängen in Flüssigkeiten. *Mitteilungen über Forschungsarbeiten auf dem Gebiete des Ingenieurwesens ,* 131(1), pp. 1-41.

Bouaifi, M., Herbrard, G., Badtoul, D. & Roustan, M., 2001. A comparative study of gas hold-up, bubble size, interfacial area and mass transfer coefficients in stirred gas–liquid reactors and bubble columns. *Chemical Engineering and Processing: Process Intensification,* 40(2), pp. 97-111.

Boyle, W. C., Mueller, J. A. & Popel, H. J., 2002. *Aeration: Practices and Principles.* 1st ed. London: CRC Press.

Brennan, C., 2005. *Fundamentals of multiphase flow.* 1st ed. Cambridge: Cambridge University Press.

British Standard, 2003. *Wastewater treatment plants - Part 15: Measurement of the oxygen transfer in clean water in aeration tanks of activated sludge plants - BS EN 12255-15:2003.* London: British Standard.

British Standards, 2003. *Measurement of fluid flow by means of pressure differential devices inserted in circular cross-section conduits running full - Part 4: Venturi tubes - 5167-4:2003, BS EN ISO:.* London: British Standards.

Burton, C., 1992. A review of the strategies in the aerobic treatment of pig slurry: purpose, theory and method. *Agriculture, Ecosystems and Environment,* 53(1), pp. 249-272.

Calabrese, R., Chang, T. & Dang, P., 1986. Droplet breakup in turbulent stirred tank contactors. Part I: Effect of dispersed phase viscosity. *A. I. Ch. E,* 32(4), pp. 657-666.

Calderbank, P., 1958. Physical Rate Processes in Industrial Fermentations - Part I: - The interfacial area in gas liquid contacting with mechanical agitation. *Chemical Engineering Research and Design,* 36a(1), pp. 443 - 463.

Camarasa, E. et al., 1999. Influence of coalescence behaviour of the liquid and of the gas sparging on hydrodynamics and bubble characteristics in a bubble column. *Chemical Engineering and Processing: Process Intensification,* 38(4-6), pp. 329-344.

Changfeng, X., Renjie, L. & Gance, D., 1991. Mass transfer characteristics of the jet gas, liquid reactor in the air - water system. *Chemical Reaction Engineering and Technology,* 7(2), pp. 26-33.

Chatzi, E. & Lee, J., 1987. Analysis of interaction for liquid-liquid dispersion in agitated vessels. *Industrial and engineering chemistry research,* 26(11), pp. 2263-2267.

Chawla, R. & Pourhashemi, A., 2004. *A Mass Transfer Experiment Using Deoxygenation and Aeration of Water.* Washington, DC, American society of Engineering education.

Chisholm, D., 1973. Pressure gradient due to friction during the flow of evaporating two phase mixture in smooth tubes and channels. *International Journal of Heat and Mass Transfer,* 16(2), pp. 347-358.

Chisti, Y., 1989. *Airlift Bioreactors.* 1st ed. London: Elsevier.

Christian, D., Attarakih, M. & Bart, H., 2009. Coupling of CFD with DPBM for an RDC extractor. *Chemical engineering science,* 64(4), pp. 721-732.

Clift, R., Grace, J. & Weber, M., 1978. *Bubbles, Drops and particles.* 1st ed. Mineola NY: Dover publications Inc.

Coulaloglou, C. & Tavlarides, L., 1977. Description of interaction processes in agitated liquid-liquid dispersions. *Chemical engineering science,* 32(11), pp. 1289-1297.

Couvert, A., Roustan, M. & Chatellier, P., 1999. Two-phase hydrodynamic study of a rectangular arlift loop reactor with an internal baffle. *Chemical Engineering Science,* 54(21), pp. 5245-5252.

Cramers, P. & Beenackers, A., 2001. Influence of the ejector configuration, scale and the gas density on the mass transfer characteristics. *Chemical Engineering Journal,* 82(1-3), pp. 131-141.

Cramers, P. et al., 1993. Hydrodynamics and local mass transfer characteristics of gas-liquid ejectors. *The Chemical Engineering Journal and the Biochemical Engineering Journal,* 53(1), pp. 67-73.

Cussler, E., 1997. *Diffusion: Mass transfer in fluid systems.* 2nd ed. New York: Cambridge University Press.

Danckwerts, P., 1951. ance of liquid film coefficients in gas absorption. *Ind. Eng. Chem.,* 43(1), pp. 1960-1967.

Delfos, R., Rops, C., Kockx, J. & Nieustadt, F., 2001. Measurement of the re-coalescence flux into the rear of a taylor bubble. *Phys. Fluids,* 13(1), pp. 1141-1151.

Delfos, R., Wisse, C. & Oliemans, R., 2001. Measurement of air entrainment from a stationary Taylor bubble in a vertical pipe. *Internationl journal of multiphase flow,* 27(10), pp. 1769-1787.

Delnoij, E., Kuipers, J. & Van Swaaij, W., 1999. A three-dimensional CFD model for gas-liquid bubble columns. *Chemical engineering science,* 54(13-14), pp. 2217-2226.

Diemer, R. & Olson, J., 2002. A moment methodology for coagulation and breakage problems. *Chemical engineering science,* 57(12), pp. 4187-4198.

Dirix, C. & Van der Wiele, K., 1990. Mass transfer in jet loop reactors. *Chemical Engineering Science,* 45(8), pp. 2333-2340.

Douglas, J., Gasiorek, J., Jack, L. & J.Swaffield, 2005. *Fluid Mechanics.* 4th ed. NJ: Prentice Hall.

Drew, D., 1983. Mathematical modelling of two-phase flow. *Annual reviews in fluid mechanics,* 15(1), pp. 261-291.

Environmental dynamics Inc, 2003. *Technical Bulletin 127 - Energy consumption and typical performance of various types of aeration equipment.* Columbia, Missouri: Environmental dynamics Inc.

Environmental Dynamics Inc, 2013. *Technical Bulletin 109: - Typical Fine bubble fouling problems,* Missouri: Environmental Dynamics International.

EPA, 1983. *The Water Quality Standards Handbook: First Edition.* 1st ed. Washington DC: Environmental Protection Agency.

Evans, G., 1990. *A study of a plunging jet bubble column, PhD Thesis,* University of Newcaslte, Australia: Academic Print.

Evans, G., Bin, A. & Machniewski, P., 2001. PErformance of confined plunging liquid jet bubble column as a gas-liquid reactor. *Chem. Eng. Sci.,* 56(1), pp. 1151-1157.

Evans, G., Jameson, G. & Atkinson, B., 1992. Prediction of the bubble size generated by a plunging liquid jet bubble column. *Chemical Engineering Science,* 47(13-14), pp. 3265-3272.

Evans, G., Jameson, G. & Reilly, C., 1996. Fee jet expansion and gas entrainment characteristics of a plunging liquid jet. *Experimental thermal and fluid science,* 12(1), pp. 142-149.

Evans, G. & Machniewski, P., 1999. Mass transfer in a confined plunging liquid jet bubble column. *Chem. Eng. Sci,* 54(1), pp. 4981-4990.

Evans, G., Machniewski, P. & Bin, K., 2004. Bubble size distribution and void fraction in the wake region below a ventilated gas cavity in downward pipe flow. *Chemical Engineering Research and Design,* 82(9), pp. 1095-1104.

Fabiyi, M., 2008. *Understanding the alpha factor.* [Online]
Available at: http://www.wwdmag.com/aeration/understanding-alpha-factor [Accessed 03 05 2013].

Fabre, J. & Line, A., 1992. Modelling of two phase slug flow. *Annual Review of Fluid Mechanics,* 24(1), pp. 21-46.

Fick, A., 1855. Ueber Diffusion. *Annalen der Physik,* 170(1), pp. 59-86.

Forrester, S. & Rielly, C., 1998. bubble formation from cylindrical, flat and concave sections exposed to a strong liquid cross-flow. *Chemcial engineering science,* 53(8), pp. 1517-1527.

French, M. & Widden, M., 2001. The exploitation of low head hydropower by pressure interchange with air, using siphons. *Journal of Power and Energy,* 215(2), pp. 223-230.

Friedel, L., 1979. *Improved friction pressure drop correlation for horizontal and vertical two phase flow.* Ispra, European two phase flow group.

Gaddis, E., 1999. Mass transfer in gas-liquid contactors. *Chemical Engineering and Processing,* 38(10), pp. 503 - 510.

Gaylard, M., 2001. *Comparison of a Conventional RANS and a Lattice Gas Dynamics Simulation - A Case Study in High Speed Rail Aerodynamics.* 1st ed. Guernsey: Computational Fluid Dynamics in Practice.

Gourich, B., El Azher, N., Vial, C. & Belhaj, M., 2007. Influence of operating conditions and design parameters on hydrodynamics and mass transfer in emulsion loop-venturi reactor. *Chemical Engineering and Processing,* 46(2), pp. 139-149.

Gourich, B., Soulami, M. B., Zoulalian, A. & Ziyad, M., 2005. Simultaneous measurement of gas hold-up and mass transfer coefficient by tracer dynamic technique in "Emulsair" reactor with an emulsion venturi-distributor. *Chemical Engineering Science,* 60(22), pp. 6414-6421.

Gupta, A., Lilley, D. & Syred, N., 1984. *Swirl flows.* 1st ed. Lancaster, PA: Technomic Publishing Company.

Hagesather, L., 2002. *Coalescence and breakup of drops and bubbles - PhD Thesis.* Trondheim, Norway: Norweigen university of science and technology.

Health and Safety Executive, 2000. *Legionnaires' disease. The control of legionella in water systems - Approved code of practice and guidance.* L8 ed. London: Health and Safety Executive.

Helmut Kaiser Consultancy, 2006. *Markets for Aeration Systems Worldwide 2004 -2015,* Tübingen, Germany: Helmut Kaiser Consultancy.

Henstock, W. & Hanratty, T., 1979. Gas absorption by a liquid layer flowing on the wall of a pipe. *AIChE Journal,* 25(1), pp. 122-131.

Hesketh, R., Russell, T. & Etchells, A., 1987. Bubble size in horizontal pipelines. *AIChE,* 33(4), pp. 663-667.

Higbie, R., 1935. The rate of absoprtion of a pure gas into a still liquid. *Trans. Am. Inst. CHme. Eng,* 35(1), pp. 36-60.

Hill, T. & Wood, D., 1994. *Slug Flow: Occurrence, consequences and prediction.* Tulsa, OK, USA, Conditional Petroleum Engineering Symposium.

Hinze, J., 1955. Fundamentals of the hydrodynamic mechanisms of splitting dispersion processes. *AIChE Journal,* 1(3), pp. 289-295.

Hughes, R. R., Handlos, A. E., Evans, H. D. & Maycock, R., 1955. The formation of bubbles at simple orifices. *Chem. Eng. Prog.,* 51(12), pp. 557-567.

Indicators and Assessment Office of Environment Canada, 2001. *The State of Municipal Wastewater Effluents in Canada,* Ottawa, Canada: Minister of Public Works and Gorvernment Services Canada.

Ishii, M., Kim, s., Paranjape, S. & Sun, X., 2004. Interfacial structures and interfacial are transport in downward two-phase bubbly flow. *International Journal of Multiphase Flow,* 30(7-8), pp. 779-801.

Jackson, M. & Collins, W., 1964. Scale up of a venturi aerator. *Industrial and engineering Chemistry Process Design and Development,* 3(4), pp. 386-393.

Jakobsen, H., Lindborg, H. & Dorao, C., 2005. Modelling of bubble column reactors: progress and limitation. *Industrial and chemical engineering research,* 44(14), pp. 5107-5151.

Jensen, N. & Hvitved-Jacobsen, T., 1991. MEthod for measurement of reaeration in gravity sewers using radiotracers. *Res. J. WCPF,* 63(5), pp. 758-767.

Joshi, J. & Sharma, M., 1979. A circulation cell model for bubble columns. *Chemical Engineering Research and Design,* 57(A), pp. 244-251.

Karapantsios, S., Paras, S. & Karabelas, A., 1989. Statistical characteristics of free falling films at high reynolds numbers. *International Journal of Multiphase Flow,* 15(1), pp. 1-21.

Kashinshky, O. & Randin, V., 1999. Downward bubbly gas-liquid flow in a vertical pipe. *International Journal of Multiphase Flow,* 25(1), pp. 109-138.

Khurana, A. & Kumar, R., 1969. Studies in bubble formation - III. *Chemical Engineering Science,* 24(11), pp. 1711-1723.

Kockx, J., Nieuwstadt, F., Oliemans, R. & Delfo, R., 2005. Gas entrianment by a liquid film falling around a stationary taylor bubble in a vertical tube. *International Journal of Multiphase Flow,* 31(1), pp. 1-24.

Kulkarni, A. & Joshi, J., 2005. Bubble formation and bubble rise velocity in gas liquid systems: a review. *Ind Eng Chem Res,* 44(16), pp. 5873-5931.

Kulkarni, A., Joshi, J., Kumar, V. & Kulkarni, B., 2001. Application of multiresolution analysis for simultaneous measurement of gas and liquid velocities and fractional gas hold up in bubble column using LDA. *Chemical Engineering Science,* 56(17), pp. 5037-5048.

Kulkarni, A. & Shah, Y., 1984. Gas phase dispersion in a downflow bubble column. *Chemical Engineering Communications,* 28(4-6), pp. 311-326.

Kumar, R. & Kuloor, N., 1970. *The formation of bubbles and drops.* 8 ed. NY: Academic Press: Advanced chemical engineering.

Lara, P., 1979. Onset of air entrainment for a water jet impinging vertically on a water surface. *AIChE,* 34(9), pp. 1164-1165.

Launder, B. & Spalding, D., 1974. The numerical computation of turbulent flow. *Computer methods in applied mechanics and engineering,* 3(2), pp. 269-289.

Lee, Y., 1998. *Large bubbles beneath sparger in gas-liquid downflow, PhD Thesis.* Cambridge, UK: Department of Chemical Engineering.

Lee, Y., Scott, D. & Thorpe, R., 1997. The scale-up of large bubbles attached to sparger in downward two-phase flow. *Chemical engineering science,* 54(17), pp. 3893-3898.

Lee, Y., Scott, D. & Thorpe, R., 2000. Energy losses due to large bubbles beneath spargers in circulating bubble columns. *Chemical Engineering Science,* 55(1), pp. 97-112.

Lehr, F., Millies, M. & Mewes, D., 2002. Bubble size distributions and flow fields in bubble columns. *AIChE Journal,* 48(11), pp. 2426-2442.

Levich, V., 1962. *Physciochemical hydrodynamics: Volume 2.* 2 ed. N.J: Prentice Hall.

Lewis, D. & Davidson, J., 1982. Bubble splitting in shear flow. *Chemical Engineering Research and Design ,* 60(a), pp. 283-291.

Lewis, W. & Whitman, W., 1924. *Principles of Gas Absorption.* Massachusetts, Industrial and engineering chemistry.

Lockhart, R. & Martinelli, R., 1949. Proposed Correlation of Data for Isothermal Two Phase Flow, Two Component Flow in Pipes. *Chem. Eng. Prog.,* 45(1), pp. 39-48.

Lopez be Bertodano, M., Lee, S., Lahey, R. & Drew, D., 1990. The prediction of two phase turbulence and phase distribution phenomema using reynolds stress model.. *Journal of fluids engineering,* 112(1), pp. 107-113.

Luo, H. & Svendsen, H., 1996. Theoretical model for drop and bubble breakup in turbulent dispersions. *AIChE Journal,* 42(5), pp. 1225-1233.

Mahmud, H., 2012. *Multiphase transient flow in pipe - Phd Thesis.* Curtin: Department of Chemical Engineering.

Maier, C., 1927. Bulletin 260. *US Bureau of Mines,* 22(1), pp. 62-122.

Mao, W., Evans, G. & Jameson, G., 1993. *Mass transfer study in pluging jet bubble column.* Queensland, Fifth Asutraliasian heat and mass transfer conference.

Marchisio, D., Virgil, R. & Fox, R., 2003. Quadrature method of moments for aggregation-breakage processes. *Journal of colloid and interface science,* 258(2), pp. 322-334.

Marshall, S., Chudacek, M. & Bagster, D., 1993. A model for bubble formation from an orifice with liquid cross flow. *Chemical engineering science,* 48(11), pp. 2049-2059.

Martinez-Bazan, C., Montanes, J. & Lasheras, J., 1999. On the breakup of an air bubble injected into a fully developed turbulent flow. *Journal of fluid mechanics,* 401(1), pp. 157-182.

Martin, M., Montes, F. & Galan, M., 2009. Physical explanation of the empirical coefficients of gas-liquid mass transfer equations. *Chemical engineering science,* Volume 64, pp. 410-425.

Massey, B., 2006. *Mechanics of Fluids.* 8th ed. London: Francis and Taylor.

Mazzei, 2012. *Mazzei Injector Company LLC.* [Online]
Available at: http://www.mazzei.net/ [Accessed 14 11 2012].

Mckeogh, E. & Ervine, D., 1981. Air entrainment rate and diffusion pattern of plunging liquid jets. *Chemical engineering science,* 36(7), pp. 1161-1172.

Miller, D., 1971. *Internal Flow: A guide to losses in pipe and duct systems.* 1st ed. Bedford, U.K.: British Hydromechanics Research Association.

Nernst, W. & Lehfeldt, R., 1904. *Theoretical chemistry from the standpoint of Avogadro's rule & thermodynamics.* 1st ed. London: Macmillan and co.

Newton Innovative Technologies, 2011. *Scientific Basis of Newton Gravity Aerator,* Wirral, U.K: Newton Innovative Technologies.

O'connor, D. & Dobbins, W., 1958. Mechanisms of reaeration in natural streams. *Trans. Am. Soc. Civ. Eng.,* 123(1), pp. 641-684.

Ohkawa, A., Kawai, Y., Kusabiraki, D. & Sakai, N., 1987. Bubble size, interfacial area and volumetric liquid-phase mass transfer coefficient in downflow bubble column with gas entrainment by liquid jet. *Journal of chemical engineering of japan,* 20(1), pp. 99-101.

Oshinowo, O. & Charles, M., 1974. Vertical two-phase flow part I: flow pattern correlations. *The canadian journal of chemical engineering,* 52(1), pp. 25-35.

Prince, M. & Blanch, H., 1990. Bubble coalescence and break up in air sparged bubble columns. *AIChE Journal,* 36(10), pp. 1485-1499.

Quigley, C., Johnson, A. & Harris, B., 1955. *Size and mass transfer studies of gas bubbles.* Chemical Engineering Progress Symposium Series 16 (31): AIChE.

Ramkrishna, D., 2000. *Population balances: Theory and application to particualte systems in engineering.* 1st ed. San Diego: Academic press.

Ranade, V., 2002. *Computational flow modelling for chemical reactor engineering..* 5th ed. London: Academic Press.

Randolph, A. & Larson, M., 1971. *Theory of particulate processes: analysis and techniques on continuous crystallization..* 1st ed. San diego, CA: Academic press.

Riiser, K., Fabre, J. & Suzanne, C., 1992. *Gas entrainment at the rear of Taylor bubble.* stockholm, sweden, European two-phase flow group.

Rosso, D., Larson, L. & Stenstrom, M., 2008. Aeration of large municipal wastewater treatment plants: state of the art. *Water science and technology,* 57(7), pp. 973-978.

Rosso, D. & Stenstrom, M., 2005. Economic implications of fine pore diffuser aging. *WEFTEC, Annual technical exhibition and conference,* 78(8), pp. 2465-2477.

Saien, J. & Moradi, V., 2012. Low interfacial tnesion liquid-liquid extraction with impinging-jets contacting method: Influencing parameters and relationship. *Industrial and Chemical Engineering,* 18(4), pp. 1293-1300.

Sauter, J., 1926. *Die Grössenbestimmung der in Gemischnebeln von Verbrennungskraftmaschinen vorhandenen Brennstoffteilchen.* 1st ed. Dusseldorf: VDI-Verlag.

Schiller, L. & Naumann, Z., 1935. A drag coefficient correlation. *Z ver. Deutch. Ing,* 77(318), pp. 77-318.

Schugerl, K., 1991. *Bioreaction engineering: characteristics features of bioreactors, Volume 2.* 2nd ed. UK: John Wiley and Sons.

Sene, K., 1988. Air entrainment by plunging liquid jets. *Chemical Engineering Science,* 43(10), pp. 2615-2623.

Sevik, M. & Park, H., 1973. The splitting of drops and particles by turbulent fluid flow. *Journal of Fluids Engineering,* 95(1), p. 53.

Shammas, N. K., 2007. Chapter 8: Fine pore aeration of water and wastewater. In: N. Shammas, ed. *Handbook of Environmental Engineering - Volume 5.* Totowa, NJ: Humana Presss Inc, pp. 391-448.

Shannak, B. A., 2008. Frictional Pressure Drop of gas liquid two phase flow in pipes. *Nuclear Engineering and Design,* 238(12), pp. 3277-3284.

Soo, S., 1967. *Fluid dynamics of multiphase systems.* 1st ed. Waltham, Massachusetts: Blaisdell Publishing Company.

Sotiriadis, A., 2005. *Liquid recirculation and mass transfer beneath ventilated cavities in vertical two-phase downsflows,* Surrey: University of Surrey.

Sotiriadis, A. & Thorpe, R., 2005. Liquid re-circulation in turbulent vertical pipe flow behind a cylindrical bluff body and a ventialted cavity attached to a sparger. *Chemical engineering science,* 60(1), pp. 981-994.

Sotiriadis, A., Thorpe, R. & Smith, J., 2005. Bubble size and mass transfer characteristics of sparged downwards two-phase flow. *Chemical Engineering Science,* 60(22), pp. 5917-5929.

Su, C., 1995. *Gas entrainment at the bottom of a taylor bubble in vertical gas-liquid slug flow, PhD Thesis.* Houston, USA: Department of Chemical Engineering.

Sullivan, S., Hardy, B. & Holland, C., 1964. formation of air bubbles at orifices submerged beneath liquids. *american institue of chemcial engineering journal,* 10(6), pp. 848-854.

Tan, R., Chen, W. & Tan, K., 2000. A non spherical model for bubble formation with liquid cross flow. *chemical engineering science,* 55(24), pp. 6259-6267.

Taricska, J. et al., 2008. Submerged Aeration. In: N. Shammas, ed. *Handbook of Environmental Engineering, Volume 8: Biological Treatment Processes.* Totowa, NJ: Humana Press, p. 818.

Tchobanoglous, G., Burton, F. & Stensel, H., 2002. *Wastewater engineering: Treatment and reuse.* IV ed. University of California: McGraw-Hill Higher Education.

Therning, P. & Ramuson, A., 2005. LDA measurements of liquid velocities in a refractive index matched packed bubble column. *Chemical Engineering Science,* 60(3), pp. 717-726.

Thorne, J., 2006. *Engineering Data Book III, Wolverine Tube Inc.* 1st ed. Lausanne, Switzerland: Wolverine Tube Inc.

Thoroddsen, S., Etoh, T. & Takehara, K., 1997. experiments on bubble pinch off. *physics of fluids,* 19(4), pp. 42101-1-42101-29.

Thorpe, R., Evans, G., Zhang, K. & Machniewski, P., 2001. Liquid recirculation and bubble break up beneath ventilated cavities in downward pipe flow. *Chemical Engineering Science,* 56(1), pp. 6399-6409.

Toor, H. & Marchello, J., 1958. Film-penetration model for mass and heat transfer. *AIChE,* 4(1), pp. 97-101.

Valentas, K., Bilous, O. & Amundson, N., 1966. Analysis of breakage in dispersed phase systems. *Industrial engineering chemistry fundamentals,* 5(2), pp. 271-279.

ValorSabio, 2013. *Valor Sabio Engineering Innovation.* [Online]
Available at: www.valorsabio.com [Accessed 02 March 2013].

Varley, J., 1995. Submerged gas-liquid jets. *Chemical Engineering Science,* 50(5), pp. 901-905.

Versteeg, H. & Malalasekera, W., 1996. *An Introduction to computational fluid dynamics: the finite volume method.* 2nd ed. s.l.:Prentice Hall.

Wallis, G. B., 1969. *One Dimensional Two Phase Flow.* 1st ed. Michigan: University of Michigan.

Wang, L., Pereira, N. & Hung, Y., 1973. *Handbook of environmental enginering: Volume 8 - Biological Treatment Processes.* 1st ed. NY: Hummana Press.

Welty, J., Wicks, C., R.Wilson & Rorrer, G., 2000. *Fundamentals of Momentum, Heat, and Mass Transfer.* 5th ed. Oregon state university: John Wiley and sons, Inc.

Westerman, P. & Zhang, R., 1997. Aeration of livestock manure slurry and lagoon liquid for odor control: a review. *Appl. Eng. Agric,* 13(2), pp. 245-249.

West, H., 2009. *Apparatus and method for introducing a gas into a liquid - GB 2471280 A,* London: UK Patent Application.

West, H. & Faram, M., 2010. *Low-energy wastewater aeration using advanced venturi technology.* Leeds, UK, 4th European water and wastewater management conference.

Whalley, P., 1980. *Multiphase flow and pressure drop.* 2nd ed. Washington DC: Heat exchanger design handbook.

Wongsuchoto, P., Charinpanitkul, T. & Pavasant, P., 2003. Bubble size distribution and gas-liquid mass transfer in airlift reactors. *Chemical Engineeing Journal,* 92(1), pp. 81-90.

Zhang, Z. & Zhu, J., 2005. Effectiveness of short-term aeration in treating swine finishing manure to reduce odour generation potential. *Agriculture, Ecosystems and Environment,* 105(1), pp. 115-125.

Zhu, J., 2000. A review of microbiology in swine manure odor control. *Agric. Ecosyst. Environ,* 78(1), pp. 93-106.

Zun, I., 1980. The transverse migration of bubble influence by walla in vertical bubbly flow. Volume 6.

APPENDIX A

MASS TRANSFER DIMENSIONAL ANALYSIS

A.1. Dimensional analysis for mass transfer

Considering the mass transfer of oxygen from bubbles of air to a flowing liquid through a pipe. The transfer is a result of the concentration driving force. The important variables, their symbols and their dimensional representations are listed in Table A.1.

Table A.1: - Relevant quantities and their dimensions for aeration.

Quantity	Symbol	Dimension
Mass transfer coefficient	k	$\frac{L}{t}$
Diffusion coefficient	D	$\frac{L^2}{t}$
Bubble diameter	d	L
Bubble velocity	U_a	$\frac{L}{t}$
Water density	ρ	$\frac{M}{L^3}$
Water Viscosity	μ	$\frac{M}{Lt}$

Using the Buckingham method of grouping the variables, it can be determined that there will be three dimensionless groups. Using the core variables as D, ρ and d, the three pi groups to be formed are,

$$\pi_1 = D^a \rho^b d^c k \quad [A.1]$$

$$\pi_2 = D^a \rho^b d^c u \quad [A.2]$$

and

$$\pi_3 = D^a \rho^b d^c \mu \quad [A.3]$$

Writing π_1 in dimensional form,

$$\pi_1 = D^a \rho^b d^c k \quad [A.4]$$

$$\pi_1 = \left(\frac{L^2}{t}\right)^a \left(\frac{M}{L^3}\right)^b (L)^c \left(\frac{L}{t}\right) \quad [A.5]$$

Equating the indices of the fundamental dimensions on both sides of the equation we have for,

$$\text{M:} \quad 0 = 2a - 3b + c + 1 \quad [A.6]$$

$$\text{t:} \quad 0 = -a - 1 \quad [A.7]$$

and

$$\text{L:} \quad 0 = b \quad [A.8]$$

The solution of these equations for the three unknown exponents yields, a = - 1, b = 0 and c = 1. Thus π_1 is

$$\pi_1 = \frac{kd}{D} \quad [A.9]$$

which is the Sherwood number, Sh.

Using the same method, the other two pi groups can be determined, shown in Equations A.10 and A.11.

$$\pi_2 = \frac{du}{D} \quad [A.10]$$

and

$$\pi_3 = \frac{\mu}{\rho D} \quad [A.11]$$

where π_3 is the Schmidt number. Dividing π_2 by π_3 gives,

$$\frac{\pi_2}{\pi_3} = \frac{du\rho}{\mu} = Re \quad [A.12]$$

the Reynolds number.

The result of the dimensional analysis of mass transfer from a bubble in a fluid indicates a correlating relation could be of the form,

$$Sh = f(Re, Sc) \quad [A.13]$$

A.2. Dimensional analysis for pressure loss

Considering the pressure loss from a two-phase mixture of air and water flowing through a pipe. The important parameters, their symbols and their dimensional representations are listed in Table A.2.

Table A.2: - Relevant quantities and their dimensions for pressure loss.

Quantity	Symbol	Dimension
Pressure Loss	ΔP	$\frac{M}{Lt^2}$
Velocity	U	$\frac{L}{t}$
Density	ρ	$\frac{M}{L^3}$
Viscosity	μ	$\frac{M}{Lt}$
Diameter	d	L
Length	L	L
Surface roughness	ε	L

Using the Buckingham method of grouping the variables, it can be determined that there will be four dimensionless groups. Using the core variables as u, ρ and d, the three pi groups to be formed are,

$$\pi_1 = u^a \rho^b d^c \Delta P \quad [A.14]$$

$$\pi_2 = u^a \rho^b d^c L \quad [A.15]$$

$$\pi_3 = u^a \rho^b d^c \mu \quad [A.16]$$

and

$$\pi_4 = u^a \rho^b d^c \varepsilon \quad [A.17]$$

Writing π_1 in dimensional form,

$$\pi_1 = u^a \rho^b d^c \Delta P \quad [A.18]$$

$$\pi_1 = \left(\frac{L}{t}\right)^a \left(\frac{M}{L^3}\right)^b (L)^c \left(\frac{M}{Lt^2}\right) \quad [A.19]$$

Equating the indices of the fundamental dimensions on both sides of the equation we have for,

$$\text{M:} \quad 0 = b + 1 \qquad [A.20]$$

$$\text{t:} \quad 0 = -a - 2 \qquad [A.21]$$

and Equation A.22 for L.

$$\text{L:} \quad 0 = a - 3b + c - 1 \qquad [A.22]$$

The solution of these equations for the three unknown exponents yields, a = - 2, b = - 1 and c = 0. Thus π_1 is,

$$\pi_1 = \frac{\Delta P}{\rho u^2} \qquad [A.23]$$

which is the Pressure number, N_p.

Using the same method, the other three pi groups can be determined such that,

$$\pi_2 = \frac{L}{d} \qquad [A.24]$$

$$\pi_3 = \frac{\mu}{\rho u d} \qquad [A.25]$$

and

$$\pi_4 = \frac{\varepsilon}{d} \qquad [A.26]$$

where π_3 is the inverse of the Reynolds number.

The result of the dimensional analysis of pressure loss from a two-phase mixture flowing down a pipe indicates a correlating relation could be of the form,

$$N_P = f\left(Re, \left(\frac{L}{d}\right), \left(\frac{\varepsilon}{d}\right)\right) \qquad [A.27]$$

As is shown in Chapter 3, the pressure drop from a flow in a circular pipe can be solved using the Moody Chart, where pressure drop is a function of friction factor. It is shown in the Moody chart, that friction factor is a function of entrance length, $\left(\frac{L}{d}\right)$ relative roughness, $\left(\frac{\varepsilon}{d}\right)$ and Re.

APPENDIX B

MASS TRANSFER TESTING

B.1 Dissolved Oxygen, DO

For the mass transfer testing measurements, water in the whole system was de-aerated by sparging it with nitrogen until the DO concentration had fallen to a low (< 2 mg/l) and stable value. The nitrogen was then stopped, the nitrogen bubbles were then allowed to rise from the tank and then a continuous air flow was injected into the downcomer via the insert. The changes in DO concentration was recorded with time until the water became saturated with oxygen.

DO is the term commonly used in liquid analytical work for the measurement of the amount of oxygen dissolved in a unit volume of water. A volume of water in contact with air will absorb air and therefore oxygen until the pressure of the absorbed oxygen exerts at the air-water interface is equal to the pressure exerted at the same interface by the oxygen in the air. At this point the water is said to be saturated with oxygen. The amount of oxygen actually absorbed is quite small, in the region of 5 to 10 parts per million parts of water. Since the DO content is important in many biological and chemical processes, measurements of the amount of DO actually in a water sample is of great importance.

B.2 Clark polarographic oxygen electrode

Membrane oxygen electrodes are the most widely used and accepted method for real-time measurements of DO in water. The Data Harvest Ltd, 3131 oxygen electrode used in this experimental work, shown in Figure B.1 is of the Polarographic (Clark cell) type. The oxygen electrode was based on a simple electrochemical reaction that occurred in water when oxygen was present. The anode and cathode are immersed in electrolyte and separated from the sample by a semi-permeable membrane. This membrane permits the oxygen dissolved in the sample to pass through it to the electrode, while preventing liquids and most ions from doing so. The silver anode is held at a potential of + 750 mV (the polarising voltage) with respect to the gold cathode. The cathode electrochemically reduces the oxygen to hydroxyl ions in the following reaction,

$$O_2 + 4H^+ + 4e^- \rightarrow 2H_2O$$

creating a point of zero oxygen tension (partial pressure) at the cathode.

Provided that diffusion through the membrane is the rate-controlling step in the path of the oxygen to the cathode, the signal current that flows from the anode to the cathode is proportional to the concentration (partial pressure) of oxygen in the sample. This current is dependent on temperature because the

permeability of the membrane changes with temperature by typically 1.5 % per degree C. The adapter converts this tiny current signal into a voltage, compensates it for the temperature of the sample, and allows the output to be calibrated and scaled appropriately.

A thermistor is used to compensate the output for changes in the oxygen permeability of the membrane with temperature over the range 5 to 45 °C. The thermistor is integrated internally in the electrode tip.

The Clark probe type sensor can measure directly at the source without having to sample and therefore risking that the sample will be contaminated either by losing oxygen to or absorbing oxygen from the atmosphere. This method of measurement does not depend on any change in colour, such as in the Winkler method, and this method is also free from interference from other colour bearing components that may already exists in the water. Furthermore, the electrode method does not involve any introduction of reagents, which are dependent on operator error and reagent ageing.

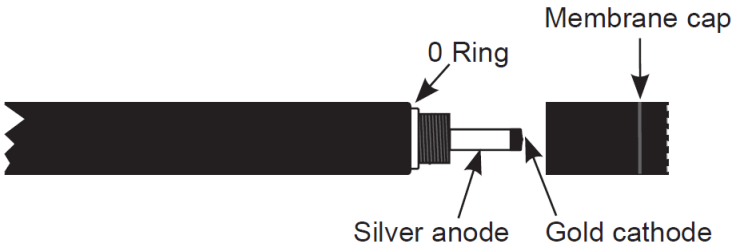

Figure B.1: - The Data Harvest Ltd, model 3131 DO electrode.

B.3 Spatial Variation and mixing testing

At the initial stages of the mass transfer testing, three locations were chosen within the secondary in-active tank, where no air bubbles were found to be present. In addition the DO probe was located at the base of the downcomer. A location within the downcomer was chosen to try and establish the difference in the mass transfer in the downcomer and any further mass transfer in the primary, active tank. Unfortunately, due to the high liquid flow rates and turbulent nature of the flow within the pipe, any DO concentration curves were highly scattered and the measurements were not repeatable.

The three locations within the in-active tank, as depicted in Figure B.2, were at equally spaced intervals down the centre line of the tank and located at half way depth. The ASCE (2007) requirement for spatial variation is that for an individual test, 75 % of the $k_L a_{20}$ values are within ± 10 % of the mean for that test. The lower end of the range of the water and air flow rates, $U_w \approx 1$ ms^{-1}, $Q_a = 50$ slm, was chosen for the spatial variation test. This is because it was seen to have the least amount of mixing, based on visual inspection of the water free surface. The tests were conducted using the V1 insert.

Table B.1: - Spatial variation results across the three DO probe locations.

Probe Position	Q_w (L/s)	Q_a (slm)	Water Temp (˚C)	$k_L a_{20}$ (hr^{-1})	% Difference from mean
1	8.02	50	20.58	8.03	4.2
2	8.08	50	18.96	7.73	0.65
3	8.04	50	19.53	7.30	- 5.3

The results of the spatial variation tests are shown in Table B.1. The mean value for the $k_L a_{20}$ of the 3 probe locations was 7.69 hr^{-1}, with the maximum deviation being 5.3 %. Therefore, the spatial variation across the probe locations was within the ASCE (2007) requirements. From this, the location for all future tests was chosen to be location 2.

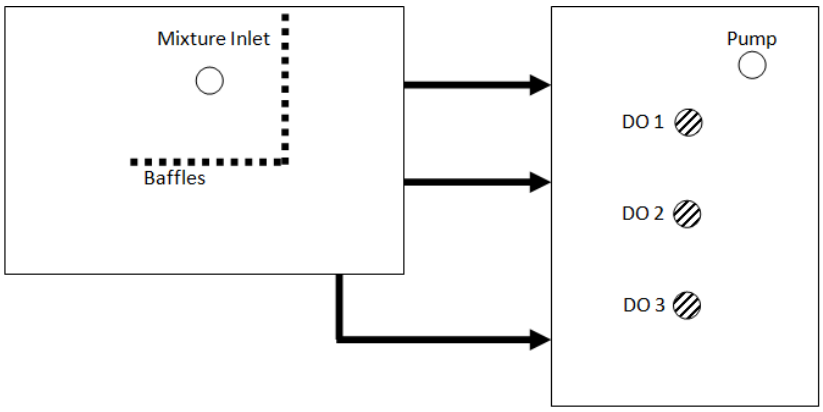

Figure B.2: - A schematic of the test arrangement depicting the three provisional DO probe locations.

B.4 Mass transfer performance calculation method

Once a DO concentration curve has been recorded, using the Easy Sense software provided with the Data Harvest Ltd DO probe, a number of steps were undertaken to determine the overall performance characteristics, Figure B.3 shows a typical DO concentration curve.

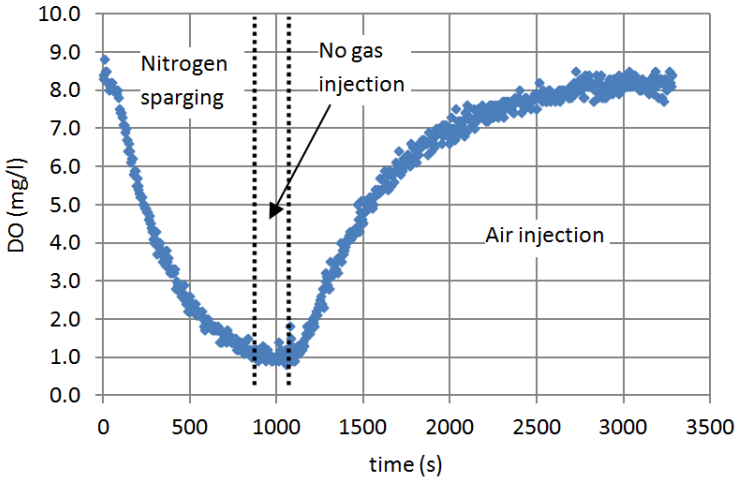

Figure B.3: - A typical DO concentration Profile versus time. This profile corresponds to the HV1 insert for $U_w \approx 1$ ms^{-1}, $Q_a = 50$ slm.

The non-linear regression analysis, NLRA, method involves assuming the initial DO concentration, C_0 and the saturation DO concentration, C_∞^*, values for the run. These are taken from the average stable value between the down step and up step of the test. The NLRA curve is determined using equations B.1

$$DO_{NLRA} = C_\infty^* - (C_\infty^* - C_0)e^{-k_L a(t-t_0)} \quad [B.1]$$

which is integrated from,

$$\frac{dC}{dt} = k_L a(C_\infty^* - C) \quad [B.2]$$

which when integrated from Equation B.3.

$$ln\frac{C_\infty^* - C_0}{C_\infty^* - C} = k_L a(t - t_0) \quad [B.3]$$

Equation B.1 is achieved by rearranging Equation B.3.

An initial guess of the $k_L a$ value is taken and using the solver method within MS excel, aiming to solve for a R^2 value of 1 the value for $k_L a$ is determined.

In order to take the values to standard conditions of a water temperature of 20 ˚C and an atmospheric pressure of 101.325 kPa, pressure and temperature correction factors are applied to the assumed value of C_∞^* and the calculated value of the $k_L a$ such that the $k_L a_{20}$ is calculated using Equation B.4. $C_{\infty 20}^*$ is calculated using Equation B.5 by allowing for the temperature, δ and pressure, Ω correction factors.

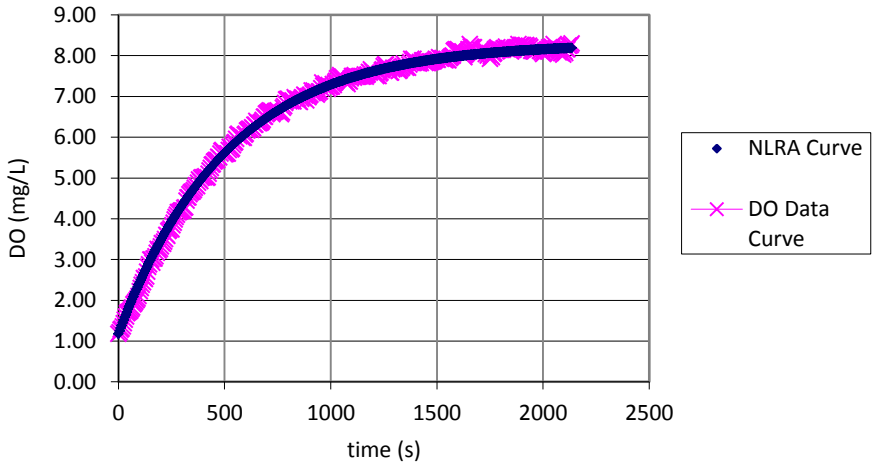

Figure B.4: - DO concentration profile on the up step of Figure B.3 where the curve for NLRA analysis has been added.

$$k_L a_{20} = k_L a \times 1.024^{(T-20)} \quad [B.4]$$

$$C_{\infty 20}^* = \frac{C_\infty^*}{\delta . \Omega} \quad [B.5]$$

where,

$$\delta = \frac{C_\infty^*}{9.09} \; and \; \Omega = \frac{P_{Atmos}}{101325} \quad [B.6] \; [B.7]$$

Using this values the overall mass transfer efficiencies can be calculated,

$$SOTR = k_L a_{20} \times C_{\infty 20}^* \times V_{2ph} \quad [B.8]$$

$$SOTE = \frac{SOTR}{\dot{m}_{O2}} \quad [B.9]$$

$$SAE = \frac{SOTR}{E \times V_{L1}} \quad [B.10]$$

APPENDIX C

EXISTING WASTEWATER VENTURI AERATION TECHNOLOGY

C.1 Existing venturi aerator liquid and gas flow rates

Within the wastewater treatment market, ABS and Mazzei are companies that supply venturi aerators, which are generally located on the base of the aeration tank, with a draft tube to the surface for the air to be entrained, as shown in Figure C.1.

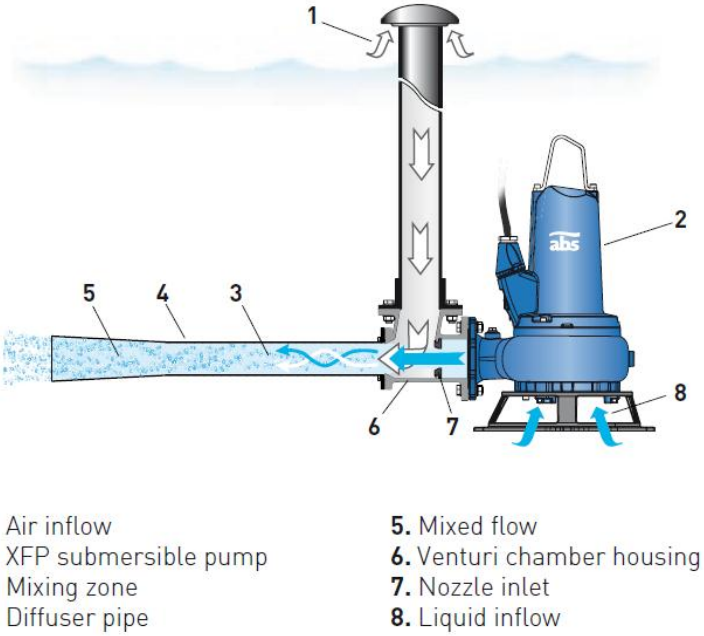

Figure C.1: - ABS Venturi Aerator (ABS Group UK, 2011).

A range of their gas and liquid flow rates, pressure losses, transfer rates and efficiencies for a venturi of the same maximum ID pipe tested in this experimental work are shown below Tables C.1 and C.2 and Figure C.2.

ABS supply a series of 100 mm ID venturi aerators, with various motors attached which operate at different liquid flow rates, as can be seen in Table C.1. Various air flow rates are determined by the depth that the aerator is located within the volume of liquid.

Table C.1: - Performance characteristics of various ABS venturi aerators (ABS Group UK, 2011).

Motor Type	Q_w (L/s)	Q_a (slm)	Power (kW)
PE13/6	13.9	500 – 830	1.6
PE22/4	19.4	670 – 1170	2.5
PE29/4	27.8	750 - 1250	3.0

Mazzei supply a venturi aerator separate from a pump and Table C.2 shows the data for the upper and lower values of the liquid velocities quoted (Mazzei, 2012).

Table C.2: - Mazzei 4inch venturi aerator performance (Mazzei, 2012).

Q_w (L/s)	Q_a (slm)	Power (kW)
8.3	292 - 543	0.05 – 0.22
28.7	242 - 1852	2.97 – 11.68

Figure C.2 below shows the characteristic performances of the ABS and Mazzei venturi aerator systems. The range of liquid flow velocities chosen for the Mazzei venturi approximates to 1, 2 and 3 ms^{-1} in a 4" pipe. There is no mention of what depth of liquid the performance characteristics are given for with the Mazzei system. However, for the ABS system the reported depth is given between 1.5 and 4 m. With the least air entrained at the greatest depth. The ABS system has a nozzle of 55 mm ID, resulting in a blockage ratio of 3.3.

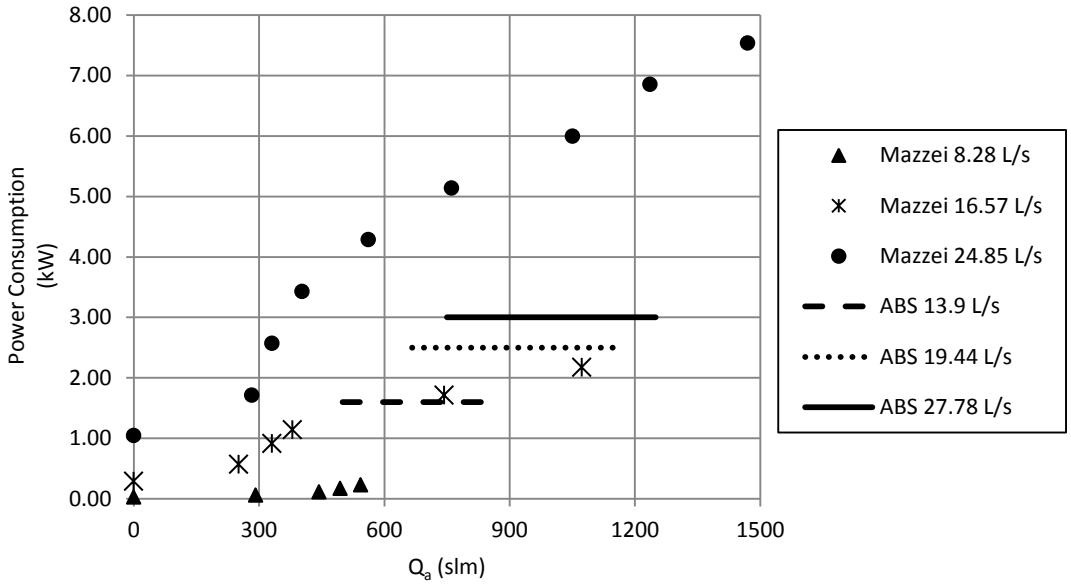

Figure C.2: - Hydraulic performance characteristics for ABS and Mazzei venturi aerators, data taken from (ABS Group UK, 2013; Mazzei, 2012).